



UNIVERSITAT DE
BARCELONA

Rationalization of the Mechanism of Bistability in Dithiazolyl-based Molecular Magnets

Tommaso Francese

ADVERTIMENT. La consulta d'aquesta tesi queda condicionada a l'acceptació de les següents condicions d'ús: La difusió d'aquesta tesi per mitjà del servei TDX (www.tdx.cat) i a través del Dipòsit Digital de la UB (diposit.ub.edu) ha estat autoritzada pels titulars dels drets de propietat intel·lectual únicament per a usos privats emmarcats en activitats d'investigació i docència. No s'autoritza la seva reproducció amb finalitats de lucre ni la seva difusió i posada a disposició des d'un lloc aliè al servei TDX ni al Dipòsit Digital de la UB. No s'autoritza la presentació del seu contingut en una finestra o marc aliè a TDX o al Dipòsit Digital de la UB (framing). Aquesta reserva de drets afecta tant al resum de presentació de la tesi com als seus continguts. En la utilització o cita de parts de la tesi és obligat indicar el nom de la persona autora.

ADVERTENCIA. La consulta de esta tesis queda condicionada a la aceptación de las siguientes condiciones de uso: La difusión de esta tesis por medio del servicio TDR (www.tdx.cat) y a través del Repositorio Digital de la UB (diposit.ub.edu) ha sido autorizada por los titulares de los derechos de propiedad intelectual únicamente para usos privados enmarcados en actividades de investigación y docencia. No se autoriza su reproducción con finalidades de lucro ni su difusión y puesta a disposición desde un sitio ajeno al servicio TDR o al Repositorio Digital de la UB. No se autoriza la presentación de su contenido en una ventana o marco ajeno a TDR o al Repositorio Digital de la UB (framing). Esta reserva de derechos afecta tanto al resumen de presentación de la tesis como a sus contenidos. En la utilización o cita de partes de la tesis es obligado indicar el nombre de la persona autora.

WARNING. On having consulted this thesis you're accepting the following use conditions: Spreading this thesis by the TDX (www.tdx.cat) service and by the UB Digital Repository (diposit.ub.edu) has been authorized by the titular of the intellectual property rights only for private uses placed in investigation and teaching activities. Reproduction with lucrative aims is not authorized nor its spreading and availability from a site foreign to the TDX service or to the UB Digital Repository. Introducing its content in a window or frame foreign to the TDX service or to the UB Digital Repository is not authorized (framing). Those rights affect to the presentation summary of the thesis as well as to its contents. In the using or citation of parts of the thesis it's obliged to indicate the name of the author.

Secció de Química Física
Departament de Ciència de Materials i Química Física
Facultat de Química



UNIVERSITAT DE
BARCELONA

Programa de Doctorat en Química Teòrica i Modelització Computacional
(HDK1G)

Rationalization of the Mechanism of Bistability in Dithiazolyl-based Molecular Magnets

Memòria de tesi presentada per Tommaso Francese per aspirar al
grau de Doctor en Ciències Químiques

Dirigida per:

Prof. dr. Juan José Novoa Vide
Secció de Química Física,
Facultat de Química
Universitat de Barcelona

Prof. dr. Ria Broer
Theoretical Chemistry,
Zernike Institute for Advanced Materials
University of Groningen

Tutor:

Dr. Fernando Mota Valeri
Secció de Química Física, Facultat de Química
Universitat de Barcelona

Barcelona, Gener 2019

A Bianca e alla mia Famiglia

"I was taught that the way of progress was neither swift nor easy"

Marie Skłodowska Curie

The work presented in this doctoral thesis has been carried out at the Materials Science and Physical Chemistry Department of the Chemistry Faculty of the University of Barcelona (UB), and within the Institute of Theoretical and Computational Chemistry (IQTUB).

This project has been possible in virtue of the financial support provided by the European Union Horizon 2020 research and innovation programme under the Marie Skłodowska Curie grant agreement no. 642294. The work has been additionally supported by the Spanish “*Ministerio de Economía, Industria y Competitividad*” (Grant: MAT2014-54025-P and Grant: CTQ2017-87773) and Catalan DURSI (Grant: 2014SGR1422 and Grant: 2017SGR348).

The computational resources were partly provided by the the Institute of Theoretical and Computational Chemistry (IQTUB), the Barcelona Supercomputing Center, the Consorci de Serveis Universitaris de Catalunya (CSUC), the Peregrine HPC cluster and the Nieuwpoort cluster from the Berendsen Center.

Contents

1	Introduction	3
1.1	From Stones to Molecules	3
1.1.1	From Bulk to Molecular Magnets: A Glimpse of the Future . .	4
1.2	Short History of Molecular Magnets	5
1.2.1	The Molar Magnetic Susceptibility	8
1.2.2	The Dithiazolyl-Based Molecular Magnets	10
1.3	Thesis Goals and Outlook	12
2	Methodology	25
2.1	Introduction	25
2.2	The <i>First-Principles Bottom-Up</i> Method	26
2.2.1	First Step: Crystal Analysis and Selection of Radical Pairs . .	26
2.2.2	Second Step: Calculation of Magnetic Exchange Interaction (J_{AB})	27
2.2.3	Third Step: Construction and Diagonalization of the HDVV Hamiltonian	30
2.2.4	Fourth Step: Derivation of the Macroscopic Properties: The Susceptibility	31
2.3	Wave Function-based Methods	33
2.3.1	The Schrödinger Equation	33
2.3.2	The Born-Oppenheimer Approximation	34
2.3.3	The Electronic Wave Function	36
2.3.4	The Hartree-Fock Method	37
2.3.5	Different Formalisms of the HF Theory	39
2.3.6	Variational Methods	42
2.3.7	Perturbative Methods	46
2.4	Density Functional Theory	47
2.4.1	The Kohn-Sham Method	49
2.4.2	The Kohn-Sham Equations	50

2.4.3	Spin Polarized Calculations	53
2.4.4	The Broken-Symmetry Approximation	54
2.4.5	Pseudopotentials	57
2.4.6	Semi-empirical Dispersion Functions: Grimme D3	61
2.4.7	Energy Decomposition Analysis	61
2.5	Dynamical Evolution of the System	62
2.5.1	<i>Ab Initio</i> Molecular Dynamics	63
2.6	Exploring the Potential Energy Surfaces	65
2.6.1	The Nudged Elastic Band Method	66
2.7	CODES	68
2.7.1	Guassain09	68
2.7.2	Quantum Espresso	68
2.7.3	CP2K	68
2.7.4	CPMD	69
2.7.5	Orca	69
3	The Dithiazolyl-based Materials	81
3.1	Introduction	81
3.2	TTTA	85
3.2.1	Crystal Packing Analysis	85
3.2.2	Magnetic Properties	86
3.2.3	Beyond the Static Analysis	87
3.3	4-NCBDTA	90
3.3.1	Crystal Packing Analysis	90
3.3.2	Magnetic Properties	91
3.4	PDTA	93
3.4.1	Crystal Packing Analysis	93
3.5	TDPDTA	96
3.5.1	Crystal Packing Analysis	96
3.6	Summary	98
4	The Origin of the Different Stability of the Two Polymorphs of a Prototypical DTA-based Bistable Material	103
4.1	Introduction	104
4.2	Computational Details	108
4.3	Results and Discussion	110
4.3.1	Intermolecular Interactions in Isolated Pairs of TTTA Radicals	110

4.3.2	Intermolecular Interactions Model System Considering Periodic Boundary Conditions	114
4.3.3	Evaluation of the Nature of the Key Intermolecular Interactions	117
4.4	Conclusions	123
4.5	Acknowledgements	124
5	The Magnetic Fingerprint of DTA-based Molecule Magnets	133
5.1	Introduction	134
5.1.1	Methodological Details	137
5.2	Results and Discussion	138
5.2.1	Magnetic susceptibility curves: calculated <i>vs.</i> experimental	139
5.2.2	Evaluating the nature of the magnetic interactions in DTA-based materials: magneto-structural correlation maps	142
5.2.3	Electronic <i>vs.</i> structural contributions	148
5.3	Conclusions	151
5.4	Acknowledgements	152
6	New Mechanism for Triggering Spin Transition in Dithiazolyl-based Materials	159
6.1	Introduction	160
6.2	Susceptibility Curves	165
6.3	Structural Models	167
6.4	Computational Information	171
6.5	Results	172
6.5.1	Optimum Configuration of HT-PDTA and HT-TDPDTA Polymorphs	172
6.6	Dynamics of the HT Polymorphs at Room Temperature	176
6.6.1	Average Structures Configuration	176
6.6.2	Thermal Ellipsoids	179
6.6.3	Distances Distribution Analysis	182
6.6.4	The Pair-Exchange Dynamic Mechanism <i>via</i> Nudged Elastic Band Algorithm	185
6.6.5	Maps Scans: Evidence of the Role of the Longitudinal Slippage	188
6.7	Conclusions	193
7	Outlook and Future Challenges	201
8	Summary	209
8.1	Introduction of the Research Project	209
8.2	Project Goals and Motivations	212

8.3	The PDTA and TDPDTA systems	213
8.4	Computational Tools	215
8.4.1	Static Analysis	215
8.5	Dynamical Analysis	219
8.5.1	Ab Initio Molecular Dynamics	219
8.6	Results	219
8.6.1	Static Analysis	219
8.7	Dynamical Analysis	224
8.8	Discussion and Conclusions	232
	Appendices	239
	A Supplementary Information of Chapter 5	241
A.1	Spin Density of TTTA, PDTA, 4-NCBDTA and TDPDTA	242
A.2	Atomic coordinates of LT and HT magnetically dominant pairs of radicals for TTTA, PDTA, TDPDTA, and 4-NCBDTA.	243
A.3	Selection of magnetic model of PDTA and TDPDTA.	245
A.4	Benchmarking the J_{AB} magnetic coupling interactions computed at DFT/UB3LYP level with Difference Dedicated Configuration Interac- tion (DDCI-3) method.	250
A.5	TDPDTA shifted configurations.	257
A.6	Interaction Energy Maps of TTTA, PDTA, 4-NCBDTA, and TDPDTA.	259
	Acknowledgements	263

Chapter 1

Introduction

This introductory Chapter is organized in order to guide the reader through the different steps that have brought to the research and development of molecular magnets. The history of magnetism and its technological applications evolve in parallel with our own history. The first examples of compasses already saw their birth in ancient China, although the real source of magnetism has remained unknown until the end of the 19th century. Since then, the new-born quantum mechanical theory gave an extraordinary contribution to the interpretation of this property. Magnetism has been extensively exploited in a countless set of devices. A brief summary of the most important results achieved in the past, as well as the current *state-of-the-art* in the field, are here reported. Finally, the motivations and goals for the research developed in this doctoral thesis are provided.

1.1 From Stones to Molecules

Since the early stages of human history, natural phenomena have triggered a continuum of experiences and discoveries, contouring the different human communities and their expansion, or extinction. As a rule of thumb, the more the society was technologically advanced, the higher were the chances to survive. At their time, the Chinese, the Egyptian and the Roman empires witnessed long periods of prosperity thanks to their technological supremacy with respect to the neighbouring populations. Nowadays, although still valid, the technological supremacy is only one of the different ways to compete in a globalized society.

In the plethora of discoveries that enhanced our knowledge of nature, magnetism is to be considered one of the most relevant. Evidences of knowledge of magnetism date back to both ancient China and Greece. The first source of magnetism discovered were the magnetite-based (Fe_3O_4) rocks, called *lodestones*. These natural bulk magnets, if properly suspended, align with the Earth magnetic field[1, 2]. Soon, the ancient populations realized that also a small piece of iron can become magnetic, once it gets in touch with a lodestone. Believed to have magical origin, this fascinating property found a practical application in the magnetic iron needles of the first compasses already around 1088 a.c., as described by Sheng Kua[3]. Before the advent of compasses, people used to “*sail by sight*”. The introduction of these tools marked a new era into navigation systems, enabling the discovery of new places and navigation routes in the following centuries. Despite the remarkable use of it in primitive compasses, it is only in the last two centuries that magnetism saw its “golden age”. The real contribution towards the rationalization and understanding of magnetism in its basic concepts started only in the late 19th century, to be extensively investigated along all the 20th century. The 19th century, defined as the “electromagnetic age”, saw the unification of apparently separate phenomena like light, electricity and magnetism thanks to Maxwell, as reported in his famous paper entitled “*A Dynamical Theory of the Electromagnetic Field*”[4] published in 1865; the 20th century, instead, witnessed the birth of the modern quantum theory, and in turn, the “understanding age” of magnetism according to Coey’s classification of the history of magnetism in seven ages[5]. Since then, magnetism has been employed in an extended class of devices. Currently, we are living in the “Age of spin electronics”, the time in which[5]

“we are just now beginning to learn how to manipulate spin currents and to make good use of them”.

Deciphering such a complex phenomenon like magnetism led us to reach technological breakthroughs. Nowadays, it can be found in daily common tools used, like clocks, smartphones and storage devices for example; but it plays also a fundamental role in the most advanced experiments that are currently being performed, like in the Large Hadron Collider (LHC) at CERN[6] or in the new generation of plasma reactors[7].

1.1.1 From Bulk to Molecular Magnets: A Glimpse of the Future

The natural reservoirs of transition elements, the natural sources[8] of strong magnetism known since the very beginning, are running out. This drawback is pushing the research for new and more environmental friendly solutions. This does not

mean to look for exotic elements or to make use of futuristic technologies. We have, instead, to consider the use of more abundant elements at our disposal[9–12](*e.g.* carbon, nitrogen, sulphur, oxygen, selenium) and to better engineer what is already known, and, eventually, to drive the synthesis of new compounds.

Thanks to organic and supramolecular chemistry, nowadays we have at our disposal an incredible number of molecular compounds, with a wide spectrum of properties (*e.g.* optical, electronic, magnetic). One of the most challenging goals that supramolecular chemistry is trying to achieve is to reproduce the bulk properties of magnets by manipulation at a molecular level. But moving from bulk systems composed of transition metals, which are intrinsically favorable to generate magnetic compounds, to organic-based ones, offers some non-trivial challenges to overcome, like the material stability, lifetime, etc. Nevertheless, potentially, there are many advantages related to the use of molecular systems, like the possibility of thin films deposition, transparency, low density, limited production costs, and so on. An ideal molecular crystal should be customizable in order to present a specific spatial molecular arrangement, favoring ferromagnetism or paramagnetism, depending on the final application of the material. Moreover, it should be stable also at room temperature, and it should have an extended lifetime use.

Molecular magnets are among the most suitable potential candidates for advanced devices like data storage, sensors and quantum computers. The structural arrangement is mainly governed by covalent bondings or weaker forces, like hydrogen bonds. Moreover, the synthesis of molecule-based materials can be done under mild conditions of temperature and pressure. The magnetic materials based on carbon, sulphur, oxygen and nitrogen requires a fraction of the energy of the inorganic counterpart. On top of that, they can be recycled, avoiding the disposal of environmentally dangerous wastes.

1.2 Short History of Molecular Magnets

The first example of ferromagnetic ordering in molecular magnets was reported by Miller and co-workers[13–15], for $[\text{Fe}(\text{C}_5\text{Me}_5)_2]^{\bullet+}[\text{TCNE}]^{\bullet-}$ (TCNE=tetracyanoethylene) (see Fig. 1.1). Although remarkable, the magnetic property of this compound arises only below a certain critical temperature ($T_C < 5 \text{ K}$). Clearly, this material was not suitable for practical applications for devices operating at room temperature (RT). Since then, a lot of effort has been devoted to the synthesis of RT molecular magnets. This breakthrough was achieved in 1991, with the synthesis of the charge-transfer salt $\text{V}(\text{TCNE})_x(\text{CH}_2\text{Cl}_2)_y$ [16]. Then, around 1995/1996, some Prussian-blue

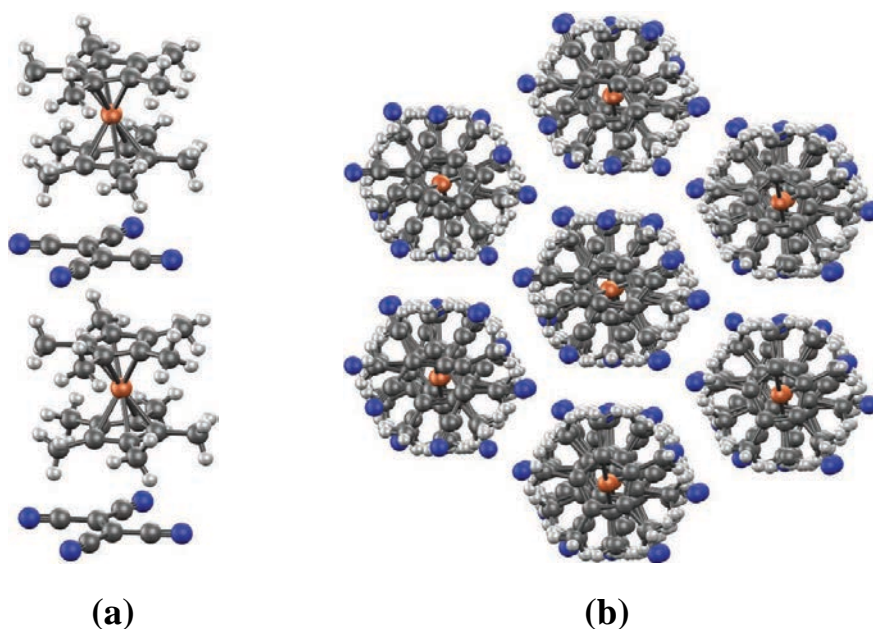


Figure 1.1: Crystal structure of the $[\text{Fe}(\text{C}_5\text{Me}_5)_2]^{\bullet+}[\text{TCNE}]^{\bullet-}$ compound, showing the (a) chain and (b) the crystal packing.

derivatives were added to the list of RT molecular magnets[17–20]. Three decades later, the list of these organic compounds has been greatly extended. Nowadays, the principal families of free radicals and corresponding derivatives investigated are verdazyl[21, 22], triphenylmethyl[23–31], phenalenyl[32, 33], nitroxide[34–42] and dithiazolyl[43–47] based radicals (see Fig. 1.2). These organic molecular magnets have all of the properties commonly attributed to metal-based (or atom-based) magnets, like, for example, coercivity[48]. While many examples of organic molecular magnets have been studied[49–58], we are still far from a complete control over their properties, and, in turn, a practical application. For a detailed description of the evolution of molecule-based magnets, the reader is encouraged to read the review “Organic magnets, a history” by Miller[59].

The basic building blocks composing molecular crystals with magnetic ordering are either pristine organic radicals, coordination compounds or a combination of both. Each single unit must host, at least, an unpaired electron. In the case of neutral radicals, many strategies have been applied to prevent their high reactivity. Among the most relevant, it is worth to mention the steric protection and the use of het-

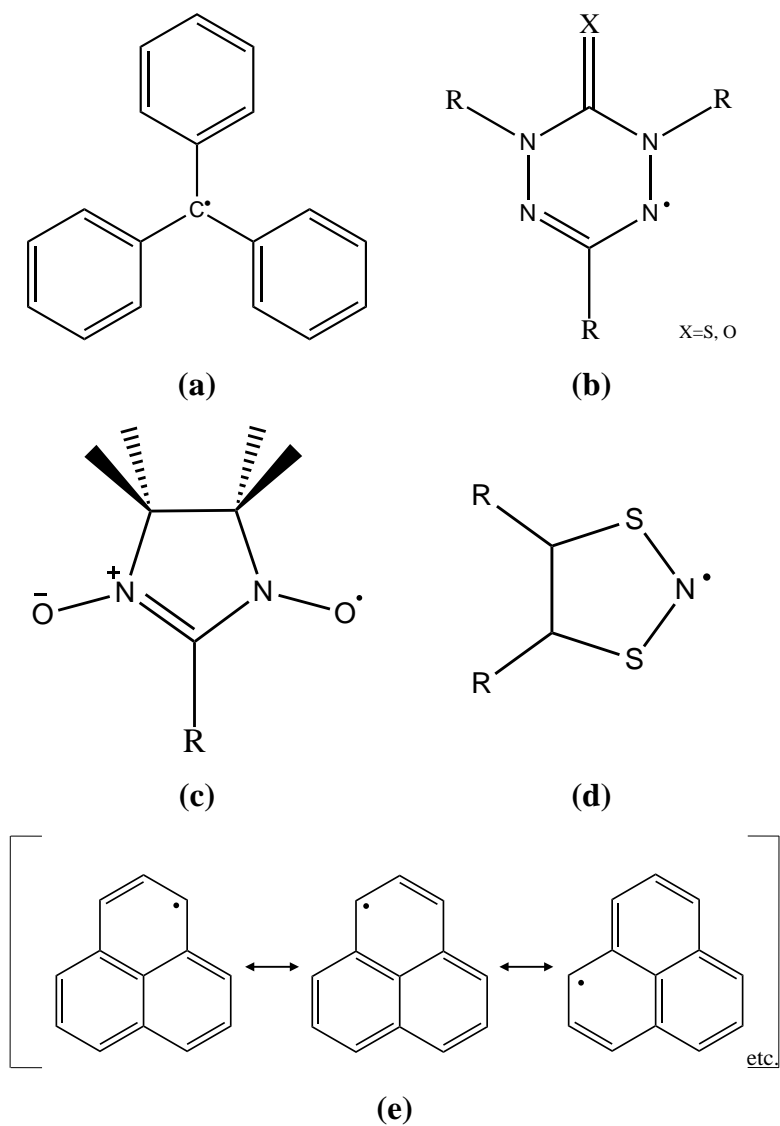


Figure 1.2: Principal families of organic free radicals: (a) Triphenylmethyl, (b) Verdazyl, (c) Nitronyl Nitroxide, (d) Dithiazolyl and (e) Phenalenyl.

eroatoms. The first can suppress the dimerization reaction and can dramatically change the crystal structure, while the latter, for example, exploits the lone pair electrons to control the intermolecular electronic interactions. The use of heteroatoms

also affects the spin density over the molecular skeleton[60]. While in the case of the ferrocenium ion of the coordination compound (*e.g.* $[\text{Fe}(\text{C}_5\text{Me}_5)_2]^{\bullet+}[\text{TCNE}]^{\bullet-}$), the unpaired electrons are highly localised in the *d* or *f* shells of the transition metal, in the case of purely organic compounds based on light elements (H, C, N, O), the unpaired electrons reside in the *s* and *p* orbitals. More recently, Oakley and co-workers have reported that making use “heavy atoms” like S or Se, is a good strategy to increase the critical temperature of magnetically-ordered systems[61]. The formation of molecule-based magnets is a consequence of the alignment of spins due to unpaired electrons with suitable interactions through π electrons[60].

As highlighted by Ratera and Veciana[60], the skeleton of stable neutral radicals plays an important role in the 1) good stabilization of the spin and 2) modulating and controlling the electronic structure which will control the intermolecular interactions responsible for the physical-chemical properties of the material.

1.2.1 The Molar Magnetic Susceptibility

Experimentally, the magnetic response of a material is evaluated by means of the magnetic susceptibility (χ), which measures to which extent a material is magnetized by an applied external magnetic field. The molar magnetic susceptibility[62] is equivalent to the ratio between the molar magnetization M , and H , the magnetic field applied to the material

$$\chi = \frac{M}{H} \quad (1.1)$$

This formulation of χ is only valid at 1) not too low temperatures and 2) very small magnetic fields. The molar susceptibility units of χ are, in CGS[63] units, $[\text{emu}\cdot\text{mol}^{-1}]$. A more advantageous and easier interpretation of the susceptibility is provided when χ is multiplied by the corresponding temperature value

$$\chi T = \frac{M}{H} \cdot T \quad (1.2)$$

The units of χT are $[\text{emu K mol}^{-1}]$. In the manuscripts reported in the thesis we made use of the second definition of the susceptibility, because it provides a more sensitive means to detect small magnetic variations associated with the structural arrangement as a function of the temperature range. If χT is constant as the temperature decreases, it means that the Curie’s law is obeyed. On one hand, if χT increases as the temperature decreases, it means that there are dominant ferromagnetic interactions. On the other hand, if χT decreases as the temperature decreases, it means that there are dominant antiferromagnetic interactions.

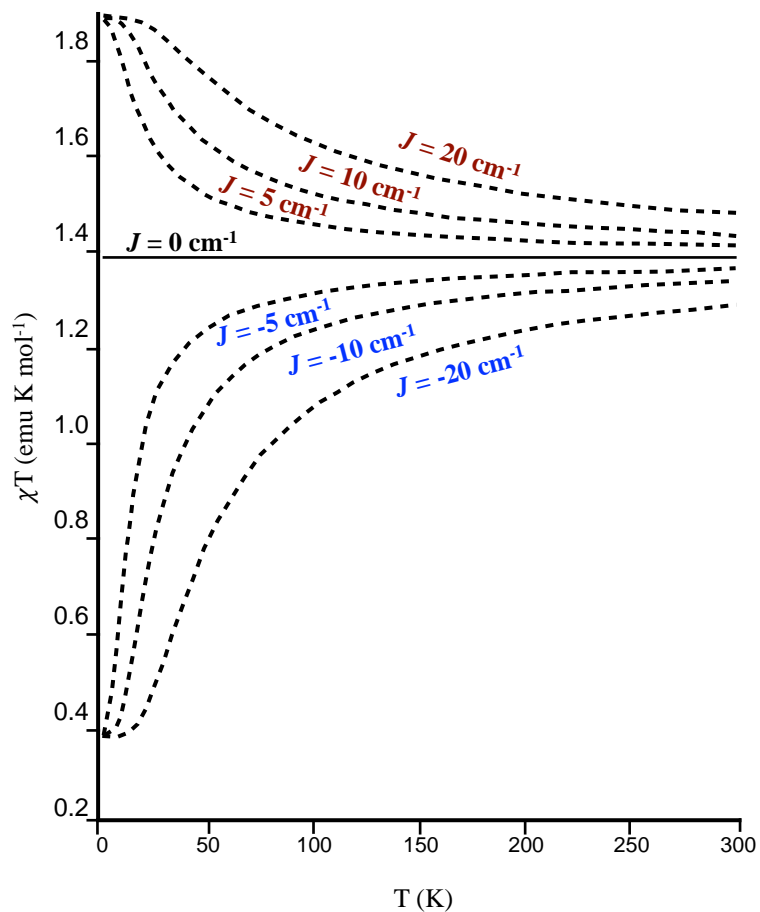


Figure 1.3: Susceptibility curves as a function of positive (FM) or negative (AFM) J values.

Magnetic materials, in the most general classification, may be diamagnetic, paramagnetic or ferromagnetic. Diamagnetic materials (*e.g.* pyrolytic carbon), are repelled by an external magnetic field. On the contrary, paramagnetic materials (*e.g.* platinum), are weakly attracted by an external magnetic field., while ferromagnetic materials (*e.g.* cobalt, iron, neodymium,..) are strongly attracted by an external magnetic field.

1.2.2 The Dithiazolyl-Based Molecular Magnets

Recent years have witnessed incredible developments in the study of organic molecular magnets based on the dithiazolyl (DTA) moiety (see Fig. 1.4). The attention

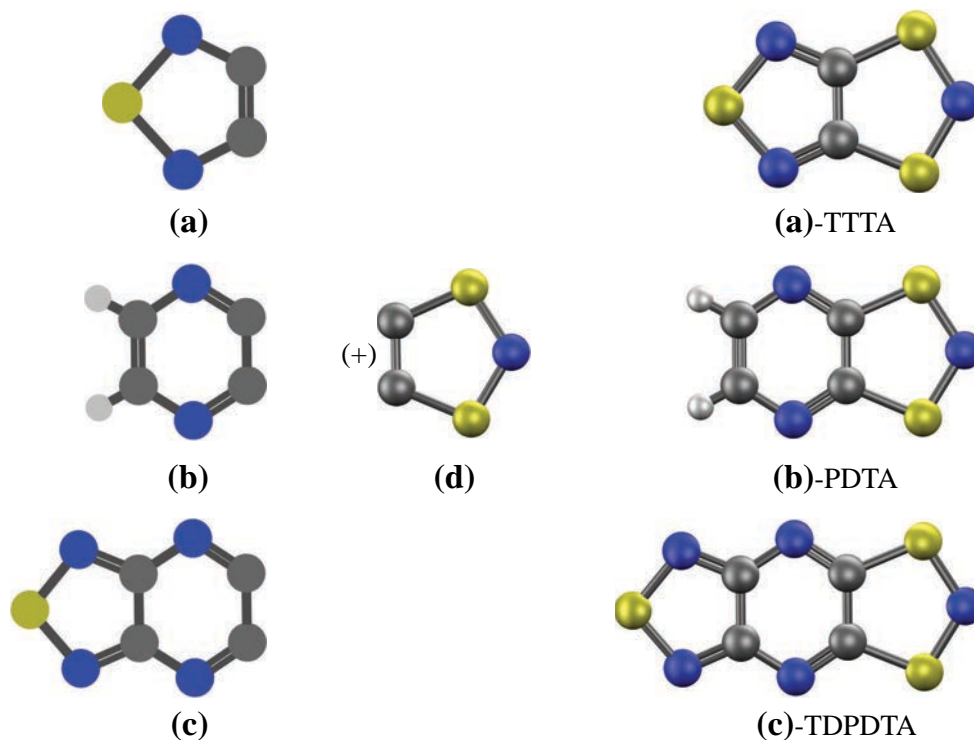


Figure 1.4: Examples of DTA-based compounds, where the DTA moiety (d) is added to different possible substituents (a), (b) and (c), creating the corresponding compounds (a)-TTTA, (b)-PDTA and (c)-TDPDTA.

paid to the DTA-based crystals comes from the possibility to have a wide range of structural arrangements that can be obtained while maintaining radical open-shell character, qualifying the corresponding compounds as persistent and stable. Banister[64] pioneered the research of these compounds, with an accurate analysis of the C/N/S rings[65]. Oakley[43, 44] and Chivers[46], among others, gave a remarkable contribution to the synthesis of these compounds, based on the original idea from Haddon[47]. The DTA radical family is composed of *circa* 40 compounds[66], presenting a spectrum of magnetic behaviors. In particular, two sets of compounds received a lot of attention in the last years. The first set contains spin-crossover (also

known as spin-switch)[67–70] materials (SCO). In this case, the spin state of the material changes without affecting the crystalline structure of the system. The second case, instead, contains compounds presenting bistability, where

“Bistability is the ability of a material to present two stable phases that can both exist within a given range of temperatures, but above and below that range, only one or the other phase exists”

The technological advantage associated with a compound with such magneto-structural behavior would be enormous. The prototype crystal presenting this bistable property and that has been extensively investigated is the 1,3,5-trithia-2,4,6-triazapentalenyl (TTTA) (see Figure 1.5). This system presents a susceptibility curve with a wide hysteresis loop that encompasses room temperature. The LT phase has a triclinic habit, whereas the HT phase is monoclinic. The structure at equilibrium of the first polymorph presents dimers. Hence, this phase is magnetically silent. The HT polymorph, instead, has been identified as an averaged structure, since a continuous coupling/decoupling mechanism occurs between dimers within the columns along the stacking direction. In turn, it has been shown that this phase is paramagnetic. A more detailed analysis of this compound will be provided in Chapter 3. Here, it is sufficient to mention that the static and dynamical analysis of this crystal, as reported in recent papers[71–74], gave for the first time a unique chance to decipher how the transition from the low temperature polymorph to the high temperature one occurs in thermodynamical terms, and how magnetic interactions within the crystal are affected. Unfortunately, the structural variables involved in the LT↔HT phase transition still remain unknown. It is also due to the fact that simulating phase transitions is by no means an easy task.

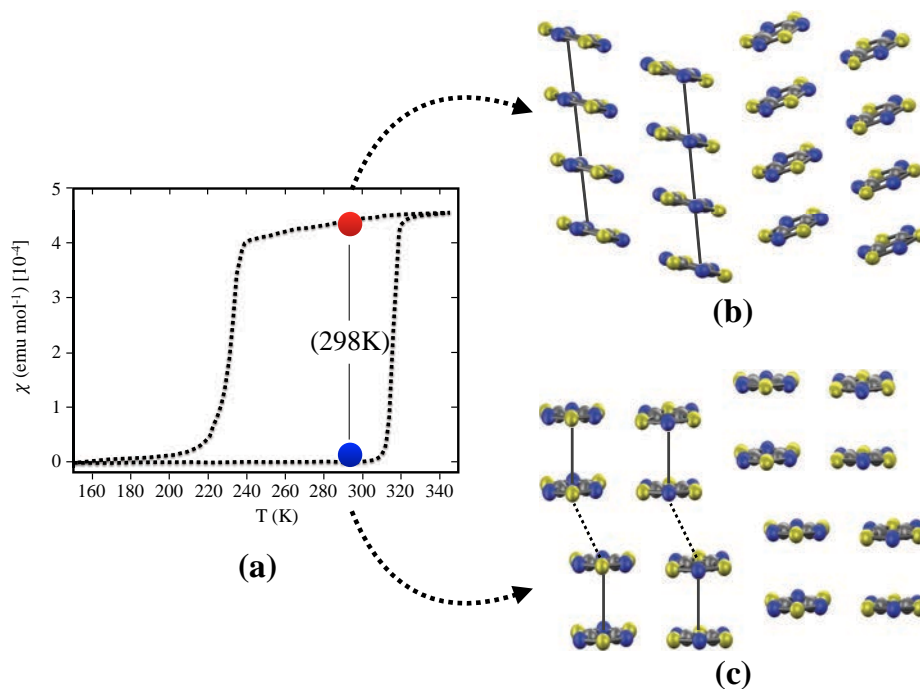


Figure 1.5: The susceptibility curve of the TTTA materials (a) and the HT (b) and LT (c) polymorphs studied. It is possible to see the particular geometrical arrangement of the two polymorphs, where the LT phase presents eclipsed dimers while the HT phase presents a uniform stack. Both these structures have been experimentally resolved at 298K.

1.3 Thesis Goals and Outlook

The general motivation that justifies the effort to study DTA-based compounds mainly concerns with the possibility of employing the DTA-based compounds to promote a new generation of more efficient devices, especially targeting the ones for memory storage. In this sense, theory plays a key role in elucidating the common and different properties between different systems, especially if they belong to the same family, in the light of the same model approach. The main goal I aim to accomplish in this work is to justify the possibility of different magnetic behaviors as a function of the kind of substituent attached to the DTA moiety and, in turn, their corresponding crystal packing. On the line of the work performed by Vela and coworkers[72–74] on the prototype TTTA material, both from a static and dynamical point of view,

the investigation of PDTA, TDPDTA and 4-NCBDTA compounds, respectively (see Fig. 1.6), will be presented. The interest on these particular structures lies on their bistable character. The PDTA and TDPDTA compounds will be analysed in details because of their rather large bistable range, as will be discussed in Chapter 3. The 4-NCBDTA instead, which is not bistable but spin-switchable, will be account for sake of comparison with respect to TTTA, PDTA and TDPDTA materials. Different

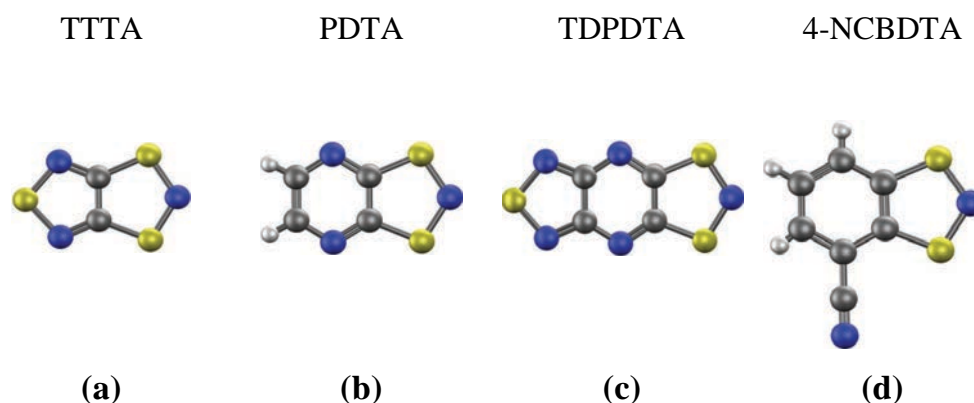


Figure 1.6: The DTA-based compounds analyzed in this thesis are TTTA (a), PDTA (b), TDPDTA (c) and 4-NCBDTA (d). To each of them a number is assigned as a shorten notation which will be used to refer to them specifically.

techniques and methodologies have been used to investigate this set of compounds from different points of view. The ultimate intent is to depict a more clear reason why some specific arrangements of some compounds favor a diamagnetic rather than a paramagnetic behavior, or *vice versa*. Moreover, a possible explanation of the driving force triggering the phase transition of these organic molecular magnets will be provided, in the light of the results achieved.

In the past, a solid computational protocol called *First-Principles Bottom-Up*[75, 76] (FPBU) approach has been successfully used in an extended analysis of the magnetic topology (*i.e.* the propagation of the magnetic interactions within the molecular crystal along the 3D axes) for a multitude of different molecular magnets. This technique is also used here with the same intent, and it will be discussed in details in Chapter 2. The derivation of the magnetic exchange interactions values have been performed at different levels of theory and methods, as will be discussed later, employing both Density Functional Theory and the (high level) wavefunction methods like Complete Active Space Self-Consistent-Field and Difference Dedicated Config-

uration Interaction. On top of the magnetic analysis, also geometry/variable-cell optimizations in the solid state and interaction energy calculations are performed. On one hand the optimized structures are fundamental to study the equilibrium configuration of the system and, eventually, to later extrapolate intermediate structures, sampling the evolution of the system as a function of time and temperature in *Ab-Initio* Molecular Dynamics calculations. On the other hand, the study of how the columns pack and how energetically they contribute to stabilize the system is a fundamental aspect for understanding the mechanisms that drive the phase transition.

The thesis is organized following the natural development of the research during the last three years, as follows:

- Chapter 2 : in this Chapter, an overview of the different theoretical methodologies used to investigate the systems is presented. In the first part of this chapter, the Hartree-Fock (HF) method will be briefly reported, with its limits. Then, the post-HF methods used to recover the correlation term will be shortly presented. In particular, attention will be put on the relation with the magnetic coupling[77]. In the second part, the Density Functional Theory (DFT) method will be presented, with particular emphasis on the DFT method applied to periodic systems, used to simulate the crystalline phases of the systems mentioned above. In the third part, a brief overview of the theory behind the AIMD method will be reported. Finally, will be presented a detailed description of the *First-Principles Bottom-Up* (FPBU) methodology. The Hartree-Fock and Post-Hartree-Fock theory provided here can be explored in deep in the reference manual "Modern Quantum Chemistry"[78], while for DFT theory is referenced to "Electronic Structure: Basic Theory and Practical Methods"[79];
- Chapter 3 : in this Chapter, a detailed description of the DTA-based compounds investigated is reported. The crystalline structures as well as the chemical properties of each single compound will be presented, underlining the similarities and differences with respect to the prototype TTTA material;
- Chapter 4 : in this Chapter, a systematic computational study of the intermolecular interactions characterising the LT and HT polymorphs of the prototype TTTA material is provided, elucidating the origin of the energy difference between them and rationalising the crystal packing of the two phases, respectively.

- Chapter 5 : in this Chapter, the different magnetic responses of the different phases of the PDTA and TDPTDA materials have been rationalised employing the FPBU approach. The detailed analysis shows that, while the PDTA material resembles the TTTA prototype compound, the TDPDTA instead deviates, showing both in the LT and HT phases a weaker magnetic coupling. The source of this difference is found in the inter-column interactions (see Appendix A.3). Thanks to the FPBU method, it was possible to unveil this hidden effect. This unusual behaviour of the TDPTDA compound is also investigated by studying the magnetic interactions as a function of the structural arrangements for each DTA-based material. To validate the FM trend predicted by DFT, supplementary *in silico* experiments are performed by means of the wave function Difference Dedicated Configuration Interaction method. To conclude, the interaction energy maps (IEMs) are provided, giving a quantitative estimation of the energetic cost necessary for each compound to be in a FM arrangement.
- Chapter 6 : in this Chapter, a new spin transition mechanism, found to operate in the TDPDTA material, is proposed for the first time, by directly comparing the results from the AIMD simulations for a set of structures sampled at different temperatures, both for the PDTA and TDPDTA systems. The comparison of the two systems is mainly focused on the respective HT phases, the most interesting ones for technological purposes. The data from the respective variable-cell (VC) optimisations as well as the analysis of the trajectories from the AIMD simulations and their post-processing elaboration are reported, complemented with several *in silico* experiments to prove the phases stability with respect to some metastable structures and the key role that some geometrical variables play in the new stabilization process featuring the TDPDTA material. The TTTA and 4-NCBDTA dynamical results have already been reported[73, 80].
- Chapter 7 : in this Chapter, some final remarks and suggestions for further research are reported as well as a discussion of the implications that the discovery reported in Chapter 6 might have in the quest for controlling the properties of the DTA-based materials for technological purposes.

Bibliography

- [1] P. Wasilewski, G. Kletetschka, *Geophysical Research Letters* **1999**, 26, 2275–2278.
- [2] C. A. Ronan, J. Needham, *The Shorter Science and Civilisation in China, Vol. 2*, Cambridge University Press., **1978**.
- [3] J. Makeham, *China: The World's Oldest Living Civilization Revealed*, Thames & Hudson, **2008**.
- [4] J. Maxwell, *Proceedings of the Royal Society of London* **1863**, 531–536.
- [5] J. Coey, *Magnetism and Magnetic Materials*, Cambridge University Press, **2010**.
- [6] The Large Hadron Collider | CERN,
<https://home.cern/topics/large-hadron-collider>.
- [7] Wendelstein 7-X: Second round of experimentation started | Max-Planck-Institut für Plasmaphysik,
https://www.ipp.mpg.de/4254576/08_17.
- [8] Critical Material Strategy,
https://www.energy.gov/sites/prod/files/DOE_CMS2011_FINAL_Full.pdf.
- [9] The Worlds of David Darling,
<http://www.daviddarling.info/>.
- [10] K. Barbalace, Periodic Table of Elements,
<http://environmentalchemistry.com/yogi/periodic/>.
- [11] J. Khuyagbaatar, A. Yakushev, C. E. Düllmann, D. Ackermann, L.-L. Andersson, M. Asai, M. Block, R. A. Boll, H. Brand, D. M. Cox, M. Dasgupta, X. Derkx, A. Di Nitto, K. Eberhardt, J. Even, M. Evers, C. Fahlander, U. Forsberg, J. M. Gates, N. Gharibyan, P. Golubev, K. E. Gregorich, J. H. Hamilton, W. Hartmann, R.-D. Herzberg, F. P. Heßberger, D. J. Hinde, J. Hoffmann, R. Hollinger, A. Hübner, E. Jäger, B. Kindler, J. V. Kratz, J. Krier, N. Kurz,

- M. Laatiaoui, S. Lahiri, R. Lang, B. Lommel, M. Maiti, K. Miernik, S. Minami, A. Mistry, C. Mokry, H. Nitsche, J. P. Omtvedt, G. K. Pang, P. Papadakis, D. Renisch, J. Roberto, D. Rudolph, J. Runke, K. P. Rykaczewski, L. G. Sarmiento, M. Schädel, B. Schausten, A. Semchenkov, D. A. Shaughnessy, P. Steinegger, J. Steiner, E. E. Tereshatov, P. Thörle-Pospiech, K. Tinschert, T. Torres De Heidenreich, N. Trautmann, A. Türler, J. Uusitalo, D. E. Ward, M. Wegrzecki, N. Wiehl, S. M. Van Cleve, V. Yakusheva, *Physical Review Letters* **2014**, *112*, 172501.
- [12] V. Alekseenko, A. Alekseenko, *Journal of Geochemical Exploration* **2014**, *147*, 245–249.
- [13] J. S. Miller, P. J. Krusic, A. J. Epstein, W. M. Reiff, J. Hua Zhang, *Molecular Crystals and Liquid Crystals* **1985**, *120*, 27–34.
- [14] J. S. Miller, J. C. Calabrese, A. J. Epstein, R. W. Bigelow, J. H. Zhang, W. M. Reiff, *Journal of the Chemical Society Chemical Communication* **1986**, 1026–1028.
- [15] J. S. Miller, J. C. Calabrese, H. Rommelmann, S. R. Chittipeddi, J. H. Zhang, W. M. Reiff, A. J. Epstein, *Journal of the American Chemical Society* **1987**, *109*, 769–781.
- [16] J. M. Manriquez, G. T. Yee, R. S. Mclean, A. J. Epstein, J. S. Miller, *Science* **1991**, *252*, 1415–1417.
- [17] O. Sato, T. Iyoda, A. Fujishima, K. Hashimoto, *Science* **1996**, *272*, 704–705.
- [18] T. Mallah, S. Thiebaut, M. Verdaguer, P. Veillet, *Science* **1993**, *262*, 1554–1557.
- [19] S. Ferlay, T. Mallah, R. Ouahès, P. Veillet, M. Verdaguer, *Nature* **1995**, *378*, 701–703.
- [20] M. Verdaguer, *Science* **1996**, *272*, 698–699.
- [21] R. G. Hicks, *Canadian Journal of Chemistry* **2004**, *82*, 1119–1127.
- [22] R. G. Hicks, M. T. Lemaire, L. Öhrström, J. F. Richardson, L. K. Thompson, Z. Xu, *Journal of the American Chemical Society* **2001**, *123*, 7154–7159.
- [23] M. Gomberg, *Journal of the American Chemical Society* **1900**, *22*, 757–771.
- [24] M. Gomberg, *Journal of the American Chemical Society* **1901**, *23*, 496–502.
- [25] M. Gomberg, *Chemical Reviews* **1924**, *1*, 91–141.
- [26] A. Rajca, *Science* **2001**, *294*, 1503–1505.
- [27] A. Rajca, K. Lu, S. Rajca, *Journal of the American Chemical Society* **1997**, *119*, 10335–10345.
- [28] A. Rajca, J. Wongsriratanakul, S. Rajca, *Journal of the American Chemical Society* **2004**, *126*, 6608–6626.

- [29] A. Rajca, *Advances in Physical Organic Chemistry* **2005**, *40*, (Ed.: J. Richard), 153–199.
- [30] A. Rajca, S. Utamapanya, S. Thayumanavan, *Journal of the American Chemical Society* **1992**, *114*, 1884–1885.
- [31] A. Rajca, *Chemical Reviews* **1994**, *94*, 871–893.
- [32] K. Nakasuji, M. Yamaguchi, I. Murata, K. Yamaguchi, T. Fueno, H. Ohya-Nishiguchi, T. Sugano, M. Kinoshita, *Journal of the American Chemical Society* **1989**, *111*, 9265–9267.
- [33] K. Goto, T. Kubo, K. Yamamoto, K. Nakasuji, K. Sato, D. Shiomi, T. Takui, M. Kubota, T. Kobayashi, K. Yakusi, et al., *Journal of the American Chemical Society* **1999**, *121*, 1619–1620.
- [34] T. Ishida, K. Shinozuka, M. Kubota, M. Ohashi, T. Nogami, *Journal of the Chemical Society Chemical Communications* **1995**, 1841.
- [35] M. D. Pace, A. W. Snow, *Macromolecules* **1995**, *28*, 5300–5305.
- [36] A. I. Smirnov, T. I. Smirnova, *Applied Magnetic Resonance* **2001**, *21*, 453–467.
- [37] K. Fukui, T. Ito, M. Tada, M. Aoyama, S. Sato, J. Onodera, H. Ohya, *Journal of Magnetic Resonance* **2003**, *163*, 174–181.
- [38] M. L. Deschamps, E. S. Pilka, J. R. Potts, I. D. Campbell, J. Boyd, *Journal of Biomolecular NMR* **2005**, *31*, 155–160.
- [39] G. Facorro, A. Bianchin, J. Boccio, A. Hager, *Applied Spectroscopy* **2006**, *60*, 1078–1084.
- [40] D. Marsh, *Journal of Magnetic Resonance* **2008**, *190*, 60–67.
- [41] M. Tudose, T. Constantinescu, A. T. Balaban, P. Ionita, *Applied Surface Science* **2008**, *254*, 1904–1908.
- [42] A. Cecchi, L. Ciani, J. Winum, J. L. Montero, A. Scozzafava, S. Ristori, C. T. Supuran, *Bioorganic Medicinal Chemistry Letters* **2008**, *18*, 3475–3480.
- [43] R. Oakley, *Canadian journal of chemistry* **1993**, *71*, 1775–1784.
- [44] R. Oakley, *Progress in Inorganic Chemistry* **1988**, *36*, 299–391.
- [45] A. Cordes, R. Haddon, R. Oakley, *Advanced Materials* **1994**, *6*, 798–802.
- [46] T. Chivers, *A Guide to Chalcogen-Nitrogen Chemistry*, World Scientific, **2005**.
- [47] R. Haddon, *Nature* **1975**, *256*, 394–396.
- [48] J. Miller, *Materials Today* **2014**, *17*, 224–235.
- [49] D. Shultz, J. Miller, M. Drillon, *In Magnetism: Molecules to Materials II: Molecule-based Materials and Experiments*, **2001**.

- [50] M. Kinoshita, *Philosophical Transactions of the Royal Society of London A: Mathematical Physical and Engineering Sciences* **1999**, 357, 2855–2872.
- [51] A. Alberola, R. Less, C. Pask, J. Rawson, F. Palacio, P. Oliete, C. Paulsen, A. Yamaguchi, R. Farley, D. Murphy, *Angewandte Chemie International Edition* **2003**, 42, 4782–4785.
- [52] A. Banister, N. Bricklebank, I. Lavender, J. M. Rawson, C. Gregory, B. Tanner, W. Clegg, M. Elsegood, F. Palacio, *Angewandte Chemie International Edition* **1996**, 35, 2533–2535.
- [53] J. Rawson, A. Banister, I. Lavender, *Advances in Heterocyclic Chemistry* **1995**, 62, 140–248.
- [54] M. Deumal, J. Rawson, A. Goeta, J. Howard, R. Copley, M. A. Robb, J. J. Novoa, *Chemistry-A European Journal* **2010**, 16, 2741–2750.
- [55] M. Mito, T. Kawae, K. Takeda, S. Takagi, Y. Matsushita, H. Deguchi, J. Rawson, F. Palacio, *Polyhedron* **2001**, 20, 1509–1512.
- [56] C. Robertson, A. Leitch, K. Cvrkalj, R. Reed, D. Myles, P. Dube, R. Oakley, *Journal of the American Chemical Society* **2008**, 130, 8414–8425.
- [57] C. Robertson, A. Leitch, K. Cvrkalj, D. Myles, R. Reed, P. Dube, R. Oakley, *Journal of the American Chemical Society* **2008**, 130, 14791–14801.
- [58] A. Leitch, X. Yu, S. Winter, R. Secco, P. Dube, R. Oakley, *Journal of the American Chemical Society* **2009**, 131, 7112–7125.
- [59] J. Miller, *Advanced Materials* **2002**, 14, 1105.
- [60] I. Ratera, J. Veciana, *Chem. Soc. Rev.* **2012**, 41, 303–349.
- [61] S. Winter, S. Hill, R. Oakley, *Journal of the American Chemical Society* **2015**, 137, 3720–3730.
- [62] O. Kahn, *VCH Publishers Inc.(USA)* **1993**, 393.
- [63] Quantum Mechanics, by Littlejohn, R.
<http://bohr.physics.berkeley.edu/classes/221/1718/221.html>.
- [64] A. Banister, *Nature Physical Science* **1972**, 237, 92–93.
- [65] J. Rawson, A. Alberola, A. Whalley, *Journal of Materials Chemistry* **2006**, 16, 2560.
- [66] The Cambridge Crystallographic Data Centre (CCDC),
<https://www.ccdc.cam.ac.uk/structures/>?
- [67] P. Gütllich, A. Hauser, H. Spiering, *Angewandte Chemie International Edition in English* **1994**, 33, 2024–2054.

- [68] P. Gütllich, Y. Garcia, H. Goodwin, *Chemical Society Reviews* **2000**, 29, 419–427.
- [69] J. Rawson, J. Hayward, *In Spin-Crossover Materials: Properties and Applications*, John Wiley & Sons: Chichester, UK, **2013**.
- [70] M. Halcrow, *Spin-crossover materials: properties and applications*, John Wiley & Sons, **2013**.
- [71] A. Domingo, M. Verot, F. Mota, C. de Graaf, J. J. Novoa, V. Robert, *Physical Chemistry Chemical Physics* **2013**, 15, 6982–6989.
- [72] S. Vela, A. Sopena, J. Ribas-Arino, J. J. Novoa, M. Deumal, *Chemistry-A European Journal* **2014**, 20, 7083–7090.
- [73] S. Vela, F. Mota, M. Deumal, R. Suizu, Y. Shuku, A. Mizuno, K. Awaga, M. Shiga, J. Novoa, J. Ribas-Arino, *Nature Communications* **2014**, 5.
- [74] S. Vela, M. Deumal, M. Shiga, J. J. Novoa, J. Ribas-Arino, *Chemical Science* **2015**, 6, 2371–2381.
- [75] M. Deumal, M. Bearpark, J. Novoa, M. Robb, *The Journal of Physical Chemistry A* **2002**, 106, 1299–1315.
- [76] C. S. Clarke, J. Jornet-Somoza, F. Mota, J. J. Novoa, M. Deumal, *Journal of the American Chemical Society* **2010**, 132, 17817–17830.
- [77] C. De Graaf, R. Broer, *Magnetic Interactions in Molecules and Solids*, Springer, **2016**.
- [78] A. Szabo, N. Ostlund, *Modern Quantum Chemistry: Introduction to Advanced Electronic Structure Theory*, Courier Corporation, **2012**.
- [79] R. Martin, *Electronic Structure: Basic Theory and Practical Methods*, Cambridge university press, **2004**.
- [80] S. Vela, M. Reardon, C. E. Jakobsche, M. Turnbull, J. Ribas-Arino, J. Novoa, *Chemistry-A European Journal* **2017**, 23, 3479–3489.

Chapter 2

Methodology

In this chapter, the complete set of computational methodologies used to compute several properties of the compounds investigated is presented. Depending on the nature of the property of interest, we made use, for instance, of the *First-Principles Bottom-Up* approach to compute the macroscopic magnetic properties of the compounds, starting from the microscopic analysis of all the magnetic interactions. On the other hand, to study the structural behavior of the materials as a function of temperature, we employed the *Ab Initio* Molecular Dynamics technique. The whole set of methods properly combined, helped us to create a reference model to rationalize the magneto-structural behavior of the systems investigated.

2.1 Introduction

The research presented in the following chapters starts from the microscopic analysis of the radical-radical interactions and how they propagate through the crystal. As a consequence, a rationalization of the magnetic behavior of the crystal, correlated to the structural arrangement at a molecular level, is possible. The ultimate goal is to highlight the most important magnetic contributions that drive the general magnetic behavior at a macroscopic level. Ideally, a clever design of new molecule-based materials might follow, once 1) the radical-radical interactions giving rise to a specific magnetic coupling are known and 2) the proper control of the crystal arrangement is performed at the molecular level. Although the engineering of these magnetic molecular crystals is still in a developer stage, the general understanding of the “laws” involved in the nature of these compounds has been greatly improved

over the last few years[1–17]. In this context, theory provides a remarkable contribution towards the fundamental understanding of these systems. In particular, the *First-Principles Bottom-Up* (FPBU) procedure has been proved to be a valid and robust tool to determine the magnetic topology, *i.e.* how the magnetic interactions propagate within the crystal under investigation, and to reproduce the macroscopic property of interests, like susceptibility (χ) (see subsection 2.2.4), magnetization (M) or heat capacity (C_P). Many features characterize the FPBU approach, particularly relevant are 1) the construction of the Heisenberg-Dirac van Vleck Hamiltonian and 2) the use of the resulting spin states for the evaluation of the macroscopic properties. The FPBU methodology is also described in some reviews and papers[18, 19] and in some manuscripts included in this doctoral thesis; but in this chapter a detailed description of each step of the method is provided. It follows an overview of the methods based on wave function and density functional theory, both used to derive magnetic exchange coupling values. The chapter concludes with a brief description of the molecular dynamics techniques, used to investigate the impact of the thermal fluctuations on the structure, and the minimal energy path formalism employed to explore the activation energy that drives the phase transition.

2.2 The *First-Principles Bottom-Up* Method

2.2.1 First Step: Crystal Analysis and Selection of Radical Pairs

The macroscopic property of interest we want to compute in this research by means of the FPBU approach is the magnetic susceptibility χT of the PDTA and TDPDTA compounds. In the case of TTTA and 4-NCBDTA materials, it has already been reported[19–22]. The first step is the extraction of all the possible magnetic relevant radical-radical pairs from the crystalline structures as resolved experimentally from X-ray diffraction. In the case of the bistable systems under investigation, both low and high temperature polymorphs were chosen in order to reproduce the experimental susceptibility. It turns out that the spin density of the DTA radicals is strongly delocalized over the skeleton of the DTA moiety[23]. The TTTA, PDTA, TDPDTA and 4-NCBDTA compounds will be described in details in Chapter 3. In particular, all the systems mentioned are characterized to have sets of neutral radicals which pile up forming columns with a preferential stacking direction. Then, the J_{AB} values will be estimated by making use of two-molecule clusters. The structural files used for the analysis were taken from the Cambridge Crystallographic Database[24]. The AB pairs selection is done according to the N*-N* distance, where N* is, in the case of the dithiazolyl-based compounds, the nitrogen atom that formally hosts the unpaired electron. The distance threshold used to select the radical

pairs was set to 10 Å, since the magnetic interaction between them exponentially decays with distance[25].

2.2.2 Second Step: Calculation of Magnetic Exchange Interaction (J_{AB})

Once all possible dimer combinations from the LT and HT polymorphs of the crystal under investigation have been extracted, the calculation of the corresponding J_{AB} values can be performed. The J_{AB} values do not correspond to an experimental observable, but they are obtained by fitting the experimental susceptibility curves with specific models. The calculation of the J_{AB} values, from a theoretical point of view, is extremely challenging, because of the great accuracy required since they depend upon tiny energy differences, of the order of a few cm^{-1} (0.01 kcal/mol), within absolute energy values that are often 10^{10} times larger[26]. Moreover, the exchange coupling values are also strongly structural (and environmentally) dependent, meaning that, a small distortion of the molecule considered or the presence of intercalated molecular species (*e.g.* anions), can dramatically change the resulting magnetic exchange interaction.

In the research presented here, we made use of both wave function-based methods (like CASSCF and DDCI), and density functional theory (DFT). Moreover, we used the *Ab Initio* Molecular Dynamics (AIMD) technique to obtain several sets of configurations, at different temperatures, with the ultimate intent to examine how the temperature affects the crystal ordering of the molecules and, eventually, the corresponding magnetic coupling in a specific model cluster. In the next section, the Heisenberg-Dirac Van Vleck Hamiltonian (HDVV) will be introduced, followed by a general overview of the Hartree-Fock, post-Hartree-Fock and Density Functional Theory methods used to compute the J_{AB} values at different levels of accuracy, highlighting the advantages and limits of each technique employed.

The Heisenberg-Dirac van Vleck Hamiltonian

The Heisenberg-Dirac van Vleck (HDVV) Hamiltonian is a model Hamiltonian that gives the relative energies of the lowest states of a system with two or more magnetic centers. For two magnetic centers or radicals A and B, it is defined as

$$\hat{H} = -2J_{AB} \hat{S}_A \cdot \hat{S}_B \quad (2.1)$$

where the J_{AB} value is the magnetic exchange constant, and \hat{S}_A and \hat{S}_B are the total spin operators acting on the magnetic orbitals of radicals A and B, respectively. The

multiplication by the factor of 2 depends on the authors choice, and an equivalent derivation of J_{AB} without it can be found [27]. It is customary referring to positive J_{AB} values ($J_{AB} > 0$) as ferromagnetic interactions (FM), while to negative ones ($J_{AB} < 0$) as antiferromagnetic couplings (AFM).

The J_{AB} values for a system with two electronic states with consecutive multiplicity may be derived considering the relation

$$\hat{S}^2 = (\hat{S}_A + \hat{S}_B)^2 = \hat{S}_A^2 + \hat{S}_B^2 + 2\hat{S}_A\hat{S}_B \quad (2.2)$$

and re-arranging it

$$2\hat{S}_A\hat{S}_B = \hat{S}^2 - \hat{S}_A^2 - \hat{S}_B^2 \quad (2.3)$$

This relation leads to the alternative formulation of the HDVV Hamiltonian

$$\hat{H} = -J_{AB}(\hat{S}^2 - \hat{S}_A^2 - \hat{S}_B^2) \quad (2.4)$$

The corresponding eigenvalues can be written down directly as

$$E(S) = -J_{AB}[S(S+1) - S_A(S_A+1) - S_B(S_B+1)] \quad (2.5)$$

Because the energetic reference point can be selected arbitrarily, then Eq. 2.5 can be simplified by adding a constant term equal to $-J_{AB}[S_A(S_A+1) + S_B(S_B+1)]$, obtaining

$$E(S) = -J_{AB}S(S+1) \quad (2.6)$$

For two subsequent eigenvalues (S and $S-1$), the derived energy difference is given by

$$2J_{AB}S = E(S-1) - E(S) \quad (2.7)$$

where S runs from $S_A + S_B$ to $|S_A - S_B|+1$, forming a regular Landé pattern. The HDVV Hamiltonian for an extended system with M magnetic centers is

$$\hat{H} = -2 \sum_{i=1}^M \sum_{j>i}^M J_{ij} \hat{S}_i \hat{S}_j \quad (2.8)$$

In principle the sum runs over all pairs of magnetic centers, in practice only a limited number of pairs can be included. In the Density Functional Theory (DFT) section, the derivation of J_{AB} within the Broken Symmetry (BS) approximation will be presented.

Selection of the Minimal Magnetic Model

The selection of the *Minimal Magnetic Model*[18] (MMM), in practical terms, is performed based on the limitation of the HDVV matrix that will be fully diagonalized, as explained in the next Section. The different models chosen as possible suitable candidates to be representative for computing the macroscopic property of interest, in this case the magnetic susceptibility, should span the 1D, 2D and 3D arrangements (see Figure 2.1). This is extremely important, because, according to the magnetic coupling distributions, the final response may vary a lot. As a function of the number of spin centers, usually it is worth to explore how, extending the MMM, the magnetic susceptibility changes. In the Figure 2.1 different models are reported for illustrative purposes.

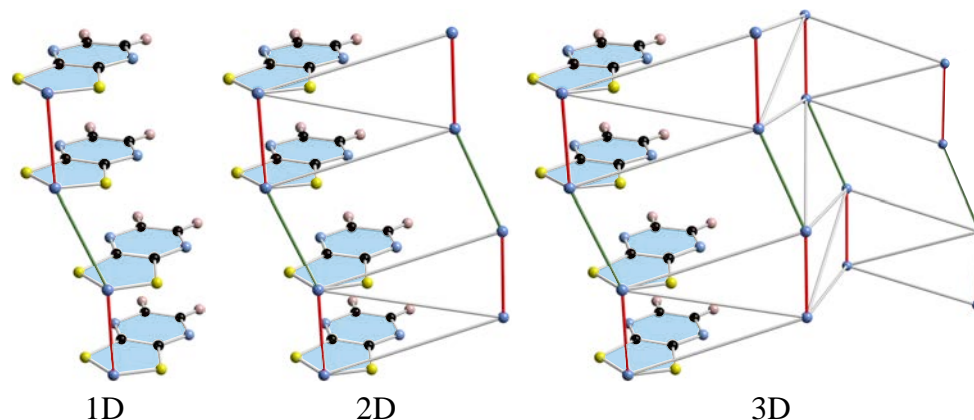


Figure 2.1: Examples of 1D, 2D and 3D minimal magnetic models, showing the propagation direction of the strongest J_{AB} exchange values (red and green bars). The grey lines are the intercolumn J_{AB} values, generally characterized by weaker interactions.

The most critical part that comes with the selection of the MMM is the inclusion or exclusion of the weakest spin coupling interactions. This is rather straightforward when dealing with diamagnetic polymorphs, because usually, there is a negative dominant J_{AB} value that forces the system to be magnetically silent. But when dealing with HT polymorphs, the selection is much more delicate. It can be noticed that still there is a J_{AB} value that is more antiferromagnetic compared to the rest, but many interactions now are of the same order of magnitude, or at most one order of magnitude smaller. This is well illustrated in the selection, computation and analysis of the results for the PDTA and TDPDTA cases, as discussed in Chapter 5. While

in the HT-PDPA case, increasing the model size does not affect χT , in the TDPDPA case instead it has a significant influence, showing that the inter-columns interactions have to be considered in order to properly describe the HT-TDPDPA magnetic response.

2.2.3 Third Step: Construction and Diagonalization of the HDVV Hamiltonian

The derivation of the magnetic susceptibility χT , or heat capacity $C_P(T)$, is performed accounting for all the energy levels obtained from the diagonalization of the HDVV Hamiltonian, Eq. 2.8, which, in turn, has been parametrized in Step 2 based on the computed J_{AB} values. The compounds investigated, being molecular crystals, require a limited model system, representative of the infinite one. This “*minimal magnetic model*” comprises the smallest number of radicals whose propagation along the three crystallographic axes reproduces the magnetic topology of an infinite crystal[18]. The energy levels (see Fig. 2.3) are obtained from the diagonalization of the HDVV Hamiltonian, Eq. 2.8. The dimension of the eigenvalue problem, $K(n)$, is defined as

$$K(n) = \frac{n!}{\left(\frac{n}{2}\right)! \left(\frac{n}{2}\right)!} \quad (2.9)$$

where n is the number of doublet radical centers. For example, in case of a two-radical cluster with two unpaired electrons, the spins can couple forming a singlet and a triplet state, respectively. Instead, if the system is doubled, the four unpaired electrons can form two singlets, three triplets and one quintet states, respectively. Fig. 2.2 shows schematically how the different eigenvalues are derived as a function of the number of spin centers in the model chosen, for a system that is not subjected to an external electric or magnetic field. It follows that the maximum number of spin centers *per* model we can consider is 18. This would lead to a matrix of 48620×48620 elements. Nevertheless, the models chosen have been reported to be sufficiently accurate to reproduce the macroscopic properties of some nitronyl nitroxide molecular crystals[18]. A critical analysis was also performed to establish if the models to use to reproduce the macroscopic properties of periodic crystals have to be truncated chains of spin centers (open model) or a sequence of spin centers where the last one “*interact*” with the first one (cyclical model). The reader is addressed to the reference paper for the details of this investigation[18]. In summary, if the minimal magnetic model is properly chosen, as it is enlarged the macroscopic properties should converge towards the experimental data.

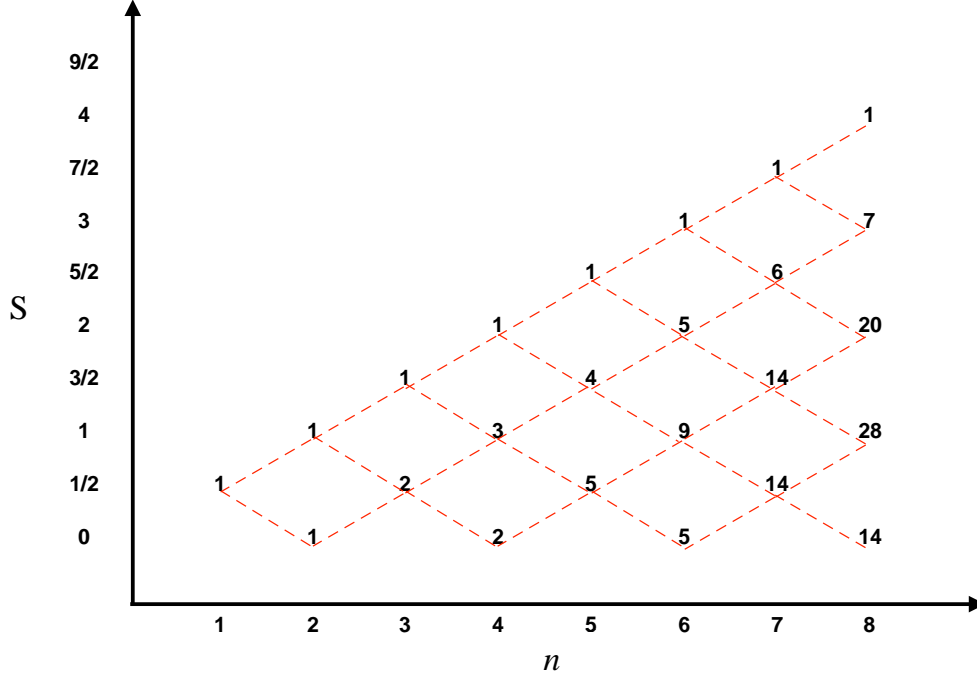


Figure 2.2: *Branching Diagram* showing the number of spin eigenfunctions corresponding to different numbers n of electrons in singly occupied spatial orbitals as a function of the different spin quantum numbers S .

2.2.4 Fourth Step: Derivation of the Macroscopic Properties: The Susceptibility

The final step to accomplish in order to compute the magnetic susceptibility of the compound of interest is to make use of statistical mechanics. It employs the energy spectrum computed in step 3. The expression used to compute the macroscopic magnetic susceptibility is

$$\chi = \frac{Ng^2\mu_B^2}{3k_B T} \mu_0 \left[\frac{\sum_n S_n(S_n + 1)(2S_n + 1) \exp\left[-\frac{E_n - E_0}{k_B T}\right]}{\sum_n (2S_n + 1) \exp\left[-\frac{E_n - E_0}{k_B T}\right]} \right] \quad (2.10)$$

written in terms of the microscopic energy levels at zero magnetic field[18]. E_n is the n th energy level from the HDVV Hamiltonian, S_n is the spin of the n th energy level ($m_{S_n} = -S_n, \dots, -1, 0, +1, \dots, +S_n$), g is the gyromagnetic factor, and the constants N , μ_B , k_B , and μ_0 are Avogadro's number, Bohr magneton, Boltzmann constant and

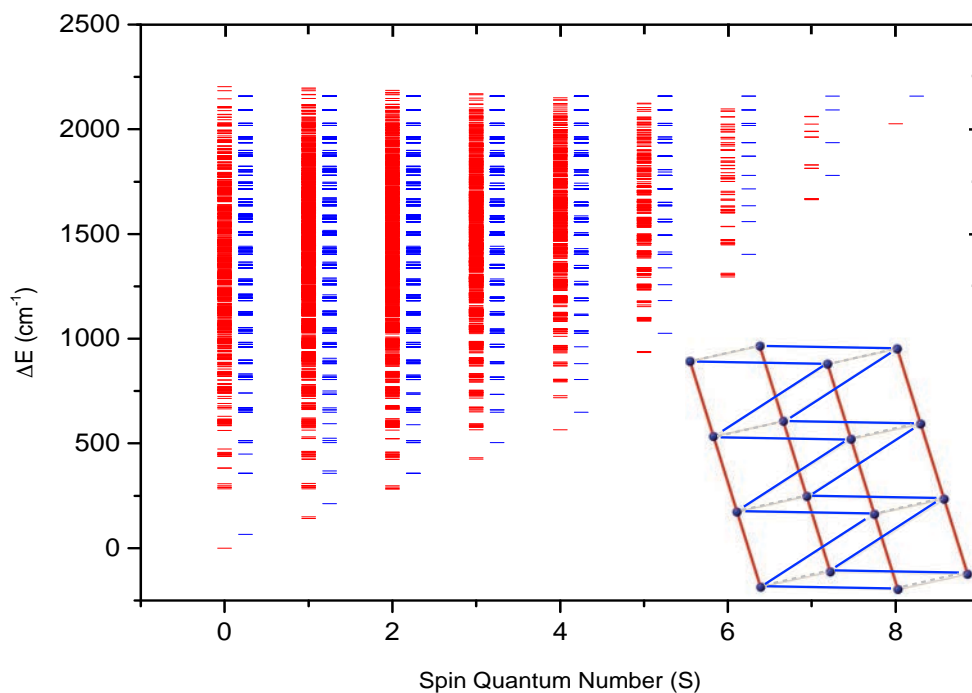


Figure 2.3: Example of energy spectra of the magnetic states found for a 3D MMM reported in the right-hand side of the plot, comprising 16 spin states (12870 energy levels). In the particular case of this model, the strongest J_{AB} value propagates along the stacking direction (red bar), $J_{AB} = -110.5 \text{ cm}^{-1}$, while the second strongest coupling interconnect two adjacent columns (blue bar), $J_{AB} = 10.1 \text{ cm}^{-1}$. The two layers are interconnected by a tiny J_{AB} exchange value, that is not considered in the energy spectra plot (grey dashed lines).

permeability of free space, respectively. As already mentioned above, the units are in CGS, emu mol^{-1} . It is therefore necessary to point out that, since we are working with molecular systems, the reference in the “ mol^{-1} ” term refers to moles of magnetic centers (radicals).

2.3 Wave Function-based Methods

2.3.1 The Schrödinger Equation

The time-dependent non-relativistic Schrödinger Equation (TDSE, 2.11) describes the evolution of a quantum state of a system as a function of time. It was formulated in 1925 and published in 1926[28] by Erwin Schrödinger, leading to the development of quantum mechanical tools that still today are used to study and explore material properties.

$$\hat{H}(\mathbf{r}, t)\Psi(\mathbf{r}, t) = i\hbar \frac{\partial}{\partial t}\Psi(\mathbf{r}, t) \quad (2.11)$$

Often, the TDSE is considered to be the equivalent in quantum mechanics to what Newton's law is in the classical one. In the TDSE, the wave function $\Psi(\mathbf{r}, t)$ represents a mathematical description of the quantum state of a system; onto this wave function, the differential Hamiltonian (\hat{H}) operator is applied, allowing to derive the total energy (\mathcal{E}_{TOT}) of the system. If the system considered is isolated such that \hat{H} is not dependent on time, the wave function can be written as a product of a time independent function and a time dependent part as

$$\Psi(\mathbf{r}, t) = \Psi(\mathbf{r})F(t) \quad (2.12)$$

After substituting Eq. 2.12 in Eq. 2.11, the separation of variables follows, leading to two equations, one depending on space and the other on time. In particular, the equation that depends on space is called the time-independent Schrödinger equation (TISE), and it has the form

$$\hat{H}(\mathbf{r})\Psi(\mathbf{r}) = E\Psi(\mathbf{r}) \quad (2.13)$$

Despite this simplification, the TISE remains a formidable equation to solve, except for very simple cases, like the hydrogen atom or hydrogen-like models. This problem triggered the research for a possible reliable but approximate solution of the TISE all along the 20th century, and it proceeds still today.

In the general case of a system with multiple electrons and nuclei interacting through the Coulomb potential, the general Hamiltonian \hat{H} operator can be expressed as the sum of different terms:

$$\hat{H} = \hat{T}_N + \hat{T}_e + \hat{V}_{NN} + \hat{V}_{ee} + \hat{V}_{Ne} \quad (2.14)$$

where

- \hat{T}_N is the nuclear kinetic energy operator;
- \hat{T}_e is the electronic kinetic energy operator;
- \hat{V}_{NN} is the internuclear repulsion potential energy operator;
- \hat{V}_{ee} is the interelectronic repulsion potential energy operator;
- \hat{V}_{Ne} is the electron-nuclei attraction potential energy operator.

The analytical expression, in atomic units, is

$$\hat{H} = -\frac{1}{2} \sum_{A=1}^M \frac{\nabla_A^2}{M_A} - \frac{1}{2} \sum_{i=1}^n \nabla_i^2 + \sum_{A=1}^M \sum_{B>A}^M \frac{Z_A Z_B}{r_{AB}} + \sum_{i=1}^n \sum_{j>i}^n \frac{1}{r_{ij}} - \sum_{i=1}^n \sum_{A=1}^M \frac{Z_A}{r_{iA}} \quad (2.15)$$

where i, j and A, B refer to electrons and nuclei, respectively; M_A and Z_A denote the mass and nuclear charge of nucleus A , r_{iA} is the distance between electron i and nucleus A , r_{ij} is the distance between electron i and electron j , and r_{AB} is the distance between nucleus A and nucleus B .

2.3.2 The Born-Oppenheimer Approximation

The Born-Oppenheimer (BO) approximation is extremely important in quantum chemistry and condensed matter physics fields. It was proposed by physicists Max Born and J. Robert Oppenheimer[29], in 1927. In qualitative terms, since the electron mass is ~ 2000 times smaller than the proton one and the electrons adapt instantaneously to the nuclear motion (*i.e.* rotations and vibrations), then the electronic motion can be decoupled from the nuclear one. Generally, nuclei and electrons positions of a given molecular structure are described by the vectors $\mathbf{R}=\mathbf{R}_j$ ($j=1, \dots, N_n$) and $\mathbf{r}=\mathbf{r}_i$ ($i=1, \dots, N_e$), respectively. The partition in nuclear and electronic components can be solved in two consecutive steps:

Step 1 : The nuclear kinetic energy term, \hat{T}_N , is subtracted from the molecular Hamiltonian (Eq.2.14), and the nuclear repulsion terms are considered to be constant. Thus, the remaining terms are grouped into the electronic Hamiltonian (\hat{H}_e)

$$\hat{H}_e = -\sum_{i=1}^n \frac{1}{2} \nabla_i^2 - \sum_{i=1}^n \sum_{A=1}^M \frac{Z_A}{r_{iA}} + \sum_{i=1}^n \sum_{j>1}^n \frac{1}{r_{ij}} \quad (2.16)$$

which leads to the corresponding Schrödinger equation

$$\hat{H}_e \Psi_e(\mathbf{r}; \mathbf{R}) = \mathcal{E}_e(\mathbf{R}) \Psi_e(\mathbf{r}; \mathbf{R}) \quad (2.17)$$

yielding the electronic wave function $\Psi_e(\mathbf{r}; \mathbf{R})$, which describes the motion of the electrons, explicitly depending on the electronic coordinates but parametrically on the nuclear ones. Each atomic arrangement yields a different function of the electronic coordinates. The total energy of the system, to which the BO approximation is applied, must include also the constant nuclear repulsion term

$$\mathcal{E}_{\text{PES}}(\mathbf{R}) = \sum_{A=1}^M \sum_{B>A}^M \frac{Z_A Z_B}{r_{AB}} + \mathcal{E}_e(\mathbf{R}) \quad (2.18)$$

Computing \mathcal{E}_{PES} for many nuclear conformations yields a Potential Energy Surface (PES).

Step 2 : Once the electronic problem is solved, then it is possible to solve the SE of the nuclei. The nuclear Hamiltonian to use in the description of the motion of nuclei is

$$\hat{H}_{nucl} = - \sum_{A=1}^M \frac{1}{2M_A} \nabla_A^2 + \mathcal{E}_{\text{PES}}(\mathbf{R}) \quad (2.19)$$

As a consequence, in the BO approximation, the nuclei are moving on a PES obtained by solving the electronic problem. The solution to the corresponding Schrödinger equation involving the nuclear Hamiltonian is $\Psi_{nucl}(\mathbf{R})$, which describes the motion of nuclei like rotation, vibration and translation.

Therefore, the total energy \mathcal{E}_{TOT} , comprises both the nuclear and electronic contributions. Finally, the total wave function, which includes both the electronic and nuclear contributions, can be defined as

$$\Psi(\mathbf{r}, \mathbf{R}) = \Psi_e(\mathbf{r}; \mathbf{R}) \Psi_{nucl}(\mathbf{R}) \quad (2.20)$$

2.3.3 The Electronic Wave Function

The BO approximation, although very useful, in general is not sufficient to solve the Schrödinger equation for a molecular system. It is convenient to introduce the *one-electron approximation*. It consists in decoupling the movement of the electrons in the system under investigation assuming that each single electron is moving in an average potential, which represents the average electron-electron repulsion. As a consequence of this assumption, each single electron can be described by means of an *effective one-electron Hamiltonian* \hat{h}_i and by a spatial function (*orbital*), $\psi(\mathbf{r}_i)$, both depending only on the position of the i -th electron characterized by vector \mathbf{r}_i . From each single spatial orbital $\psi(\mathbf{r}_i)$ two different “spinorbitals” can be formed

$$\phi(\mathbf{x}_i) = \begin{cases} \psi(\mathbf{r}_i) \alpha(\theta_i) \equiv \phi \\ \psi(\mathbf{r}_i) \beta(\theta_i) \equiv \bar{\phi} \end{cases} \quad (2.21)$$

where $\alpha(\theta_i)$ and $\beta(\theta_i)$ define two orthonormal spin functions describing the spin up and spin down configurations, respectively. Then, a possible many-body electronic wave function $\Psi_e(\mathbf{x}_1, \mathbf{x}_2, \dots, \mathbf{x}_n)$ would be equivalent to the product of the one-electron spinorbitals

$$\Psi_e(\mathbf{x}_1, \mathbf{x}_2, \dots, \mathbf{x}_n) = \phi_i(\mathbf{x}_1) \phi_j(\mathbf{x}_2) \dots \phi_k(\mathbf{x}_n) \quad (2.22)$$

where the spatial and spin coordinates are grouped in $\mathbf{x}_i = \{\mathbf{r}_i; \theta_i\}$. The wave function defined by the product of spinorbitals in Eq. 2.22 is called *Hartree product* (HP). The HP does not account for the indistinguishability of electrons and does not obey the antisymmetry principle, which states that

“a many electron wave function must be antisymmetric with respect to the interchange of the coordinate \mathbf{x}_i (representing both space and spin) of any two electrons”[30]

or, in mathematical representation

$$\Psi_e(\mathbf{x}_1, \mathbf{x}_2, \dots, \mathbf{x}_i, \dots, \mathbf{x}_j, \dots, \mathbf{x}_n) = -\Psi_e(\mathbf{x}_1, \mathbf{x}_2, \dots, \mathbf{x}_j, \dots, \mathbf{x}_i, \dots, \mathbf{x}_n) \quad (2.23)$$

which is a general statement of the Pauli exclusion principle[31]. To accomplish this requirement, the *Hartree product* is replaced by a determinant as

$$\Psi_e(\mathbf{x}_1, \dots, \mathbf{x}_n) = (N!)^{-\frac{1}{2}} \begin{vmatrix} \phi_i(\mathbf{x}_1) & \phi_j(\mathbf{x}_1) & \cdots & \phi_k(\mathbf{x}_1) \\ \phi_i(\mathbf{x}_2) & \phi_j(\mathbf{x}_2) & \cdots & \phi_k(\mathbf{x}_2) \\ \vdots & \vdots & \ddots & \vdots \\ \phi_i(\mathbf{x}_N) & \phi_j(\mathbf{x}_N) & \cdots & \phi_k(\mathbf{x}_N) \end{vmatrix} \quad (2.24)$$

where $(N!)^{-\frac{1}{2}}$ is a normalization factor. The antisymmetric wave function defined in Eq. 2.24 is called *Slater determinant*.

A Slater determinant represents a specific electronic configuration. A linear combination of an infinite number of Slater determinants can provide the exact solution for a given system.

Linear Combination of Atomic Orbitals (LCAO)

The next approximation we consider in order to find approximate solutions of the Schrödinger equation for a molecular system is called *linear combination of atomic orbitals* (LCAO). The linear combination of M atomic orbitals $\{\chi_j, j=1, \dots, M\}$ (basis set) defines a molecular orbital ψ_i as

$$\psi_i = \sum_{j=1}^M c_{ij} \chi_j \quad (2.25)$$

where the coefficients c_{ij} are the constants to be determined. If equation 2.25 is multiplied by the spin functions, $\alpha(\theta_i)$ or $\beta(\theta_i)$, the spinorbital ϕ_i or $\bar{\phi}_i$ is obtained.

2.3.4 The Hartree-Fock Method

The Slater determinant (Eq. 2.24) associated with the many-electron ground state (GS) of a generic system, in the Dirac notation, is written as

$$|\Psi_0\rangle = |\phi_1 \phi_2 \dots \phi_N\rangle \quad (2.26)$$

The goal of the Hartree-Fock method is to obtain the best wave function, or alternatively the best set of spinorbitals, which gives the lowest energy possible, applying the *variation theorem*[30]

$$E_0 = \langle \Psi_0 | \hat{H}_e | \Psi_0 \rangle \quad (2.27)$$

where \hat{H}_e is the electronic Hamiltonian. Minimizing E_0 with respect to the spinorbital selection, brings us to the Hartree-Fock (HF) equation (for a detailed derivation, see Chapter 3[30]). The HF energy is the lowest possible energy for a single determinant wave function, an eigenvalue equation of the form

$$f(\mathbf{x}_1) \phi_i(\mathbf{x}_1) = \mathcal{E}_i \phi_i(\mathbf{x}_1) \quad (2.28)$$

where $f(\mathbf{x}_1)$ is an effective one-electron operator defined as

$$f(\mathbf{x}_1) = -\frac{1}{2} \nabla_1^2 - \sum_{A=1}^M \frac{Z_A}{r_{1A}} + v^{HF}(\mathbf{x}_1) \quad (2.29)$$

The $v^{\text{HF}}(\mathbf{x}_1)$ term represents the sum of two fundamental energetic contributions

$$v^{\text{HF}}(\mathbf{x}_1) = \sum_j [\hat{J}_j(\mathbf{x}_1) - \hat{K}_j(\mathbf{x}_1)] \quad (2.30)$$

where \hat{J} , the mono-electronic *Coulomb* operator, accounts for the average potential field experienced by the first electron with respect to the others, and where \hat{K} , the mono-electronic *exchange* operator, correlates the electrons with parallel spin within the single determinantal approximation of the wave function. The $v^{\text{HF}}(\mathbf{x}_1)$ depends on the spinorbitals of the other electrons, that is the *Fock* operator depends upon its eigenfunctions. For an electron in ϕ_a , the expectation values of the *Coulomb* and *exchange* potentials J_b and K_b are

$$\langle \phi_a(\mathbf{x}_1) | J_b(\mathbf{x}_1) | \phi_a(\mathbf{x}_1) \rangle = \int d\mathbf{x}_1 d\mathbf{x}_2 \phi_a^*(\mathbf{x}_1) \phi_a(\mathbf{x}_1) \frac{1}{r_{12}} \phi_b^*(\mathbf{x}_2) \phi_b(\mathbf{x}_2) = (aa|bb) \quad (2.31)$$

and

$$\langle \phi_a(\mathbf{x}_1) | K_b(\mathbf{x}_1) | \phi_a(\mathbf{x}_1) \rangle = \int d\mathbf{x}_1 d\mathbf{x}_2 \phi_a^*(\mathbf{x}_1) \phi_b(\mathbf{x}_1) \frac{1}{r_{12}} \phi_b^*(\mathbf{x}_2) \phi_a(\mathbf{x}_2) = (ab|ba) \quad (2.32)$$

The *exchange* operator \hat{K} emerges because of the antisymmetric nature of the wave function[30]. The HF equation is solved iteratively by means of the Self-Consistent-Field (SCF) procedure because the Fock operator depends upon its own solution. The initial wave function is supposed to be a good initial condition, ϕ_{trial} , but it is not a solution of the HF equation. Once the iterative process is converged, the final wave function is then a solution of the HF equation. This procedure is not explained in details here, since it is fully described in the reference textbook[30]. The great advantage that the HF theory brings is to reduce the many-electron problem into a one-electron problem. The accuracy of this method depends on the number of spatial basis functions $\chi(\mathbf{r}_i)$ used to approximate the spatial distribution of an electron, where $|\psi(\mathbf{r}_i)|^2 d\mathbf{r}_i$ is the probability of finding the electron in the small volume element $d\mathbf{r}_i$ surrounding \mathbf{r}_i . The more basis functions $\chi(\mathbf{r}_i)$ are added, the lower is going to be the expectation value $E_0 = \langle \Psi_0 | \hat{H} | \Psi_0 \rangle$, reaching the so-called *Hartree-Fock limit*. In practical terms, the basis function expansion has to be truncated and the expectation value E_0 obtained for any finite number of basis functions will be always higher in energy with respect so far to the HF limit.

2.3.5 Different Formalisms of the HF Theory

The nature of the system to treat may put some serious challenges in the correct representation and definition of its electronic structure. To properly represent it, the HF method has been successfully developed into three different formalisms, the Restricted HF (RHF), Restricted Open-Shell HF (ROHF) and Unrestricted Hartree-Fock (UHF). The first method is better suited for the treatment of closed-shell systems, where the electrons come in an even number and are all paired. These systems can easily be represented by a single determinant. The ROHF and UHF instead, have been developed in order to treat open-shell systems, that are generally holding an unpaired electron in the outer valence shell. In the next three paragraphs, a brief summary of the three methods is provided.

Restricted Hartree-Fock (RHF)

The RHF procedure provides a “*simplified*” view of the electronic interactions within atoms and molecules, supposing that the spatial part of the spinorbitals is identical for each electron within the considered pair. For a N_e number of even electrons, there are $\frac{1}{2}N_e$ spatial orbitals of the form $\psi_m(\mathbf{r}_i)$, which lead to the HF wave function

$$\psi_0 = \frac{1}{\sqrt{N_e!}} \det |\psi_a^\alpha(1) \psi_a^\beta(2) \dots \psi_z^\beta(N_e)| \quad (2.33)$$

This wave function gives the name to the RHF formalism.

Restricted Open-Shell Hartree-Fock (ROHF)

The ROHF formalism, like the UHF discussed in the next paragraph, is mainly used to treat open-shell systems. In the case of the ROHF approach, all the electrons, except the unpaired ones, are forced to occupy doubly occupied spatial orbitals, (see Fig. 1.4). The ROHF method was first formulated by Clemens C. J. Roothaan[32] in 1960.

The energy expression in the ROHF is

$$E_{\text{ROHF}} = 2 \sum_a f_a h_{aa} + \sum_{ab} f_a f_b (2p_a^b (ab|ab) - q_a^b (ab|ba)) \quad (2.34)$$

where the h_{ab} are the one-electron integrals, the $(ab|kl)$ are the two-electron integrals, p_a^b and q_a^b are the coupling coefficients and f_a are the orbital occupations. The ROHF is preferred to generate the initial wave functions in case of serious spin contamination of the UHF ones.

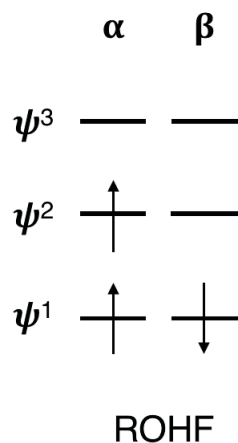


Figure 2.4: ROHF scheme. The pairs of electrons are constrained to have the same spatial orbital ψ^1 , while the unpaired electron has its own spatial orbital, ψ^2 . It can be either in α or β configuration.

Unrestricted Hartree-Fock (UHF)

In the UHF method there are no constraints applied onto wave functions. This formalism allows for a lowering of the variational energy. Each single electron is described by its own molecular orbital. The energy expression in the UHF method is

$$\begin{aligned}
 E_{\text{UHF}} = & \sum_a^{N_\alpha} h_{aa}^\alpha + \sum_a^{N_\beta} h_{aa}^\beta + \frac{1}{2} \sum_a^{N_\alpha} \sum_b^{N_\beta} (J_{ab}^{\alpha\alpha} - K_{ab}^{\alpha\alpha}) + \frac{1}{2} \sum_a^{N_\beta} \sum_b^{N_\beta} (J_{ab}^{\beta\beta} - K_{ab}^{\beta\beta}) + \\
 & + \sum_a^{N_\alpha} \sum_b^{N_\beta} J_{ab}^{\alpha\beta}
 \end{aligned}
 \tag{2.35}$$

where h_{aa}^α and h_{aa}^β are the expectation values of the kinetic energy and nuclear attraction of an electron in the unrestricted orbitals ψ_a^α and ψ_b^β . $J_{ab}^{\alpha\beta}$ is the *Coulomb* interaction between two electrons, one in the orbital ψ_a^α and ψ_b^β , respectively. $J_{ab}^{\alpha\alpha}$ and $J_{ab}^{\beta\beta}$ are the *Coulomb* interactions between electrons with parallel spin, while $K_{ab}^{\alpha\alpha}$ and $K_{ab}^{\beta\beta}$ correspond to the *exchange* interaction between electrons with parallel spin. The main drawback of the UHF formalism is called *spin contamination*. The spin contamination, in practical terms, is a non-negligible deviation of the expectation value S^2 for the unrestricted wave function with respect to the true value $S(S+1)$ for the ground state. The separation in α and β orbitals brings the formation of unrestricted spinorbitals with different spatial orbitals for different spins. In the

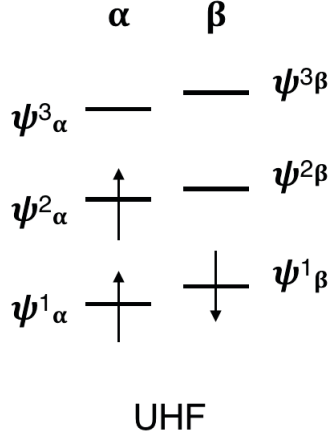


Figure 2.5: UHF scheme. The electrons are unconstrained and each electron occupies a different spatial orbital.

case of the ROHF formalism, the expectation value of S^2 , not affected by the above mentioned spin contamination, is

$$\langle S^2 \rangle_{\text{ROHF}} = \langle S^2 \rangle_{\text{exact}} = \left(\frac{N_\alpha - N_\beta}{2} \right) \left(\frac{N_\alpha - N_\beta}{2} + 1 \right) \quad (2.36)$$

whereas, in the case of the UHF

$$\langle S^2 \rangle_{\text{UHF}} = \langle S^2 \rangle_{\text{exact}} + N_\beta - \sum_{i,j}^{\text{Occp.}} |S_{ij}^{\alpha\beta}|^2 \quad (2.37)$$

where N_α and N_β are the numbers of spinorbitals with spin α and spin β belonging to the N -electron wave function, and $-\sum_{i,j}^{\text{Occp.}} |S_{ij}^{\alpha\beta}|^2$ is the contribution from the “contaminants”, where $S_{ij}^{\alpha\beta}$ is the overlap matrix between the spatial functions of electrons i and j . The UHF wave functions are not eigenfunctions of S^2 . They contain admixtures of higher spin states. If the $\langle S^2 \rangle$ computed in the UHF approximation is far from the expected, then the results are affected by spin contamination.

Beyond the Hartree-Fock Method

The main limitation of the HF method is the neglect of the instantaneous electron-electron correlation (or *correlation potential*), E_{corr} . The E_{corr} term is defined as the difference between the exact non-relativistic energy \mathcal{E}_0 and the Hartree-Fock energy, E_0 , in the limit of the basis set completeness (HF *limit*)

$$E_{\text{corr}} = \mathcal{E}_0 - E_0 \quad (2.38)$$

The total wave function represented by a single determinant does not account for the *correlation* between electrons. The post-HF methods try to improve the HF method, by including to some extent electron correlation, either in a variational or perturbative fashion. To the first class belong, for example, the Configuration Interaction[30] (CI) method and the Multi-Reference Self-Consistent-Field[30] (MCSCF), while to the second class belong the Møller-Plesset[30] (MP), the CASPT2[33–35] and NEVPT2[35–38] methods. A method which instead is variational in spite of a perturbative consideration is the *so-called* Difference Dedicated CI[35, 39, 40] method.

Ideally, including all possible determinants would lead to the lowest possible expectation value. But at the same time, it would increase enormously the computational cost. In practical terms it is necessary to truncate the multi-determinant wave function. In the next sections an overview of the post-HF methods used in this work will be presented. For a complete and detailed description of them, the reader is addressed to the referenced papers and textbooks, and references therein[30, 41].

2.3.6 Variational Methods

Configuration Interaction

A Configuration State Functions (CSF) is a symmetry and spin adapted linear combination of Slater determinants. One electronic configuration may give rise to several CSFs, presenting the same total quantum number for spin and spatial parts but differing in their intermediate couplings. The ground state (GS) wave function Ψ in the Configuration Interaction (CI) method is obtained by linear combination of all possible Slater determinants of the correct symmetry (CSF) as

$$\Psi = C_0\Psi_0 + \sum_{a,r} C_a^r\Psi_a^r + \sum_{\substack{a<b \\ p<q}} C_{ab}^{pq}\Psi_{ab}^{pq} + \dots \quad (2.39)$$

where the Ψ_a^r is the singly excited CFSs (different from Ψ_0 because it has the spinorbital ϕ_a replaced by the spinorbital ϕ_r), Ψ_{ab}^{pq} is the doubly excited CFSs and so on, up to include all the possible excited CFSs. The expansion coefficients C_i are determined applying the variational principles defined as

$$\Xi = \frac{\langle \Psi_{trial} | \hat{H} | \Psi_{trial} \rangle}{\langle \Psi_{trial} | \Psi_{trial} \rangle} \quad (2.40)$$

for which the *variation theorem*[30] states that for any Ψ_{trial} , $\Xi \geq E_0$, where E_0 is the exact energy of the system. If all the CSF are used for a specific basis set, then the calculation is called *full-CI*. The exact GS energy derived from the CI method is the

exact non-relativistic GS energy derived in the Born-Oppenheimer approximation. For a *given basis set*, the difference between the GS energy obtained from the HF and the one obtained from a full-CI, is called *basis set correlation energy*. It would be possible to obtain the exact energy of a system by including all CSF, but in practice it is necessary to limit their number. This is called *truncated CI*. One possibility of selection of the determinants to include in equation 2.39, accounts only for the ones which differ from the Hartree-Fock wave function Ψ_0 by no more than some defined number of spinorbitals. The general CI protocol is not to improve the spinorbitals but to include more and more excited determinants into the wave function expansion. The use of truncated CI comes with a drawback, called *size-consistency*. In practice, the total energy of the system AB computed when the subsystems A and B are at infinite distance from each other should be equal to the sum of the systems A and B, separately computed making use of the same method. Truncated CI is not *size-consistent*.

Multiconfiguration Methods: The Complete Active Space SCF

Differently from the CI method, where only the coefficients associated to the linear combination of Slater determinants are variationally optimized, in the general definition of the Multiconfiguration Methods also the coefficients associated to the linear combination of the atomic orbitals (c_{ij}) are optimized[41]. The procedure is named Multiconfiguration Self-Consistent Field Method (MCSCF). The optimization of both the coefficients c_{ij} and C_i gives more accurate results, *a priori*, including a smaller number of CSFs. Like in the CI case, also in MCSCF it is necessary to reduce the number of determinants to be used by applying an efficient truncation scheme that allows to obtain a good compromise between accuracy and computational cost. A special case of MCSCF is the Complete Active Space SCF[42–50] method and its extension, the Restricted Active Space SCF (RASSCF)[51] method. For the latter, the reader is addressed to the original paper references[51] therein.

The CASSCF scheme is an important and efficient variational method which treats the full CI expansion of the wave function within a specific restricted set of orbitals. The spatial wave functions ψ_i , whose c_{ij} coefficients are also optimized along the SCF procedure, are divided into three subspaces: Inactive, Active and Virtual.

Inactive Orbitals : the spatial wave functions with the lowest energy that are doubly occupied in all configurations;

Active Orbitals : the spatial wave functions are energetically located around the highest occupied molecular orbital and they are partially occupied;

Virtual Orbitals : the spatial wave functions are very high in energy, and they are unoccupied in all configurations.

The selection of the active space depends upon the nature of the system investigated. Once the active space is defined, the CSF included in the calculation are all

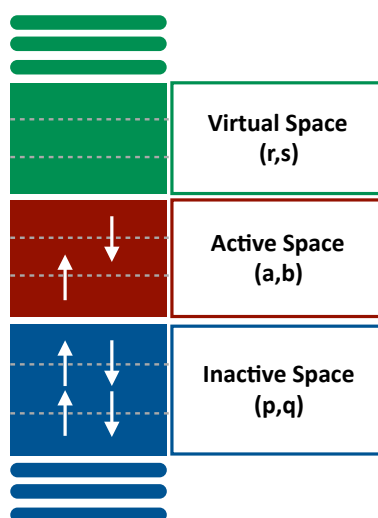


Figure 2.6: Schematic representation of the electronic partitioning within the CASSCF framework.

the configurations with proper spin and spatial symmetry that come from all possible permutations of the active electrons over the active orbitals. The choice of the active space is very critical in CASSCF, because the number of CSF rises exponentially as the number of active orbitals increases. This method recovers the *static* correlation contribution, that is the inadequacy of the single determinant GS (Ψ_0) to describe the *quasi-degenerate* states of a given molecular configuration[52]. The CASSCF scheme does not account for the *dynamical* correlation, that is related to the movements of the individual electrons and their short range interactions. The HF method, treating the electrons in an *average* field, overestimates the probability of finding two electrons close together, and as a consequence there is an overestimation of the electronic repulsion energy. In order to account for the dynamical correlation, other methods have been developed, like Multi Reference CI[52] or Multi Reference PT[52]. In the variational flavor, the Difference Dedicated Configuration Interaction is one of them, used in a benchmark process as described in Chapter 5.

Difference Dedicated Configuration Interaction (DDCI)

The DDCI methodology is designed to obtain accurate energy differences rather than total energies[35, 39, 40, 53]. DDCI, using the CASSCF wave function as reference, generates eight different kinds of excited Slater determinants. These are organized into classes (see Figure 2.7) based on the numbers of holes and electrons in the occupied and virtual orbitals (alternatively called “degrees of freedom”), respectively. In general, the class considering the double replacement from the inactive to virtual orbitals ($2h-2p$), is omitted from the CI expansion of the N -electron wave function (see Fig. 2.7). This set of double excitations is the most numerous and contributes typically for more than 90% to the total correlation energy. The elimination of the

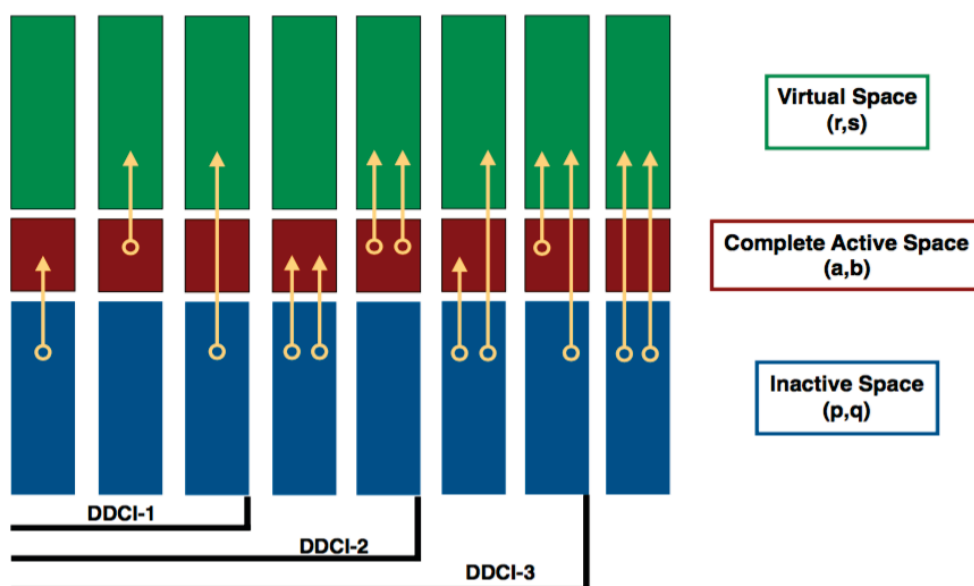


Figure 2.7: Schematic representation of the DDCI-1, DDCI-2 and DDCI-3 configurations.

$2h-2p$ class is justified by the fact that the corresponding double excitations do not contribute to second order to the energy differences needed to evaluate the magnetic couplings (J_{AB}). This simplification relies on the second-order perturbation theory in its quasi-degenerate formulation as explained in details in the review of Malrieu[53] and co-workers or in the textbook of De Graaf and Broer[27]. In line to DDCI method, three other levels of calculations are defined, the DDCI-1, 2 and 3, and their definition depend on the number of degrees of freedom solicited in the CI. This methodology was originally developed by Jean Paul Malrieu[54–57], and it

has been applied in many works involving the precise analysis of the J_{AB} magnetic coupling values. The drawback of this method is the extremely high computational cost due to the extended use of a large set of determinants. On top of that, the size-consistency problem remains. Both these problems are successfully overcome in the NEVPT2 method, explained in the next section.

2.3.7 Perturbative Methods

N-Electron Valence State Perturbation Theory

The NEVPT2 method is based on the combination of the CASSCF *zeroth*-order wave function and on the *zeroth*-order Hamiltonian with a bi-electronic nature[35, 53]. The \hat{H}_0 is derived from the Dyall's model Hamiltonian \hat{H}_D [35, 53], which is mono-electronic in the doubly occupied and virtual orbitals, whereas it is bi-electronic in the CAS. From the partition of the *zeroth*-order energies and wave functions, three different NEVPT2 variants can be obtained, called totally, partially and strongly contracted. In particular, the last two variants, labelled PC-NEVPT2 and SC-NEVPT2, have been implemented in the Orca[58] code. Among the many key features characterizing the NEVPT2 method, making the approach reliable and solid, it is worth to mention:

No intruder states : In perturbation theory the intruder states are originated from the *quasi*-degeneracy in the *zeroth* order Hamiltonian[59]. The presence of intruder states may cause a break-down of the perturbation theory. In principle, NEVPT2 is not affected by this problem;

Size Consistency : NEVPT2 satisfies this condition, for which total energy of the system AB computed when the systems A and B are at infinite distance correspond to the sum of total energy of the system A and B, separately. This property is extremely important when evaluating the dissociation reactions, for instance.

For more details on the NEVPT2 methodology, the reader is referred to the original works[36–38] and references therein.

2.4 Density Functional Theory

Density Functional Theory (DFT) provides a good compromise between accuracy and computational cost, giving the chance to treat moderately large electronic systems from first principles. It is nowadays one of the most popular computational procedures for electronic structure calculations and it is used in a wide range of fields, from physics to material science to chemistry. The DFT method is based on functionals. A functional is a mapping of an entire function f to a resulting number, $F[f]$; whereas a common function is defined to be a mapping of a variable x to a number, $f(x)$. DFT describes the electronic states of atoms, molecules and solids in terms of the three-dimensional electronic density, ρ , upon which the functionals depend. Hohenberg and Kohn, in 1964, published a ground-breaking article[60] which led to the development of DFT. They showed that there exists a functional $F[\rho]$ such that the ground state energy can be expressed as the minimum of the functional:

$$E[\rho] = F[\rho] + \int d\mathbf{r} V(\mathbf{r}) \rho(\mathbf{r}) \quad (2.41)$$

where $\rho(\mathbf{r})$ is the charge density, and $F[\rho]$ does not depend on the system. In principle, the ground state properties of the system of interacting electrons can be described in terms of the charge density only, rather than on the far more complicated many-particle wave function.

Thomas-Fermi Model

The original DFT method was developed by Thomas and Fermi in 1927[61, 62]. The conventional approaches use the wavefunction as the central quantity, since it contains the full information of the system. Nevertheless, it is a very complex quantity that cannot be probed experimentally, and that depends on the $4N$ degrees of freedom (three spatial variables and one spin variable), where N is the number of electrons. In the Thomas-Fermi approach, the kinetic energy of the system of electrons is approximated as an explicit functional of the density. Electrons are supposed to be in an ideal system, where they do not interact with each other, and they belong to a homogeneous gas with density equal to the local density at any given point. The kinetic energy functional proposed is:

$$T_{\text{TF}}[\rho(\mathbf{r})] = \frac{3}{10} (3\pi^2)^{\frac{2}{3}} \int \rho(\mathbf{r})^{\frac{5}{3}} d\mathbf{r} \quad (2.42)$$

The TF energy functional is then

$$E_{\text{TF}}[\rho(\mathbf{r})] = \frac{3}{10} (3\pi^2)^{\frac{2}{3}} \int \rho(\mathbf{r})^{\frac{5}{3}} d\mathbf{r} - Z \int \frac{\rho(\mathbf{r})}{r} d\mathbf{r} + \frac{1}{2} \int \frac{\rho(\mathbf{r}_1) \rho(\mathbf{r}_2)}{r_{12}} d\mathbf{r}_1 d\mathbf{r}_2 \quad (2.43)$$

where the Z is the nucleus charge in atomic units. The GS density and energy are found once the functional, Eq. 2.43, is minimized for all possible $\rho(\mathbf{r})$ subject to the constraint on the total number of electrons

$$\int \rho(\mathbf{r})d(\mathbf{r}) = N \quad (2.44)$$

Variational Principle in the Ground State Configuration

In analogy with the variation theorem seen in the wave function Eq. 2.40, also in DFT the same principle applies in order to obtain the ground state energy for a given system, as stated in the Hohenberg-Kohn variational theorem

“the energy computed from a guessed density function $\rho(\mathbf{r})$ is an upper bound to the true ground state energy E_0 ”.

The full minimization of the functional $E[\rho]$ with respect to all allowed N -electrons wave functions will give the ground state, ρ_0 , and the corresponding energy E_0 (Levy and Lieb method [63])

$$E_0 = \min_{\psi \rightarrow \psi_{\rho(\mathbf{r})}} E[\rho] = \min_{\psi \rightarrow \psi_{\rho(\mathbf{r})}} \langle \psi | \hat{T}_e + \hat{V}_{ee} | \psi \rangle \quad (2.45)$$

The variation principle defines a procedure to determine the ground state wave function ψ_0 and energy E_0 for a given system with N electrons and a given nuclear potential V_{ext} . In conclusion, the ground state energy is a functional of the total number of electrons and the nuclear potential V_{ext}

$$E_0 = E[N, V_{ext}] \quad (2.46)$$

The First Hohenberg-Kohn Theorem

The first Hohenberg-Kohn theorem[60] shows that the electron density uniquely determines the Hamiltonian operator and, as a consequence, all the properties of the system[64]. It states as follow :

“the external potential $V_{ext}(\mathbf{r})$ is, to within a constant, a unique functional of $\rho(\mathbf{r})$; since, in turn $V_{ext}(\mathbf{r})$ fixes \hat{H} , we see that the full many particle ground states is a unique functional of $\rho(\mathbf{r})$ ”

Corollary I

Being the Hamiltonian fully determined, except for a constant shift of the energy, it follows that the many-body wave functions for all states, ground and excited, are determined. Therefore all properties of the system are *completely determined* given only the ground state density $\rho_0(\mathbf{r})$.

The Second Hohenberg-Kohn Theorem

The second Hohenberg-Kohn theorem ensures that a certain density is the ground state density that we are looking for, and it is formulated as follows

“ $F_{HK}[\rho]$, the functional that delivers the ground state energy of the system, delivers the lowest energy if and only if the input density is the true ground state density”

Corollary II

It states that only the functional $E[\rho]$ is sufficient to determine the exact ground state energy and density.

Key Problem

The implicit problem that follows from the theorems proposed above is that the allowed densities need to be compatible with a wave function. This problem is named V-representability problem. It is clear that while the real ground state is V-representable, it is not possible to know *a priori* if the density used is V-representable, marking a big problem because the trial densities to use may not satisfy the condition. To overcome the problem, the definition of $F[\rho]$ might be extended to include such densities, as long as the E_0 is still minimized by the correct GS density.

2.4.1 The Kohn-Sham Method

In 1965 Kohn and Sham[65] proposed the revolutionary idea that made available the use of the DFT approach in computational chemistry and condensed matter physics, by re-introducing the concept of *orbitals* in the description. The idea was to substitute the complex interacting many-body system obeying the Hamiltonian in equation 2.15, with an *auxiliary system*. This system can be solved because it is formed by a set of independent non-interacting particles. The Kohn-Sham *ansatz* assumes that the ground state density of the original interacting systems is equal to that of the non-interacting ones and it is built upon two main assumptions:

Assumption n°1 : the exact GS density is equal to the ground state density of the auxiliary system of non-interacting particles;

Assumption n°2 : the auxiliary Hamiltonian is chosen in order to have the usual kinetic operator and an effective *local* potential $V_{\text{eff}}^{\sigma}(\mathbf{r})$ acting on an electron of spin σ at point \mathbf{r} . The local form is not essential, but it is a useful simplification which is considered as one of the *KS* equation main features.

The KS *ansatz* is summarized in Fig. 2.8.

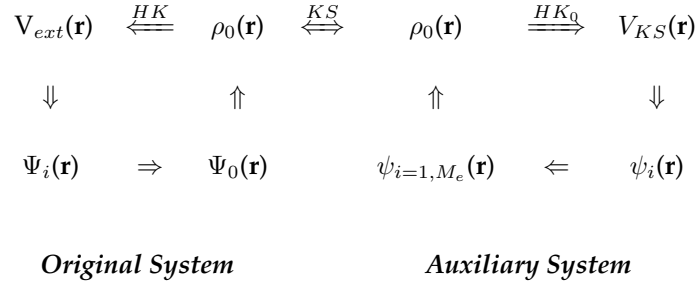


Figure 2.8: This is a schematic representation of the Kohn-Sham (KS) *ansatz*, that links the original many-body system to the *auxiliary* one, where the Hohenberg-Kohn (HK₀) theorem is applied.

The double arrow labeled with KS provides the connection in both directions between the many-body system and the non-interacting particle system; so that the arrows connect any point to any other point.

2.4.2 The Kohn-Sham Equations

How are the fundamental physical quantities of a real system taken into consideration? The ground state density of the interacting system is assumed to be equal to the ground state of the non-interacting one. The electron density $\rho(\mathbf{r})$ and the kinetic energy $T_{KS}[\rho]$ are respectively defined as

$$\rho(\mathbf{r}) = \sum_{i=1}^N |\psi_i(\mathbf{r})|^2 \quad (2.47)$$

and

$$T_{KS}[\rho] = -\frac{1}{2} \sum_{i=1}^N \langle \psi_i | \nabla^2 | \psi_i \rangle \quad (2.48)$$

where ψ_i represents the occupied molecular orbitals and the sum runs over each occupied molecular orbital N . Similarly, the kinetic energy associated to the complex system is replaced by the kinetic energy associated to the auxiliary one. So, the universal functional $F[\rho]$ is rewritten as

$$F[\rho] = T_{KS}[\rho] + \frac{1}{2} \int \frac{\rho(\mathbf{r}) n(\mathbf{r}')}{|\mathbf{r} - \mathbf{r}'|} d(\mathbf{r}) d(\mathbf{r}') + E_{xc}[\rho] \quad (2.49)$$

where $T_{\text{KS}}[\rho]$ represents the kinetic energy of the auxiliary system, that is a functional of the ground state density $\rho_0(\mathbf{r})$. The second term, instead, is the expression for the Hartree energy in terms of the Hartree density and potential

$$E_{\text{HT}}[\rho(\mathbf{r})] = \frac{1}{2} \int d\mathbf{r} v_H(\mathbf{r})\rho(\mathbf{r}) = \frac{1}{2} \int \frac{\rho(\mathbf{r})\rho(\mathbf{r}')}{|\mathbf{r} - \mathbf{r}'|} d(\mathbf{r})d(\mathbf{r}') \quad (2.50)$$

All the many-body effects of exchange and correlation are grouped into the exchange-correlation energy $E_{xc}[\rho]$. $E_{xc}[\rho]$ can be written in terms of the *HK* functional as

$$E_{xc} = E_{\text{HK}}[\rho] - (T_{\text{KS}}[\rho] + E_{\text{HT}}[\rho]) \quad (2.51)$$

The determination of the orbitals ψ_i proceed exactly like in Hartree-Fock theory, by solving, this time, the so called Kohn-Sham equations

$$H^{\text{KS}}\psi_i^{\text{KS}} = \varepsilon_i^{\text{KS}}\psi_i^{\text{KS}} \quad \text{for } i = 1, \dots, N \quad (2.52)$$

In analogy with the HF method, in Eq. 2.52 we have the Kohn-Sham operator H^{KS} . The Fock operator and the Kohn-Sham one are almost the same except for the exchange correlation potential part, that, in DFT, is defined by the operator $V_{xc}(\mathbf{r})$, in contrast to the complicated term defined in HF. Finally, this exchange correlation potential operator is such that it contains *all* the many electron effects, in contrast again to the HF one, which includes the exchange but not the electron correlation.

The optimization of the orbitals ψ_i is, exactly like in HF method, performed self-consistently. This leads, in the end, to the ground state density of the system from which, *a priori*, all the properties of the system can be subsequently derived. The critical point is to find a way to describe the exchange correlation energy functional. This point brought to the development, along the years, of a plethora of functionals with different “*flavors*”, among which it is worth to mention the “Local Density Approximation” (LDA), the “Generalized Gradient Approximation” (GGA) and so-called hybrid functionals. These types of functionals will be described below.

The Local Density Approximation

The LDA approximation, that considers the exchange correlation potential term of a given particle located in \mathbf{r} , depends only on the electron density at that specific point

$$E_{xc}^{\text{LDA}} = \int \rho(\mathbf{r}) \epsilon_{xc}^{\text{LDA}}[\rho(\mathbf{r})] d\mathbf{r} \quad (2.53)$$

where the $\varepsilon_{xc}(\mathbf{r})$ term is the sum of the exchange and correlation contribution

$$\varepsilon_{xc}^{\text{LDA}}(\mathbf{r}) = \varepsilon_x^{\text{LDA}}(\mathbf{r}) + \varepsilon_c^{\text{LDA}}(\mathbf{r}) \quad (2.54)$$

The LDA exchange energy term is derived from the uniform electron gas definition, in a point \mathbf{r} , as

$$\varepsilon_x^{\text{LDA}}(\mathbf{r}) = -\frac{3}{4} \left(\frac{3}{\pi} \right)^{\frac{1}{3}} \rho(\mathbf{r})^{\frac{4}{3}} \quad (2.55)$$

The correlation terms are inferred from parametric equations fitting perturbative or Quantum Monte Carlo[66, 67] calculation results. The most used are the Wigner[68], Perdew-Zunger[69] (PZ), Lee-Yang-Parr[70] (LYP), Perdew-Wang[71] (PW92). The LDA, being *exact* for the uniform electron gas, is well suited for the investigation of homogeneous electron densities, like systems based on the elements of the *s* and *p* blocks of the periodic table. But, in the case the electron density is inhomogeneous, it is necessary to account for the shape of $\rho(\mathbf{r})$ around the point \mathbf{r} , hence the density gradient.

The Generalized Gradient Approximation

In the GGA, differently from the previous case, the gradient of the functional is also used, introducing a semi-local character of the electron density in the formulation of E_{xc} , in order to account for the shape of the electron density around the point \mathbf{r}

$$E_{xc}^{\text{GGA}}[\rho, \nabla\rho] = \int \rho(\mathbf{r}) \varepsilon_{xc}^{\text{GGA}}(\rho(\mathbf{r}), \nabla\rho(\mathbf{r})) d\mathbf{r} \quad (2.56)$$

Then, the exchange energy term turns out to be

$$E_x^{\text{GGA}}[\rho, \nabla\rho] = \int F_x(s(\mathbf{r})) \rho(\mathbf{r})^{\frac{4}{3}} d\mathbf{r} \quad (2.57)$$

with F_x corresponding to a function of the reduced density gradient defined as

$$s(\mathbf{r}) = \frac{|\nabla\rho(\mathbf{r})|}{6\pi^2\rho(\mathbf{r})^{\frac{4}{3}}} \quad (2.58)$$

A lot of effort has been put and is still on going in the generation of GGA functionals, since they provide a better description of not only systems based on the elements of the *s* and *p* blocks, but also, to some extent, to the *f* and *d* ones. Among the most popular GGA functionals there are the PW91[72], BLYP[73] and PBE[74]. The last one was used in the structure optimizations and *ab initio* molecular dynamics calculations in this thesis.

Hybrid Functionals

The hybrid functionals, introduced by Becke in 1993, are a class of functionals used to approximate the exchange-correlation that contains a part of the “exact exchange” from the HF exchange and a part inferred by interpolation of post-HF and semi-empirical results. The hybrid functional used in the computation of the broken symmetry solution for obtaining singlet and triplet relative energies, in this research, is the B3LYP[75, 76], that stands for Becke, 3-parameters, Lee-Yang-Parr. The B3LYP is defined as

$$E_{xc}^{\text{B3LYP}} = (1 - a_0)E_x^{\text{LDA}} + a_0E_x^{\text{HF}} + a_x\Delta E_x^{\text{B88}} + a_cE_c^{\text{LYP}} + (1 - a_c)E_c^{\text{VWN}} \quad (2.59)$$

where $a_0=0.20$, $a_x=0.72$ and $a_c=0.81$ [76]. The E_x^{LDA} is the standard local exchange functional[77], ΔE_x^{B88} is Becke’s gradient correction to the exchange functional, E_c^{LYP} is the term for the correlation functional from Lee, Yang and Parr[70], and E_c^{VWN} is the Vosko-Wilk-Nusair[78] local density approximation to the correlation functional.

2.4.3 Spin Polarized Calculations

DFT, in its general formulation, treats closed-shells systems, where pairs of alpha and beta spinorbitals are “occupying” the same spatial orbital, therefore, it is *spin unpolarised*. Instead, when dealing with open-shell systems, the DFT theory as defined above cannot be used. In order to overcome the problem, like in the UHF method, a *spin polarised* DFT formalism has been developed. Like in UHF, also in this case the α and β spinorbitals have different spatial orbitals, thus, different energies. Treating separately the α and β spinorbitals leads to separate kinetic and exchange-correlation energies for each spin considered, while the Coulomb and external potential energies are calculated for the total density. Then, a different exchange-correlation operator, one for electrons with α spin and one for electrons with β spin, results in a different *KS* Hamiltonian,

$$\hat{h}_{\text{KS}}^{\alpha} = -\frac{1}{2}\nabla^2 + V_{\text{ext}}(\mathbf{r}) + V_{\text{Coul}}[\rho](\mathbf{r}) + V_{xc}[\rho^{\alpha}](\mathbf{r}) \quad (2.60)$$

and

$$\hat{h}_{\text{KS}}^{\beta} = -\frac{1}{2}\nabla^2 + V_{\text{ext}}(\mathbf{r}) + V_{\text{Coul}}[\rho](\mathbf{r}) + V_{xc}[\rho^{\beta}](\mathbf{r}) \quad (2.61)$$

It follows that the iterative process will provide the solution of the *KS* orbitals for each spin type, but, since the Hamiltonians depend upon the total density through the Coulomb operator, it means that the two Hamiltonians are coupled and they need to be solved simultaneously. Usually the computational cost of a *spin polarised* calculation is *ca.* twice of a restricted one. Like in the UHF formalism, also here the final solution might suffer from spin contamination.

2.4.4 The Broken-Symmetry Approximation

The derivation of the J_{AB} values within the single determinant description of the spin states like in DFT has led to the development of the *Broken Symmetry* (BS) approximation. For a system with two electrons in two open-shell orbitals, the BS approximation makes use of two determinants, in particular, the High Spin (HS) one

$$\phi_{\text{HS}} = |\phi_1 \phi_2| \quad (2.62)$$

and the Broken Symmetrical (BS) one

$$\phi_{\text{BS}} = |\phi_1 \bar{\phi}_2| \quad (2.63)$$

where the closed-shell orbitals have been omitted for convenience. Because in the HS determinant the closed shell spinorbitals appear in pairs with slightly different spatial orbitals[27], the corresponding \hat{S}^2 expectation value will be not exactly equal to 2. Nevertheless, it is generally considered to be a valid description of the triplet state of the system, leading to

$$\phi_{\text{HS}} \approx \phi_{\text{T}} \quad (2.64)$$

and

$$E_{\text{HS}} = \langle \phi_{\text{HS}} | \hat{H} | \phi_{\text{HS}} \rangle \approx E_{\text{T}} \quad (2.65)$$

More complex is the nature of the BS determinant. Its \hat{S}^2 expectation value is somewhere in between the singlet and triplet states, prompting the use of a linear combination of the spin restricted singlet and triplet states[27] like

$$|\phi_{\text{BS}}\rangle = \lambda |\phi_{\text{S}}\rangle + \mu |\phi_{\text{T}}\rangle \quad (2.66)$$

where $\lambda^2 + \mu^2 = 1$ is the normalization condition. Accordingly, the energy of the BS state is

$$E_{\text{BS}} = \langle \lambda \phi_{\text{S}} + \mu \phi_{\text{T}} | \hat{H} | \lambda \phi_{\text{S}} + \mu \phi_{\text{T}} \rangle = \lambda^2 E_{\text{S}} + \mu^2 E_{\text{T}} \quad (2.67)$$

while the \hat{S}^2 expectation value is

$$\langle \hat{S}^2 \rangle_{\text{BS}} = \lambda^2 \langle \phi_{\text{S}} | \hat{S}^2 | \phi_{\text{S}} \rangle + \mu^2 \langle \phi_{\text{T}} | \hat{S}^2 | \phi_{\text{T}} \rangle = 2\mu^2 \quad (2.68)$$

Rearranging the normalization condition, we obtain two expressions for μ^2 and λ^2 respectively

$$\mu^2 = \frac{\langle \hat{S}^2 \rangle_{\text{BS}}}{2} \quad (2.69)$$

and

$$\lambda^2 = 1 - \frac{\langle \hat{S}^2 \rangle_{\text{BS}}}{2} \quad (2.70)$$

These two expressions can replace the corresponding terms of Eq. 2.67, obtaining

$$E_{\text{BS}} = \left[1 - \frac{\langle \hat{S}^2 \rangle_{\text{BS}}}{2} \right] E_{\text{S}} + \left[\frac{\langle \hat{S}^2 \rangle_{\text{BS}}}{2} \right] E_{\text{T}} \quad (2.71)$$

From here, the formulation for the energy difference between the BS and HS determinants is derived

$$\begin{aligned} E_{\text{BS}} - E_{\text{HS}} &= E_{\text{S}} - \left[\frac{\langle \hat{S}^2 \rangle_{\text{BS}}}{2} \right] (E_{\text{S}} - E_{\text{T}}) - E_{\text{T}} \\ &= \frac{2 - \langle \hat{S}^2 \rangle_{\text{BS}}}{2} (E_{\text{S}} - E_{\text{T}}) \end{aligned} \quad (2.72)$$

Finally, following the definition of the HDVV given in Eq. 2.1, the expression for magnetic exchange coupling J , defined as the difference between the singlet and the triplet states is obtained

$$J = \frac{E_{\text{S}} - E_{\text{T}}}{2} = \frac{(E_{\text{BS}} - E_{\text{HS}})}{2 - \langle \hat{S}^2 \rangle_{\text{BS}}} \quad (2.73)$$

In the generalization of Eq. 2.73, the unrestricted determinant ϕ_{HS} is considered to be a good approximation of the spin eigenfunction with maximum multiplicity ϕ_{max}

$$\langle \hat{S}^2 \rangle_{\text{HS}} = S_{\text{max}}(S_{\text{max}} + 1) \quad (2.74)$$

and the corresponding energy

$$E_{\text{HS}} = E_{\text{max}} \quad (2.75)$$

Following the same procedure like in Eq. 2.66, the BS determinant is accordingly written as

$$|\phi_{\text{BS}}\rangle = \lambda |\phi_{\text{S}}\rangle + \mu |\phi_{\text{max}}\rangle = \lambda |\phi_{\text{S}}\rangle + \mu |\phi_{\text{HS}}\rangle \quad (2.76)$$

where the corresponding expression for \hat{S}^2 is

$$\langle \hat{S}^2 \rangle_{\text{BS}} = \lambda^2 \langle \phi_{\text{S}} | \hat{S}^2 | \phi_{\text{S}} \rangle + \mu^2 \langle \phi_{\text{HS}} | \hat{S}^2 | \phi_{\text{HS}} \rangle = \mu^2 \langle \hat{S}^2 \rangle_{\text{HS}} \quad (2.77)$$

leading to the energy expression of the form

$$E_{\text{BS}} = \left[1 - \frac{\langle \hat{S}^2 \rangle_{\text{BS}}}{\langle \hat{S}^2 \rangle_{\text{HS}}} \right] E_{\text{S}} + \left[\frac{\langle \hat{S}^2 \rangle_{\text{BS}}}{\langle \hat{S}^2 \rangle_{\text{HS}}} \right] E_{\text{HS}} = \lambda^2 E_{\text{S}} + \mu^2 E_{\text{HS}} \quad (2.78)$$

Finally, the energy difference between the BS and HS states, derived like in case of Eq. 2.71, is equivalent to

$$\begin{aligned} E_{\text{BS}} - E_{\text{HS}} &= E_{\text{S}} - \left[\frac{\langle \hat{S}^2 \rangle_{\text{BS}}}{\langle \hat{S}^2 \rangle_{\text{HS}}} \right] (E_{\text{S}} - E_{\text{HS}}) - E_{\text{HS}} \\ &= \frac{\langle \hat{S}^2 \rangle_{\text{HS}} (E_{\text{BS}} - E_{\text{HS}})}{\langle \hat{S}^2 \rangle_{\text{HS}} - \langle \hat{S}^2 \rangle_{\text{BS}}} = E_{\text{S}} - E_{\text{HS}} \end{aligned} \quad (2.79)$$

The previous equation leads to the Yamaguchi[79] expression for the magnetic exchange coupling J , defined as

$$J = \frac{E_{\text{S}} - E_{\text{HS}}}{S_{\text{max}}(S_{\text{max}} + 1)} = \frac{E_{\text{S}} - E_{\text{HS}}}{\langle \hat{S}^2 \rangle_{\text{HS}}} = \frac{E_{\text{BS}} - E_{\text{HS}}}{\langle \hat{S}^2 \rangle_{\text{HS}} - \langle \hat{S}^2 \rangle_{\text{BS}}} \quad (2.80)$$

that, in the limit case where the magnetic orbitals do not overlap, simplifies to

$$J = \frac{E_{\text{BS}} - E_{\text{HS}}}{S_{\text{max}}(S_{\text{max}} + 1) - S_{\text{max}}} = \frac{E_{\text{BS}} - E_{\text{HS}}}{S_{\text{max}}^2} \quad (2.81)$$

This formulation of the J was first derived by Noodleman[80] and, in the case of two magnetic centers with $S=\frac{1}{2}$, it simplifies to

$$J = E_{\text{BS}} - E_{\text{HS}} \quad (2.82)$$

Kohn-Sham in Plane Waves

The periodic nature of many materials favored the development of DFT based on plane waves, which better reproduces the repetitive network of atomic or molecular interactions within a crystal. To accomplish it, the Bloch theorem[64] for a periodic lattice is efficiently exploited to express the one-electron wave function in terms of a Fourier expansion. The use of plane waves has the advantage of being mathematically simple to handle and, in principle, it completely spans the Hilbert space[64]. Plane wave basis sets have also the advantage of covering all space equally. The last thing is extremely important if one does not know *a priori* the form of the electronic wave function. In order to achieve a finite basis set, the Fourier expansion needs to be truncated, introducing a kinetic energy *cutoff* (E_{cf}), defined as

$$E_{cf} = \frac{\hbar^2}{2m} |\mathbf{k} + \mathbf{G}|^2 \quad (2.83)$$

where \mathbf{k} represents the wave vector and \mathbf{G} is the reciprocal lattice vector. The choice of the energy cutoff value determines the truncation of the plane wave expansion at a particular \mathbf{G} . The *KS* equations are then rewritten as

$$\sum_{\mathbf{G}'} \left[\frac{1}{2} |\mathbf{k} + \mathbf{G}|^2 + V_{ion}(\mathbf{G} - \mathbf{G}') + V_H(\mathbf{G} - \mathbf{G}') \right] c_{i,\mathbf{k}+\mathbf{G}} = \epsilon_i c_{i,\mathbf{k}+\mathbf{G}} \quad (2.84)$$

The reciprocal space representation of the kinetic energy is diagonal, where the potentials are described in terms of Fourier components. In principle, the secular equation 2.84 could be solved by diagonalizing the Hamiltonian matrix $H_{\mathbf{k}+\mathbf{G}, \mathbf{k}+\mathbf{G}'}$. The size of the matrix is defined by the energy cutoff E_{cf} . The final energy value depends upon the pseudopotential chosen to describe the atomic species.

2.4.5 Pseudopotentials

The pseudopotential is a mathematical effective potential that mimics the effect of ionic nuclei and core electrons (see Fig. 2.9). The use and development of pseudopotentials is justified by the fact that the expansion in the plane waves of the all-electron wavefunction, considering both core and valence electrons, would become prohibitive. Moreover, it would lead to the use of high kinetic energy cutoffs, because of the “different nature” of the two kind of electrons: the first strongly bound to the nucleus, the second highly flexible. Since the majority of the physical properties take place as a consequence of the valence electron interactions between atoms, then it is reasonable to separate the core from the valence contribution. In this way, the core states are frozen and are not taken into consideration, and the valence electrons are described by means of pseudo wave functions, making the plane wave basis sets usable in practice. Smoothness and transferability are main properties which

define if a pseudopotential is efficient for a particular atomic species. Pseudopotentials should be as *smooth* as possible in order to have a convenient plane waves expansion (small kinetic cutoff values). While the *transferability* (thus accuracy) property is correlated with the ability of the pseudopotential to produce pseudo-orbitals that are as close as possible to true orbitals outside the core region, for all the systems containing a given atom[64]. The pseudopotentials come in different flavors and, among the most popular, there are the *so-called* Norm-Conserving[81], Ultrasoft[82] and projector augmented[83] ones.

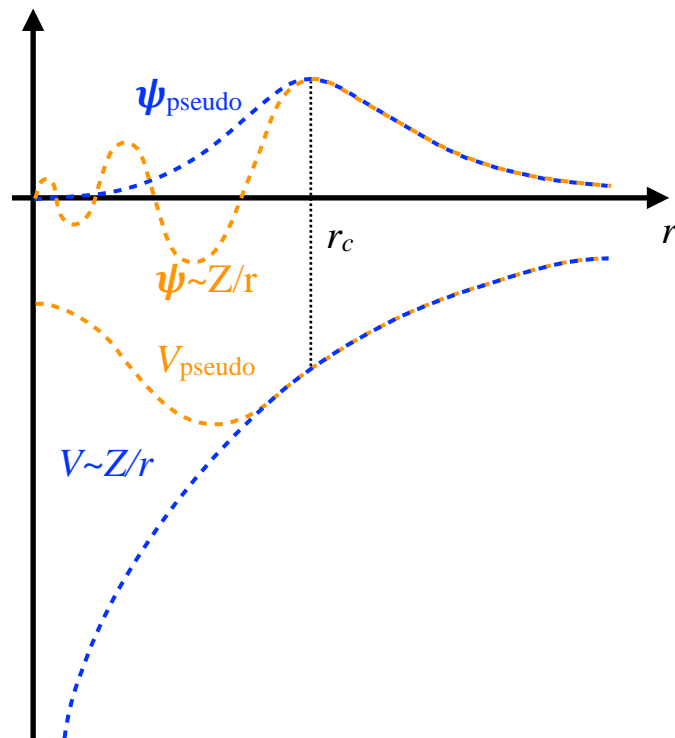


Figure 2.9: Scheme showing the trend of a pseudo wavefunction and potential (orange), compared to the real Coulomb potential and wavefunction trend of a nucleus (blue). The match between real and pseudo wavefunction is found above a certain cutoff radius r_c .

Norm-Conserving

The *ab initio* Norm-Conserving pseudopotentials (NCP) are generated based on a specific set of requirements as defined in the work of D. R. Hamann, Schlüter and Chiang[81]. These requirements guarantee the NCP to be *smooth* and *transferable*, fixing that

Req. 1: The pseudo-valence and all-electron eigenvalues coincide for a chosen *prototype* atomic configuration;

Req. 2: The all-electron and pseudo atomic wave functions coincide beyond a chosen *core radius* R_c ;

As a consequence, the NCP equals the atomic potential outside the *core region* of radius R_c [64]. The potential is uniquely determined by the wave function and the energy ε .

Req. 3: The logarithmic derivatives of the all-electron and pseudo-wave functions coincide in R_c ;

It follows that both the wave function ψ_l and its first derivative W_{ln} , defined as

$$W_{ln}(\varepsilon, r) = r \frac{\psi_l'(\varepsilon, r)}{\psi_l(\varepsilon, r)} = r \frac{d}{dr} \ln \psi_l(\varepsilon, r) \quad (2.85)$$

are continuous in R_c for any *smooth* potential.

Req. 4: Norm-Conservation condition: the charge, integrated inside R_c , agrees for each wave function;

The integrated charge

$$Q_{ln} = \int_0^{R_c} dr r^2 |\psi_{ln}(r)|^2 = \int_0^{R_c} dr \phi_{ln}(r)^2 \quad (2.86)$$

is the same for Ψ_l^{PS} , radial pseudo-potential, as for the all-electron radial orbital ψ_l^{PS} , for a valence state. Q_{ln} conservation ensures that:

- total charge in the core region is correct;
- the normalized pseudo-potential is equal to the orbital outside of R_c .

Req. 4 ensures that the wave function $\psi_l(r)$ and its radial derivative $\psi_l'(r)$ are continuous at R_c , for any smooth potential, leading also to a correct representation of the region between atoms, outside R_c .

Req. 5: The first energy derivative of the logarithmic derivatives of both the all-electron and pseudo wave functions coincides in R_c .

Finally, according to Req. 5, spherical atoms can be generated and employed in the description of complex environments like molecules or solids. In other words, it guarantees that the pseudopotential adapts as a function of the system to simulate.

In particular, for the geometry optimization, variable-cell optimization and AIMD obtained by means of the CP2K code with the Quickstep[84, 85] engine, we made use of the norm-conserving Goedecker-Teter-Hutter[86–88] (GTH) pseudopotentials, which present some advantages like a faster real space integration for large systems and the high accuracy and efficiency correlated to the use of plane waves.

Ultrasoft

Ultrasoft pseudopotentials were first introduced by Vanderbilt[82] in 1990. As the name suggests, the idea of UPP is to relax the norm-conserving conditions in order to generate much softer potentials. It follows that fewer plane-waves can be employed for simulating systems with almost the same accuracy of the NCPP. However, it is correlated to a little loss of *transferability*. In this scheme the pseudo-wave functions are allowed to be as soft as possible within the core region, so that the cut-off energy can be reduced dramatically. Technically, this is achieved by introducing a generalized orthonormality condition. The electron density given by the squared moduli of the wave functions has to be augmented in the core region in order to recover the full electronic charge. The electron density is then subdivided into:

- a smooth part that extends throughout the unit cell;
- a hard part localized in the core regions.

The augmented part appears in the density only, not in the wavefunctions. The UPP have another advantage besides being much softer than the NCPP ones. The UPP generation algorithm guarantees good scattering properties over a pre-specified energy range, which results in a much better transferability and accuracy of pseudopotentials. UPP usually also treats “shallow” core states as valence by including multiple sets of occupied states in each angular momentum channel. This also contributes to high accuracy and transferability of the potentials, although at a price of computational efficiency.

2.4.6 Semi-empirical Dispersion Functions: Grimme D3

In the geometry optimizations as well as in the molecular dynamic calculations of the molecular crystals investigated in this work, the van der Waals interactions play a critical role, and they have to be accounted for properly. On the other hand, these interactions have, *in practice*, no effect on the derivation of the J_{AB} values, being these values derived as the difference of the total energies for the singlet and triplet solutions, to which the same contribution for the van der Waals interactions has been added (because we are dealing with interactions between the same molecular species). Both LDA and GGA functionals omit this important term. Recently, several methods have been developed, based on two different “strategies”: the *ad hoc* methods and the self-consistent methods[89]. In all the geometry optimizations and AIMD calculations reported in this work, we adopted the *ad hoc* method called DFT-D3[90, 91]. In this case, a three-body independent correction term is added to the DFT energy, mimicking the van der Waals interactions. For a detailed discussion of these schemes, the reader is addressed to the original paper of Grimme and co-workers and references therein[90, 92].

2.4.7 Energy Decomposition Analysis

The Energy Decomposition Analysis[93, 94] (EDA) is a powerful method that allows for a quantitative investigation of the intermolecular interactions on the basis of single-determinant Hartree-Fock (RHF, ROHF and UHF) wavefunctions as well as in DFT. In our case, the EDA is employed within the DFT framework, evaluating the intermolecular interactions for the two polymorphic phases of TTTA, the LT and HT respectively, as reported in Chapter 4. The technical details of the technique are covered in several articles[93–95] and reviews[96], where also the different implementations are reported, like, for instance, the EDA-Natural Orbital for chemical Valence (NOVC)[97] or the EDA-Generalized Product Function (BLW)-EDA of Mo[95, 98–100]. In general terms, within the DFT framework, the EDA algorithm allows to decompose the Kohn-Sham interaction energy (E^{KS}) between the supermolecule X comprising the monomers A, in several energetic terms, namely the electrostatic, exchange, repulsion, polarisation and dispersion components,

$$\Delta E^{KS} = \Delta E^{ele} + \Delta E^{ex} + \Delta E^{rep} + \Delta E^{pol} + \Delta E^{disp} \quad (2.87)$$

where the E^{KS} energy is defined as

$$E^{KS} = E_X^{KS} - \sum_A E_A^{KS} \quad (2.88)$$

Since the intermolecular interactions govern the formation and packing of crystals, the EDA is found to be very useful when an evaluation of the forces acting between the monomers composing the supersystem is required.

2.5 Dynamical Evolution of the System

The FPBU methodology is mainly used to simulate either the magnetic susceptibility χ or the magnetization M or the heat capacity C_P . The ultimate intent, in this work, is the study and comprehension of how the magnetic exchange couplings propagate and affect the crystals. But, in order to complete the overview and to rationalize differences and similarities within the DTA-based compounds group, it is necessary to study the effects of thermal fluctuations in the magnetic response of the compounds. To this purpose, the *Ab Initio* Molecular Dynamics method has been extensively used. The results will be discussed later in Chapter 6. Here a brief overview of the method is reported, addressing the reader to more exhaustive reviews on the topic[101, 102].

Towards the *Ab Initio* Approach

Classical molecular dynamics is based on the integration of the Hamilton's equation of motion, once the atomic coordinates q and the linear momenta p are defined

$$p = -\frac{\partial H}{\partial q} \quad (2.89)$$

$$q = -\frac{\partial H}{\partial p} \quad (2.90)$$

The Hamiltonian can be decomposed in two contributions, kinetic and potential

$$H(q, p) = T(p) + U(q) \quad (2.91)$$

and the equation of motion can be expressed as

$$m\ddot{q} = -\nabla_q U \quad (2.92)$$

that is numerically integrated making use of the Verlet[103] algorithm. Once 2.92 is integrated, the new atomic positions are found. This process takes place until a user-defined criterion for convergency is met.

2.5.1 *Ab Initio* Molecular Dynamics

The study of complex systems like the TTTA, PDTA, TDPDTA and 4-NCBDTA requires high accuracy and precision due to the complex interacting environment. This descriptive power cannot be achieved by means of the classical MD, because of the lack of *force fields* parametrized for neutral radicals. The problem is overcome by taking advantage of the *Ab Initio* Molecular Dynamics (AIMD), an approach that is *free* from empirical parameters, used instead in classical MD. This “freedom” comes at a certain cost: the number of atoms that can be treated is limited, around thousands, whereas in the classical one, *a priori* millions of atoms per time can be accounted for. The AIMD[101, 102] comes in different fashions like the Born-Oppenheimer molecular dynamics (BO-MD) or the Car-Parrinello molecular dynamics (CPMD), just to cite the most common used. The BO-MD includes the quantum mechanical electronic effects in the calculation of forces and energies. The CPMD method[104–106] considers the explicit inclusion of a fictitious electron mass to ensure the adiabaticity in the energy transfer from nuclei to electrons.

The BO-MD Method

If the ionic motion obeys classical dynamics, the Lagrange function of a general many body system composed of N classical particles, in the BO approximation is

$$L(\mathbf{R}_I, \dot{\mathbf{R}}_I) = \sum_I^N \frac{1}{2} M_I \dot{\mathbf{R}}_I^2 + U(\mathbf{R}_I) \quad (2.93)$$

where the term $U(\mathbf{R}_I)$ contains the nuclei-nuclei interaction energy and the interaction energy between nuclei and electrons. In the BO-MD, the PES is given by the solution of the Schrödinger equation for an isolated system as

$$U(\mathbf{R}_I) = \sum_{A < B} \frac{Z_A Z_B}{|\mathbf{R}_A - \mathbf{R}_B|} + \min_{\phi_i} [E^{\text{KS}}(\{\phi_i\}, \{\mathbf{R}_I\})] \quad (2.94)$$

The effect of the ionic motion on the electronic one is neglected, being only considered as a parametrical contribution. On top of that, being the equations solved at every single time step, the electrons constantly remain in the ground state. This implies that the potential will be always at the ground state, for each given set of atomic coordinates. From equation 2.93 follows the derivation of the equation of motion, by means of the Euler-Lagrange equations, as

$$\frac{d}{dt} \frac{\partial L(\mathbf{R}_I, \dot{\mathbf{R}}_I)}{\partial \dot{\mathbf{R}}_I} = \frac{\partial L(\mathbf{R}_I, \dot{\mathbf{R}}_I)}{\partial \mathbf{R}_I} \quad (2.95)$$

So then, the equation of motion (EOM) becomes

$$M\ddot{\mathbf{R}}_{\mathbf{I}} = -\frac{\partial U(\mathbf{R}_{\mathbf{I}})}{\partial \mathbf{R}_{\mathbf{I}}} \quad (2.96)$$

The delicate electronic term, in the KS approach, is replaced by the extended energy function of the converged electronic wave function ϕ_i as

$$\min_{\{\phi_i\}} [E_{\text{KS}}(\{\phi_i\}, \{\mathbf{R}_{\mathbf{I}}\})] = \epsilon^{\text{KS}} = E^{\text{KS}} + \sum_{ij} \Lambda_{ij} [\langle \phi_i | \phi_j \rangle - \delta_{ij}] \quad (2.97)$$

that includes the orthonormality constraint with the Lagrange multipliers Λ_{ij} . It follows that the electronic forces are obtained by taking the derivative of equation 2.97 with respect to $\mathbf{R}_{\mathbf{I}}$. Once the minimum is reached applying the variation theorem, then

$$F^{\text{KS}}(\mathbf{R}_{\mathbf{I}}) = \frac{\partial E^{\text{KS}}}{\partial \mathbf{R}_{\mathbf{I}}} + \sum_{ij} \Lambda_{ij} \frac{\partial}{\partial \mathbf{R}_{\mathbf{I}}} \langle \phi_i | \phi_j \rangle \quad (2.98)$$

where the last term of this equation corresponds to the derivative of the wave function with respect to the ionic positions, and it is maintained only in the case Gaussian or Slater basis functions are used.

The CP-MD Method

The Car-Parrinello method uses *fictitious* dynamics[104–106] to keep electrons in the ground state, by introducing a *fictitious* electron kinetic mass (K_{fict}), to ensure the *adiabaticity* in the energy transfer between nuclei and electrons

$$K_{\text{fict}} = \mu \sum_i \langle \dot{\phi}_i | \dot{\phi}_i \rangle \quad (2.99)$$

Like in BO-MD case, the Euler-Lagrange equations, applied to the Lagrangian containing the orbitals as fictitious degrees of freedom, give rise to the EOM as

$$M_i \ddot{\mathbf{R}}_{\mathbf{i}} = -\nabla_{\mathbf{i}} E [\{\phi_i\}, \mathbf{R}_{\mathbf{i}}] \quad (2.100)$$

and to

$$\mu \ddot{\phi}_i(r) = -\frac{\partial}{\partial \phi_i^*(r)} E [\{\phi_i\}, \mathbf{R}_{\mathbf{i}}] + \sum_j \Lambda_j \phi_j(r) \quad (2.101)$$

where, like in the BO-MD case, the Λ_j is a set of Lagrange multipliers used to preserve orthonormality. Starting from a set of atomic coordinates and wave functions (*orbitals*), the positions of the nuclei and corresponding electrons evolve following, in an iterative process, equations 2.100 and 2.101.

2.6 Exploring the Potential Energy Surfaces

The description of the systems investigated is pursued also through the detailed analysis of how each single polymorph is spatially arranged and which are the main interactions that take place between molecules. To accomplish this kind of analysis, a representative supercell of each polymorph of each compound investigated is built and subsequently geometrically optimized. The optimization is not limited to the atomic positions, but it can also include the cell parameters, through the so-called *variable-cell* (VC) optimization. By exploring the Potential Energy Surface (PES) (see PES definition within subsection 2.3.2), it was possible to identify 1) the key variables to account to describe the TDPDTA system and according to those variables, 2) the minimal energy path, explored employing the Nudged Elastic Band method (see subsection 2.6.1). The results of these analyses are reported in Chapter 6. The algorithm used to optimize these compounds is the Broyden-Fletcher-Goldfarb-Shanno[107–111] (BFGS), implemented in many quantum chemistry codes. Each optimization has been performed at PBE[74] level, with plane wave DFT codes (Quantum Espresso and CP2K, see section 2.7) at Γ point. The VC optimization of the LT polymorphs of the PDTA and TDPDTA compounds confirmed that they are already in a minimum of the PES, as expected. The case of the HT phases, instead, is much more intriguing. The VC optimization of the PDTA material showed the occurrence of a dimerization process; in other terms, the columns presenting a uniform stack arrangement propagating along the b axes rearranged in order to form alternated eclipsed dimers and π -shifted dimers, in an even way. This effect has already been observed and reported in the literature[112].

Completely unexpected, instead, is the result of the VC optimization for the TDPDTA compound. The HT polymorph is already in a minimum of the PES. As a consequence, the structure is practically preserved, and it almost coincides with the experimentally resolved one. This peculiar result triggered our curiosity to research the cause of this stability. To do so, we employed the corresponding PES of the TDPDTA system, targeting the effect of the longitudinal translation of the monomers in the two-molecule clusters. For sake of comparison, the same kind of analysis is carried out also for the PDTA system. The procedure follows two steps:

- exploration of the PES by means of the DFT calculations at PBE-D2 level for a set of two-molecule cluster combinations;
- selection and validation of the minimal energy path connecting the two minima in the PES at NEVPT2 level with def2-TZVP basis set.

The PES of the PDTA and TDPDTA systems represents the difference in energy com-

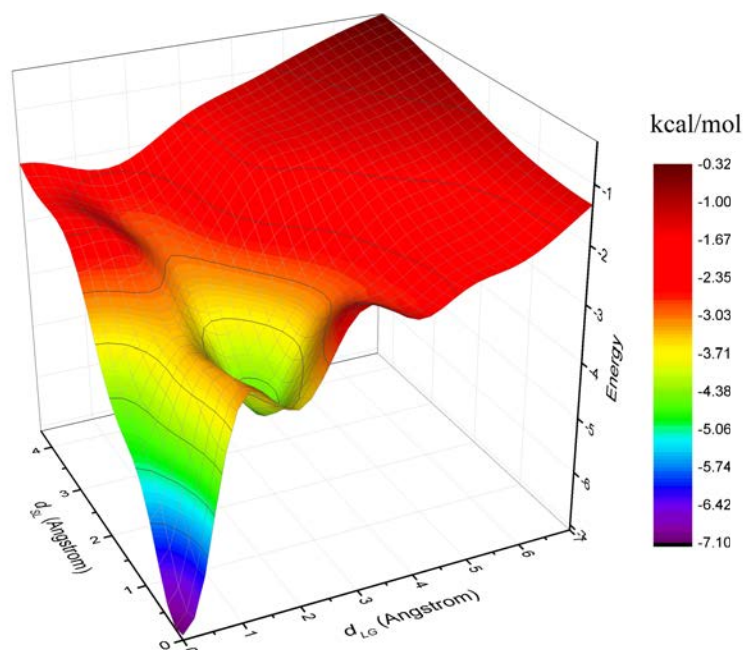


Figure 2.10: Example of PES computed for the PDTA and TDPDTA systems.

pared to their most stable cluster. In Chapter 6 the detailed description of the corresponding energy landscapes as well as the selection and validation of the minimal energy paths will be provided.

2.6.1 The Nudged Elastic Band Method

The study of how the two-molecule clusters give rise to the FM or AFM magnetic couplings is only one part of the work needed to rationalize the behavior of the DTA-based compounds we selected. To find a possible explanation to the intriguing question concerning the mechanism that drives the LT polymorph to rearrange its internal ordering, giving rise to the HT one, with a new magnetic ordering, we took advantage of the technique called Nudged Elastic Band[113–117] (NEB), used to explore and possibly find the minimum energy path (MEP) between two or more structural configurations. In general, the MEP is found by constructing a *trajectory* based on linear interpolation of a set of replicas, named *images*, of the system. Between each two *images*, a spring interaction is added in order to mimic an elastic band, preserving the distance between images. The MEP is found once these springs are optimized, minimizing the force acting on each single image. Differ-

ently from other methods[118–121], the force projection algorithm guarantees the spring's *forces* to not affect the convergence of the MEP, preserving also the correct distribution of the replicas. At every iteration and on each replica, the *true* force and the *spring* force are decomposed in parallel and perpendicular components, once the tangent to the path is estimated. In this way, only the perpendicular part of the *true* force and the parallel of the *spring* force are considered (nudging). The profile obtained in the MEP can be subsequently used to describe the activation energy of the reaction path, or, like in our case, to estimate the energy necessary to trigger the molecular crystal to swap from a LT configuration to a HT one, and *vice versa*. The details of the technique are explained elsewhere[118–121].

2.7 CODES

A brief summary of the principal codes used is here presented, highlighting their principal features.

2.7.1 Gaussian09

The Gaussian09 (G09) code[122] is a package widely used to perform a vast series of calculations at different levels, ranging from the QM/MM approach to post-HF methods. Firstly developed by Pople and his research group in 1970, the code has been extensively improved since then. Now it includes a wide range of DFT functionals and basis sets. It includes many important approximations, like the Broken Symmetry one. This code has been extensively used in this thesis, especially in the computation of the J_{AB} values implied in the creation of the magneto-structural correlation maps.

2.7.2 Quantum Espresso

The Quantum Espresso project[123, 124] is an integrated suite of different codes, specially targeted to the treatment of crystals and periodic structures. It is based on DFT, plane waves and pseudopotentials, allowing for the treatment of big clusters and the optimization of supercells.

2.7.3 CP2K

The CP2K[125] code is the principal code used to run the *Ab Initio* MD simulations. It is a quantum chemistry and solid physics state software package. It can be “seen” as an evolution of the CPMD code. It is based on DFT, using a combination of Gaussian and plane waves approaches called GPW[126] and GAPW[126]. In particular, the CP2K code takes advantage of the Orbital Transformation[127] (OT) scheme, which is used for an efficient minimization of the wave functions. It has been extensively used in the research presented here, to compute the molecular dynamics trajectories of the PDTA and TDPDTA compounds, exploring a wide range of temperatures.

The Gaussian and Plane Wave Method

The key feature of the CP2K code is an efficient scheme which takes advantage of the Gaussian and plane waves method (GPW). This method presents many advantages, like the linear scaling of the Kohn-Sham matrix with the system size, or the use of

rather large Gaussian basis sets[126]. The Gaussian orbitals are used to represent the wave functions, whereas the plane waves are used to represent the density matrix. The main advantages of this hybrid approach are:

- linear scaling of KS energy and matrix, taking advantage of the FFT to compute the Hartree energies;
- The KS matrix and density become sparse as the system size increases, allowing for a linear scaling of the methods to perform density matrix optimization;
- It is memory *friendly* because of the small number of wave functions and basis functions to be used, compared to the common plane wave codes.

For more information, the reader is addressed to the original papers where the Quickstep[84, 85] engine, the GPW method and OT transformation approaches are discussed in detail.

2.7.4 CPMD

This *Ab Initio* MD code, based on the Car-Parrinello[104–106] propagation scheme, is based on DFT and plane waves, and was used to compare the results obtained with the CP2K one.

2.7.5 Orca

The Orca[58] code is a freeware alternative to G09 code. It has been developed since 1999 in the research group of Neese, and it has been extensively used in this thesis because efficient modules for the post-Hartree-Fock calculations are implemented, like the Difference Dedicated CI or NEVPT2.

Bibliography

- [1] D. R. Talham, M. W. Meisel, *Chemical Society Reviews* **2011**, *40*, 3356.
- [2] S. Sanvito, *Chemical Society Reviews* **2011**, *40*, 3336.
- [3] A. Bousseksou, G. Molnár, L. Salmon, W. Nicolazzi, *Chemical Society Reviews* **2011**, *40*, 3313.
- [4] C. Train, M. Gruselle, M. Verdaguer, *Chemical Society Reviews* **2011**, *40*, 3297.
- [5] J. S. Miller, *Chemical Society Reviews* **2011**, *40*, 3266.
- [6] P. Dechambenoit, J. R. Long, *Chemical Society Reviews* **2011**, *40*, 3249.
- [7] M. Nakano, H. Oshio, *Chemical Society Reviews* **2011**, *40*, 3239.
- [8] X.-Y. Wang, C. Avendaño, K. R. Dunbar, *Chemical Society Reviews* **2011**, *40*, 3213.
- [9] J. J. Novoa, M. Deumal, J. Jornet-Somoza, *Chemical Society Reviews* **2011**, *40*, 3182.
- [10] D.-F. Weng, Z.-M. Wang, S. Gao, *Chemical Society Reviews* **2011**, *40*, 3157.
- [11] A. Palii, B. Tsukerblat, S. Klokishner, K. R. Dunbar, J. M. Clemente-Juan, E. Coronado, *Chemical Society Reviews* **2011**, *40*, 3130.
- [12] F. Troiani, M. Affronte, *Chemical Society Reviews* **2011**, *40*, 3119.
- [13] T. Sugawara, H. Komatsu, K. Suzuki, *Chemical Society Reviews* **2011**, *40*, 3105.
- [14] L. Sorace, C. Benelli, D. Gatteschi, *Chemical Society Reviews* **2011**, *40*, 3092.
- [15] A. Cornia, M. Mannini, P. Sainctavit, R. Sessoli, *Chemical Society Reviews* **2011**, *40*, 3076.
- [16] G. A. Timco, T. B. Faust, F. Tuna, R. E. P. Winpenny, *Chemical Society Reviews* **2011**, *40*, 3067.
- [17] J. S. Miller, D. Gatteschi, *Chemical Society Reviews* **2011**, *40*, 3065.
- [18] M. Deumal, M. Bearpark, J. Novoa, M. Robb, *The Journal of Physical Chemistry A* **2002**, *106*, 1299–1315.

- [19] C. S. Clarke, J. Jornet-Somoza, F. Mota, J. J. Novoa, M. Deumal, *Journal of the American Chemical Society* **2010**, *132*, 17817–17830.
- [20] S. Vela, M. Reardon, C. E. Jakobsche, M. Turnbull, J. Ribas-Arino, J. Novoa, *Chemistry-A European Journal* **2017**, *23*, 3479–3489.
- [21] S. Vela, M. Deumal, M. Shiga, J. J. Novoa, J. Ribas-Arino, *Chemical science* **2015**, *6*, 2371–2381.
- [22] S. Vela, F. Mota, M. Deumal, R. Suizu, Y. Shuku, A. Mizuno, K. Awaga, M. Shiga, J. J. Novoa, J. Ribas-Arino, *Nature communications* **2014**, *5*, 4411.
- [23] J. M. Rawson, A. Alberola, A. Whalley, *Journal of Materials Chemistry* **2006**, *16*, 2560–2575.
- [24] The Cambridge Crystallographic Data Centre (CCDC), <https://www.ccdc.cam.ac.uk/structures/>?
- [25] C. Herring, *Direct exchange between well-separated atoms*, in *Magnetism*, Vol. 2, **1965**, pp. 1–181.
- [26] S. Vela Llausí, *Computational Modeling of Molecular Magnetic Materials*, Universitat de Barcelona, **2014**.
- [27] C. De Graaf, R. Broer, *Magnetic Interactions in Molecules and Solids*, Springer, **2016**.
- [28] E. Schrödinger, *Annalen der physik* **1926**, *385*, 437–490.
- [29] M. Born, R. Oppenheimer, *Annalen der physik* **1927**, *389*, 457–484.
- [30] A. Szabo, N. Ostlund, *Modern Quantum Chemistry: Introduction to Advanced Electronic Structure Theory*, Courier Corporation, **2012**.
- [31] Pauli. W., Nobel Lecture: Exclusion principle and quantum mechanics, https://www.nobelprize.org/nobel_prizes/physics/laureates/1945/pauli-lecture.pdf.
- [32] C. C. J. Roothaan, *Rev. Mod. Phys.* **1960**, *32*, 179–185.
- [33] K. Andersson, P. A. Malmqvist, B. O. Roos, A. J. Sadlej, K. Wolinski, *Journal of Physical Chemistry* **1990**, *94*, 5483–5488.
- [34] K. Andersson, P.-Å. Malmqvist, B. O. Roos, *The Journal of chemical physics* **1992**, *96*, 1218–1226.
- [35] N. Queralt, D. Taratiel, C. de Graaf, R. Caballol, R. Cimiraglia, C. Angeli, *Journal of computational chemistry* **2008**, *29*, 994–1003.
- [36] C. Angeli, R. Cimiraglia, S. Evangelisti, T. Leininger, J.-P. Malrieu, *The Journal of Chemical Physics* **2001**, *114*, 10252–10264.

- [37] C. Angeli, R. Cimiraglia, J.-P. Malrieu, *Chemical physics letters* **2001**, 350, 297–305.
- [38] C. Angeli, R. Cimiraglia, J.-P. Malrieu, *The Journal of chemical physics* **2002**, 117, 9138–9153.
- [39] J. Miralles, J.-P. Daudey, R. Caballol, *Chemical physics letters* **1992**, 198, 555–562.
- [40] J. Miralles, O. Castell, R. Caballol, J.-P. Malrieu, *Chemical physics* **1993**, 172, 33–43.
- [41] P. Atkins, R. Friedman, *Molecular quantum chemistry*, Oxford, **1983**.
- [42] D. Hegarty, M. A. Robb, *Molecular Physics* **1979**, 38, 1795–1812.
- [43] R. H. Eade, M. A. Robb, *Chemical Physics Letters* **1981**, 83, 362–368.
- [44] H. Schlegel, M. A. Robb, *Chemical Physics Letters* **1982**, 93, 43–46.
- [45] F. Bernardi, A. Bottoni, J. J. W. McDouall, M. A. Robb, H. B. Schlegel, *Faraday Symposia of the Chemical Society* **1984**, 19, 137.
- [46] M. Frisch, I. N. Ragazos, M. A. Robb, H. B. Schlegel, *Chemical Physics Letters* **1992**, 189, 524–528.
- [47] N. Yamamoto, T. Vreven, M. A. Robb, M. J. Frisch, H. B. Schlegel, *Chemical Physics Letters* **1996**, 250, 373–378.
- [48] P. E. Siegbahn, *Chemical Physics Letters* **1984**, 109, 417–423.
- [49] M. A. Robb, U. Niazi, *Computer Physics Reports* **1984**, 1, 127–236.
- [50] M. Klene, M. A. Robb, M. J. Frisch, P. Celani, *The Journal of Chemical Physics* **2000**, 113, 5653–5665.
- [51] P. Å. Malmqvist, A. Rendell, B. O. Roos, *Journal of Physical Chemistry* **1990**, 94, 5477–5482.
- [52] F. Jensen, *Introduction to computational chemistry*, John wiley & sons, **2017**.
- [53] J. P. Malrieu, R. Caballol, C. J. Calzado, C. De Graaf, N. Guihery, *Chemical reviews* **2013**, 114, 429–492.
- [54] P. De Loth, P. Cassoux, J. Daudey, J. Malrieu, *Journal of the American Chemical Society* **1981**, 103, 4007–4016.
- [55] C. J. Calzado, J. Cabrero, J. P. Malrieu, R. Caballol, *The Journal of chemical physics* **2002**, 116, 2728–2747.
- [56] J. Malrieu, *The Journal of Chemical Physics* **1967**, 47, 4555–4558.
- [57] S. Diner, J. Malrieu, P. Claverie, F. Jordan, *Chemical Physics Letters* **1968**, 2, 319–323.

- [58] F. Neese, *Wiley Interdisciplinary Reviews: Computational Molecular Science* **2012**, 2, 73–78.
- [59] C. Camacho, H. A. Witek, S. Yamamoto, *Journal of computational chemistry* **2009**, 30, 468–478.
- [60] P. Hohenberg, W. Kohn, *Physical review* **1964**, 136, B864.
- [61] L. H. Thomas in *Mathematical Proceedings of the Cambridge Philosophical Society, Vol. 23*, Cambridge University Press, **1927**, pp. 542–548.
- [62] E. Fermi, *Rend. Accad. Naz. Lincei* **1927**, 6, 32.
- [63] M. Levy, *Proceedings of the National Academy of Sciences* **1979**, 76, 6062–6065.
- [64] R. Martin, *Electronic Structure: Basic Theory and Practical Methods*, Cambridge university press, **2004**.
- [65] W. Kohn, L. J. Sham, *Physical review* **1965**, 140, A1133.
- [66] D. M. Ceperley, B. Alder, *Physical Review Letters* **1980**, 45, 566.
- [67] G. Ortiz, P. Ballone, *Physical Review B* **1994**, 50, 1391.
- [68] E. Wigner, *Physical Review* **1934**, 46, 1002.
- [69] J. P. Perdew, A. Zunger, *Physical Review B* **1981**, 23, 5048.
- [70] C. Lee, W. Yang, R. G. Parr, *Physical review B* **1988**, 37, 785.
- [71] J. P. Perdew, J. A. Chevary, S. H. Vosko, K. A. Jackson, M. R. Pederson, D. J. Singh, C. Fiolhais, *Physical Review B* **1992**, 46, 6671.
- [72] K. Burke, J. P. Perdew, Y. Wang in *Electronic Density Functional Theory*, Springer, **1998**, pp. 81–111.
- [73] A. D. Becke, *Physical review A* **1988**, 38, 3098.
- [74] J. P. Perdew, K. Burke, M. Ernzerhof, *Physical review letters* **1996**, 77, 3865.
- [75] K. Kim, K. Jordan, *The Journal of Physical Chemistry* **1994**, 98, 10089–10094.
- [76] P. Stephens, F. Devlin, C. Chabalowski, M. J. Frisch, *The Journal of Physical Chemistry* **1994**, 98, 11623–11627.
- [77] D. R. Salahub, M. C. Zerner, *The Challenge of d and f Electrons: Theory and Computation*, ACS Publications, **1989**.
- [78] S. H. Vosko, L. Wilk, M. Nusair, *Canadian Journal of physics* **1980**, 58, 1200–1211.
- [79] K. Yamaguchi, H. Fukui, T. Fueno, *Chemistry Letters* **1986**, 15, 625–628.
- [80] L. Noodleman, *The Journal of Chemical Physics* **1981**, 74, 5737–5743.

- [81] D. Hamann, M. Schlüter, C. Chiang, *Physical Review Letters* **1979**, 43, 1494.
- [82] D. Vanderbilt, *Physical Review B* **1990**, 41, 7892.
- [83] G. Kresse, D. Joubert, *Physical Review B* **1999**, 59, 1758.
- [84] M. Krack, M. Parrinello, *High performance computing in chemistry* **2004**, 25, 29.
- [85] J. VandeVondele, M. Krack, F. Mohamed, M. Parrinello, T. Chassaing, J. Hutter, *Computer Physics Communications* **2005**, 167, 103–128.
- [86] S. Goedecker, M. Teter, J. Hutter, *Physical Review B* **1996**, 54, 1703.
- [87] C. Hartwigsen, S. Goedecker, J. Hutter, *Physical Review B* **1998**, 58, 3641.
- [88] M. Krack, *Theoretical Chemistry Accounts* **2005**, 114, 145–152.
- [89] Van der Waals Functionals,
https://www.abinit.org/sites/default/files/infos/8.6/topics/generated_files/topic_vdw.html.
- [90] S. Grimme, *Journal of computational chemistry* **2006**, 27, 1787–1799.
- [91] S. Grimme, J. Antony, S. Ehrlich, H. Krieg, *The Journal of chemical physics* **2010**, 132, 154104.
- [92] S. Grimme, S. Ehrlich, L. Goerigk, *Journal of computational chemistry* **2011**, 32, 1456–1465.
- [93] K. Kitaura, K. Morokuma, *International Journal of Quantum Chemistry* **1976**, 10, 325–340.
- [94] P. Su, H. Li, *The Journal of chemical physics* **2009**, 131, 014102.
- [95] Y. Mo, S. D. Peyerimhoff, *The Journal of chemical physics* **1998**, 109, 1687–1697.
- [96] M. v. Hopffgarten, G. Frenking, *Wiley Interdisciplinary Reviews: Computational Molecular Science* **2012**, 2, 43–62.
- [97] M. P. Mitoraj, A. Michalak, T. Ziegler, *Journal of Chemical Theory and Computation* **2009**, 5, 962–975.
- [98] Y. Mo, J. Gao, S. D. Peyerimhoff, *The Journal of Chemical Physics* **2000**, 112, 5530–5538.
- [99] Y. Mo, *The Journal of chemical physics* **2003**, 119, 1300–1306.
- [100] Y. Mo, *Current Organic Chemistry* **2006**, 10, 779–790.
- [101] D. Marx, J. Hutter, *Ab initio molecular dynamics: basic theory and advanced methods*, Cambridge University Press, **2009**.
- [102] T. D. Kühne, *Wiley Interdisciplinary Reviews: Computational Molecular Science* **2014**, 4, 391–406.

- [103] L. Verlet, *Physical review* **1967**, 159, 98.
- [104] D. Marx, J. Hutter in *Modern Methods and Algorithms of Quantum Chemistry*, (Ed.: J. Grotendorst), NIC, Publicly available at the URL: <http://www2.fz-juelich.de/nic-series/Volume3/marx.pdf>, Forschungszentrum Jlich, **2000**, Chapter 13, pp. 301–449.
- [105] W. Andreoni, A. Curioni, *Parallel Computing* **2000**, 26, 819–842.
- [106] D. Marx, J. Hutter, *Ab Initio Molecular Dynamics*, **2009**.
- [107] C. G. Broyden, *IMA Journal of Applied Mathematics* **1970**, 6, 76–90.
- [108] R. Fletcher, *New York* **1987**, 80.
- [109] D. Goldfarb, *Mathematics of computation* **1970**, 24, 23–26.
- [110] D. F. Shanno, *Mathematics of computation* **1970**, 24, 647–656.
- [111] D. F. Shanno, P. C. Kettler, *Mathematics of Computation* **1970**, 24, 657–664.
- [112] S. Vela, F. Mota, M. Deumal, R. Suizu, Y. Shuku, A. Mizuno, K. Awaga, M. Shiga, J. Novoa, J. Ribas-Arino, *Nature Communications* **2014**, 5.
- [113] H. Jónsson, G. Mills, K. W. Jacobsen in *Classical and quantum dynamics in condensed phase simulations*, World Scientific, **1998**, pp. 385–404.
- [114] G. Henkelman, H. Jónsson, *The Journal of chemical physics* **2000**, 113, 9978–9985.
- [115] G. Henkelman, B. P. Uberuaga, H. Jónsson, *The Journal of chemical physics* **2000**, 113, 9901–9904.
- [116] G. Henkelman, G. Jóhannesson, H. Jónsson in *Theoretical Methods in Condensed Phase Chemistry*, Springer, **2002**, pp. 269–302.
- [117] D. Sheppard, R. Terrell, G. Henkelman, *The Journal of chemical physics* **2008**, 128, 134106.
- [118] R. Elber, M. Karplus, *Chemical Physics Letters* **1987**, 139, 375–380.
- [119] R. Czerminski, R. Elber, *International Journal of Quantum Chemistry* **1990**, 38, 167–185.
- [120] R. Czerminski, R. Elber, *The Journal of Chemical Physics* **1990**, 92, 5580–5601.
- [121] R. E. Gillilan, K. R. Wilson, *The Journal of chemical physics* **1992**, 97, 1757–1772.

- [122] M. J. Frisch, G. W. Trucks, H. B. Schlegel, G. E. Scuseria, M. A. Robb, J. R. Cheeseman, G. Scalmani, V. Barone, G. A. Petersson, H. Nakatsuji, X. Li, M. Caricato, A. V. Marenich, J. Bloino, B. G. Janesko, R. Gomperts, B. Mennucci, H. P. Hratchian, J. V. Ortiz, A. F. Izmaylov, J. L. Sonnenberg, D. Williams-Young, F. Ding, F. Lipparini, F. Egidi, J. Goings, B. Peng, A. Petrone, T. Henderson, D. Ranasinghe, V. G. Zakrzewski, J. Gao, N. Rega, G. Zheng, W. Liang, M. Hada, M. Ehara, K. Toyota, R. Fukuda, J. Hasegawa, M. Ishida, T. Nakajima, Y. Honda, O. Kitao, H. Nakai, T. Vreven, K. Throssell, J. A. Montgomery, Jr., J. E. Peralta, F. Ogliaro, M. J. Bearpark, J. J. Heyd, E. N. Brothers, K. N. Kudin, V. N. Staroverov, T. A. Keith, R. Kobayashi, J. Normand, K. Raghavachari, A. P. Rendell, J. C. Burant, S. S. Iyengar, J. Tomasi, M. Cossi, J. M. Millam, M. Klene, C. Adamo, R. Cammi, J. W. Ochterski, R. L. Martin, K. Morokuma, O. Farkas, J. B. Foresman, D. J. Fox, Gaussian16 Revision B.01, Gaussian Inc. Wallingford CT, **2016**.
- [123] P. Giannozzi, S. Baroni, N. Bonini, M. Calandra, R. Car, C. Cavazzoni, D. Ceresoli, G. L. Chiarotti, M. Cococcioni, I. Dabo, A. Dal Corso, S. de Gironcoli, S. Fabris, G. Fratesi, R. Gebauer, U. Gerstmann, C. Gougoussis, A. Kokalj, M. Lazzeri, L. Martin-Samos, N. Marzari, F. Mauri, R. Mazzarello, S. Paolini, A. Pasquarello, L. Paulatto, C. Sbraccia, S. Scandolo, G. Sclauzero, A. P. Seitsonen, A. Smogunov, P. Umari, R. M. Wentzcovitch, *Journal of Physics: Condensed Matter* **2009**, *21*, 395502 (19pp).
- [124] P. Giannozzi, O. Andreussi, T. Brumme, O. Bunau, M. B. Nardelli, M. Calandra, R. Car, C. Cavazzoni, D. Ceresoli, M. Cococcioni, N. Colonna, I. Carnimeo, A. D. Corso, S. de Gironcoli, P. Delugas, R. A. D. Jr, A. Ferretti, A. Floris, G. Fratesi, G. Fugallo, R. Gebauer, U. Gerstmann, F. Giustino, T. Gorni, J. Jia, M. Kawamura, H.-Y. Ko, A. Kokalj, E. Kkbenli, M. Lazzeri, M. Marsili, N. Marzari, F. Mauri, N. L. Nguyen, H.-V. Nguyen, A. Otero-de-la-Roza, L. Paulatto, S. Ponc, D. Rocca, R. Sabatini, B. Santra, M. Schlipf, A. P. Seitsonen, A. Smogunov, I. Timrov, T. Thonhauser, P. Umari, N. Vast, X. Wu, S. Baroni, *Journal of Physics: Condensed Matter* **2017**, *29*, 465901.
- [125] J. Hutter, M. Iannuzzi, F. Schiffmann, J. VandeVondele, *Wiley Interdisciplinary Reviews: Computational Molecular Science* **2014**, *4*, 15–25.
- [126] G. Lippert, J. Hutter, M. Parrinello, *Theoretical Chemistry Accounts* **1999**, *103*, 124–140.
- [127] J. VandeVondele, J. Hutter, *The Journal of chemical physics* **2003**, *118*, 4365–4369.

Chapter 3

The Dithiazolyl-based Materials

3.1 Introduction

The study and rationalization of the key features of organic molecular magnets, and in this particular case, of the DTA-based ones, is still in the spotlight after many years, because of their complex nature, which couples magnetic interactions with structural disposition. As previously mentioned, tailoring these materials to specific geometrical arrangement rather than specific electronic structure, might favor the overcoming of the current technological limits. These systems might be used to reduce the dimension of transistors (currently of ~ 5 nm) below the nanometer range scale[1]. Many problems still remain unsolved, like the kind of stabilization mechanism operating in the different molecular radicals, also within the same family. The practical use of molecular magnets in daily systems is still pretty far from being real. On the other hand, the lack of knowledge is being quickly and systematically covered as the theoretical models and experimental approaches to study and investigate these materials are refined and improved. In this Chapter, the detailed description of TTTA, PDTA, TDPDTA and 4-NCBDTA compounds, already introduced in Chapter 1, is provided, highlighting the structural and electronic similarities and differences. The TTTA and 4-NCBDTA systems are presented first, since they have already being investigated in details and many publications[2–9] describing their key features, are available. Then, the PDTA and TDPDTA systems follow, although the description is limited to the structural and magnetic characteristics as experimentally defined. The computational results concerning these two systems will be presented in the subsequent Chapters formed by the published papers. The purpose of this insight is to provide the reader with a model of the structures analyzed, favoring the debate that has driven our research and led to the development of the subsequent chapters

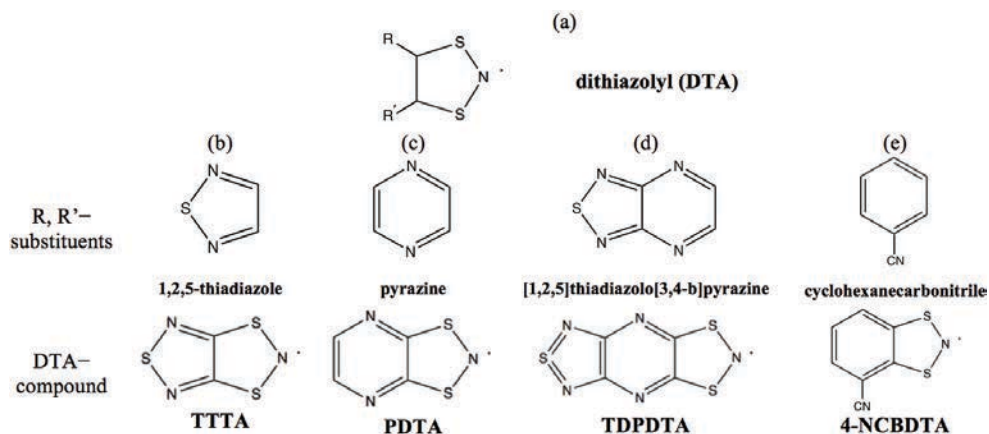


Figure 3.1: (a) Chemical skeleton of DTA moiety, with R and R' substituents. The corresponding R and R' substituents are shown as well as the corresponding structures, in particular (b) TTTA, (c) PDTA, (d) TDPDTA and (e) 4-NCBDTA.

based on the papers submitted and published. The TTTA, PDTA and TDPDTA systems present magnetic and structural bistability, associated to a hysteretic behavior. They share the same dithiazolyl (DTA) moiety, while the nature of the corresponding substituents changes, going from a five-member ring (1,2,5-thiadiazole), in the case of the TTTA compound, to two-fused rings ([1,2,5]thiadiazolo-[3,4b]pyrazine), in the case of the TDPDTA material. The implications of such substituents are dramatic, as it will be shown later.

The extensive study of the dithiazolyl fragment in the past ended up with the synthesis of the prototype 1,3,5-trithia-2,4,6-triazapentalenyl (TTTA)[2] material, performed by Wolmershäuser and co-workers in 1989, being one of the first examples of a purely organic molecular magnets based on neutral radicals. This success followed the discovery of the possibility to have FM ordering in organic-based compounds with π electrons by Miller in 1986[10]. The systematic study and investigation of DTA-based materials with remarkable magnetic and structural properties, gave rise to a wide family of DTA-derived materials compounds[11]. Their properties may vary a lot, depending on the nature of the substituent attached to the DTA ring. The DTA family displays a wide spectrum of chemical-physical behaviors, that, in first approximation, can be classified based on their magnetic response (see Fig. 3.2) and how these relates to the structural rearrangements, following the warming and cooling process of the systems during the susceptibility curves measurements. Thus, the systems associated with a hysteretic behavior that accompanies the spin transition

are classified as bistable and define the class of major interested investigated here. The absence of hysteresis defines the second class, which is characterized only by spin transition. Finally, the last class of materials feature a complete absence of spin and phase transition (see Fig. 3.2c)

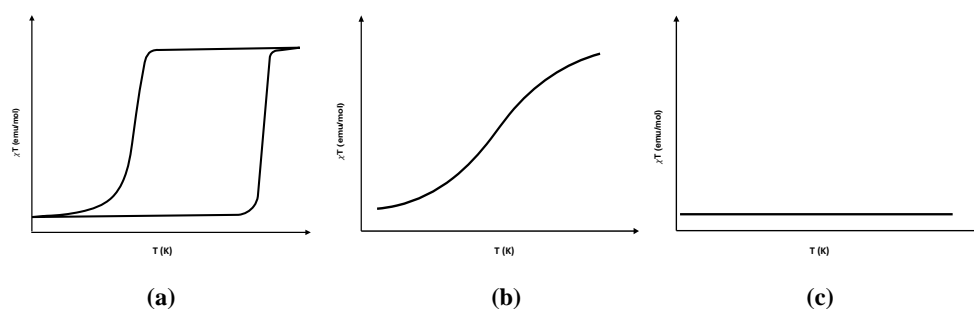


Figure 3.2: Susceptibility curves models showing the three kind of behaviors classified based on the magnetic response to the warming and cooling ramp of the materials. (a) represents the hysteretic behavior present in bistable materials, while (b) displays the response of materials characterized only by spin transition, and (c) the typical response of materials that do not exhibit any spin transition.

Our attention is focused on the first class of materials. The potential applicability of these compounds is twofold:

- if the system is used to store information, the association of the two phenomena can guarantee a more reliable source of stability of the same, in other terms the information does not *degrade*;
- the synthesis process can be done in mild conditions, requiring only a small fraction of the energy used for processing alloy-based magnets;

The static analysis of the magnetic interactions has clearly shown how these magnetic couplings propagate within the 3D crystal structure and which is the strength associated to these interactions. Nevertheless, the quest for the mechanism associated to the phase transition is still not completely clear. In a recent paper[6] a part of the puzzle have been solved, analyzing in extreme details the dynamical behavior of a wide set of supercells for both the LT and HT phases, sampled at different temperatures along the experimental susceptibility curve of the TTTA system. Vela and co-workers identified the vibrational entropy of the system as one of the key factors driving the phase transition between LT and HT.

Thanks to the great amount of available experimental data , TTTA is taken as a

reference while comparing the PDTA, TDPDTA and 4-NCBDTA materials. On one side, the same kind of physics was expected to be responsible for the rearrangement of the molecules within the crystal. Recent analysis has proven that is not always the case. In particular, the HT-TDPDTA polymorph is found to be stable in the uniform stack configuration, contrary to the other HT-DTA polymorphs, where the regular stacking motif is found to be unstable against dimerization at 0 K. On the other side, the different nature of the substituent associated to the DTA moiety might influence the packing of the crystal, driving the corresponding magnetic response. This suggests that the problem is a combination of these two factors. The influence of the substituent is not a brand-new novelty, but it assumes a new light in the perspective of the research presented in Chapter 5, where the study of the magneto-structural correlation interaction of the selected compounds put in evidence the necessity to consider a new variable to describe the TDPDTA compound. In turn, a new possible stabilization mechanism was found to operate in the HT-TDPDTA polymorph.

3.2 TTTA

3.2.1 Crystal Packing Analysis

The neutral radical 1,3,5-trithia-2,4,6-triazapentalenyl (TTTA), is a bistable system derived from the fusion of a 1,2,5-thiadiazole and a dithiazolyl ring and its susceptibility curve encompasses room temperature (see Fig. 3.3). In particular, the range of bistability is comprised between $T_C^\downarrow = 220$ K and $T_C^\uparrow = 315$ K. The compound presents two stable phases, namely low temperature (LT) and high temperature (HT) polymorphs, and it undergoes to a first-order phase transition[12].

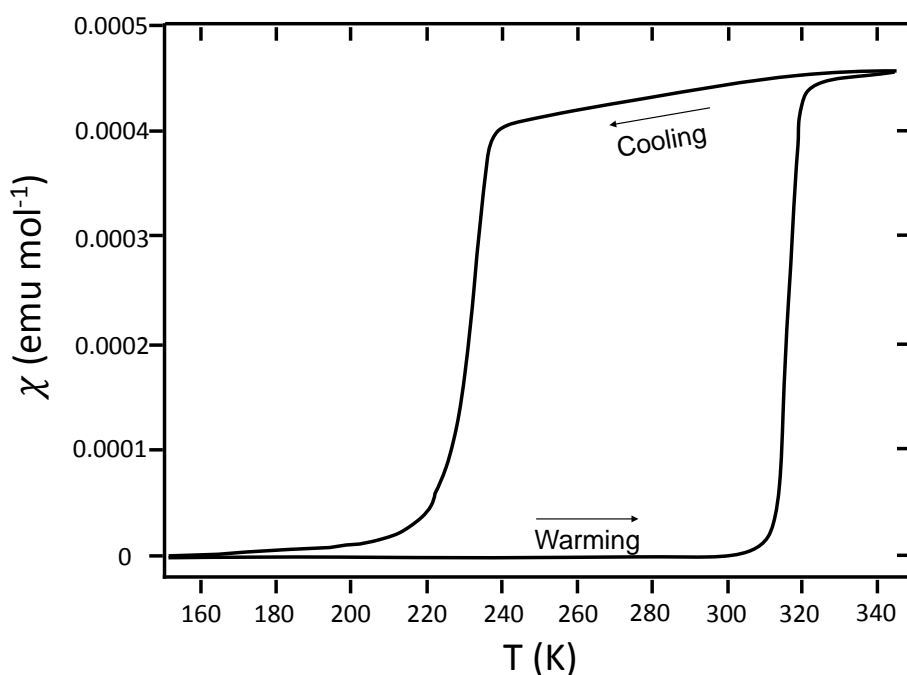


Figure 3.3: Susceptibility curve of TTTA showing the hysteric path followed during the warming (→) and cooling (←) process.

The LT polymorph is a diamagnetic phase, with triclinic ($P\bar{1}$) crystal habit, whereas the HT polymorph is weakly paramagnetic, presenting a monoclinic ($P2_1/c$) habit. These phases have been resolved at different temperatures (150, 225, 250, 300 and 310 K) along the experimental susceptibility curve[12].

Each single TTTA molecule is also the carrier for the unpaired electron, which, interacting with the upper and lower radicals, gives rise to the magnetic interactions. Formally, the unpaired electron is hosted by the nitrogen belonging to the dithiazolyl ring, although DFT/WF calculations and EPR[2, 13] experiments proved the electron to be partially delocalized over the entire molecule[5]. The system undergoes a first-order phase transition between LT and HT phases, displaying a dramatic change in the experimental susceptibility curve at *ca.* 323 K. As a consequence, TTTA goes from a diamagnetic configuration to a weakly paramagnetic one, following a rearrangement of the crystalline habit. Both the LT and HT phases comprise four molecules in the unit cell, presenting a preferential propagation direction along the stacking direction of the molecular columns[5] (see Fig. 3.4). The stabilization of the crystal is another important aspect that characterizes the nature of these organic radical magnets. While the magnetic interactions between neighbouring columns has been proved to have a negligible effect in the stabilization process, on the other hand, the mutual interactions between nitrogens and sulfurs through van der Waals interactions is crucial[5].

Fig. 3.4 shows the column disposition for the LT (a-b) and HT (c-d) polymorphs. The LT one presents an alternation between eclipsed dimers (blue dash bars). The HT phase, instead, shows a uniform stacking disposition of the columns. The structural rearrangement that occurs going from the LT to the HT phase, is reflected not only on the molecular disposition within the column, but also on the column orientation that follows the molecular disposition. In particular, a characteristic herringbone trend is found.

3.2.2 Magnetic Properties

The diamagnetic and weak paramagnetic characters found in **1** and associated to the LT and HT phases, respectively, are ascribed to the presence of the unpaired electron in the DTA ring, and the particular geometrical disposition of the dimers within the crystal structure. The respective phases have been investigated in details along the years, both experimentally and from a theoretical point of view[2–9]. In particular, the LT-TTTA phase shows the strongest AFM coupling, equal to *ca.* -1755 cm^{-1} [5], in agreement with the experimental investigations[13, 14]. On the other hand, the **1**-HT shows a AFM coupling that is one order of magnitude smaller compared to the one found in the LT phase, equal to *ca.* -135 cm^{-1} . This value is a strong indicator of the weakly paramagnetic nature of the HT-TTTA phase, as experimentally observed (see Fig. 3.5).

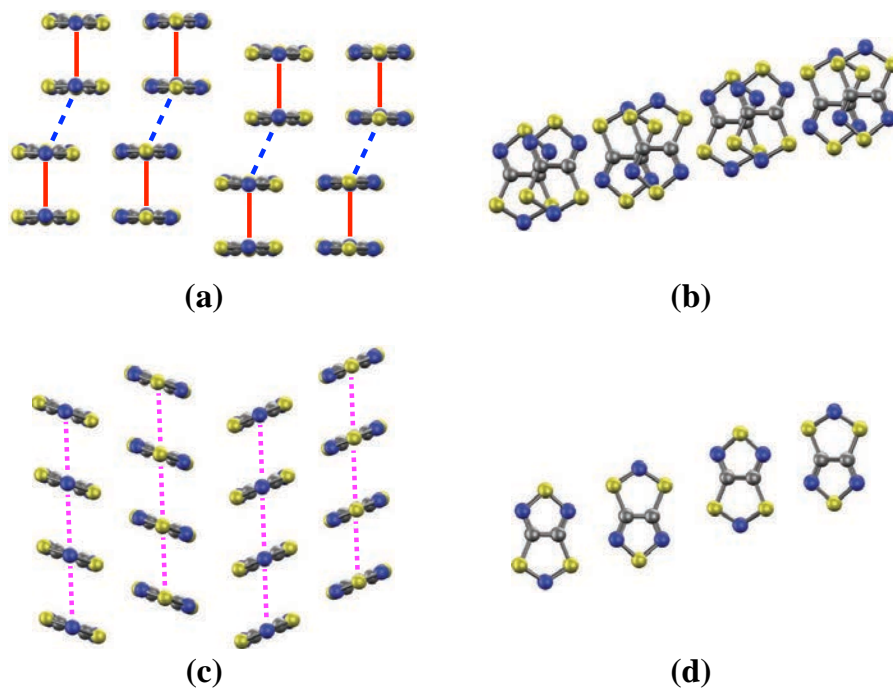


Figure 3.4: (a-b) Side view and top view of the LT-TTTA polymorph. It can be clearly seen the alternation between π -dimers (red bars) alternated to π -shifted dimers (blue dashed bars). (c-d) Side view and top view of the HT-TTTA polymorph, showing the uniform stacking trend common to high temperature phases (purple dashed bar).

3.2.3 Beyond the Static Analysis

The static analysis, as already anticipated, does not take into considerations the influence of thermal fluctuations and how these dynamically affect the system. Although in a first approximation, this approach offers a simplified model to rely on for the distribution of the magnetic interactions. A very interesting and detailed analysis to corroborate the importance of thermal fluctuations and their effect on the crystal and on the magnetic couplings, has been provided by Vela and co-workers[6, 7].

A key feature emerges from the extended analysis of the impact of the thermal fluctuations on the magnetic coupling and it seems to be ubiquitous in the HT phases of the DTA-based compound, that is, the Pair-Exchange Dynamics (PED) mecha-

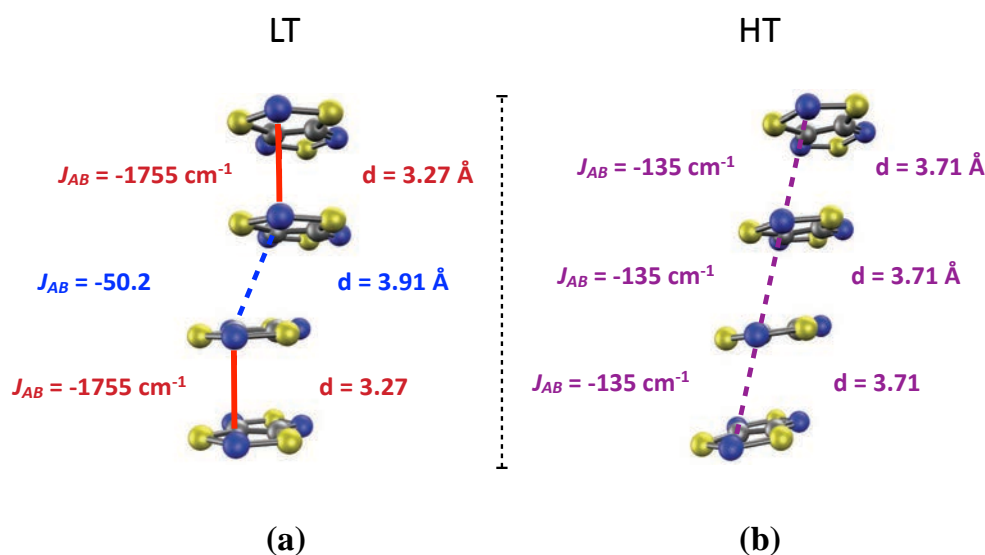


Figure 3.5: J_{AB} values and corresponding monomer-monomer distances for the LT (a) and HT (b) polymorphs, respectively, as reported in literature[5]. It can be seen the dominance of the AFM coupling LT phase, inducing the system to be magnetically silent.

nism (see Fig. 3.6). The PES withstands a double-well model, where two minima are connected by an energy barrier. The two minima correspond to two degenerate dimerized configurations. As temperature increases, the double-well tends to disappear, since the energy barrier is overcome and the two configurations merge, giving rise to continuous exchange between the two possible states in the picosecond time scale. The averaged structure is what is portrayed by X-ray powder diffraction, and what is displayed averaging the AIMD trajectory computed at 300 K.

In particular, it has been shown that including thermal fluctuations in the calculation of the magnetic susceptibility curve, in this case of the LT-TTTA and HT-TTTA phases, allows for a refinement and good agreement with the experimental data. The bottomline message is that, once dealing with the treatment of the high temperature structures of DTA-based compounds, in this case of the TTTA material, the single J_{AB} value provided by the static analysis is really a big limitation in the description of the magnetic behavior of the system. Instead, the distribution of the J_{AB} values, computed for each dimer monitored along the AIMD trajectory, and its subsequently averaging, is instead a better choice, that, in turn, allows for a more

punctual description of the magnetic interactions within the HT polymorph. In the case of the LT phase instead, albeit the system undergoes to extended intra-dimer fluctuations of the J_{AB} values, the dominant J_{AB} values are so strongly AFM that dimers remain diamagnetic. In this sense, the J_{AB} coupling values resulting from the static analysis are a good approximation.

Associated to the HT-TTTA phase, likewise in the other bistable DTA-based materials, the structural disposition of the crystal helps in maintaining the PED active. Moreover, the PED was found to act as a source of vibrational entropy, stabilizing the HT polymorph[6]. Conversely, the decrease of the temperature of the crystal induces a progressive disappearing of the PED, until the crystal switches back to the dimerized form that, at this point, is not affected by PED anymore and presents a different crystalline habit. For more information about these interesting aspects of the complex nature of DTA-based system the reader is addressed to the cited manuscripts[6, 7].

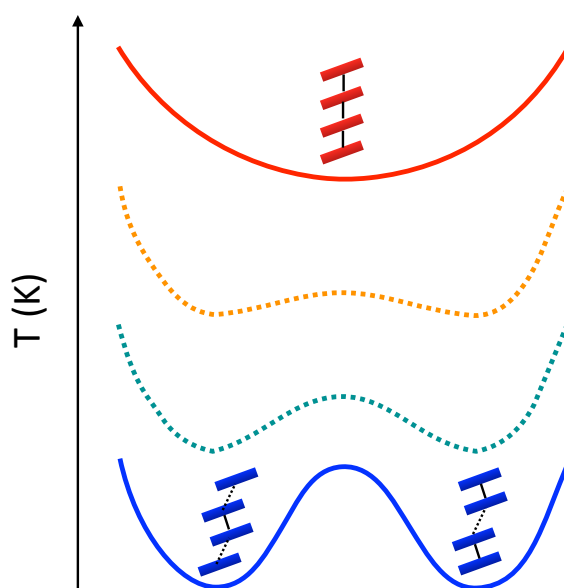


Figure 3.6: Pair-Exchange Mechanism (PED). The increasing of the temperature diminishes the energy barrier separating the two LT dispositions, ending up into a merged structure that coincides with the HT phase with a uniform stack disposition.

3.3 4-NCBDTA

3.3.1 Crystal Packing Analysis

The presence of a hysteretic phase transition coupled with spin transition, that is the key topic investigated in this thesis, is only one of the many interesting aspects that characterize these materials. Systems like the 4-cyanobenzo-1,3,2-dithiazolyl compound (4-NCBDTA), which display only spin transition without a hysteretic behavior associated to the phase transition (see Fig. 3.7), have also been studied[15]. There is no associated change of crystal symmetry, which is monoclinic ($P2_1/c$),

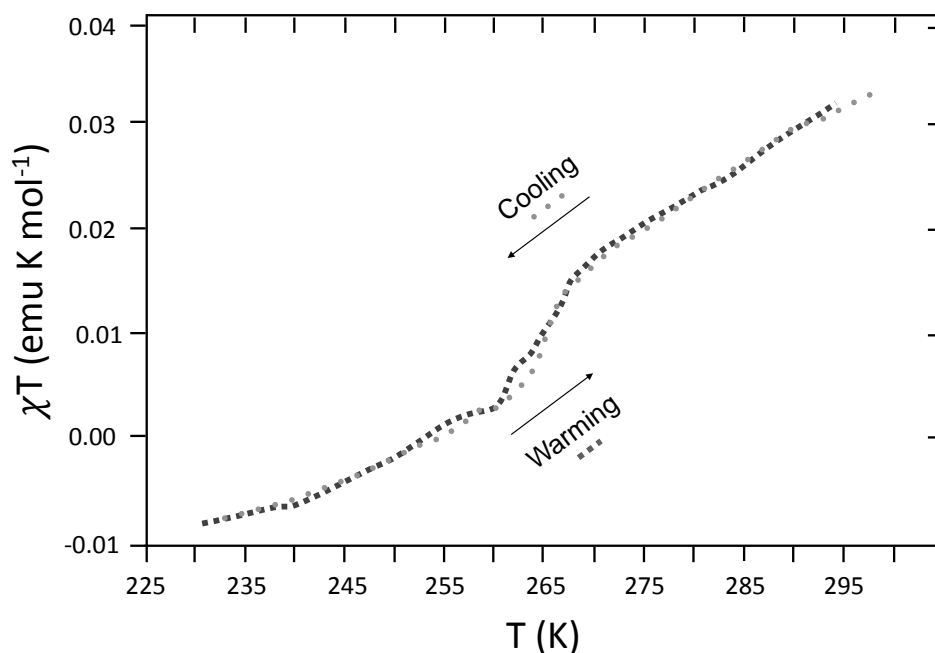


Figure 3.7: Susceptibility curve of the 4-NCBDTA material, showing the path followed during the warming (\rightarrow) and cooling (\leftarrow) process.

both in the LT and HT polymorphs, that have been resolved at 180 K and at 300 K, respectively, by X-ray powder diffraction[15]. The LT-4-NCBDTA polymorph, like in the TTTA case, presents an alternation between eclipsed π -dimers with π -shifted ones. The coupling for the eclipsed dimers is $J_{AB}=-1723.1 \text{ cm}^{-1}$, while for the shifted ones is $J_{AB}=-82.3 \text{ cm}^{-1}$. Although the magnetic topology is three dimensional, for

computational purposes we can assume it to be one dimensional, propagating along the stacking direction (see Fig. 3.8). The LT polymorph displays the strongest AFM J_{AB} value, defining a diamagnetic system. Conversely, the HT polymorph shows a magneto-structural behavior very similar to the one exhibited by HT-TTTA, and, like in that case, the PED is found to operate. Ultimately, TTTA and 4-NCBDTA systems display some common features like:

- the dimerized structure of the LT phases, showing in both the cases a very strong AFM coupling;
- the respective HT phases show a uniform stack propagation of the columns, with J_{AB} exchange magnetic values of one or two orders of magnitude smaller compared to the LT ones;
- both the HT-TTTA and HT-4-NCBDTA phases undergo the PED mechanism, presenting a fast inter-exchange coupling between monomers within the column stacks.
- the regular stacks found in the HT-4-NCBDTA phase do not correspond to a minimum of the PES, but they result from the presence of the PED phenomenon;

The major difference between the two systems lies on the fact that, while the TTTA material undergoes a first-order phase transition highlighted by an important hysteretic behavior, in the case of the 4-NCBDTA system a second-order phase transition takes place, allowing for a smooth change in the magnetic coupling within the crystal, but preserving the geometrical disposition (space group). As discussed in a recent paper[9], the HT-4-NCBDTA phase, once optimized, converges to the dimerized LT phase. This is the only case, among the selected set of compounds, in which there is a match between optimized HT phase and LT one. The reason for the mismatch found in the case of the the optimized structures, *e.g.* HT-TTTA→LT-TTTA, lies on the complexity of the structural re-arrangement that governs the first-order phase transition.

3.3.2 Magnetic Properties

The magnetic properties of the 4-NCBDTA material have been extensively investigated in the same work[9], leading to the conclusion that a similar behavior to the one found in the case of TTTA and PDTA compounds is present. Likewise in the case of LT-TTTA, the strong magnetic coupling experienced at LT induces a magnetically silent system, while the HT-4-NCBDTA polymorph, as already described, presents interesting weak paramagnetic properties. In this thesis the 4-NCBDTA

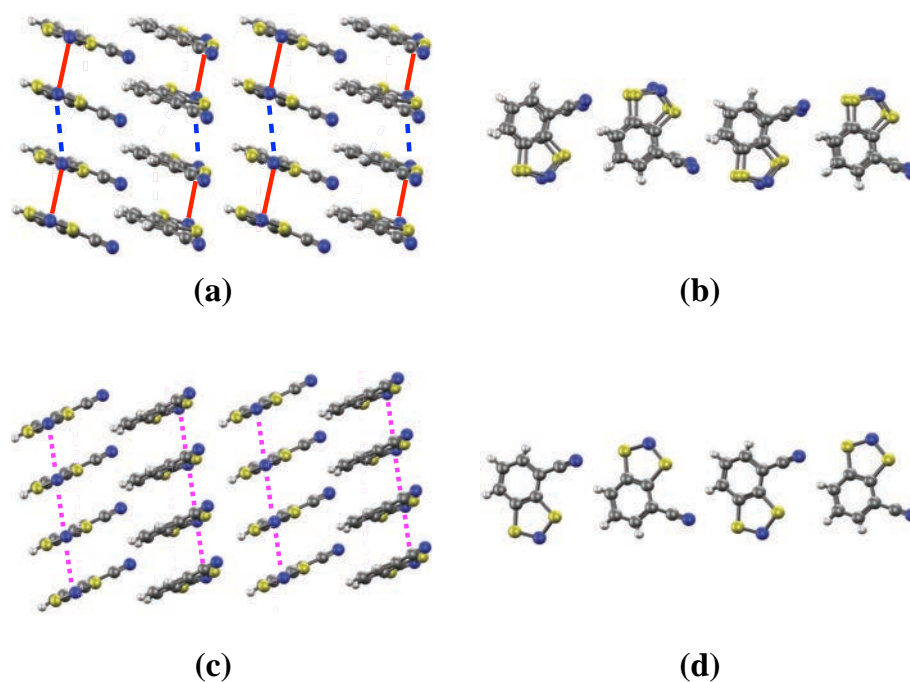


Figure 3.8: (a-b) Side view and top view of the LT-4-NCBDTA polymorph. It can be clearly seen the alternation between π -dimers (red bars) alternated to π -shifted dimers (blue dashed bars). (c-d) Side view and top view of the HT-4-NCBDTA polymorph, showing the uniform stacking trend common to high temperature phases (magenta dashed bar).

system has been employed only in the construction of the magneto-structural correlation maps[16]. The detailed description of these maps is reported in Chapter 5. It is worth to mention here that, despite the fact of being a non-bistable system, particular arrangements of the HT-4-NCBDTA polymorph can lead to the possibility to have FM coupling. Moreover, a small fraction of the suitable two-molecule cluster arrangements are energetically accessible. This is extremely important because it means that bistability, that is found in a particular subset of DTA-based systems, is not necessarily a “*must have*” in order to present possible FM couplings; conversely, the absence of bistability, does not mean that, for the considered system, is not possible to assume a geometrically favourable FM configuration.

3.4 PDTA

3.4.1 Crystal Packing Analysis

The 1,3,2-pyrazinodithiazol-2-yl (PDTA) material displays similar properties to the TTTA one. It is a planar bistable system, whose susceptibility curve[17, 18] encompasses room temperature, ranging from $T_C^\downarrow=297$ K to $T_C^\uparrow=343$ K (see Fig. 3.9).

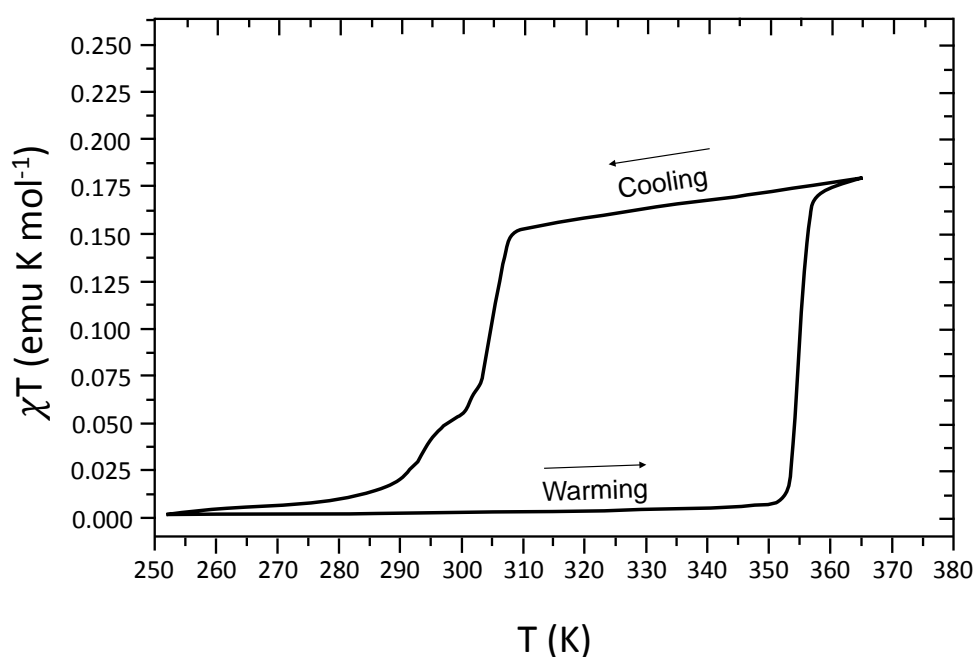


Figure 3.9: Susceptibility curve of PDTA showing the hysteric path followed during the warming (\rightarrow) and cooling (\leftarrow) process.

The material has been experimentally characterized at 95 K, 293 K, and 323 K. Our attention focuses on the LT-PDTA and HT-PDTA polymorphs resolved both at 323 K, because they can be directly compared (see Fig. 3.10). The PDTA material presents a dramatic change in the structural arrangement as a function of the temperature variation, following a first-order phase transition process. The unit cell of the LT-PDTA phase contains four molecules. It has a triclinic ($P\bar{1}$) habit consisting of centrosymmetric pairs of dimers, and, like in the TTTA case, an even alternation of complete eclipsed π -dimers with π -shifted ones is present. The HT-PDTA phase, instead, be-

longs to the monoclinic space group ($C2/c$) and it contains eight molecules.

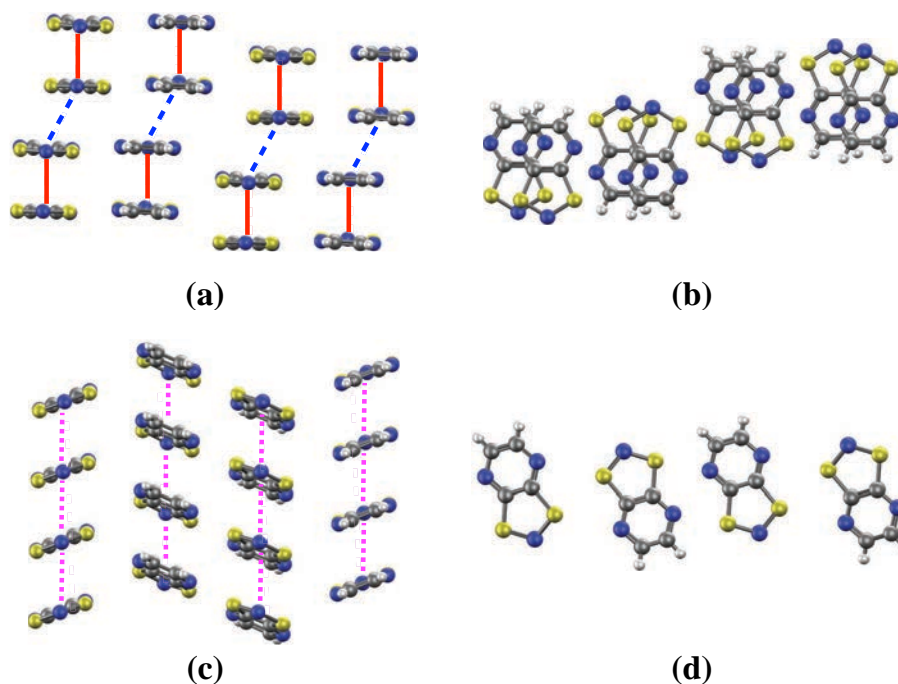


Figure 3.10: (a-b) Side view and top view of the LT-PDPA polymorph. It can be clearly seen the alternation between π -dimers (red bars) alternated to π -shifted dimers (blue dash bars). (c-d) Side view and top view of the HT-PDPA polymorph, showing the uniform stacking trend common to high temperature phases (magenta dashed bar).

Despite having a pyrazine attached to the DTA ring, the PDPA compound resembles in almost every aspect the prototype TTTA materials. Also in this case, the HT phase is characterized by a uniform stack propagation. The nature of the HT-PDPA phase will be analyzed in details in Chapter 6, where a summary of the AIMD results will be presented. The similarities between the two systems suggest that, based on the results for the TTTA material, we might have the same kind of mechanisms operating also in PDPA, expecting that:

- the LT-PDPA is magnetically dominated by AFM coupling interactions that, like in the case of LT-TTTA, are mainly due to eclipsed π -dimers;
- the LT phase already belongs to a minimum of the potential energy surface

(PES), and, as a consequence, the trajectory sampled for a column will show very narrow oscillations of the dimers;

- the HT-PDTA phase, displaying a uniform stack in the experimentally resolved structure, might correspond to an averaged structure, with a continuous interchange between two, or more, minima configurations. This also suggests that the pair-exchange mechanism (PED) might be operating likewise in the HT-TTTA compound.

These are the key points that might be inferred, *a priori*, from the previously investigated DTA-based systems. From a chemical engineering perspective, the PDTA system offers remarkable chances of modifications of its substituent part. In particular, the two hydrogens can be changed with another substituent group, generating compounds like TDPDTA that will be discussed later, or steric groups like, for instance $-\text{CH}_3$ or $-\text{CF}_3$. These groups may stabilize, *a priori*, a favorable radical · · · radical FM disposition.

3.5 TDPDTA

3.5.1 Crystal Packing Analysis

The neutral radical TDPDTA[19] is the second system fully analyzed in this thesis. TDPDTA has a substituent with two fused rings, one 1,2,5-thiadiazole fused to a pyrazine, forming a 1,2,5-thiadiazole[3,4-b]pyrazine planar substituent. The compound presents the same triclinic crystalline habit, both in the LT and HT polymorphs, with space group $P\bar{1}$. It shows a hysteretic behavior, like in the TTTA and PDTA cases, but without a net dramatic change in the magnetic susceptibility. Instead, an elongated and slightly flattened hysteretic loop appears (see Fig. 3.11). The

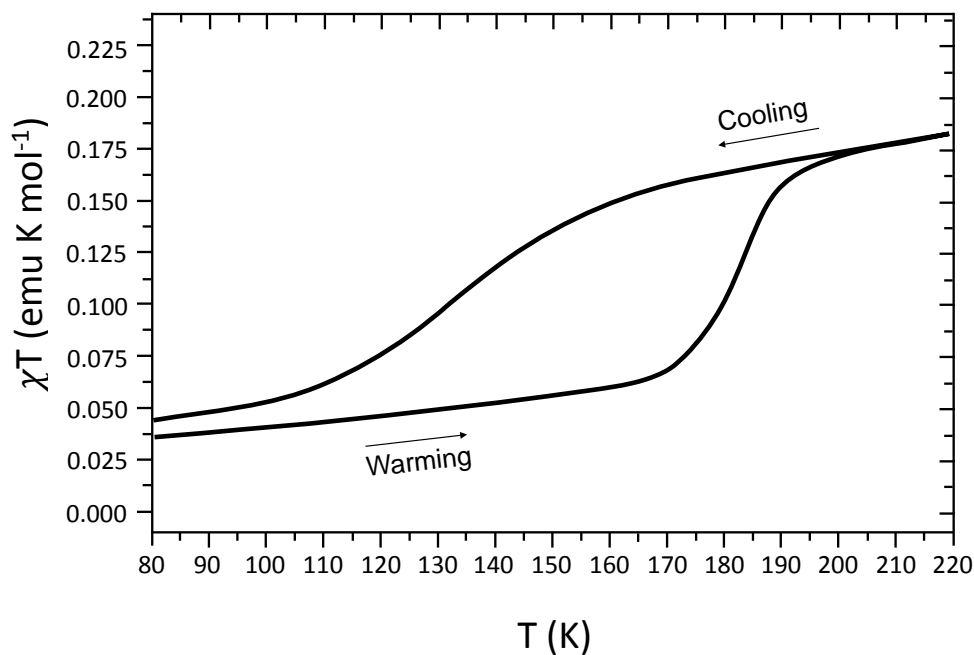


Figure 3.11: Susceptibility curve of TDPDTA showing the hysteretic path followed during the warming (\rightarrow) and cooling (\leftarrow) process.

LT phase presents a combined structure arrangements, somewhere in between the usual LT phase with eclipsed π -dimers and a HT phase with a uniform disposition. The peculiarity of this LT structure is that, each single *quasi*-eclipsed π -dimer, alternated with a *quasi*-shifted one, undergoes a longitudinal translation (see Fig. 3.12).

Conversely, the HT phase shows a clear uniform stack propagation arrangement, as exhibited by the other HT phases of the same family.

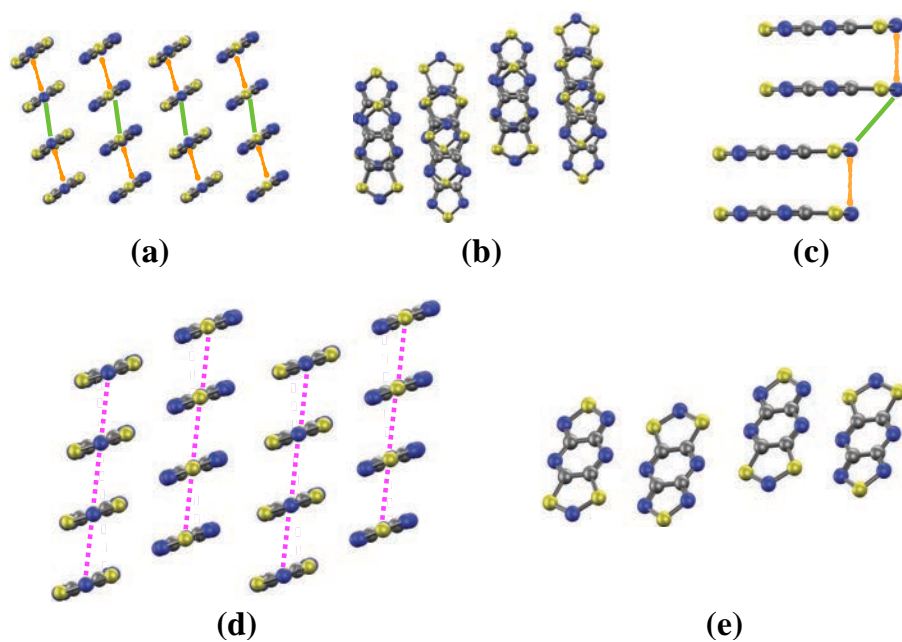


Figure 3.12: (a-c) Side view, top view and the lateral view of the LT-TDPDTA polymorph and of the corresponding single column. It can be noticed the particular disposition of the *quasi*-eclipsed π -dimers with respect to the shifted ones (orange and green bars, respectively). (d-e) Side view and top view of the HT-TDPDTA polymorph, showing the uniform stacking trend common to high temperature phases (magenta dashed bar).

3.6 Summary

The goal of this independent chapter is to introduce the reader to the nature of the systems investigated in this thesis, as a perspective for the work developed in the successive Chapters. The respective structures and packing motif is herein shown, combined with the respective experimental susceptibility curves. The TTTA and 4-NCBDTA systems have been presented first, because they define the background on top of which this study is built up. The two compounds present on one side a hysteretic behavior associated with the spin and phase transition (referred to as first-order phase transition), on the other side a smooth change in the magnetic susceptibility, but with the absence of a hysteretic response (referred to as second-order phase transition). Between these two *extreme* behaviors, the PDTA and TDPDTA structures are found. In particular, the former displays a first-order phase transition associated to a hysteretic response to thermal variation, displaying a dimerized structure configuration in the LT phase case, whereas a uniform stack, exactly like in case of HT-TTTA, is found for its correspondent high temperature polymorph. The latter, TDPDTA, instead, is again a bistable system which, differently from TTTA and PDTA, preserves its crystal symmetry upon phase transition. The column disposition of the LT phase is particularly complex, showing an alternation between *quasi*-eclipsed dimers with *quasi*-shifted ones, comprising a longitudinal slippage every two dimers. The HT-TDPDTA phase is resembling the usual uniform stack propagation disposition found also in the other systems. The goal is to understand the origins of the particular susceptibility curve shown by this material, and also if in this case the PED mechanism is operating or not.

Bibliography

- [1] 5nm Fab Challenges,
<http://semiengineering.com/5nm-fab-challenges/>.
- [2] G. Wolmershäuser, R. Johann, *Angewandte Chemie International Edition in English* **1989**, *28*, 920–921.
- [3] H. Matsuzaki, W. Fujita, K. Awaga, H. Okamoto, *Physical review letters* **2003**, *91*, 017403.
- [4] J. M. Rawson, A. Alberola, A. Whalley, *Journal of Materials Chemistry* **2006**, *16*, 2560–2575.
- [5] C. S. Clarke, J. Jornet-Somoza, F. Mota, J. J. Novoa, M. Deumal, *Journal of the American Chemical Society* **2010**, *132*, 17817–17830.
- [6] S. Vela, F. Mota, M. Deumal, R. Suizu, Y. Shuku, A. Mizuno, K. Awaga, M. Shiga, J. J. Novoa, J. Ribas-Arino, *Nature communications* **2014**, *5*, 4411.
- [7] S. Vela, M. Deumal, M. Shiga, J. J. Novoa, J. Ribas-Arino, *Chemical science* **2015**, *6*, 2371–2381.
- [8] D. Bates, C. M. Robertson, A. A. Leitch, P. A. Dube, R. T. Oakley, *Journal of the American Chemical Society* **2018**, *140*, 3846–3849.
- [9] S. Vela, M. Reardon, C. E. Jakobsche, M. Turnbull, J. Ribas-Arino, J. Novoa, *Chemistry-A European Journal* **2017**, *23*, 3479–3489.
- [10] J. S. Miller, J. C. Calabrese, A. J. Epstein, R. W. Bigelow, J. H. Zhang, W. M. Reiff, *Journal of the Chemical Society Chemical Communication* **1986**, 1026–1028.
- [11] The Cambridge Crystallographic Data Centre (CCDC),
<https://www.ccdc.cam.ac.uk/structures/>?
- [12] Advanced Thermodynamics,
http://casey.brown.edu/chemistry/misspelled-research/crp/Edu/Documents/00_Chem201/index.html.

- [13] G. D. McManus, J. M. Rawson, N. Feeder, J. van Duijn, E. J. McInnes, J. J. Novoa, R. Burriel, F. Palacio, P. Oliete, *Journal of Materials Chemistry* **2001**, *11*, 1992–2003.
- [14] W. Fujita, K. Awaga, *Science* **1999**, *286*, 261–262.
- [15] A. Alberola, R. J. Collis, S. M. Humphrey, R. J. Less, J. M. Rawson, *Inorganic chemistry* **2006**, *45*, 1903–1905.
- [16] T. Francese, J. Ribas-Arino, J. Novoa, R. Havenith, R. Broer, M. Deumal, et al., *Physical chemistry chemical physics: PCCP* **2018**.
- [17] J. L. Brusso, O. P. Clements, R. C. Haddon, M. E. Itkis, A. A. Leitch, R. T. Oakley, R. W. Reed, J. F. Richardson, *Journal of the American Chemical Society* **2004**, *126*, 8256–8265.
- [18] J. L. Brusso, O. P. Clements, R. C. Haddon, M. E. Itkis, A. A. Leitch, R. T. Oakley, R. W. Reed, J. F. Richardson, *Journal of the American Chemical Society* **2004**, *126*, 14692–14693.
- [19] T. Barclay, A. Cordes, N. George, R. Haddon, M. Itkis, M. Mashuta, R. Oakley, G. Patenaude, R. Reed, J. Richardson, et al., *Journal of the American Chemical Society* **1998**, *120*, 352–360.

Chapter 4

The Origin of the Different Stability of the Two Polymorphs of a Prototypical DTA-based Bistable Material

This chapter is based on:

Francesca, T., Mota, F., Deumal, M., Novoa, J. J., Havenith, R. W. A., Broer, R., Ribas-Ariño, J.

Paper Submitted

Abstract

The spin transitions undergone by several molecular organic crystals of dithiazolyl (DTA) radicals make this type of radicals promising candidates for future sensors and memory devices. Here, we present a systematic computational study of the intermolecular interactions existing in the two polymorphs of the neutral radical 1,3,5-trithia-2,4,6-triazapentalenyl (TTTA) in order to elucidate the origin of the difference in energy between the two polymorphs involved in its spin transition and to understand the crystal packing of this prototype of molecule-based bistable materials. The π - π interactions between radicals are the main driving force for the crystal packing of both polymorphs, which comprises π -stacks of radicals. Among the interstack interactions, the strongest ones are those mediated by six- and four-center S...N bridges. The difference in energy between polymorphs, in turn, is mainly controlled also by the π - π intermolecular interactions along the π -stacks and the in-

terstack S··S contacts instead of the S··N contacts. Given that the supramolecular motifs herein identified as important for the crystal packing and/or for the energy difference between polymorphs (and, thus, for the spin transition temperature) are common to other members of the DTA family, the results reported for TTTA provide valuable information to understand better the structure and spin-transition properties of other switchable DTA-based materials.

4.1 Introduction

Thiazyl-based radicals have been intensively investigated during the last decades because they can be used as versatile building blocks for molecular materials with interesting magnetic and/or electric properties [1–7]. These radicals have also become main actors in the field of switchable molecular materials, *i.e.*, materials whose physical properties can be altered by means of external stimuli, such as temperature and light [8–10]. Indeed, the family of dithiazolyl (DTA) neutral radicals has furnished multiple examples of metal-free compounds capable of undergoing structural phase transitions that entail a drastic change in the magnetic response of the material when it is subjected to changes of temperature [11–22] and, in some cases, when it is irradiated with light [19, 23]. It should be mentioned that the closely-related family of dithiadiazolyl radicals has also provided two examples of switchable magnetic materials in recent years[24, 25]. In some of the DTA phase transitions[11–14, 16, 22] the transition temperature in the warming cycle is found to be higher than the transition temperature in the cooling cycle. This hysteretic behaviour gives rise to a loop in the magnetic susceptibility *vs.* temperature plot, yielding a temperature range of magnetic bistability wherein the crystal can be observed in two different states depending on its immediate history. This intriguing property, which can also be observed in transition-metal based spin-crossover compounds[26–28] and in other purely organic materials[29–31], makes these radicals potential candidates for future sensors and future memory devices[8, 32].

All the phase transitions of DTAs that have been reported so far involve the formation/cleavage of dimers of radicals. In many cases[11–15, 17, 21], the dimers present in the crystal structure are cofacial π -dimers, which are held together by means of a long, multicenter bond[33, 34] (alternatively called “pancake” bond[35–38]). These cofacial or eclipsed π -dimers are always found in the low-temperature (LT) phases of this family of switchable DTA compounds, where the cofacial, eclipsed π -dimers pile giving rise to distorted π -stacks of DTA radicals that contain slipped pairs of cofacial π -dimers. Conversely, in the high-temperature (HT) phases of this family of switchable DTA compounds, the radicals pile giving rise to regular π -stacks with a

uniform distance between the slipped radicals. The distinctly different magnetic response of the LT and HT phases (LT phases are typically diamagnetic, while the HT phases exhibit weak paramagnetism) originates in large changes in the magnetic exchange couplings between adjacent radicals in the π -stacks upon phase transition[39, 40].

The transition temperature is a key property of any switchable material. Since the electronic energy⁰ difference between phases is one of the most important factors controlling the transition temperature, the identification of the elements that govern the energy difference between phases within a family of materials is a mandatory exercise in the quest of new materials with tailored transition temperatures. Here, we present a detailed computational study aimed at identifying the intermolecular interactions that play a key role in defining the energy difference between phases in switchable materials based on the formation/dissociation of eclipsed π -dimers between DTA radicals. As a model system of these materials, our study will focus on the 1,3,5-trithia-2,4,6-triazapentalenyl (TTTA) neutral radical[41], which has become a prototypical example of molecule-based bistable materials on account of its spin transition with a wide hysteresis loop encompassing room temperature (see Figure 4.1 that can be induced both with temperature and absorption of light[12, 23, 39, 42–53]). The hysteretic phase transition of TTTA involves a LT diamagnetic phase and a HT paramagnetic phase. The triclinic ($P\bar{1}$ space group) LT polymorph, which is the single polymorph observed on cooling below the bistability range, presents distorted π -stacks of radicals comprising slipped pairs of cofacial π -dimers. As displayed in Figure 4.2a, two types of intermolecular interactions between radicals are present in these distorted stacks: the long, multicenter bond between radicals in the eclipsed π -dimers (hereafter referred to as π -ecl interaction), and the interaction between slipped pairs of radicals (π -slip interaction). Conversely, the monoclinic ($P21/c$ space group) HT polymorph, which is the single polymorph observed on heating above the bistability range, presents regular π -stacks of radicals, where each molecule exhibits a slipped overlap with its two adjacent molecules along the stacking direction (π -slip interaction in Figure 4.3a).

The π -stacks of both LT and HT polymorphs of TTTA form 2D layers, where the π -stacks are laterally linked by a series of intermolecular 6-center S \cdots N bridges (which will be referred to as N-S_{6c} interactions) and intermolecular S \cdots S contacts (S-S_{lat} interactions, see Figure 4.2b and 4.3b). The 2D layers in LT contain one single molecular plane orientation (Figure 4.2c), whereas the 2D layers in HT contain two distinct

⁰ Note that both vibrational energy and entropy might play a non-negligible role. However, this is beyond the scope of the present manuscript.

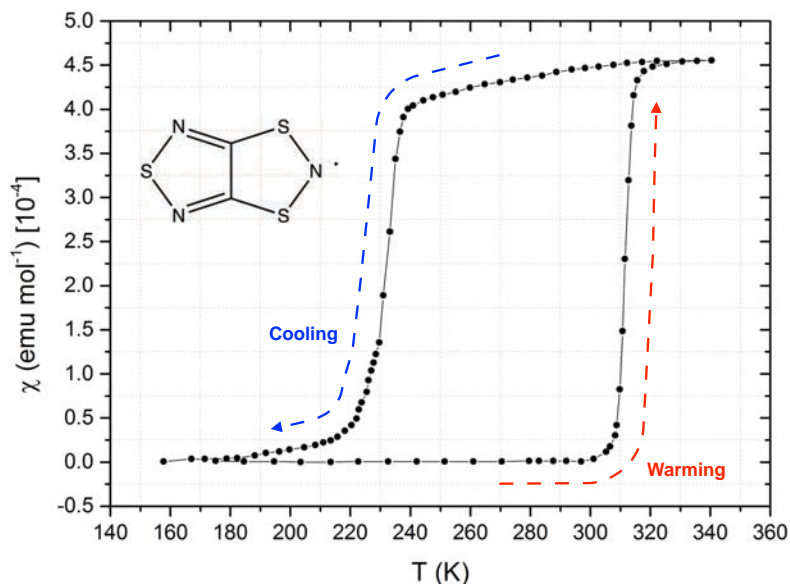


Figure 4.1: Temperature dependence of the paramagnetic susceptibility of the TTTA compound in the warming and cooling cycles. The inset shows the molecular structure of a TTTA neutral radical. The unpaired electron of the radical is formally located at the nitrogen atom of the dithiazolyl ring.

molecular plane orientations (Figure 4.3c). The S-S_{lat} contacts in the 2D layers of both LT and HT phases define a zigzag pattern (Figure 4.2c and 4.3c). While the zigzag pattern in HT is regular (*i.e.*, all the shortest interstack S··S contacts have the same distance), the zigzag pattern of LT features three different S-S_{lat} contacts: S-S_{lat1}, S-S_{lat2} and S-S_{weak}, the latter having the longest S··S distance (see Figure 4.2c). The different 2D layers of both phases of the TTTA crystal are linked by a series of interstack contacts, as shown in Figure 4.2d and 4.3d: 4-center S··N bridges involving radicals in the sample plane (N-S_{4c} interactions), 4-center S··N bridges involving radicals of out-of-registry stacks (N-S_{4c_out_reg} interactions), and S··N contacts (N-S_{long} interactions). In this computational work, we will rationalize the different stability of the LT and HT polymorphs of TTTA on the basis of differences in intermolecular interactions between radicals. Specifically, the intermolecular interactions playing a leading role in establishing the energy difference between polymorphs and, thus, the transition temperature will be determined. In addition, we will identify which are the stronger intermolecular interactions and, thus, the interactions that drive the crystal packing of the polymorphs. Finally,

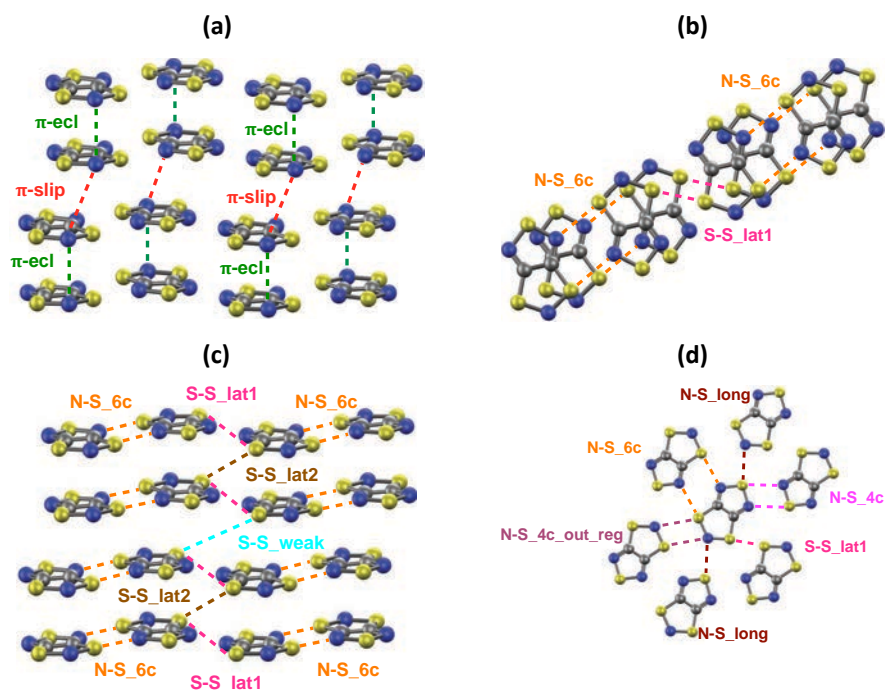


Figure 4.2: Different views of the crystal packing of the LT polymorph of TTTA (CCDC refcode = SAXPOW06) at room temperature. The different types of intermolecular interactions between radicals are marked.

the nature of the key intermolecular interactions present in the polymorphs will be evaluated. Since many of the intermolecular interactions herein considered are also present in other DTA-based crystals, the conclusions that will be drawn for TTTA will also be relevant for the other members of the family of DTA-based switchable materials.

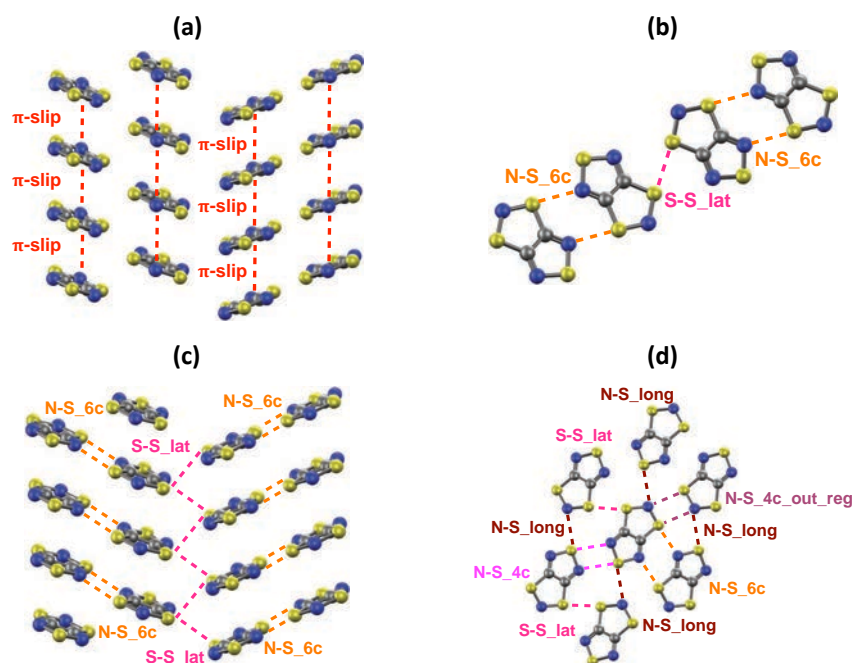


Figure 4.3: Different views of the crystal packing of the HT polymorph of TTTA (CCDC refcode = SAXPOW05) at room temperature. The different types of intermolecular interactions between radicals are marked.

4.2 Computational Details

The analysis of the origin of the different stability of the two polymorphs of TTTA was performed by means of a set of single-point electronic structure calculations using different model systems: i) supercells containing 32 TTTA radicals for the solid-state calculations, ii) isolated π -stacks and isolated pairs of π -stacks of radicals, and iii) isolated dimers of radicals and isolated radicals. The single-point calculations of all these model systems were done using the atomic coordinates as directly extracted from the X-ray structures of the LT and HT polymorphs recorded at 300 K[12]. The supercells employed for the solid-state calculations include 8 stacks of radicals, each of them containing 4 radicals. The lattice parameters of these supercells are collected in Table 4.1. In the calculations of the isolated π -stacks and isolated pairs of π -stacks, each stack comprised 4 radicals and periodic boundary conditions were considered along the stacking direction (the supercell vectors associated with the stacking direction were the same ones as those employed in the solid-state cal-

culations). In a recent work[53], we demonstrated that the regular π -stacking motif $(\cdots A \cdots A \cdots A \cdots A \cdots)_n$ of the HT phase of TTTA is not a potential energy minimum but the average structure arising from a dynamic inter-conversion between two degenerate dimerized configurations: $(\cdots A-A \cdots A-A \cdots)_n \leftrightarrow (-A \cdots A-A \cdots A-)_n$. We also demonstrated that the regular π -stacking motif is a minimum in the free energy surface of the system at 300 K. Consequently, the regular stacks of the X-ray recorded structure of the HT polymorph properly represent this phase and are thus adequate for the analysis herein presented.

Table 4.1: Supercell parameters employed in the calculations of the LT and HT polymorphs of TTTA. The a , b and c parameters are given in Angstrom. The α , β and γ angles are given in degree.

	a	b	c	α	β	γ
LT ¹	15.06	20.05	14.05	100.60	96.98	77.64
HT	18.89	14.84	15.06	90.00	104.63	90.00

The single-point electronic structure calculations for all model systems were carried out with plane wave pseudopotential calculations using the PBE exchange-correlation functional[54, 55] within the spin unrestricted formalism, together with Vanderbilt ultrasoft pseudopotentials[56], and Γ -point sampling of the Brillouin zone, as implemented in the Quantum Espresso package[57]. The semiempirical dispersion potential introduced by Grimme[58] (D2 version) was added to the conventional Kohn-Sham DFT energy in order to properly describe the van der Waals interactions between the different TTTA radicals. The plane wave basis set was expanded at a kinetic energy cutoff of 35 Ry. Some of the plane wave pseudopotential calculations of isolated π -stacks and isolated pairs of π -stacks and the plane wave pseudopotential calculations of isolated pairs of radicals were benchmarked against all-electron PBE-D2 calculations using the aug-cc-pVTZ basis set[59, 60], as implemented in the CRYSTAL09 code[61, 62]. The DFT calculations of isolated pairs of radicals, in turn, were validated by means of NEVPT2[63, 64]/aug-cc-pVTZ calculations using the ORCA code[65].

The interaction energy decomposition analysis performed for a selected subset of pairs of radicals was carried out using an Energy Decomposition Analysis[66] method that can be applied within the DFT framework[67], as implemented in the GAMESS

¹ The (a,b,c) supercell parameters of LT and HT are multiples of the (a,b,c) parameters defining the unit cells of the LT-300 and HT-300 X-ray resolved structures, respectively. The relations between the supercell (sc) parameters and the unit cell (uc) parameters are the following ones: $a_{LT,sc} = 2 \cdot a_{LT,uc}$; $b_{LT,sc} = 2 \cdot b_{LT,uc}$; $c_{LT,sc} = 2 \cdot c_{LT,uc}$; $a_{HT,sc} = 2 \cdot a_{HT,uc}$; $b_{HT,sc} = 4 \cdot b_{HT,uc}$; $c_{HT,sc} = c_{HT,uc}$

suite of programs[68]. In the method herein employed the interaction energy is decomposed into electrostatic, exchange, repulsion, polarization, and dispersion terms. The nature of the bonding between radicals was also evaluated using the “Atoms in Molecules” (AIM) methodology, as implemented in AIMAll[69].

4.3 Results and Discussion

The presentation of the results is organized as follows. We will first analyze the intermolecular interactions between isolated pairs of radicals (Subsection 4.3.1). Then, we will investigate the different stability of the two polymorphs of TTTA on the basis of the energetics of isolated π -stacks of radicals and isolated pairs of π -stacks of radicals (Subsection 4.3.2). Finally, we will explore the nature of the intermolecular interactions that play a key role in determining the different stability of the two polymorphs of TTTA (Subsection 4.3.3).

4.3.1 Intermolecular Interactions in Isolated Pairs of TTTA Radicals

In this subsection, we shall compute the interaction energy between radicals in different isolated pairs of TTTA radicals in order to i) identify the strongest intermolecular interactions in the TTTA polymorphs, *i.e.*, the interactions that are key driving forces in the crystal packing, ii) provide insights into the origin of the different stability of the two phases of TTTA, and iii) validate the DFT methodology used in the calculations carried out with periodic boundary conditions (subsection 2).

Table 4.2: Interaction energies² (given in kcal mol⁻¹) between pairs of radicals in the LT polymorph of TTTA

Pair ³	PBE-D2/USP-PW ⁴	PBE-D2/cc-PVTZ ⁵	NEVPT2/cc-PVTZ ⁶
π -ecl	-7.66	-9.01	-16.04
π -slip	-4.81	-5.64	-11.13
N-S _{6c}	-5.10	-5.72	-8.22
N-S _{4c}	-3.77	-4.36	-6.63
S-S _{lat1}	-2.13	-2.44	-3.73
S-S _{lat2}	-2.31	-2.60	-3.86
S-S _{weak}	-0.57	-0.73	-0.98
N-S _{long}	-1.35	-1.67	-2.81

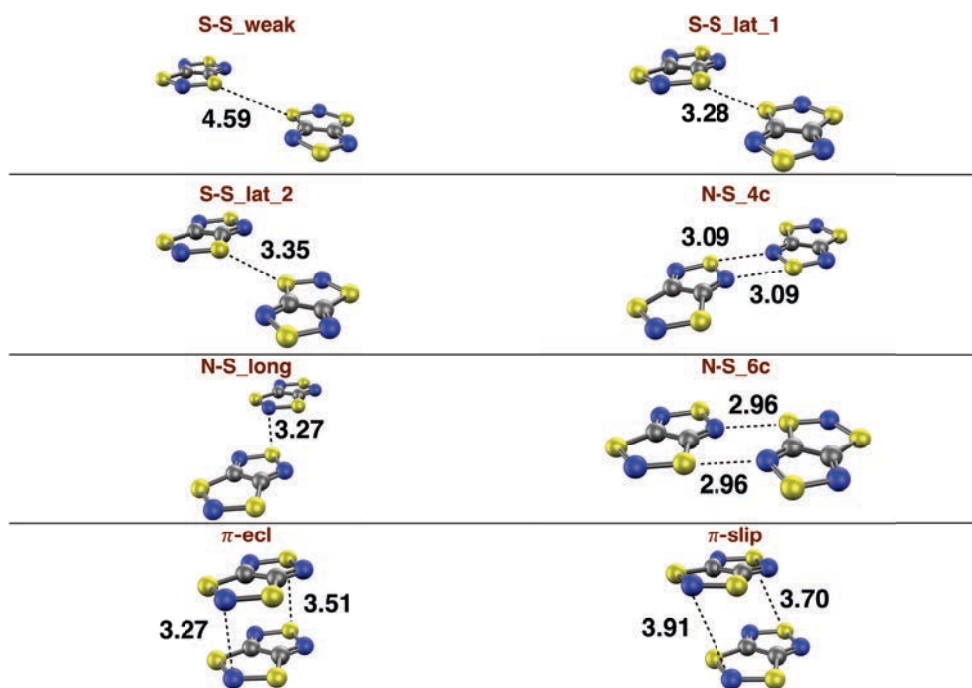


Figure 4.4: Different pairs of radicals in the LT polymorph of the TTTA crystal. The set of pairs considered in our study include those pairs with the shortest intermolecular contacts. The distances associated with the shortest intermolecular contacts in each pair are indicated in each image.

The set of isolated pairs of radicals that have been considered for the LT and HT

² Each interaction energy was computed as $E(\text{pair}) - E(\text{radical}_1) - E(\text{radical}_2)$, where $E(\text{pair})$ is the energy of the pair of radicals and $E(\text{radical}_1)$ and $E(\text{radical}_2)$ are the energies of the isolated radicals forming the dimer.

³ The structures of the different types of pairs of radicals are displayed in Figure 4.4.

⁴ Plane wave pseudopotential DFT calculations carried out with Quantum Espresso.

⁵ All-electron DFT calculations using Gaussian basis sets carried out with Crystal.

⁶ Correlated wave function all-electron calculations carried out with ORCA.

⁷ Each interaction energy was computed as $E(\text{pair}) - E(\text{radical}_1) - E(\text{radical}_2)$, where $E(\text{pair})$ is the energy of the pair of radicals and $E(\text{radical}_1)$ and $E(\text{radical}_2)$ are the energies of the isolated radicals forming the dimer.

⁸ The structures of the different types of pairs of radicals are displayed in Figure 4.5.

⁹ Plane wave pseudopotential DFT calculations carried out with Quantum Espresso.

¹⁰ All-electron DFT calculations using Gaussian basis sets carried out with Crystal.

¹¹ Correlated wave function all-electron calculations carried out with ORCA.

Table 4.3: Interaction energies⁷ (given in kcal mol⁻¹) between pairs of radicals in the HT polymorph of TTTA

Pair ⁸	PBE-D2/USP-PW ⁹	PBE-D2/cc-PVTZ ¹⁰	NEVPT2/cc-PVTZ ¹¹
π -slip	-5.04	-5.91	-11.42
N-S_6c	-4.83	-5.50	-7.75
N-S_4c	-3.65	-4.21	-6.48
S-S_lat	-2.24	-2.54	-4.05
N-S_long	-1.61	-1.94	-3.31

polymorphs are displayed in Figure 4.4 and 4.5, respectively. The results collected in Tables 4.2 and 4.3 reveal that the strongest intermolecular interaction between radicals in both polymorphs is found in the pairs exhibiting a π - π interaction (be it either of the π -ecl or the π -slip type of interaction). It then follows that the intermolecular interactions along the π -stacks are the most attractive interactions in the crystals of TTTA. Among the other types of interaction between radicals (*i.e.* the interactions that link the π -stacks together), the N-S_6c and N-S_4c interactions are significantly stronger than the others.

Table 4.4: Difference in energies (given in kcal mol⁻¹) between pairs of TTTA radicals of the HT polymorph and pairs of radicals of the LT polymorph¹².

HT	LT	PBE-D2/USP-PW ¹³	PBE-D2/cc-PVTZ ¹⁴	NEVPT2/cc-PVTZ ¹⁵
π -slip	π -ecl	2.58	2.96	4.77
π -slip	π -slip	-0.27	-0.41	-0.14
N-S_6c	N-S_6c	0.24	0.09	0.63
N-S_4c	N-S_4c	0.09	0.02	0.31
S-S_lat	S-S_lat1	-0.14	-0.21	-0.13
S-S_lat	S-S_lat2	0.04	-0.05	-0.03
S-S_lat	S-S_weak	-1.70	-1.94	-2.91
N-S_long	N-S_long	-0.29	-0.40	-0.34

According to the differences in energy between pairs of radicals gathered in Table 4.4, the different stability of the LT and HT phases of TTTA is mainly controlled by the two following types of interaction: the interactions along the π -stacks and the interstack S · · S contacts. The former type of interactions favour the LT polymorph because the transformation of the π -ecl interactions into π -slip interactions in going

¹² The difference in energy between two different pairs (pair1 and pair2) was computed as: ΔE (pair1, pair2) = E (pair1, HT) - E (pair2, LT).

¹³ Plane wave pseudopotential DFT calculations carried out with Quantum Espresso.

¹⁴ All-electron DFT calculations using Gaussian basis sets carried out with Crystal.

¹⁵ Correlated wave function all-electron calculations carried out with ORCA.

from LT to HT results in a much less attractive interaction (~ 4.7 kcal mol $^{-1}$ less attractive, according to NEVPT2 calculations) and, thus, in a lower stability of HT. The interstack S $\cdot\cdot$ S contacts, instead, favour the HT polymorph due to the disruption of the regular zigzag pattern of S $\cdot\cdot$ S contacts in going from HT to LT. As a result of this disruption, one out of every four S $\cdot\cdot$ S contacts increases its distance (*i.e.*, one out of every four S-S_{lat} interactions in HT transforms itself into a S-S_{weak} interaction), thereby decreasing significantly its associated interaction energy (by about 2.9 kcal mol $^{-1}$, according to NEVPT2 calculations). The results collected in Tables 4.2, 4.3 and 4.4 also demonstrate that PBE-D2 calculations properly capture the main trends observed in the NEVPT2 calculations. Although the interaction energies and the differences in interaction energy obtained at the PBE-D2 level are smaller than those obtained at the NEVPT2 level, the conclusions that can be drawn from the PBE-D2 calculations are fully consistent with the conclusions drawn from the NEVPT2 calculations. It thus follows that the PBE-D2 methodology is adequate for describing the intermolecular interactions between TTTA radicals and, thus, adequate for the calculations considering periodic boundary conditions that will be presented in the next subsection.

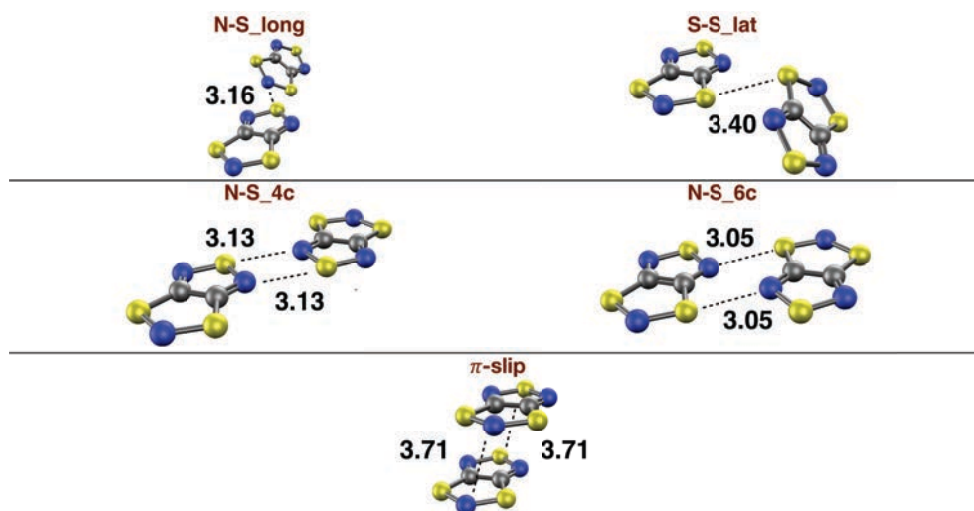


Figure 4.5: Different pairs of radicals in the HT polymorph of the TTTA crystal. The set of pairs considered in our study include those pairs with the shortest intermolecular contacts. The distances associated with the shortest intermolecular contacts in each pair are indicated in each image.

4.3.2 Intermolecular Interactions Model System Considering Periodic Boundary Conditions

In this subsection we shall further investigate the origin of the different stability of the two polymorphs of TTTA by means of PBE-D2 calculations of isolated π -stacks and isolated pairs of π -stacks.

Let us set the stage by first establishing the difference in lattice energy between the two phases of TTTA. According to plane wave pseudopotential PBE-D2 solid-state calculations carried out using supercells of 32 radicals, the LT phase of TTTA is 0.92 kcal mol⁻¹ more stable (given per TTTA molecule) than the HT phase (Table 4.5).

Table 4.5: Differences in energy, ΔE (given in kcal mol⁻¹), between the HT and LT polymorphs of TTTA and between an isolated π -stack of HT and an isolated π -stack of LT.

ΔE polymorphs ¹⁶	ΔE isolated π -stacks
0.92	1.08 ¹⁷

The calculations carried out on isolated π -stacks, in turn, show that an isolated π -stack of LT is 1.08 kcal mol⁻¹ more stable than an isolated π -stack of HT. The fact that these two values are so similar demonstrates that the intermolecular interactions along the π -stacks are the leading factor behind the different stability of the two polymorphs of TTTA. In fact, the difference in energy between a π -stack of LT and a π -stack of HT can be accurately predicted on the basis of the differences in energy gathered in Table 4.4. If we assume that the energy of a given column (given per radical) is determined exclusively by the energy of the TTTA radical and the sum of interaction energies between this radical and its nearest neighbours, the expression of the energies of the π -stacks of LT and HT can be written as:

$$E_{\text{stack}}(\text{LT}) = E_{\text{rad}} + \frac{1}{2}E_{\text{int}}(\pi - \text{ecl}) + \frac{1}{2}E_{\text{int}}(\pi - \text{slip,LT}) \quad (4.1)$$

$$E_{\text{stack}}(\text{HT}) = E_{\text{rad}} + E_{\text{int}}(\pi - \text{slip,HT}) \quad (4.2)$$

where E_{rad} is the energy of a single radical and E_{int} refers to the interaction energies between radicals. Note that in the expressions given above we distinguish

¹⁶ The differences in energy are calculated as $E(\text{HT}) - E(\text{LT})$, and are given per TTTA radical. The values were obtained by means of plane wave pseudopotential DFT calculations carried out with Quantum Espresso.

¹⁷ This value, obtained with Quantum Espresso, was further corroborated with all-electron calculations using a cc-pVTZ basis set (carried out with CRYSTAL09), which furnished a very similar difference in energy of 1.27 kcal mol⁻¹.

the π -interaction between slipped radicals in LT from that of HT because they do not present the same interaction energy (cf. 4.2, 4.3 and 4.4). On the basis of Eqs. 4.1 and 4.2, the difference in energy between an isolated π -stack of HT and isolated π -stack of LT can be expressed as:

$$E_{\text{stack}}(\text{HT}) - E_{\text{stack}}(\text{LT}) = \frac{1}{2} (E_{\text{int}}(\pi - \text{slip}, \text{HT}) - E_{\text{int}}(\pi - \text{ecl})) + \frac{1}{2} (E_{\text{int}}(\pi - \text{slip}, \text{HT}) - E_{\text{int}}(\pi - \text{slip})) \quad (4.3)$$

The difference in energy between the HT and LT π -stacks that results from inserting the values of the first two entries of the “PBE-D2/USP-PW” column of Table 4.4 in the equation above is 1.15 kcal mol⁻¹. The close correspondence between this value and the value obtained from the PBE-D2 calculations of isolated π -stacks (1.08 kcal mol⁻¹) demonstrates that the difference in energy between the HT and LT isolated π -stacks is essentially governed by the short-range two-body interactions between radicals, primarily by the difference in energy between the π -ecl dimers of LT and the π -slip dimers of HT.

Table 4.6: Interaction energies (given in kcal mol⁻¹) between π -stacks of radicals in both HT and LT polymorphs¹⁸

Type of Interaction	HT	LT
N-S_6c	-3.46	-3.34
N-S_4c	-2.29	-2.41
S-S_lat ¹⁹	-2.13	-1.86
N-S_long	-1.06	-1.17
N-S_4c_out_reg ²⁰	-1.38	-1.48

Upon comparing the difference in lattice energy between the HT and LT polymorphs (0.92 kcal mol⁻¹) with the difference in energy between the HT and LT isolated π -stacks (1.08 kcal mol⁻¹), it is concluded that the former is largely dominated by the

¹⁸ The interaction energies are given per TTTA radical. The values reported were obtained by means of plane wave pseudopotential DFT calculations carried out with Quantum Espresso.

¹⁹ Note that the S-S_lat-type interaction in HT involves only one type of interaction between pairs of radicals (the S-S_lat interaction, see Figure 4.3c). Conversely, the S-S_lat-type interaction in LT involves three different types of interaction between radical pairs, namely: S-S_lat1, S-S_lat2 and S-S_weak (see Figure 4.2c).

²⁰ The “N-S_4c_out_reg” type of interaction present in these columns resembles the type of interaction present in the “N-S_4c” case. However, in the former case the π -stacks are out-of-registry, whereas in the latter they are in-registry (see Figures 4.2d and 4.3d).

latter and that the interactions between π -stacks make a non-negligible contribution in tuning the energy gap between HT and LT, specifically by decreasing it. In view of the importance of the interstack interactions, we shall now study them in detail. The interaction energies between π -stacks in both HT and LT polymorphs (cf. Table 4.6) follow the same trend as that observed in the interaction energies for the isolated pairs of radicals (Tables 4.2 and 4.3). Indeed, the strongest interaction between π -stacks is found for the stacks that interact through the N-S_6c interactions, which feature the largest interaction energy among the interstack contacts. The other interstack contacts are, in decreasing order of interaction strength, those mediated by N-S_4c contacts, lateral S · · S contacts and N-S_long contacts (cf. Table 4.6). As can be seen in Tables 4.2 and 4.3, the interaction energies of isolated pairs of radicals follow the same order. However, the values of the interaction energies between π -stacks in Table 4.6 are considerably larger than the values that would be predicted on the basis of the interaction energies of isolated pairs of radicals (note that the values of Table 4.6 are given per radical, while the values of Tables 4.2 and 4.3 are given per pairs of radicals). This means that the interaction energy between π -stacks cannot be expressed solely in terms of a sum of pairwise interaction energies between nearest neighbours. When considering the difference in interaction energies between the π -stacks of HT and the π -stacks of LT (cf. Table 4.7), it is observed that all types of interactions result in small but not negligible relative stabilizations of either one or the other polymorph. Among all types of lateral interactions, the lateral S · · S contacts

Table 4.7: Differences in interaction energies (given in kcal mol⁻¹) between π -stacks of radicals in the HT and LT polymorphs of TTTA.

Type of Interaction	$\Delta E_{\text{int}}^{\text{21}}$
N-S_6c	-0.11
N-S_4c	0.12
S-S_lat	-0.27 ²²
N-S_long	0.11
N-S_4c_out_reg	0.10

are those that lead to a larger stabilization of one polymorph relative to the other one. Specifically, the lateral S · · S contacts lead to a significant relative stabilization of the HT polymorph because the interaction energy between π -stacks through this

²¹ For a given type of interaction, the difference in interaction energy (ΔE_{int}) was obtained via: $\Delta E_{\text{int}} = E_{\text{int}}(\text{HT}) - E_{\text{int}}(\text{LT})$. Note that the values of $E_{\text{int}}(\text{HT})$ and $E_{\text{int}}(\text{LT})$ are collected in Table 4.6.

²² This value, obtained with Quantum Espresso, was further corroborated with all-electron calculations using a cc-pVTZ basis set (carried out with CRYSTAL09), which furnished a very similar difference in interaction energy of -0.30 kcal mol⁻¹.

type of contacts in HT is $0.27 \text{ kcal mol}^{-1}$ more stable than in LT. This result is in line with the intermolecular interactions evaluated for isolated pairs of radicals (see previous subsection), which showed that the increase of the S · · S distance in going from the S-S_lat interaction in HT to the S-S_weak interaction in LT entailed a strong weakening (by $0.85 \text{ kcal mol}^{-1}$, cf. Table 4.4)²³ of the intermolecular interaction between radicals. It should be mentioned, though, that the relative stabilization of $0.27 \text{ kcal mol}^{-1}$ is slightly smaller than the value that might have been expected on the basis of the results obtained for the isolated pairs. As explained in the previous paragraph, this is due to the fact that the interaction energy between π -stacks cannot be expressed solely in terms of a sum of pairwise interaction energies between nearest neighbours.

4.3.3 Evaluation of the Nature of the Key Intermolecular Interactions

In this subsection we shall gain further insight into the energetic differences between the LT and HT polymorphs of TTTA by means of an analysis of the intermolecular bond critical points (BCPs) present in the different pairs of radicals and an energy decomposition analysis of the interaction energy for the most relevant pairs. The number of BCPs (Figures 4.6 and 4.7) and the electronic density at these BCPs (Table 4.8) correlate well with the strength of interaction energies of the isolated pairs of radicals (cf. Tables 4.2 and 4.3). The π -ecl interaction of LT, which is the most attractive interaction, features the largest number of BCPs (six), together with the largest value of the density on some of these critical points. In going from the π -ecl interaction of LT to the π -slip interaction of HT, not only the number of BCPs decreases (from six to five) but also the corresponding electronic densities. Interestingly, the BCP between the nitrogen atoms of the dithiazolyl rings, which are the atoms that formally hold the unpaired electron of the radical, disappears upon transformation of the π -ecl(LT) interaction into the π -slip(HT) interaction. Among all lateral interactions, the N-S_6c type of interactions exhibit both the largest number of BCPs and the largest values of electronic density, which is consistent with the fact that these are the strongest lateral interactions. The analysis of BCPs also reflects the strong weakening of the lateral S · · S contact in going from the S-S_lat interaction in HT to the S-S_weak interaction in LT. Even though the elongated S · · S contact in S-S_weak(LT) still features a BCP, the data in Table 4.8 shows that its associated value of the electronic density is one order of magnitude smaller than the corresponding value in the BCP associated with the S · · S contact in the S-S_lat(HT) interaction.

²³ Note that value of $0.85 \text{ kcal mol}^{-1}$ comes from dividing the value of $1.70 \text{ kcal mol}^{-1}$ in Table 4.4 by 2 in order to give the difference in energy per TTTA radical.

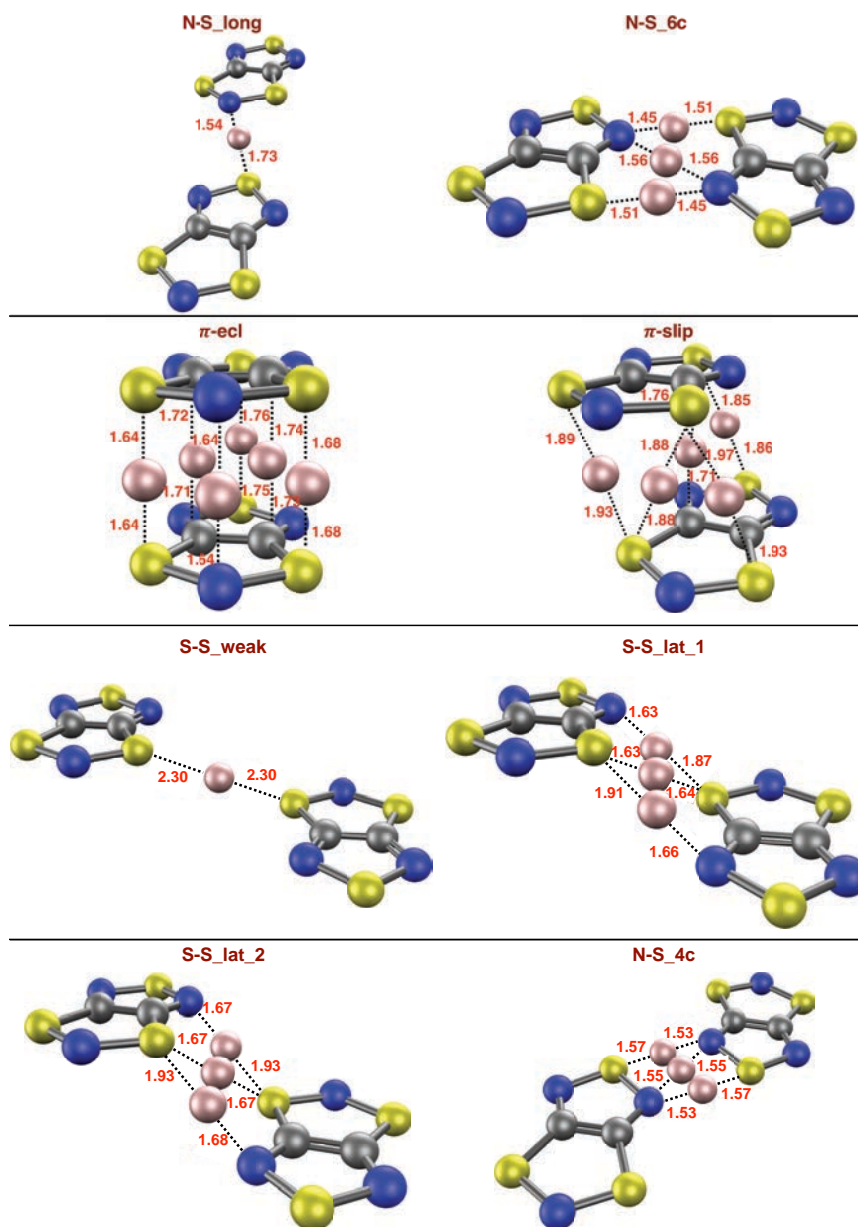


Figure 4.6: Bond critical points (marked with pink spheres) associated with several interatomic contacts of the different types of intermolecular interactions between radicals in the LT polymorph of TTTA. The images show the distances (given in Å) between the bond critical points and the atoms.

Table 4.8: Values of the electronic density at the bond critical points associated with the intermolecular contacts in the LT and HT polymorphs of TTTA. For each type of intermolecular interaction (see Figs. 4.6 and 4.7), the value of the electronic density is reported for all the interatomic contacts presenting a bond critical point²⁴.

HT		LT	
π -slip		π -ecl	
S(DTA)··S(DTA)	0.0064 ²⁵	S(DTA)··S(DTA)	0.0146 ²⁵
N(DTA)··N(DTA)	- ²⁶	N(DTA)··N(DTA)	0.0054
C(DTA)··N(DTA)	0.0044	C(DTA)··N(DTA)	0.0045 ²⁵
S(TDA)··S(TDA)	0.0064	S(TDA)··S(TDA)	0.0096
N-S _{6c}		N-S _{6c}	
N(TDA)··S(DTA)	0.0112 ²⁵	N(TDA)··S(DTA)	0.0134 ²⁵
N(TDA)··N(TDA)	0.0054	N(TDA)··N(TDA)	0.0067
N-S _{4c}		N-S _{4c}	
N(TDA)··S(TDA)	0.0088 ²⁵	N(TDA)··S(TDA)	0.0095 ²⁵
N(TDA)··N(TDA)	-	N(TDA)··N(TDA)	0.0074
N-S _{long}		N-S _{long}	
N(DTA)··S(TDA)	0.0092	N(DTA)··S(TDA)	0.0079
S-S _{lat}		S-S _{weak}	
S(DTA)··S(DTA)	0.0093	S(DTA)··S(DTA)	0.0008
S(DTA)··N(TDA)	0.0038	S(DTA)··N(TDA)	-
		S-S _{lat1} / S-S _{lat2}	
		S(DTA)··S(DTA)	0.0106
		S(DTA)··N(TDA)	0.0047 ²⁵

The evaluation of the nature of the key intermolecular interactions behind the different stability of the two polymorphs of TTTA was carried out by means of an energy decomposition analysis (EDA). Since the difference in stability between polymorphs is primarily dictated by the energy difference between the π -ecl(LT) and π -slip(HT) interactions and the energy difference between the S-S_{weak}(LT) and S-S_{lat}(HT) interactions, the EDA was carried out for these types of interaction only. A comparison between the interaction energy components of the π -ecl dimers of LT and the π -slip dimers of HT reveals that all the attractive components of the inter-

²⁴ The interatomic contacts are identified on the basis of the atoms of the heterocyclic rings (DTA and TDA refer to the dithiazolyl and thiazazole rings, respectively) involved in the contact.

²⁵ This value results from taking the average of the density values of different bond critical points of the same type (see Figures 4.6 and 4.7).

²⁶ There is no critical point associated with this contact.

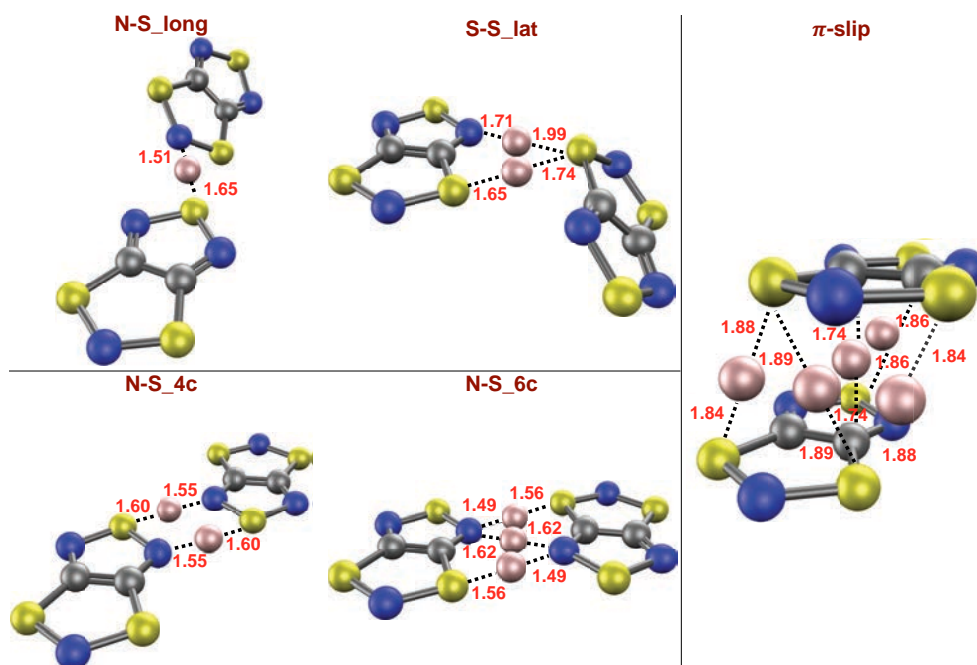


Figure 4.7: Bond critical points (marked with pink spheres) associated with several interatomic contacts of the different types of intermolecular interactions between radicals in the HT polymorph of TTTA. The images show the distances (given in Å) between the bond critical points and the atoms.

action energy of the former are larger than those of the latter (the largest differences are found for the polarization and dispersion components, cf. Tables 4.9 and 4.10). Conversely, the repulsion energy between radicals is much larger in the former than in the latter. Therefore, the π -ecl dimers of LT are more stable than the π -slip dimers of HT because the larger attractive components of the interaction energy (of which, the polarization and dispersion are the dominant ones) compensate the increase in repulsion energy in going from π -ecl(LT) to π -slip(HT). On the other hand, the values gathered in Table 4.11 demonstrate that the weakening of the lateral S...S bonds in going from HT to LT is due to a weakening of all the attractive components of the interaction energy, especially the dispersion and polarization energies.

Table 4.9: Energy decomposition analysis of the interaction energy of π -slip and π -ecl-type interactions in TTTA. All the components of the interaction energy are given in kcal mol⁻¹.

	π -slip (HT)	π -slip (LT)	π -ecl (LT)
Electrostatic	-3.23	-3.03	-7.30
Exchange	-2.74	-2.46	-6.35
Repulsion	15.28	14.09	33.07
Polarization	-3.95	-3.55	-11.46
DFT Dispersion ²⁷	-5.77	-5.32	-10.81
Grimme Dispersion ²⁸	-5.63	-5.47	-6.59
Total Dispersion ²⁹	-11.40	-10.79	-17.40

Table 4.10: Difference between the various components of the interaction energy of π -slip and π -ecl-type interactions in TTTA. All the differences are given in kcal mol⁻¹.

	$E(\pi\text{-slip,HT})-E(\pi\text{-ecl,LT})$	$E(\pi\text{-slip,HT})-E(\pi\text{-slip,LT})$
Electrostatic	4.07	-0.20
Exchange	3.61	-0.28
Repulsion	-17.79	1.19
Polarization	7.51	-0.40
DFT Dispersion	5.04	-0.45
Grimme Dispersion	0.96	-0.16
Total Dispersion	6.00	-0.61

²⁷ This accounts for the dispersion that the PBE functional is able to recover by itself.

²⁸ This accounts for the dispersion recovered by Grimme's D2 semiempirical approach.

²⁹ The values reported in this entry are just the sum of the values of "DFT dispersion" and "Grimme dispersion".

Table 4.11: Energy decomposition analysis of the interaction energy of S-S_lat and S-S_weak type interactions in TTTA. All the components of the interaction energy are given in kcal mol⁻¹.

	S-S_lat (HT)	S-S_weak (LT)	ΔE^{30}
Electrostatic	-1.61	0.02	-1.63
Exchange	-1.66	-0.12	-1.54
Repulsion	7.38	0.10	7.28
Polarization	-2.81	-0.36	-2.45
DFT Dispersion ³¹	-2.12	0.04	-2.16
Grimme Dispersion	-1.83	-0.39	-1.44
Total Dispersion	-3.95	-0.35	-3.60

³⁰ Given a component of the interaction energy, this column collects the difference between the value of this component in S-S_lat(HT) and in S-S_weak(LT).

³¹ This accounts for the dispersion that the PBE functional is able to recover by itself.

4.4 Conclusions

On the basis of the computational study herein presented, we have identified the intermolecular interactions that drive the crystal packing of the two polymorphs of TTTA and the intermolecular interactions that play a prime role in establishing the different stability of the polymorphs of this prototypical example of a bistable material based on dithiazolyl radicals. The formation of π -stacks of radicals in the two polymorphs is driven by strong π - π interactions, which are the strongest of all intermolecular interactions between TTTA radicals. Among the lateral interactions that bind the π -stacks together, the stronger ones are those mediated by six-center S \cdots N bridges, followed by those mediated by four-center S \cdots N bridges.

The difference in stability between polymorphs is primarily governed by two types of intermolecular interactions: the π - π intermolecular interactions along the π -stacks and the S \cdots S lateral contacts between π -stacks. The π - π interactions result in a substantial stabilization of the LT phase (relative to the HT phase) because the binding between radicals in the eclipsed π -dimers of the LT phase is stronger than in the slipped π -dimers of the HT phase. The stronger binding of the eclipsed π -dimers mainly originates in larger values of the the polarisation and dispersion components of the energy interaction. The interstack S \cdots S contacts, in turn, result in a destabilisation of the LT phase (relative to the HT phase) because some of the lateral S \cdots S contacts of LT have a significantly weaker interaction than the lateral S \cdots S contacts of HT. The interplay between the effects of the π - π and the S \cdots S interactions (in which the effect of the π - π interactions is the dominant one) in defining the difference in energy between polymorphs is tuned to a small but non-negligible extent by other types of interstack interactions, including those interactions mediated by six- and four-center S \cdots N bridges.

The results herein presented are not only relevant for the prototypical TTTA compound, but also for other members of the family of dithiazolyl-based switchable materials because many of the supramolecular motifs identified as being important for driving the crystal packing and/or determining the difference in stability between polymorphs of TTTA are common to other members of this family[11, 13–15, 22]. Therefore, our results provide valuable information for the rationalisation of the crystal packing and spin transition temperatures of DTA-based switchable crystals, as well as for the design of new materials of this type.

4.5 Acknowledgements

FM, MD, JJN and JRA acknowledge financial support from MINECO through Grant CTQ2017-87773-P/AEI/FEDER, UE and Spanish Structures Excellence María de Maeztu program through grant MDM-2017767. FM, MD, JJN and JRA are also thankful to the Catalan DURSI (2017SGR348 grant) and to BSC and CSUC for the allocation of computer time. TF acknowledges funding from the European Union Horizon 2020 research and innovation programme under the Marie Curie Skłodowska-Curie grant agreement no. 642294.

Bibliography

- [1] J. M. Rawson, A. Alberola, A. Whalley, *Journal of Materials Chemistry* **2006**, *16*, 2560–2575.
- [2] K. E. Preuss, *Dalton Transactions* **2007**, 2357–2369.
- [3] R. G. Hicks, *Organic & biomolecular chemistry* **2007**, *5*, 1321–1338.
- [4] P. M. Lahti in *Advances in Physical Organic Chemistry*, Vol. 45, Elsevier, **2011**, pp. 93–169.
- [5] I. Ratera, J. Veciana, *Chemical Society Reviews* **2012**, *41*, 303–349.
- [6] S. Winter, S. Hill, R. Oakley, *Journal of the American Chemical Society* **2015**, *137*, 3720–3730.
- [7] A. Mailman, J. W. Wong, S. M. Winter, R. C. Claridge, C. M. Robertson, A. Assoud, W. Yong, E. Steven, P. A. Dube, J. S. Tse, et al., *Journal of the American Chemical Society* **2017**, *139*, 1625–1635.
- [8] O. Sato, *Nature chemistry* **2016**, *8*, 644.
- [9] A. Bousseksou, G. Molnár, L. Salmon, W. Nicolazzi, *Chemical Society Reviews* **2011**, *40*, 3313–3335.
- [10] M. Halcrow, *Spin-crossover materials: properties and applications*, John Wiley & Sons, **2013**.
- [11] T. Barclay, A. Cordes, N. George, R. Haddon, M. Itkis, M. Mashuta, R. Oakley, G. Patenaude, R. Reed, J. Richardson, et al., *Journal of the American Chemical Society* **1998**, *120*, 352–360.
- [12] W. Fujita, K. Awaga, *Science* **1999**, *286*, 261–262.
- [13] J. L. Brusso, O. P. Clements, R. C. Haddon, M. E. Itkis, A. A. Leitch, R. T. Oakley, R. W. Reed, J. F. Richardson, *Journal of the American Chemical Society* **2004**, *126*, 8256–8265.

- [14] J. L. Brusso, O. P. Clements, R. C. Haddon, M. E. Itkis, A. A. Leitch, R. T. Oakley, R. W. Reed, J. F. Richardson, *Journal of the American Chemical Society* **2004**, *126*, 14692–14693.
- [15] A. Alberola, R. J. Collis, S. M. Humphrey, R. J. Less, J. M. Rawson, *Inorganic chemistry* **2006**, *45*, 1903–1905.
- [16] K. Lekin, S. M. Winter, L. E. Downie, X. Bao, J. S. Tse, S. Desgreniers, R. A. Secco, P. A. Dube, R. T. Oakley, *Journal of the American Chemical Society* **2010**, *132*, 16212–16224.
- [17] A. Alberola, D. J. Eisler, L. Harvey, J. M. Rawson, *CrystEngComm* **2011**, *13*, 1794–1796.
- [18] J. M. Rawson, J. J. Hayward, *Spin-Crossover Materials: Properties and Applications* **2013**, 225–237.
- [19] H. Phan, K. Lekin, S. M. Winter, R. T. Oakley, M. Shatruk, *Journal of the American Chemical Society* **2013**, *135*, 15674–15677.
- [20] K. Lekin, H. Phan, S. M. Winter, J. W. Wong, A. A. Leitch, D. Laniel, W. Yong, R. A. Secco, J. S. Tse, S. Desgreniers, et al., *Journal of the American Chemical Society* **2014**, *136*, 8050–8062.
- [21] S. Vela, M. Reardon, C. E. Jakobsche, M. Turnbull, J. Ribas-Arino, J. Novoa, *Chemistry-A European Journal* **2017**, *23*, 3479–3489.
- [22] D. Bates, C. M. Robertson, A. A. Leitch, P. A. Dube, R. T. Oakley, *Journal of the American Chemical Society* **2018**, *140*, 3846–3849.
- [23] H. Matsuzaki, W. Fujita, K. Awaga, H. Okamoto, *Physical review letters* **2003**, *91*, 017403.
- [24] R. Suizu, A. Iwasaki, Y. Shuku, K. Awaga, *Journal of Materials Chemistry C* **2015**, *3*, 7968–7977.
- [25] E. M. Fatila, R. A. Mayo, M. Rouzieres, M. C. Jennings, P. Dechambenoit, D. V. Soldatov, C. Mathoniere, R. Clerac, C. Coulon, K. E. Preuss, *Chemistry of Materials* **2015**, *27*, 4023–4032.
- [26] S. Brooker, *Chem. Soc. Rev.* **2015**, *44*, 2880–2892.
- [27] T. Romero-Morcillo, M. Seredyuk, M. C. Muñoz, J. A. Real, *Angewandte Chemie International Edition*, *54*, 14777–14781.
- [28] V. Gómez, C. Sáenz de Pipaón, P. Maldonado-Illescas, J. C. Waerenborgh, E. Martin, J. Benet-Buchholz, J. R. Galán-Mascarós, *Journal of the American Chemical Society* **2015**, *137*, 11924–11927.
- [29] M. E. Itkis, X. Chi, A. W. Cordes, R. C. Haddon, *Science* **2002**, *296*, 1443–1445.

- [30] R. G. Hicks, *Nature Chemistry* **2011**, *3*, 189 EP -.
- [31] T. Li, G. Tan, D. Shao, J. Li, Z. Zhang, Y. Song, Y. Sui, S. Chen, Y. Fang, X. Wang, *Journal of the American Chemical Society* **2016**, *138*, 10092–10095.
- [32] O. Kahn, C. J. Martinez, *Science* **1998**, *279*, 44–48.
- [33] J. S. Miller, *Accounts of Chemical Research* **2007**, *40*, 189–196.
- [34] D. Jose, A. Datta, *Crystal Growth & Design* **2011**, *11*, 3137–3140.
- [35] W. B. P. R. S. Mulliken, *Molecular Complexes: A Lecture and Reprint Volume*, Wiley Interscience: New York, **1969**.
- [36] K. E. Preuss, *Polyhedron* **2014**, *79*, 1–15.
- [37] Z.-h. Cui, H. Lischka, M. Beneberu, Habtamu Z. and Kertesz, *Journal of the American Chemical Society* **2014**, *136*, 12958–12965.
- [38] H. Z. Beneberu, Y.-H. Tian, M. Kertesz, *Phys. Chem. Chem. Phys.* **2012**, *14*, 10713–10725.
- [39] C. S. Clarke, J. Jornet-Somoza, F. Mota, J. J. Novoa, M. Deumal, *Journal of the American Chemical Society* **2010**, *132*, 17817–17830.
- [40] T. Francese, J. Ribas-Arino, J. J. Novoa, R. W. Havenith, R. Broer, C. de Graaf, M. Deumal, *Phys. Chem. Chem. Phys.* **2018**, *20*, 20406–20416.
- [41] G. Wolmershäuser, R. Johann, *Angewandte Chemie International Edition in English* **1989**, *28*, 920–921.
- [42] G. D. McManus, J. M. Rawson, N. Feeder, J. van Duijn, E. J. L. McInnes, J. J. Novoa, R. Burriel, F. Palacio, P. Oliete, *J. Mater. Chem.* **2001**, *11*, 1992–2003.
- [43] W. Fujita, K. Awaga, H. Matsuzaki, H. Okamoto, *Phys. Rev. B* **2002**, *65*, 064434.
- [44] T. Tanaka, W. Fujita, K. Awaga, *Chemical Physics Letters* **2004**, *393*, 150–152.
- [45] Y. Takahashi, T. Suemoto, S. Oguri, J. Takeda, *Phys. Rev. B* **2006**, *74*, 193104.
- [46] M. Furuya, Y. Kawazoe, K. Ohno, *Science and Technology of Advanced Materials* **2004**, *5*, 689.
- [47] K. Ohno, Y. Noguchi, T. Yokoi, S. Ishii, J. Takeda, M. Furuya, *ChemPhysChem*, *7*, 1820–1824.
- [48] P. Naumov, J. P. Hill, K. Sakurai, M. Tanaka, K. Ariga, *The Journal of Physical Chemistry A* **2007**, *111*, 6449–6455.
- [49] T. Kon, S. Oguri, I. Katayama, T. Kodaira, J. Takeda, *Phys. Rev. B* **2009**, *79*, 035106.
- [50] I. Katayama, T. Kon, K. Mitarai, J. Takeda, *Phys. Rev. B* **2009**, *80*, 092103.

- [51] A. Domingo, M. Vérot, F. Mota, C. de Graaf, J. J. Novoa, V. Robert, *Phys. Chem. Chem. Phys.* **2013**, *15*, 6982–6989.
- [52] S. Vela, F. Mota, M. Deumal, R. Suizu, Y. Shuku, A. Mizuno, K. Awaga, M. Shiga, J. J. Novoa, J. Ribas-Arino, *Nature Communications* **2014**, *5*, Article, 4411 EP -.
- [53] S. Vela, M. Deumal, M. Shiga, J. J. Novoa, J. Ribas-Arino, *Chem. Sci.* **2015**, *6*, 2371–2381.
- [54] J. P. Perdew, K. Burke, M. Ernzerhof, *Phys. Rev. Lett.* **1996**, *77*, 3865–3868.
- [55] J. P. Perdew, K. Burke, M. Ernzerhof, *Phys. Rev. Lett.* **1997**, *78*, 1396–1396.
- [56] D. Vanderbilt, *Phys. Rev. B* **1990**, *41*, 7892–7895.
- [57] P. Giannozzi, O. Andreussi, T. Brumme, O. Bunau, M. B. Nardelli, M. Calandra, R. Car, C. Cavazzoni, D. Ceresoli, M. Cococcioni, N. Colonna, I. Carnimeo, A. D. Corso, S. de Gironcoli, P. Delugas, R. A. D. Jr, A. Ferretti, A. Floris, G. Fratesi, G. Fugallo, R. Gebauer, U. Gerstmann, F. Giustino, T. Gorni, J. Jia, M. Kawamura, H.-Y. Ko, A. Kokalj, E. Kkbenli, M. Lazzeri, M. Marsili, N. Marzari, F. Mauri, N. L. Nguyen, H.-V. Nguyen, A. Otero-de-la-Roza, L. Paulatto, S. Ponc, D. Rocca, R. Sabatini, B. Santra, M. Schlipf, A. P. Seitsonen, A. Smogunov, I. Timrov, T. Thonhauser, P. Umari, N. Vast, X. Wu, S. Baroni, *Journal of Physics: Condensed Matter* **2017**, *29*, 465901.
- [58] S. Grimme, *Journal of Computational Chemistry*, *27*, 1787–1799.
- [59] T. H. Dunning, *The Journal of Chemical Physics* **1989**, *90*, 1007–1023.
- [60] D. E. Woon, T. H. Dunning, *The Journal of Chemical Physics* **1993**, *98*, 1358–1371.
- [61] R. Dovesi, V. R. Saunders, C. Roetti, R. Orlando, C. M. Zicovich-Wilson, F. Pascale, B. Civalleri, K. Doll, N. M. Harrison, I. J. Bush, P. D'Arco, M. Llunell, *CRYSTAL09 User's Manual*. University of Torino, Torino, **2009**.
- [62] R. Dovesi, R. Orlando, B. Civalleri, C. Roetti, V. Saunders, C. Zicovich-Wilson, *Zeitschrift fur Kristallographie - Crystalline Materials* **2005**, *220*, 517–573.
- [63] C. Angeli, R. Cimiraglia, S. Evangelisti, T. Leininger, J.-P. Malrieu, *The Journal of Chemical Physics* **2001**, *114*, 10252–10264.
- [64] C. Angeli, R. Cimiraglia, J.-P. Malrieu, *The Journal of Chemical Physics* **2002**, *117*, 9138–9153.
- [65] F. Neese, *Wiley Interdisciplinary Reviews: Computational Molecular Science*, *2*, 73–78.

- [66] K. Kitaura, K. Morokuma, *International Journal of Quantum Chemistry*, *10*, 325–340.
- [67] P. Su, H. Li, *The Journal of Chemical Physics* **2009**, *131*, 014102.
- [68] M. W. Schmidt, K. K. Baldridge, J. A. Boatz, S. T. Elbert, M. S. Gordon, J. H. Jensen, S. Koseki, N. Matsunaga, K. A. Nguyen, S. Su, T. L. Windus, M. Dupuis, J. A. Montgomery, *Journal of Computational Chemistry*, *14*, 1347–1363.
- [69] T. A. Keith, AIMAll (Version 17.11.14), TK Gristmill Software, Overland Park KS, USA, 2017 (aim.tkgristmill.com), **2017**.

Chapter 5

The Magnetic Fingerprint of DTA-based Molecule Magnets

This chapter is based on:

Tommaso Francese, Jordi Ribas-Ariño, Juan J. Novoa, Remco W. A. Havenith, Ria Broer, Coen de Graaf & Mercè Deumal

Phys.Chem.Chem.Phys., 2018, 20, 20406.

DOI: 10.1039/c8cp03173h

Abstract

Magnetic bistability in organic-radical based materials has attracted significant interest due to its potential application in electronic devices. The FPBU study herein presented aims at elucidating the key factors behind the different magnetic response of the low and high temperature phases of four different switchable dithiazolyl (DTA)-based compounds. The drastic change in the magnetic response upon spin transition is always due to the changes in the J_{AB} magnetic interactions between adjacent radicals along the π -stacks of the crystal, which in turn are driven mostly by the changes in the interplanar distance and degree of lateral slippage, according to the interpretation of a series of magneto-structural correlation maps. Furthermore, specific geometrical dispositions have been recognized as a ferromagnetic fingerprint in such correlations. Our results thus show that an appropriate substitution of the chemical skeleton attached to the DTA ring could give rise to new organic

materials with dominant ferromagnetic interactions

5.1 Introduction

Theoretical predictions of the magnetic properties of switchable purely organic molecule-based magnets have experienced an incredible development during the last two decades[1–5]. Some of these compounds present peculiarities that could not be easily explained. Our attention is paid to dithiazolyl (1,3,2-DTA, see Fig. 5.1a) compounds because they are one of the most prominent candidates for potential technological applications, like memory storage devices, sensors and quantum computers[6–11]. Therefore, here we focus on why some DTA compounds present not only spin transition from a low (LT) to a high (HT) temperature configuration, but also bistability. In general terms, a bistable system presents two stable phases that can coexist within a reasonably wide temperature range. Often, the phase transition from LT to HT for DTA compounds can be driven by temperature and/or light[12, 13]. In fact, this is why they can be exploited for technological purposes. Note that the mechanism *per se* of the phase transition that characterizes these systems is out of the scope of this paper. Instead we are interested in describing the static magneto-response of experimentally well-characterized planar bistable DTA compounds. Let us stress the fact that, in a static study, it is assumed that a molecule-based material can be described by a single crystal structure (usually characterized by X-ray/powder diffraction experiments) over a range of temperatures of interest for simulation purposes, neglecting the effect that, for example, thermal fluctuations might have on these systems. In particular, the properties of TTTA[14–16], PDTA[17], TDPDTA[12], and 4-NCBDTA[18] materials will be investigated. According to magnetic susceptibility $\chi T(T)$ data, all of them show bistability except 4-NCBDTA, which presents just a spin transition. Specifically, TTTA and PDTA bistabilities encompass room temperature, while for TDPDTA it occurs at much lower temperature. They all share the same dithiazolyl (DTA) chemical skeleton, where the nitrogen formally hosts an unpaired electron (see Fig. 5.1a-e).

We are interested in understanding how the R, R' substituents of the DTA-moiety (Fig. 5.1a) affect the magnetic behavior. The four selected DTA compounds present a common trend in the solid state: the planar DTA radicals pile up forming stacks (see the schematic representation in Fig. 5.2a-c). Accordingly, the interaction between the π -systems of neighboring DTA-radicals is expected to be responsible for the dominant intermolecular magnetic interactions in these systems, as concluded from a previous First-Principles Bottom-Up (FPBU)[19] study on the TTTA compound[20]. Let us now briefly describe the main features of the compounds under

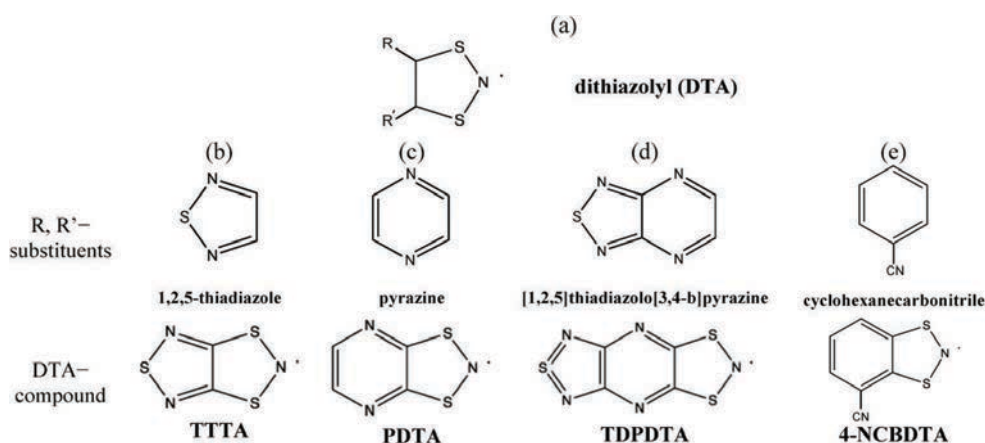


Figure 5.1: (a) General chemical skeleton of the DTA-ring, with R, R' substituents. Note that the formal position of the unpaired electron is marked with a dot on the N atom of the DTA-ring. For (b) TTTA, (c) PDTA, (d) TDPDTA, and (e) 4-NCBDTA, the corresponding R, R' substituents that, together with the DTA moiety, give rise to the DTA-based compounds investigated in this paper are shown

study. TTTA exhibits bistability at room temperature (namely, $T_{C\downarrow} = 220$ K to $T_{C\uparrow} = 315$ K). It has been extensively studied both from the structural and the electronic perspectives[14–16]. The structure has been experimentally resolved at different temperatures (150, 225, 250, 300 and 310 K). The system undergoes a first-order phase transition between the LT and HT phases. The LT-TTTA diamagnetic phase belongs to the triclinic $P1$ space group. The HT-TTTA paramagnetic phase instead is monoclinic with space group $P2_1/c$. The columns of radicals in the LT phase are distorted π -stacks consisting of slipped pairs of nearly-eclipsed radicals (Fig. 5.2a-LT). In contrast, the columns of the HT phase at room temperature are regular π -stacks of radicals, where each single TTTA molecule exhibits a tilted overlap with its two adjacent TTTA molecules along the stacking direction (Fig. 5.2a-HT). The PDTA system presents many similarities compared to TTTA. It is a planar bistable system, whose susceptibility curve encompasses room temperature (namely, $T_{C\downarrow} = 297$ K to $T_{C\uparrow} = 343$ K). The compound has been experimentally characterized at 95 K, 293 K and 323 K[17]. As TTTA, it experiences a first-order phase transition. The LT-PDTA motif presents eclipsed π -pairs alternated with π -shifted pairs (Fig. 5.2b-LT); whereas the HT-PDTA phase presents a uniform π -stack pair pattern (Fig. 5.2b-HT). The LT-PDTA crystal structure belongs to the triclinic space group $P1$, consisting of centrosymmetric pairs of PDTA dimers, while the HT-PDTA phase be-

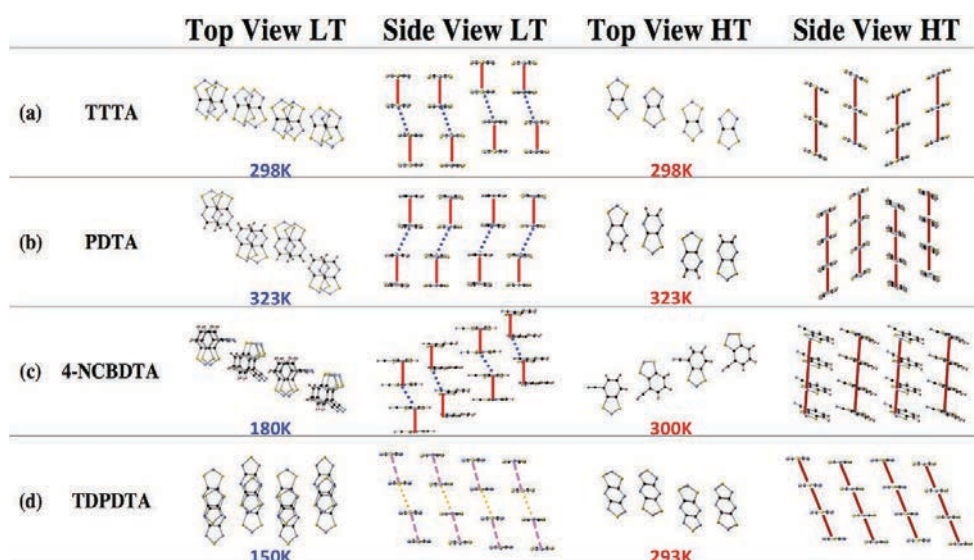


Figure 5.2: Schematic representation of the crystal packing showing the top and side views of the common pattern of the DTA stacking for the low temperature (LT) and high temperature (HT) phases of TTTA, PDTA, 4-NCBDTA and TDPDTA (a-d, respectively). In the LT phases, a common crystal packing trend is followed by TTTA, PDTA and 4-NCBDTA where the eclipsed- π dimers (red line) are alternated with π -slipped dimers (dashed blue line). For the (d) LT-TDPDTA phase, the packing differs from the other three compounds, presenting an almost uniform arrangement (dashed purple and orange lines represent two different distances between radicals within the same column). In the HT configurations instead, all four materials follow the same regular π -stack configuration

longs to the monoclinic space group $C2/c$. The 4-NCBDTA system is not bistable but presents spin transition. The 4-NCBDTA structures studied were resolved at 180 K (LT) and 300 K (HT) by X-ray powder diffraction[18]. Both the LT-4-NCBDTA and the HT-4-NCBDTA phases belong to the monoclinic space group $P2_1/c$. For the LT-4-NCBDTA phase, there is an alternation between eclipsed π -pairs and π -shifted pairs (Fig. 5.2c-LT). In contrast, for the HT-4-NCBDTA structure, the packing is uniform (Fig. 5.2c-HT). The TDPDTA radical presents three fused rings, *i.e.* two five membered rings coupled by a six-membered ring. This has a direct effect on the crystal packing. Both the LT-TDPDTA and HT-TDPDTA phases belong to the triclinic space group $P1$ [12]. The system shows a hysteretic behavior, with the temperature range between $T_{C\downarrow} = 50$ K and $T_{C\uparrow} = 200$ K. The HT phase dis-

plays the common uniform packing of ribbons of the TDPDTA radicals packed in a slipped π -stack arrangement, as the other three crystals (Fig. 5.2d-HT). However, the LT phase presents alternate layers of TDPDTA shifted laterally every two radicals within a given column, giving rise to almost uniform arrays of dimers (see Fig. 5.2d-LT). To sum up, the current study of TTTA, PDTA, TDPDTA, and 4-NCBDTA addresses three main issues from a static perspective. Our first goal is to study by means of the FPBU[19] approach the magnetic interactions between pairs of radicals to identify the magnetic topology of the molecule-based DTA crystals. Next, we aim at providing a magneto-structural correlation map as a function of the substituents of the DTA-moiety to highlight the ferromagnetic fingerprint region in DTA-based materials. At this point, we would like to stress that this magneto-structural map could be used as a practical tool to help experimentalists to design more stable and efficient purely organic radicals with ferromagnetic properties in the solid state. Finally, our objective is to assess whether structural (geometrical) as well as electronic (DTA-chemical skeleton, interactions between substituents) factors affect or not the magnitude of the significant radical-radical J_{AB} magnetic couplings.

5.1.1 Methodological Details

The First-Principles Bottom-Up (FPBU) working strategy has been extensively used to study molecule-based magnets[19–25]. First, one selects all possible magnetically relevant pairs of radicals in the crystal by analysis of the crystal packing from the X-ray resolved experimental structure. As for the DTA-based crystals, although the spin density of a DTA radical is delocalized over the atoms of the entire DTA-ring (see Appendix A.1), the pairs of radicals have been chosen based on the $N^* \cdots N^*$ distance, where N^* refers to the nitrogen atom that formally holds the unpaired electron (Fig. 5.1a). The $N^* \cdots N^*$ threshold distance was set to 10.0 Å to select *di* pairs of radicals because it is known that the spin-coupling interaction exponentially decays with distance[26]. Next, one calculates the radical-radical J_{AB} spin-coupling interaction for each pair of radicals selected in the crystal. The microscopic J_{AB} magnetic interactions is evaluated in terms of energy differences. Therefore, for the energy calculations, the neutral environment of any given DTA-radical must be well described. Direct observation of the crystal hints at using a two-radical cluster as a model. From the general Heisenberg Hamiltonian ($\hat{H} = -2 J_{AB} \hat{S}_A \cdot \hat{S}_B$) for an A-B pair of $S=1/2$ radicals, the J_{AB} value can be defined as $J_{AB} = [E_{BS} - E^T]^1$, [19]

¹ From the Heisenberg Hamiltonian $\hat{H} = -2 J_{AB} \hat{S}_A \cdot \hat{S}_B$ for a pair of A and B radicals, the J_{AB} value is computed as the energy difference between biradical open-shell singlet S and triplet T states, $\Delta E^{S-T} = E^S - E^T = 2J_{AB}$. Open-shell singlet systems can localize alpha spin density and beta spin density on different radicals. In our case, within the DFT framework, once the broken symmetry approximation (BS) is applied, the energy difference can be expressed as: $E^S - E^T = 2(E_{BS}^S - E^T)/(1$

where E^T and E_{BS} are the triplet and singlet broken symmetry[27, 28] energies of the dimer cluster model, respectively. All energy calculations were performed at the DFT/UB3LYP[29, 30] level as implemented in the Gaussian09 package[31]. The standard 6-31+G(d) basis set[32, 33] was used in all energy calculations. Once all J_{AB} exchange couplings have been computed, one must propose the magnetic topology of the crystal in terms of the non-negligible J_{AB} magnetic interactions. This step is extremely important because it enables us to visualize how the microscopic magnetic interactions propagate. The use of Statistical Mechanics to calculate the macroscopic magnetic properties of the DTA-based crystals is bound to the selection of a magnetic model, whose extension along (a, b, c) crystallographic axes regenerates the whole magnetic topology. Finally, having chosen the magnetic models, one constructs the matrix representation that contains all J_{AB} values required to appropriately parameterize the Heisenberg Hamiltonian. The energy eigenvalues and corresponding spin quantum numbers that result from the full diagonalization of the adequate matrix on the space of spin functions of the magnetic models are used to calculate the magnetic susceptibility $\chi^T(T)$ data for each magnetic model we select using the corresponding expression provided by Statistical Mechanics[34, 35]. Finally, the simulated data for the systems studied by means of the FPBU working strategy are compared to the experimental data.

5.2 Results and Discussion

The static analysis of the four DTA-based materials studied in this work is reported in three different sections. In the first section, the compounds are analyzed by means of the FPBU approach, providing a unique view of the driving spin-coupling interactions and how they propagate within the experimentally X-ray resolved crystal. The second section, instead, deals with the study of geometrical factors and their correlation with magnetic coupling interactions. In this case, we will make use of a set of representative structural models of each system to explore the different magneto-structural correlations displayed by each DTA-based material. The aim of this study is to uncover the intermolecular arrangement that most likely favours ferromagnetic (FM) interactions. Finally, the third section will quantify the contribution of electronic and structural factors to the overall J_{AB} exchange coupling interactions.

+ S_{ab}). The resulting S_{ab} overlap between the alpha (a) SOMO and the beta (b) SOMO is very small, which means that the orbitals are localized on each of the two radicals. This leads to $S_{ab} \approx 0$. As a conclusion $J_{AB} = E_{BS}^S - E^T$.

5.2.1 Magnetic susceptibility curves: calculated *vs.* experimental

Previous studies on TTTA[20, 36] and 4-NCBDTA[37] have already reported their magnetic topology and their corresponding simulated magnetic susceptibility curves. For both compounds, good agreement was accomplished with respect to the experimental data. Notice that the magnetic topology is defined in terms of non-negligible J_{AB} exchange interactions between radicals[38]. Therefore, the magnetic topology embraces all the most important J_{AB} spin coupling interactions (see Appendix A.2, for a list of the atomic coordinates of the magnetically dominant pairs of radicals). For the LT-TTTA phase, the basic magnetic motif can be described as an antiferromagnetic (AFM) 1D chain formed by alternating eclipsed and slipped dimers. There are large AFM interactions ($J_{\text{eclipsed dimer}}^{\text{LT-TTTA}} = -1755 \text{ cm}^{-1}$) that are responsible for the overall diamagnetic behavior of this phase, which are then connected by weaker $J_{\text{slipped dimer}}^{\text{LT-TTTA}}$ coupling interactions (-50 cm^{-1}) along the π -stack slipped dimer (see Fig. 5.2a)[20]. This basic magnetic motif is then interconnected in a three-dimensional (3D) network of much weaker coupling interactions that can be neglected for simulation purposes. The HT-TTTA magnetic motif consists instead of regular AFM 1D chains ($J_{\text{regular dimer}}^{\text{HT-TTTA}} = -135 \text{ cm}^{-1}$, see Fig. 5.2b), which explains regular dimer the experimentally observed weak paramagnetism. Likewise, the 4-NCBDTA basic magnetic motifs resemble those for TTTA, presenting similar magnetic exchange coupling values, namely $J_{\text{eclipsed dimer}}^{\text{LT-4NCBDTA}} = -1700 \text{ cm}^{-1}$ and $J_{\text{slipped dimer}}^{\text{LT-4NCBDTA}} = -80 \text{ cm}^{-1}$ for the eclipsed dimer slipped dimer LT phase, and $J_{\text{regular dimer}}^{\text{HT-4NCBDTA}} = -340 \text{ cm}^{-1}$ for the HT phase[37]. Here we report the magnetic topology for both HT- and LT-phases of the PDTA and TDPDTA systems (see Fig. 5.3a and c for HT and Fig. 5.3b and d for LT). We can clearly see how the main J_{AB} magnetic interaction propagates along the DTA π -stacking direction of the crystal structure for all phases (see the strongest J_{AB} couplings highlighted in red in tables inserted in Fig. 5.3). For PDTA (Fig. 5.3a and b), the alternating eclipsed radical pair and slipped dimer pattern in the LT-phase become a regular π -stacking in the HT-phase, in accordance with the general tendency hitherto observed for DTA-based systems (see TTTA in Fig. 5.2a and b). One can realize that the magnetic topologies are three-dimensional (3D). Yet, the inter- π -stacking J_{AB} magnetic interactions are at least one order of magnitude smaller than the strongest J_{AB} π -stacking couplings (see tables inserted in Fig. 5.3). Consequently, while we are dealing with 3D magnetic topologies, for simulation purposes, the basic magnetic motif can be considered to be one-dimensional (1D) (see Appendix A.3).

Comparison between PDTA (Fig. 5.3a and b) and TDPDTA (Fig. 5.3c and d) shows that, although the inter- π -stacking J_{AB} magnetic interactions have the same order

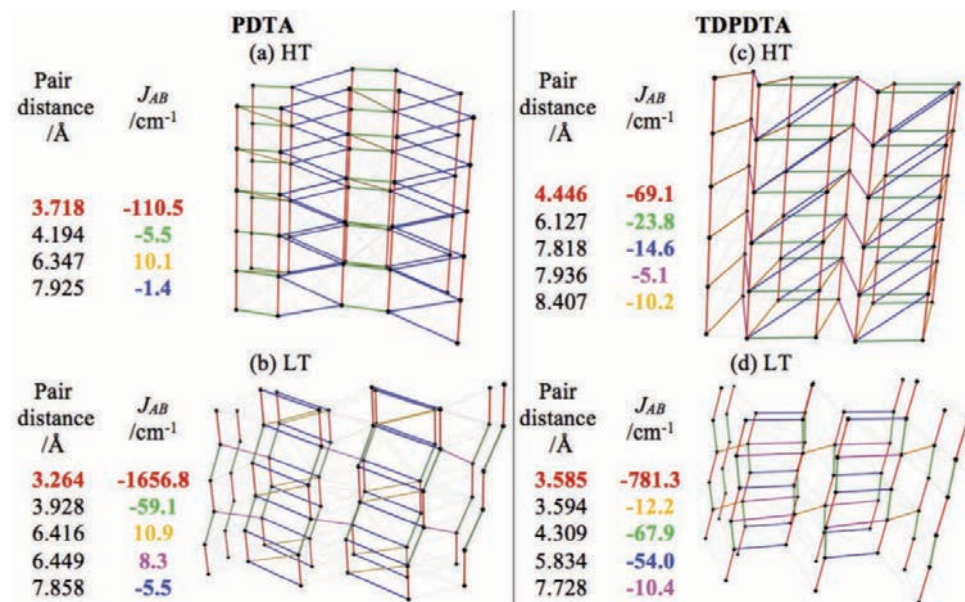


Figure 5.3: Magnetic topology for HT- and LT-phases of (a and b) PDTA and (c and d) TDPDTA crystals, respectively. Note that the $N^* \cdots N^*$ inter radical distance (in Å) and the corresponding J_{AB} (in cm^{-1}) are also given in a table next to the corresponding magnetic topology. $|J_{AB}| < 1 \text{ cm}^{-1}$ are represented by light grey lines.

of magnitude, the intra- π -stacking J_{AB} magnetic couplings for TDPDTA are weaker than for PDTA. This is not an issue for the LT-TDPDTA phase, which can still be taken to be 1D for simulation purposes. However, for the HT-TDPDTA phase the intra- and inter- π -stacking J_{AB} values might appear to be comparable. Thus, the 3D magnetic topology of the HT-TDPDTA phase has been analyzed to conclude that a 1D magnetic model can be nevertheless used for the calculation of the magnetic properties (see Appendix A.3, for a detailed discussion on the magnetic models for PDTA and TDPDTA). The experimental and computed magnetic susceptibility $\chi T(T)$ data for PDTA and TDPDTA show qualitative agreement with experiment (see Fig. 5.4). For the LT-PDTA phase, the shape of the calculated curve almost perfectly overlaps the measured $\chi T(T)$ values (Fig. 5.4a). The simulated LT-PDTA phase behaves as experimentally measured because the radicals form nearly eclipsed pairs and there is an extremely strong AFM calculated J_{AB} value (ca. -1650 cm^{-1}). The LT-PDTA phase thus becomes magnetically silent, similarly to TTTA and 4-NCBDTA. Note that the large AFM value of J_{AB} comes from the dominant

magnetic interaction propagating along the DTA π -stacking direction in all the analyzed crystals (see Fig. 5.2a). Yet the experimental and calculated $\chi T(T)$ values do not show a perfect correspondence for either the LT-TDPDTA or HT data of both crystals. The LT-TDPDTA and HT magnetic responses are qualitatively consistent with the general experimental shape. However, they do not numerically reproduce the measured $\chi T(T)$ values. Although enlarging the magnetic model improves the computed $\chi T(T)$ data (see the discussion in Appendix A.3)[36], the experimental values cannot be fully reproduced. Therefore, the study of PDTA and TDPDTA proves one more time that a static study of the magnetism of DTA-based systems has its limitations. For DTA-based materials, this flaw is due to the fact that a single geometry has been disclosed not to be representative enough of the system due to the thermal fluctuations that the crystal experiences[37, 39]. Despite being aware of the fact that molecular dynamics studies are needed to address this issue (and will soon be performed), the static results provide a rationale for the different magnetic responses of the two phases of PDTA and TDPDTA. The resulting data are in agreement with previous studies on TTTA and 4-NCBDTA. In all these four DTA-derivatives, the change in the magnetic response upon phase transition is due to different $J(\text{di})$ magnetic radical-radical interactions along the π -stacking direction. Therefore, one can safely conclude that the different magnetic behavior of the phases of bistable DTA-compounds is ruled by the same physical principles.

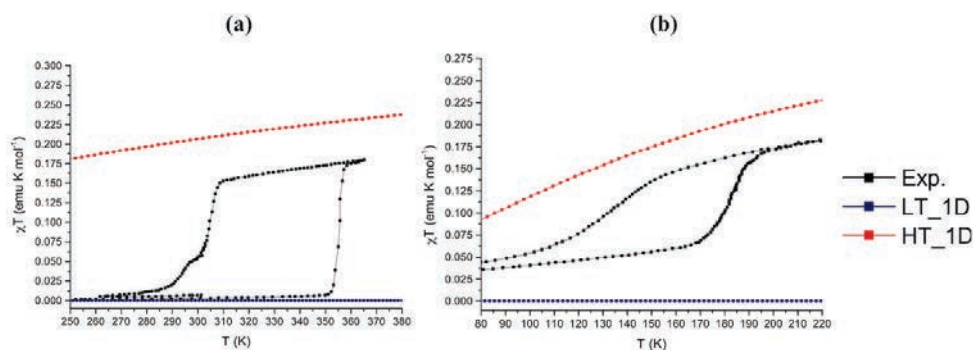


Figure 5.4: Comparison between experimental $\chi T(T)$ data (in black) and computed magnetic susceptibility $\chi T(T)$ for (a) PDTA and (b) TDPDTA using the most representative 1D minimal magnetic models that better reproduce the data for LT (in blue) and HT (in red) phases.

5.2.2 Evaluating the nature of the magnetic interactions in DTA-based materials: magneto-structural correlation maps

We complemented our FPBU investigation screening the J_{AB} values for a multiple set of DTA-based dimers as a function of two geometrical variables: namely, the interplanar distance (d_{IP}) and the degree of slippage (d_{SL}) between the two radicals. These two geometrical variables have been found to be of general application for a series of organic radicals in order to establish magneto-structural correlations[40–42]. For all DTA-based materials studied here, the HT phase is the most interesting because it is not diamagnetic. Therefore, the study that we hereafter present aims at rationalizing the different experimental data of the magnetic susceptibility displayed by the HT phases of TTTA, PDTA, 4-NCBDA and TDPDTA using magneto-structural correlation maps. To this aim, we selected one DTA-radical from the HT

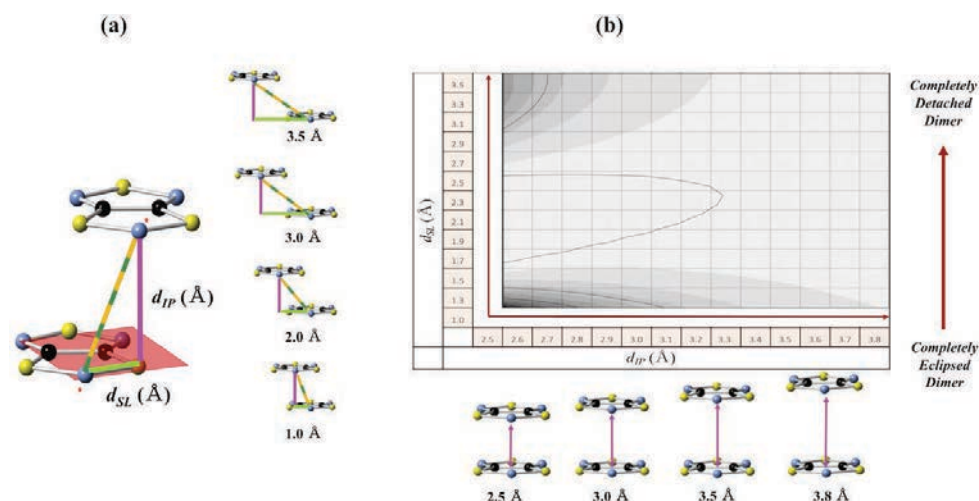


Figure 5.5: (a) Model I used for sampling the respective d_{IP} (in purple) and d_{SL} (in green) distances to compute the magneto-structural correlation maps. Note that the DTA-radical shown is TTTA. (b) Schematic representation of the correlation maps. The x -axis provides the d_{IP} contribution, whereas the y -axis provides the d_{SL} contribution. The calculated J_{AB} interactions are displayed along the z -axis, and also projected onto the xy -plane.

phase of each single crystal (TTTA, PDTA, TDPDTA, and 4-NCBDA) as a reference, keeping the bond distances as resolved experimentally. This radical was then oriented in the xy -plane, and then duplicated along the z -axis to create the model used to screen the J_{AB} values (see Fig. 5a for Model I of TTTA). Analyzing the geometry

of the DTA-radicals within the experimentally resolved crystal, it is observed that the shortest and longest d_{IP} interplanar distances belong to TDPDTA (3.305 Å) and 4-NCBDTA (3.524 Å) systems, respectively. The d_{SL} degree of slippage has, instead, the shortest value for 4-NCBDTA (1.007 Å), whereas the largest is found in TDPDTA (2.974 Å). Accordingly, we have selected d_{IP} interplanar distances ranging from 2.5 to 3.8 Å and d_{SL} degrees of slippage ranging from 1.0 to 3.5 Å to obtain the correlation maps. Note that this distance range is large enough not only to explore those already known geometrical arrangements but also other dispositions that might be magnetically important. Therefore, the configurations created extend from an almost completely eclipsed dimer ($d_{SL} = 1.0$ Å) to the completely detached pair ($d_{SL} = 3.5$ Å) (see Fig. 5b). Specifically, the number of configurations along d_{IP} is 130, while the number along d_{SL} is 25. Each single magneto-structural correlation map is thus obtained by analyzing 3250 dimers, and computing the J_{AB} coupling value for each pair of radicals. Fig. 5.6 displays the calculated J_{AB} interactions as d_{IP} and d_{SL} vary, and the corresponding projection onto the xy -plane. One can easily realize that our results show that we can locate not only regions with the expected highly AFM interactions, but also FM regions which have not yet been experimentally met. The J_{AB} range of interest considered goes from -100 cm^{-1} up to $+150$ cm^{-1} , as highlighted in the color scale legend. AFM coupling values beyond 100 cm^{-1} ($J_{AB} \ll 100$ cm^{-1}) are represented in black, because such strong J_{AB} spin coupling actually corresponds to a diamagnetic pair of radicals, which is magnetically silent. Thus, there is no possibility of exploiting the magnetic properties of the systems. In contrast, screening the different regions from $J_{AB} = -100$ cm^{-1} up to the strongest FM area allows us to identify the radical pairs with geometrical configurations that favor FM interactions. Let us remark here that the slipped geometries of other organic radicals displaying FM interactions have also been predicted in the literature[40, 42]. The four DTA-based systems present very different magneto- structural correlation maps (see Fig. 5.6). As a consequence, the extension of the FM areas varies significantly. Indeed, direct observation of the correlation maps reveals that whether the compounds are bistable or just spin switchable does not depend on J_{AB} . Contrarily, a correlation can be inferred between the number of fused rings of the DTA-radical and the tendency of the J_{AB} magnetic coupling to show AFM values. Moving from two fused ring systems (TTTA, 4-NCBDTA, and PDTA) to three fused ring radicals (TDPDTA), the probability of orbital overlap to be efficient increases and, thus, the FM coupling is quenched. The compound presenting the widest FM area is the prototypical TTTA system (Fig. 5.6a). The FM zone ranges from ($d_{IP} = 2.50$, $d_{SL} = 1.49$ Å) to ($d_{IP} = 3.24$ Å, $d_{SL} = 2.40$ Å). The J_{AB} values vary from 0 cm^{-1} (orange border line) to $+87$ cm^{-1} (brownish area). Between these two limiting values, we have a gradient of FM spin coupling values. Each depicted distinctive zone contains a set

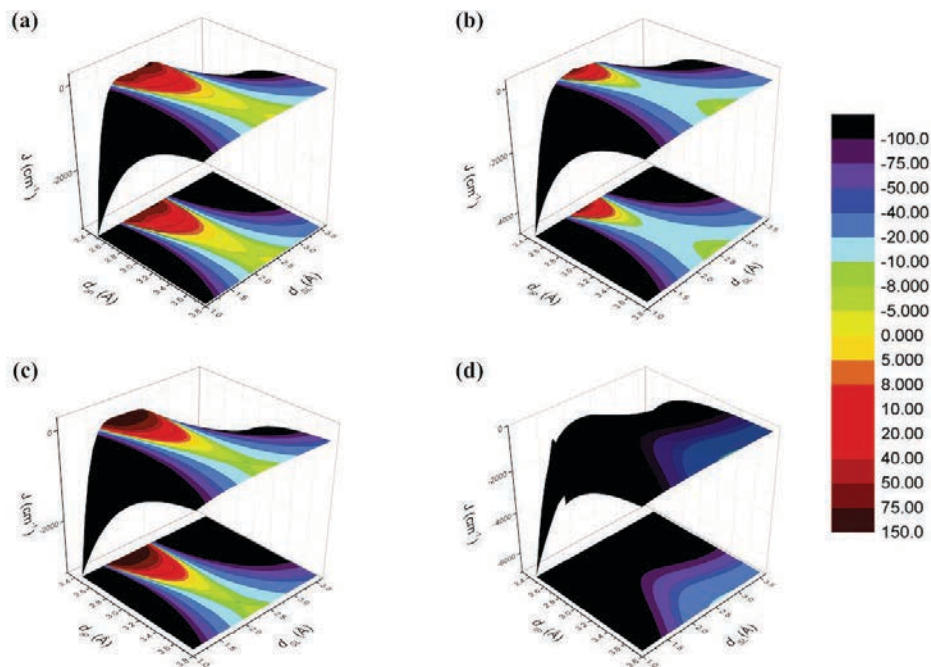


Figure 5.6: Magneto-structural correlation maps for (a) TTTA (bistable), (b) PDTA (bistable), (c) 4-NCBDTA (spin switch), and (d) TDPDTA (bistable).

of radical pairs whose arrangement enhances the FM coupling. Since all J_{AB} values have been computed at the UB3LYP[27–30] level, our next goal is to prove the good description of the magnetic interaction between TTTAs (and DTA-radicals in general) provided by DFT. First, the J_{AB} magnetic coupling interactions computed at the DFT/UB3LYP level were benchmarked with the Difference Dedicated Configuration Interaction (DDCI3)[43–45] method for our system. Therefore, a series of FM configurations from the TTTA correlation map were selected and their J_{AB} values compared to the outcomes of the DDCI calculations (see A-C models in Appendix A.4, for a detailed discussion). The corresponding J_{AB} values calculated at the DDCI level confirm the existence of FM interactions associated with certain geometrical configurations (e.g. $J_{\text{model A}}^{\text{DDCI}} = 30.6 \text{ cm}^{-1}$ vs. $J_{\text{model A}}^{\text{UB3LYP}} = 7.9 \text{ cm}^{-1}$ in Appendix A.4). In this sense, DFT, although less accurate than DDCI3, offers a cheap and consistent method to rely on for predicting FM/AFM coupling. Therefore, DFT can be trusted to evaluate FM and AFM tendencies, but not the absolute value of the J_{AB} coupling *per se*. A similar scenario to TTTA is also reported for PDTA (Fig. 5.6b) and 4-NCBDTA (Fig. 5.6c) compounds, although a contraction of the FM region is

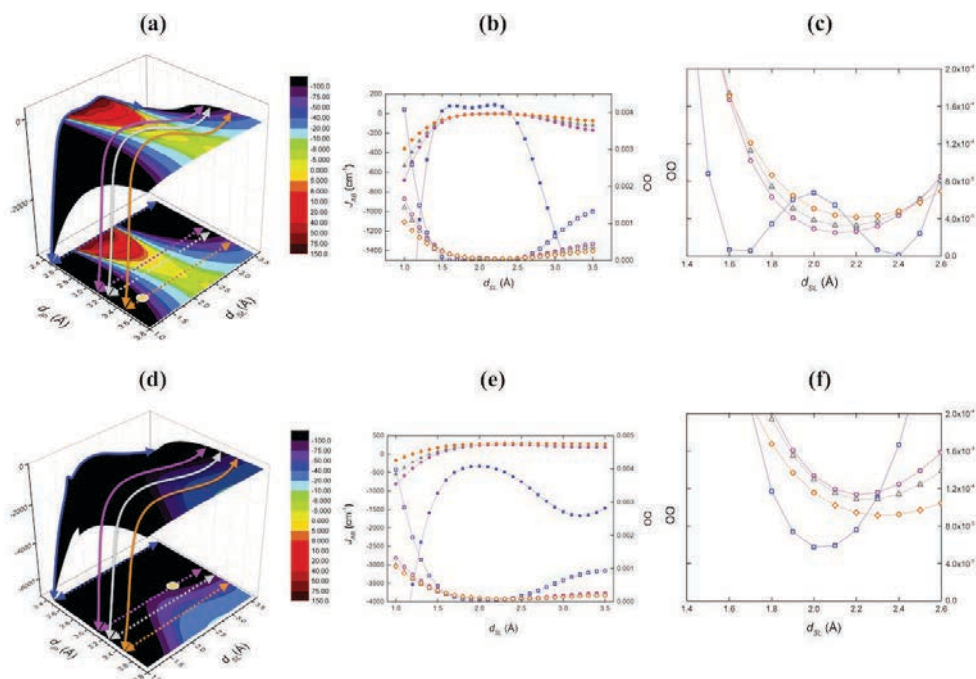


Figure 5.7: Orbital overlap (OO) analysis graphs for TTTA (a-c) and TDPDTA (d-f). (a) Fixed d_{IP} values sampled at 2.5, 3.1, 3.22 and 3.5 Å in order to analyze the most FM region (blue line), the FM boundary ($J_{AB} = 0 \text{ cm}^{-1}$, purple line), the moderate AFM region (gray line), and the region where the experimentally resolved TTTA dimer should be located (orange line and the corresponding orange dot in the projected map). (d) Same regions are analyzed for TDPDTA for comparison reasons. Note that the TDPDTA experimental geometry lies in the FM boundary (purple line). (b and e) Effective orbital analysis (OO) compared to the J_{AB} values for the four slices in (a and d). The empty symbols refer to the orbital overlap OO data, while the full symbols refer to J_{AB} data. (c and f) Zoom of the region with the smallest orbital overlap OO, ranging from 1.4 Å and 2.6 Å.

observed, *i.e.* there are fewer geometrical arrangements presenting FM coupling. Unexpectedly, a dissimilar magneto-structural correlation map is obtained by analyzing the TDPDTA compound (Fig. 5.6d). Herein, there is no presence of a FM area at all. To further investigate this trend, we have employed the orbital analysis as defined by Kahn's model[46]. Accordingly, the FM J_{AB} interactions are favored when the orbital overlap (OO) between the SOMO of the two radicals tends to be zero. Fig. 5.7 reports the orbital overlap analysis carried out for TTTA and TDPDTA

compounds. Note that, for each magneto-structural correlation map, we analyzed four slices along d_{SL} at fixed chosen d_{IP} distances, using as reference TTTA. The d_{IP} values (2.5, 3.1, 3.22 and 3.5 Å) were chosen to sample the most FM region, the FM boundary ($J_{\text{AB}} = 0 \text{ cm}^{-1}$), the moderate AFM region, and the region where the experimentally resolved dimer should be located. For TTTA, the corresponding OO values are nearly zero when the J_{AB} interaction between the radicals becomes FM (see the blue line for $d_{\text{IP}} = 2.5 \text{ Å}$ in Fig. 5.7a). In fact, the zero-orbital overlap correlates with the interstitial disposition of the p orbitals of the two radicals within the dimer (see blue squares in Fig. 5.7b and c). This structural arrangement enhances the FM coupling between TTTA radicals. Contrarily, the same slice at 2.5 Å for TDPDTA displays OO values clearly different from zero (see blue squares in Fig. 5.7e and f). Thus, it agrees with J_{AB} being AFM in all d_{SL} ranges of sampled values (see the blue line in Fig. 5.7d). Indeed, one can realize that, in the case of TDPDTA, the degree of delocalization of the spin density on the fused rings to the DTA-moiety is larger than in the other three compounds. As a result, non-zero orbital overlap (OO) within the dimer is present in a much wider geometrical range and, in turn, any possibility for FM coupling is quenched. The second cross-section of the TTTA material at $d_{\text{IP}} = 3.20 \text{ Å}$ and $d_{\text{SL}} = 1.0\text{-}3.5 \text{ Å}$ (see Fig. 5.7a, purple line) explores the boundary of the FM area. It clearly shows the tendency of OO to present non-negligible values (purple circles in Fig. 5.7b and c). The corresponding J_{AB} interactions, instead, still display some ferromagnetism, in agreement with our assumption that the OO rather than being accurate is only one of the contributions (direct exchange and spin polarization are other factors that determine the total coupling). For the sake of comparison with TTTA, the same slice of interest is taken in the TDPDTA case (purple circles in Fig. 5.7e and f). Correspondingly, the OO analysis exhibits significant values, describing AFM spin couplings. Last but not least, always using the TTTA compound as our reference, we have also considered the cross-sections just outside the FM area ($d_{\text{IP}} = 3.30 \text{ Å}$, $d_{\text{SL}} = 1.0\text{-}3.5 \text{ Å}$) and in accordance with the position of the experimentally X-ray resolved TTTA dimer ($d_{\text{IP}} = 3.47 \text{ Å}$, $d_{\text{SL}} = 1.32 \text{ Å}$) (see grey and orange lines in Fig. 5.7a). Additionally, the position of the experimental structure of the TDPDTA dimer was also considered ($d_{\text{IP}} = 3.305 \text{ Å}$, $d_{\text{SL}} = 2.97 \text{ Å}$ in Fig. 5.7d). The representation of the zoom in Fig. 5.7c and f shows the clear tendency of the orbital overlap towards larger values, both in TTTA (grey triangles) and TDPDTA (orange diamonds) cases, and hence towards larger AFM interactions. For TDPDTA, a further analysis was carried out. The geometry of the Model I dimer ($J_{\text{AB}} = -89 \text{ cm}^{-1}$) that most resembles the experimental structure ($J_{\text{AB}} = -70 \text{ cm}^{-1}$) was selected. Then, we applied successive longitudinal translations ($d_{\text{LG}} = 0.1 \text{ Å}$) between both TDPDTA monomers, generating 10 different configurations (see Appendix A.5). Specifically, one of the generated configurations (Conf. #4) presents

$d_{IP} = 3.28 \text{ \AA}$, $d_{SL} = 3.05 \text{ \AA}$ and $J_{Conf \#4}^{UB3LYP} = -69.6 \text{ cm}^{-1}$, which are very close to the experimental available data (see Table 5.1), although internal distortions and degrees of freedom have been neglected in these newly generated models. Strikingly, the longitudinal translation accomplishes TDPDTA radical arrangements that show FM coupling ($J_{Conf \#9}^{UB3LYP} = 5.0 \text{ cm}^{-1}$ and $J_{Conf \#10}^{UB3LYP} = 15.6 \text{ cm}^{-1}$). This suggests that the magneto-structural correlation map of TDPDTA must also account for longitudinal translation (d_{LG}) as well as interplanar distance (d_{IP}) and degree of slippage (d_{SL}) to capture the complete behavior. Although the concept of orbital overlap is not new[47, 48] and has inspired many groups[49], the qualitative description obtained by the orbital overlap analysis portrays remarkably well the behavior of PDTA and TDPDTA systems, and their magnetic variability as a function of the geometrical configuration. All these results are consistent with Kahn's qualitative model, and agree with other recent studies[50–52]. It thus follows that these conclusions can be exploited to drive the synthesis of compounds whose crystal packing avoids the orbital overlap and favors the FM coupling. The previous magneto-structural correlation maps for TTTA, PDTA and 4-NCBDTA undeniably show a series of radical arrangements resulting in FM coupling. Why is it that there are very few examples of DTA-based ferromagnets in nature? The answer turned out to be very simple since it relies on the energetic cost for reaching the FM area. The Interaction Energy Map (IEM) was computed for the four DTA systems (see Appendix A.6). Note that the contour of the FM and weak AFM regions ($-5 \text{ cm}^{-1} < J_{AB} < 0 \text{ cm}^{-1}$) is delimited by dashed black lines on each IEM. The only exception is the IEM for TDPDTA, since it does not present any FM sector of interest (due to the lack of screening longitudinal translations). The IEM for TTTA shows that the most FM region ($+50 \text{ cm}^{-1} < J_{AB} < +150 \text{ cm}^{-1}$) has a prohibitive energetic cost, which explains why TTTA experimentally shows no large FM coupling interactions. In fact, more than 20 kcal mol^{-1} are needed to reach this specific area. The energetically forbidden region involves an interplanar distance $d_{IP} < 3.0 \text{ \AA}$, while the energetically reachable region encompasses $3.25 \text{ \AA} < d_{IP} < 3.00 \text{ \AA}$ and $2.3 \text{ \AA} < d_{SL} < 1.8 \text{ \AA}$. The latter region partly contains the FM region of interest ($0 \text{ cm}^{-1} < J_{AB} < +10 \text{ cm}^{-1}$), which means that the adequate DTA-radical under certain conditions and specific geometrical conformation can result in a FM configuration. The main result obtained from the OO analysis coupled with the magneto-structural correlation maps is the fact that geometrical rather than electronic factors are apparently responsible for the planar DTA-based materials to exhibit FM coupling interactions. The larger and more extended the structure is, the higher the probability is to have π - π interactions and, in turn, the higher the possibility of non-zero orbital overlap and quenching of the FM interactions. This important result is also confirmed in the next section by means of a set of *in silico* experiments performed to discriminate the role of the geometrical and

electronic facets of the DTA-based compounds.

5.2.3 Electronic vs. structural contributions

Three independent computational experiments are conducted aiming at distinguishing between the structural and the electronic contribution of the different DTA-substituents. Prior to these computations, the magnetically most important J_{AB} data obtained using the corresponding dimers of the experimentally X-ray resolved HT phases were collected. From each DTA-radical dimer, the interplanar distance (d_{IP}), degree of slippage (d_{SL}), and nitrogen · · nitrogen distance (N* · · N*) were extracted, and the J_{AB} interaction computed (see data under “Experimental data” in Table 5.1). Note that the HT-4-NCBDTA material is the one presenting the strongest AFM coupling ($J_{AB} = -342 \text{ cm}^{-1}$, at 300 K), while HT-TDPDTA is the one showing the weakest AFM interaction ($J_{AB} = -69 \text{ cm}^{-1}$, at 293 K). For the first computational experiment, Model I was built as explained in subsection 5.2.2, with d_{IP} , d_{SL} , and N*-N* distance that best resemble the experimentally X-ray resolved pairs of DTA-radicals for TTTA, PDTA, 4-NCBDTA and TDPDTA (note that it was selected among 3250 different radical pair configurations). In order to prove the adequacy of these *in silico* models, we calculated the J_{AB} values (see data referred to as “Model I” in Table 5.1). Direct comparison between the J_{AB} values calculated using the experimental X-ray data and the models in the Model I section shows good agreement for each Model I system. Since we are using an isolated pair of radicals, neglecting the inner degrees of freedom of the crystal introduces a certain error in Model I, but the results are reassuring in order to be confident about the conclusions we have previously drawn for DTA-based magnets from the computed magneto-structural correlation maps. The goal of the second and third computational tests is to discretize the electronic influence of the DTA-substituent with respect to the geometrical configuration of the dimer. The second set of models is designed to determine the electronic effect on the magnetic coupling. For this purpose, we used the DTA-skeleton of the X-ray HT-TTTA pair of radicals (first column in Table 5.1 under “Experimental data”), and replaced the 1,2,5-thiadiazole substituent by the corresponding substituents of the PDTA, 4-NCBDTA and TDPDTA systems (see Fig. 5.1c and d). We refer to these TTTA-modified models as Model II. The resulting J_{AB} spin coupling interactions (see “Model II” in Table 5.1) are practically the same as the J_{AB} value computed using the TTTA dimer itself extracted directly from the X-ray data at 298 K ($J_{AB} = -135 \text{ cm}^{-1}$). This points out that the DTA-substituents do not directly influence the coupling between the radicals, and that the differences observed for the four systems have another origin. Finally, the third model isolates the geometrical factor in the magnetic coupling of the pair of radicals. Among the 3250 configurations gen-

erated in the magneto-structural correlation map for the TTTA system, we select the four arrangements of two TTTA radicals that are geometrically closest to the experimental X-ray crystal structure of PDTA, 4-NCBDTA and TDPDTA (see geometrical data in Table 5.1 for "Model III"). The J_{AB} value for the four clusters without any further change, *i.e.* maintaining the 1,2,5-thiadiazole substituent, is then calculated. In contrast to the calculations for Model II, we do observe important changes in the magnetic coupling. In fact the four J_{AB} interactions calculated using Model III are in rather good agreement with those for the four systems extracted from experiment. Hence, it can be concluded that the substituent- induced crystal packing effects are responsible for the different magnetic behavior of the four systems.

Table 5.1: Interplanar distance (d_{IP}), degree of slippage (d_{SL}), nitrogen··nitrogen distance ($N^*··N^*$), and J_{AB} coupling (cm^{-1}) for TTTA, PDTA, 4-NCBDTA and TD-PDTA. Experimental data: experimentally X-ray resolved pairs of DTA-radicals, and computed J_{AB} values at the experimental geometry. Model I: model built from each DTA-radical under investigation, computed J_{AB} values, and the corresponding errors. Model II: HT phase TTTA dimer at 298 K modified so as to include PDTA, 4-NCBDTA and TDPDTA substituents, computed J_{AB} values, and errors. Model III: TTTA Model I dimer that best reproduces the HT radical pair arrangement of PDTA, 4-NCBDTA and TDPDTA, computed J_{AB} values, and errors. Energies are all evaluated at the UB3LYP/6-31+G(d) level. Note that the error is calculated assuming the J_{AB} value corresponding to the experimentally resolved dimer is the reference value (#Exp), while the corresponding values derived from the models III are the theoretical ones (#Theo): %ERR = ABS [(#Exp-#Theo)/#Theo]×100.

Parameters	J_{AB}/cm^{-1}			
	TTTA (298K)	PDTA (323K)	4-NCBDTA (300K)	TDPDTA (293K)
Experimental Data				
d_{IP} -X-ray (Å)	3.46	3.44	3.52	3.31
d_{SL} -X-ray (Å)	1.34	1.40	1.01	2.97
$N^*·N^*$ (Å)	3.71	3.72	3.67	4.45
J_{AB} (cm^{-1})	-135	-111	-342	-69
Model I				
d_{IP} -TM (Å)	3.46	3.43	3.52	3.27
d_{SL} -TM (Å)	1.31	1.43	1.01	3.03
$N^*·N^*$ (Å)	3.69	3.71	3.66	4.46
J_{AB} (cm^{-1})	-142	-147	-295	-89
Error %	5.44	32.57	13.73	27.14
Model II				
d_{IP} -TM (Å)		3.46	3.46	3.46
d_{SL} -TM (Å)		1.34	1.34	1.34
$N^*·N^*$ (Å)		3.71	3.71	3.71
J_{AB} (cm^{-1})		-135	-125	-135
Error %		0.16	7.46	0.04
Model III				
d_{IP} -TM (Å)		3.43	3.51	3.32
d_{SL} -TM (Å)		1.43	1.03	2.92
$N^*·N^*$ (Å)		3.71	3.66	4.42
J_{AB} (cm^{-1})		-99	-295	-72
Error %		10.67	13.83	4.42

5.3 Conclusions

The characterization of a subset of four compounds of the DTA-based family is used to evaluate the nature of the spin coupling and the magnetic properties of bistable and spin switchable systems. TTTA, PDTA, and TDPDTA combine the spin transition with the crystallographic phase transition, leading to a bistable system in which two stable phases (namely LT and HT) coexist within the same range of temperatures. For comparison purposes, we also studied the 4-NCBDTA system, which just presents spin transition. The four DTA-based radicals present a common planar geometry, and have the tendency to dimerize at low temperature, quenching the possibility for FM intermolecular interactions in the LT-phase. Yet the corresponding HT-phases are all paramagnetic, providing a more interesting scenario since there is possibility of FM spin coupling. Although the magnetic topology of all four DTA-based compounds is 3D, for simulation purposes they can be considered to form 1D isolated π -stacking AFM chains because the largest and dominant J_{AB} s extend along the π -stacking direction of the planar DTA-radicals. The simulated $\chi T(T)$ magnetic susceptibility curves of PDTA and TDPDTA show that the LT-phases are magnetically silent, whereas the HT-phases are paramagnetic, in agreement with experiment[12, 17]. Some numerical discrepancies between the experimental and calculated $\chi T(T)$ data are believed to be due to the presence of thermal fluctuations, in analogy to what was established in previous studies on TTTA and 4-NCBDTA compounds[36, 39]. The distinctive macroscopic magnetic response of the HT-phase of each DTA-based compound originates in the different microscopic intra π -stacking J_{AB} radical interactions, which are found to be driven mostly by the changes in interplanar distance and degree of lateral slippage, according to the interpretation of a series of magneto-structural correlation maps. Thus, for TTTA, PDTA and 4-NCBDTA, it has been possible to predict the region where the FM interactions should appear, *i.e.* whose geometrical disposition enhances FM spin coupling. The presence of the FM regions and their location on the magneto-structural correlation maps has been qualitatively explained by the orbital overlap analysis based on Kahn's model[46]. We concluded that only an interstitial orbital arrangement can prevent the orbitals of the two radicals from overlap, and favor FM coupling. Apparently, large fused-ring DTA-compounds (e.g. TDPDTA) are not suitable candidates to display ferromagnetism, because they increase the probability of having π - π orbital overlap at any reasonable relative orientation of the two radicals and, thus, preclude FM coupling. Besides, from our study it is clear that the electronic component introduced by the different DTA-substituents does not influence the value of the J_{AB} spin coupling interaction itself. Instead, the DTA-substituents structurally affect the radical packing and, in turn, the J_{AB} magnetic coupling. These magneto-structural maps could no

doubt become a practical tool to help experimentalists to design more stable and efficient purely organic radicals with ferromagnetic properties in the solid state. The magneto-structural correlation maps as a function of the substituents of the DTA-moiety enable the static FM fingerprint region to be highlighted, which is observed to be very expensive in terms of interaction energy. Indeed, this is the reason why there are very few examples of DTA-based ferromagnets in nature. All these results give further insight into the behavior of the DTA-radical-based magnets, as a step forward for the experimental counterpart in this research field to be able to design compounds with tailored properties.

5.4 Acknowledgements

MD, JRA and JJN acknowledge “Ministerio de Economía, Industria y Competitividad” (MICINN) for projects MAT2014-54025-P and CTQ2017-87773-P/AEI/FEDER, UE, and Catalan DURSI for projects 2014SGR1422 and 2017SGR348. CdG acknowledges CTQ2017- 83566-P/AEI/FEDER, UE (MICINN), 2017SGR629 (DURSI) and COST Action ECOST-Bio CM1305 (EU). TF acknowledges funding from the European Union Horizon 2020 research and innovation programme under the Marie Curie Skłodowska-Curie grant agreement no. 642294.

Bibliography

- [1] J. S. Miller, *Advanced Materials* **2002**, *14*, 1105–1110.
- [2] R. G. Hicks, *Organic & biomolecular chemistry* **2007**, *5*, 1321–1338.
- [3] R. Hicks, *Stable radicals: fundamentals and applied aspects of odd-electron compounds*, John Wiley & Sons, **2011**.
- [4] P. M. Lahti in *Advances in Physical Organic Chemistry*, Vol. 45, Elsevier, **2011**, pp. 93–169.
- [5] I. Ratera, J. Veciana, *Chemical Society Reviews* **2012**, *41*, 303–349.
- [6] M. Halcrow, *Spin-crossover materials: properties and applications*, John Wiley & Sons, **2013**.
- [7] D. Bates, C. M. Robertson, A. A. Leitch, P. A. Dube, R. T. Oakley, *Journal of the American Chemical Society* **2018**, *140*, 3846–3849.
- [8] K. E. Preuss, *Coordination Chemistry Reviews* **2015**, *289*, 49–61.
- [9] J. M. Rawson, A. Alberola, A. Whalley, *Journal of Materials Chemistry* **2006**, *16*, 2560–2575.
- [10] K. Lekin, S. M. Winter, L. E. Downie, X. Bao, J. S. Tse, S. Desgreniers, R. A. Secco, P. A. Dube, R. T. Oakley, *Journal of the American Chemical Society* **2010**, *132*, 16212–16224.
- [11] H. Phan, K. Lekin, S. M. Winter, R. T. Oakley, M. Shatruk, *Journal of the American Chemical Society* **2013**, *135*, 15674–15677.
- [12] T. Barclay, A. Cordes, N. George, R. Haddon, M. Itkis, M. Mashuta, R. Oakley, G. Patenaude, R. Reed, J. Richardson, et al., *Journal of the American Chemical Society* **1998**, *120*, 352–360.
- [13] H. Matsuzaki, W. Fujita, K. Awaga, H. Okamoto, *Physical review letters* **2003**, *91*, 017403.
- [14] G. Wolmershäuser, R. Johann, *Angewandte Chemie International Edition in English* **1989**, *28*, 920–921.

- [15] G. D. McManus, J. M. Rawson, N. Feeder, J. van Duijn, E. J. McInnes, J. J. Novoa, R. Burriel, F. Palacio, P. Oliete, *Journal of Materials Chemistry* **2001**, *11*, 1992–2003.
- [16] W. Fujita, K. Awaga, *Science* **1999**, *286*, 261–262.
- [17] J. L. Brusso, O. P. Clements, R. C. Haddon, M. E. Itkis, A. A. Leitch, R. T. Oakley, R. W. Reed, J. F. Richardson, *Journal of the American Chemical Society* **2004**, *126*, 8256–8265.
- [18] A. Alberola, R. J. Collis, S. M. Humphrey, R. J. Less, J. M. Rawson, *Inorganic chemistry* **2006**, *45*, 1903–1905.
- [19] M. Deumal, M. Bearpark, J. Novoa, M. Robb, *The Journal of Physical Chemistry A* **2002**, *106*, 1299–1315.
- [20] C. S. Clarke, J. Jornet-Somoza, F. Mota, J. J. Novoa, M. Deumal, *Journal of the American Chemical Society* **2010**, *132*, 17817–17830.
- [21] M. Deumal, F. Mota, M. J. Bearpark, M. A. Robb, J. J. Novoa, *Molecular Physics* **2006**, *104*, 857–873.
- [22] S. Vela, A. Sopena, J. Ribas-Arino, J. J. Novoa, M. Deumal, *Chemistry—A European Journal* **2014**, *20*, 7083–7090.
- [23] S. Vela, M. Deumal, J. Ribas-Arino, J. J. Novoa, *Inorganic chemistry* **2012**, *51*, 8646–8648.
- [24] M. Fumanal, M. Deumal, *Physical Chemistry Chemical Physics* **2016**, *18*, 20738–20749.
- [25] S. Vela, M. Fumanal, M. Deumal, *Dalton Transactions* **2015**, *44*, 608–614.
- [26] C. Herring, *GT Rado and H. Suhl* **1966**.
- [27] L. Noodleman, *The Journal of Chemical Physics* **1981**, *74*, 5737–5743.
- [28] L. Noodleman, E. R. Davidson, *Chemical physics* **1986**, *109*, 131–143.
- [29] B. AD, *Physical Review A: At. Mol. Opt. Phys.* **1988**, *38*, 131.
- [30] C. Lee, W. Yang, R. G. Parr, *Physical review B* **1988**, *37*, 785.
- [31] R. D. Gaussian09, Inc. Wallingford CT **2016**.
- [32] P. C. Hariharan, J. A. Pople, *Theoretica chimica acta* **1973**, *28*, 213–222.
- [33] M. M. Francl, W. J. Pietro, W. J. Hehre, J. S. Binkley, M. S. Gordon, D. J. DeFrees, J. A. Pople, *The Journal of Chemical Physics* **1982**, *77*, 3654–3665.
- [34] R. L. Carlin, *Magnetochemistry*, Springer Science & Business Media, **2012**.
- [35] R. Boča, *Theoretical foundations of molecular magnetism, Vol. 1*, Elsevier, **1999**.

- [36] S. Vela, F. Mota, M. Deumal, R. Suizu, Y. Shuku, A. Mizuno, K. Awaga, M. Shiga, J. J. Novoa, J. Ribas-Arino, *Nature communications* **2014**, *5*, 4411.
- [37] S. Vela, M. Reardon, C. E. Jakobsche, M. Turnbull, J. Ribas-Arino, J. Novoa, *Chemistry-A European Journal* **2017**, *23*, 3479–3489.
- [38] J. Novoa, M. Deumal, J. Jornet-Somoza, *Chemical Society Reviews* **2011**, *40*, 3182–3212.
- [39] S. Vela, M. Deumal, M. Shiga, J. J. Novoa, J. Ribas-Arino, *Chemical science* **2015**, *6*, 2371–2381.
- [40] A. A. Leitch, X. Yu, S. M. Winter, R. A. Secco, P. A. Dube, R. T. Oakley, *Journal of the American Chemical Society* **2009**, *131*, 7112–7125.
- [41] J.-B. Rota, B. Le Guennic, V. Robert, *Inorganic chemistry* **2010**, *49*, 1230–1237.
- [42] M. Verot, N. Bréfuel, J. Pécaut, C. Train, V. Robert, *Chemistry–An Asian Journal* **2012**, *7*, 380–386.
- [43] J. Miralles, J.-P. Daudey, R. Caballol, *Chemical physics letters* **1992**, *198*, 555–562.
- [44] J. Miralles, O. Castell, R. Caballol, J.-P. Malrieu, *Chemical physics* **1993**, *172*, 33–43.
- [45] C. De Graaf, R. Broer, *Magnetic Interactions in Molecules and Solids*, Springer, **2016**.
- [46] O. Kahn, *VCH Publishers Inc.(USA)* **1993**, 393.
- [47] P. J. Hay, J. C. Thibeault, R. Hoffmann, *Journal of the American Chemical Society* **1975**, *97*, 4884–4899.
- [48] O. Kahn, B. Briat, *Journal of the Chemical Society Faraday Transactions 2: Molecular and Chemical Physics* **1976**, *72*, 268–281.
- [49] N. Onofrio, J.-M. Mouesca, *The Journal of Physical Chemistry A* **2010**, *114*, 6149–6156.
- [50] J. Ribas-Ariño, J. J. Novoa, J. S. Miller, *Journal of Materials Chemistry* **2006**, *16*, 2600–2611.
- [51] S. C. van der Lubbe, C. Fonseca Guerra, *Chemistry–A European Journal* **2017**, *23*, 10249–10253.
- [52] J. Zapata-Rivera, D. Maynau, C. J. Calzado, *Chemistry of Materials* **2017**, *29*, 4317–4329.

Chapter 6

New Mechanism for Triggering Spin Transition in Dithiazolyl-based Materials

The use of *state-of-the-art* comprehensive techniques allowed us to explore and to outline the key features of the selected set of DTA-based[1–11] materials, as reported in the previous chapters. To complete the investigation of these materials with such unique features, we hereby present the study of the dynamical properties of the DTA compounds. First we introduce the models employed in the study and their corresponding results from the structural optimizations. Then, we present the results from the AIMD[12] simulations, discussing how thermal motion affects the HT phases of the PDTA[13, 14] and TDPDTA[15], respectively.

By means of the dynamical and post-processing analysis of PDTA and TDPDTA, and keeping in mind the corresponding results gathered in the past for TTTA[16–24] and 4-NCBDTA[25], we propose a new stabilization mechanism, for the TDPDTA material, which depends on the longitudinal slippage (d_{LG}) between monomers. The presence of the (d_{LG}) parameter localizes the HT-TDPDTA polymorph on a minimum of the corresponding potential energy surface. The uniform weakly paramagnetic molecular arrangement of HT-TDPDTA is preserved, differently from the HT-DTA phases of other spin Peierls systems, which result as a consequence of the Pair-Exchange Dynamics process.

6.1 Introduction

Many essential aspects of the DTA-based molecular systems have been reported in the last years[1–11], with the ultimate intent to properly describe their key features and to put a firm point to their rationalization and possible practical application. The major achievements obtained so far are, in order of relevance, the i) decoupling of the static picture with respect to the dynamical one, being both essential for descriptive purposes, but necessarily to be treated separately[22, 26]; ii) the definition of the magnitude and propagation scheme of the magnetic interactions which permeate the molecular crystals[26], justifying the experimental evidence for the diamagnetic and weakly paramagnetic nature of the polymorphs following the hysteretic loop, particularly in case of the bistable systems[22–24, 26, 27]; iii) the underlying Pair-Exchange Dynamics (PED)[23] mechanism which appears to be a common feature among DTA-based compounds, providing solid evidence for the phase transition which in turn, based on the nature of the substituent attached to the DTA-ring, can lead to a *first-order* or *second-order* phase transition[25]. As highlighted in the comparative study between the prototype molecular TTTA system and the 4-NCBDTA by Vela and co-workers[25], the presence of a *first-order* or *second order* process can result in a phase transition featuring a hysteretic (*i.e.* TTTA) or non-hysteretic (*i.e.* 4-NCBDTA) response. The former process is indeed accompanied by the concomitant orientational re-arrangement and re-arrangement of the interstack contacts between the molecular units composing the crystal. The resulting LT and HT phases, in general, feature two different space groups. In the latter case, instead, the molecular columns preserve the orientation and space group during the heating and cooling process, presenting only a spin transition from a diamagnetic to a weakly paramagnetic configuration.

On the light of the study and interpretation of the dynamical properties of other DTA-based systems[23, 24], the investigation of PDTA and TDPDTA, with particular emphasis on their respective HT phases, highlighted the peculiar stability displayed by the TDPDTA material. By following the usual protocol, both PDTA and TDPDTA were first analyzed by employing the static analysis through the FPBU[26] methodology, as reported in the previous chapter. In particular, we proved that, while all the other systems considered, *i.e.* TTTA, PDTA and also the non-bistable 4-NCBDTA, are able to give birth to ferromagnetic (FM) couplings if the dimers are properly spatially arranged, on the contrary, for TDPDTA is not the case, while employing the same geometrical variables. These variables are the interplanar distance (d_{IP}) (see red dashed arrows in Figure 6.1a,b for the (a) LT- and (b)HT-PDTA cases, for instance) between two nearest-neighbouring molecules and their respec-

tive lateral slippage (d_{SL}) (see violet bars in Figure 6.1b). Conversely, in the case of TDPDTA, we figured out that an extra geometrical variable is needed to recover for the possibility to have FM molecular arrangements, namely the longitudinal slippage (d_{LG}) (see orange bars in Figure 6.2 for the (a) LT and (b) TDPDTA cases). The discovery of this additional variable to account in the post-processing analysis of the DTA-based systems has been a basic point to properly analyze and correctly interpret the thermal response of the TDPDTA system. At this moment, among the all set of systems considered, the TDPDTA is the only one to display the longitudinal displacement between monomers and within the columns, as shown by the orange bars in Figure 6.2, both in the LT and HT cases, respectively.

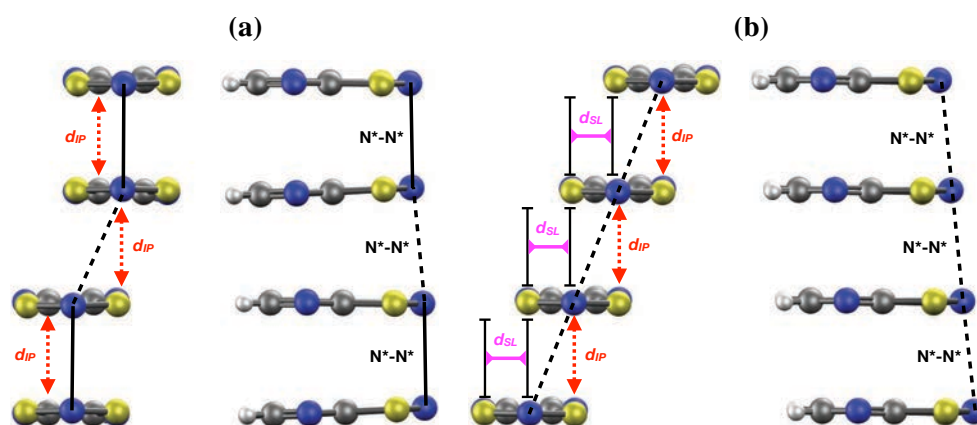


Figure 6.1: Key geometrical variables considered to describe the intermolecular arrangements between radicals in the (a) LT-PDPTA and (b) HT-PDPTA phases.

Another important aspect that comes out from the static analysis of the aforementioned compounds is the role of the substituents. We demonstrated that they do not play any relevant role in the definition of the magnetic interaction within the molecular compounds, but only in the general geometrical arrangement of the crystals. The whole set of electronic and magnetic properties follow the interaction of the DTA-rings through space, by means of long-bond “pancake” interactions[28, 29] As a consequence of the previous studies[27], at this point we aim at contextualize the PDPTA and the TDPDTA systems behavior within the interpretative picture given for the other DTA-based materials. In particular, to we want to understand the mechanism of spin transition in the two system aforementioned, as well as the stability of the HT-TDPDTA phase.

The purpose of this chapter is to present the direct comparison between the dy-

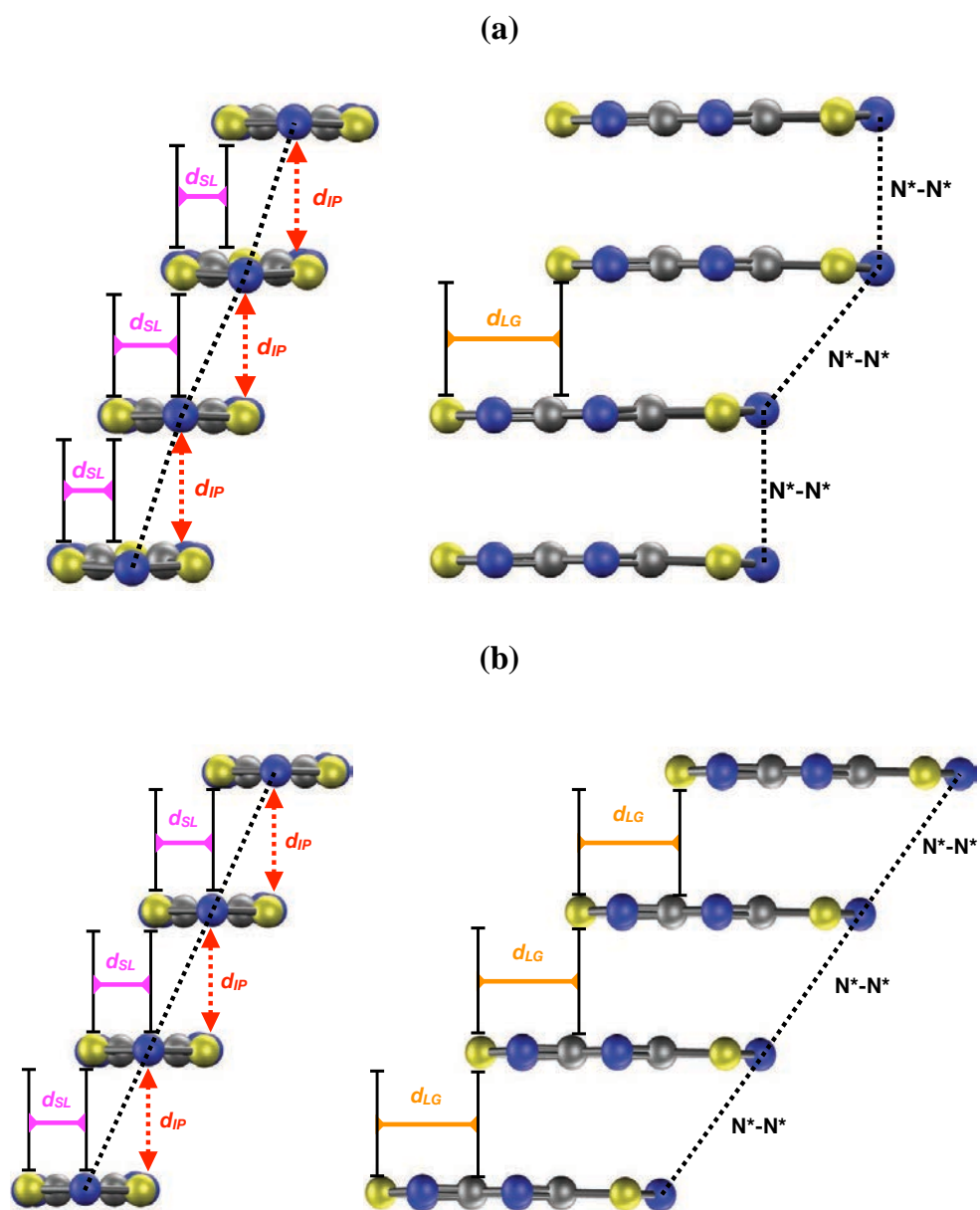


Figure 6.2: Key geometrical variables considered to describe the intermolecular arrangements between radicals in the (a) LT-TDPDTA and (b) HT-TDPDTA phases.

namical results of the PDTA and TDPDTA systems, keeping as a reference the ones concerning the prototype TTTA[23, 24]. Firstly, the models employed in this study are shown, followed by their variable-cell and geometry optimizations. Secondly, the results from the AIMD simulations are reported, in particular for the HT phases of the two materials. Then, the data from the AIMD simulations are complemented with i) the comparison between the average structures computed for the room temperature AIMD simulations, ii) the comparison between the experimental and computed thermal ellipsoids, both in the LT and HT cases, iii) the histogram distribution analysis of the N*-N* distances between adjacent radicals, iv) the study of the topology of the PES for PDTA and TDPDTA, respectively, by means of the Nudged Elastic Band (NEB) method, for isolated columns, extracted from the respective AIMD trajectories.

Here the concept of the Pair-Exchange Dynamics (PED) mechanism is reviewed. The PED concept was established in previous works[23] while characterizing TTTA and 4-NCBDTA compounds, from a dynamical point of view. The purpose of this paragraph is to present to the reader the general features of the PED process, which is considered to be the dominant dynamical process characterizing the majority of the DTA-based compounds, in order to later introduce, in the Results section, the new stabilization mechanism found to operate in the TDPDTA material.

The illustrative cartoon of the PED mechanism is reported in Figure 6.3. The PED process is associated to the dynamical interconversion of the molecular arrangements, within the crystalline system, between two degenerate states separated by an energy barrier. The two degenerate minima, hereafter referred as $(\cdots A-A \cdots A-A \cdots)_n$ and $(-A \cdots A-A \cdots A-A)_n$, respectively, present an alternated structure featuring π -eclipsed dimers alternated to π -shifted dimers. The transition point, instead, is found to belong to a uniform stack propagation of the molecular disposition, $(\cdots A \cdots A \cdots A \cdots A \cdots)_n$, where the previous dimers are no longer available. The PED occurs in the picoseconds timescale regime. The key points gathered along with the analysis of the TTTA[25] and 4-NCBDTA[25] are the fact that the PED is a i) function of the temperature, and ii) it is independent from the presence or absence of an hysteretic loop, as shown by TTTA and 4-NCBDTA, respectively. By increasing the temperature, the interchange between the two minima in the LT phase becomes subsequently more and more probable. The uniform stack propagation configuration between the two degenerate LT minima is found when the system has enough energy to overcome the barrier separating the two. The experimentally resolved HT phase displays the same uniform trend like the intermediate structure found between the two LT minima. Hence, it follows that the HT structure can be the di-

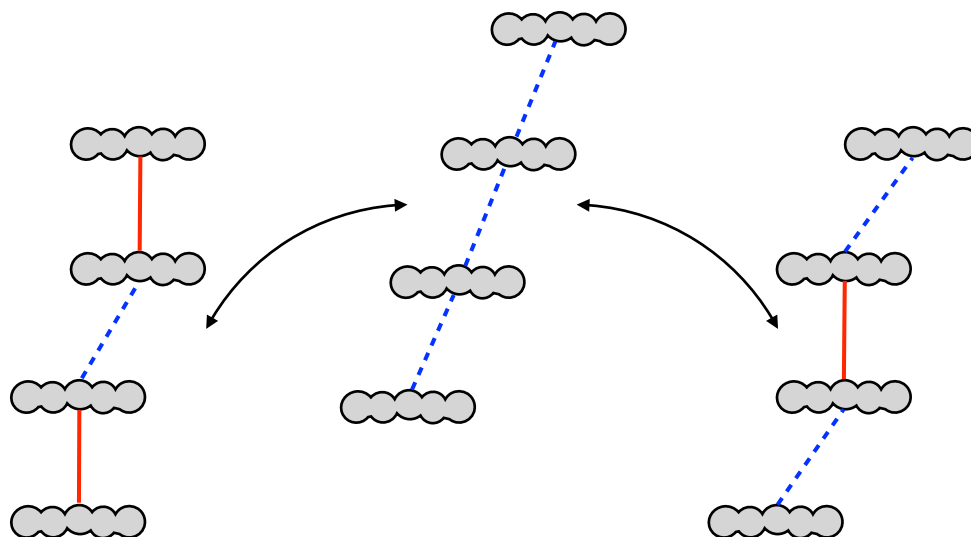


Figure 6.3: Illustrative scheme of the Pair-Exchange Dynamics process.

rect result of the PED mechanism which induces the LT polymorph to move to the HT polymorph[23]. If the activation of the PED is coupled with the variation of the interstack contacts between molecules, then we refer to a first-order phase transition. The LT and HT phases also belong to different space groups, in general terms. Whereas, if the transition between dimerized and regular stack within the crystal is coupled with the PED process, but the space group of the crystal is preserved, then we refer to a second-order phase transition.

Together with the characterization of the PED process, another important question concerning the stability of the HT phases of TTTA and 4-NCBDTA was also answered. In fact, by employing the detailed study of the thermodynamical properties of the systems, and, in particular, accounting for the Helmholtz free energy[25], it was found that the stability of the HT phases derived from the fact that the system is not a minimum on the PES but on the Free Energy Surface (FES), as a result of entropy contributions.

The TDPDTA material is peculiar because it does not strictly fall in descriptions above, neither for the *first-order* phase transition nor for the *second-order* one, but instead it can illustratively be placed somewhere in the middle, this because it presents a hysteretic loop with a transition occurring between the LT→HT polymorphs, while

keeping the same space group in both.

In the following sections the TDPDTA system is introduced, as well as the PDTA materials, reporting not only the experimental features by also illustrating with a comparative scheme where the respective susceptibility curves are placed, highlighting step by step the interesting nature of these compounds and why it plays a new key role in the panorama of the DTA-based compounds.

6.2 Susceptibility Curves

The first aspect of the TDPDTA compound that immediately captured our attention, way before studying it through the static analysis[27], as reported in Chapter 5, is its experimental characterization reported by Oakley and co-workers[15]. As a brief recap, the TDPDTA material is a three member ring molecular system (see the molecular structure in Figure 6.4 associated to the red curve), presenting an unpaired electron that is formally located on the nitrogen belonging to the DTA-ring. By X-ray diffraction refinement, two different polymorphs were resolved, one at 150 K, corresponding to the low temperature system (LT) and the other at 293 K, corresponding to the high temperature (HT) one. These two polymorphs both belong to the triclinic space group $P\bar{1}$. The hysteretic behavior appears in the range between $T_C^\downarrow = 50$ K and $T_C^\uparrow = 200$ K. The LT polymorphs present an even alternation of *quasi*- π -eclipsed dimers and π -shifted ones. The HT phase, instead, displays a uniform trend arrangement like the one presented also by the other systems analyzed[13–25]. The magnetic coupling computed between two radicals, hereby labelled as A and B, throughout the Heisenberg Hamiltonian formulation $J_{AB} = E_{BS} - E_T^1$ is equal to *ca.* -69 cm^{-1} in the case of the HT-TDPDTA, while in the case of the LT phase, the coupling is $J_{AB} = -781$ cm^{-1} . This is quite surprising compared to the order of magnitude of the couplings computed[27] or indirectly derived by experimentalist fitting the proper models[15] to the susceptibility curve of the other DTA-based systems. In general, the J_{AB} values associated to the LT and HT structures are one order of magnitude bigger (cf. $J_{AB}^{\text{HT-PDTA}} = -110$ cm^{-1} *vs.* $J_{AB}^{\text{HT-TDPDTA}} = -69$ cm^{-1}) compared to the one found in the TDPDTA case.

¹ From the Heisenberg Hamiltonian $\hat{H} = -2 J_{AB} \hat{S}_A \cdot \hat{S}_B$ for a pair of A and B radicals, the J_{AB} value is computed as the energy difference between biradical open-shell singlet S and triplet T states, $\Delta E^{\text{S-T}} = E^{\text{S}} - E^{\text{T}} = 2J_{AB}$. Open-shell singlet systems can localize alpha spin density and beta spin density on different radicals. In our case, within the DFT framework, once the broken symmetry approximation (BS) is applied, the energy difference can be expressed as: $E^{\text{S}} - E^{\text{T}} = 2(E_{\text{BS}}^{\text{S}} - E^{\text{T}})/(1 + S_{\text{ab}})$. The resulting S_{ab} overlap between the alpha (a) SOMO and the beta (b) SOMO is very small, which means that the orbitals are localized on each of the two radicals. This leads to $S_{\text{ab}} \approx 0$. As a conclusion $J_{AB} = E_{\text{BS}}^{\text{S}} - E^{\text{T}}$.

Differently from the system above is the PDTA[13, 14, 27], which resembles in almost every aspect the prototype molecular compound TTTA. PDTA shows a very extended hysteresis loop, encompassing room temperature. Moreover, both the LT and HT polymorphs have been resolved at 323 K, allowing for a direct comparison of the structural differences. The LT phase is diamagnetic, where the geometrical arrangement is a column stack of π -eclipsed dimers alternated to π -shifted ones. The π -eclipsed dimers present a strong antiferromagnetic coupling of the order of magnitude of *ca.* -1600 cm^{-1} . This strong coupling prevents the possibility for the crystal to display any FM coupling in the LT configuration. Conversely, the HT phase instead is proved to be weakly paramagnetic[13, 14], also by means of the theoretical evidence[27], as we reported in the previous chapter. An important note about the uniform stacks of the HT phases, as Vela and co-workers[23] pointed out, is that they belong, *a priori*, to an average structure that appears as a consequence of the molecular exchange between two possibly minima belonging to the potential energy surface of the system investigated. This last point will be corroborated by the analysis of the AIMD simulations reported in the Results section. In general, temperature can be used as external stimuli to trigger the phase transition in molecular compounds, switching between two states of the same material, and two different magnetic states. In this sense, it was already speculated to use DTA-based materials as molecular switches[30] to be employed in devices for storing data[22, 23, 27], or to create highly accurate sensors. However, many intrinsic difficulties, mainly correlated to the controlling aspects of the PED mechanism, reported to be responsible for the switching, are still to be bypassed. Before facing the practical aspects and possible advantages of the use of DTA-based systems, more fundamental issues need to be sorted out.

By comparing the two respective susceptibility curves of PDTA (in black) and TDPDTA (in red), as reported in Figure 6.4, it can be seen that a hysteresis loop is present in both cases, but it appears at very different temperature ranges, without overlapping. While in the PDTA case the transition between the LT phase to the HT is abrupt and neat, synonym of a sudden structural re-arrangement whose interconversion involves both the spin and space group change (*i.e. first-order transition*), in the case of the TDPDTA, instead, it is smoother. The hysteretic TDPDTA curve shows a large extent of the loop, comprising a range of *ca.* 150 K, whereas the PDTA curve is *ca.* half of the TDPDTA one. Note that, while in the case of PDTA an important geometrical re-arrangement occurs, involving the columns of radicals that ends up in a different space group featuring a herringbone disposition, in the case of the TDPDTA the space group is preserved, maintaining the stacking direction.

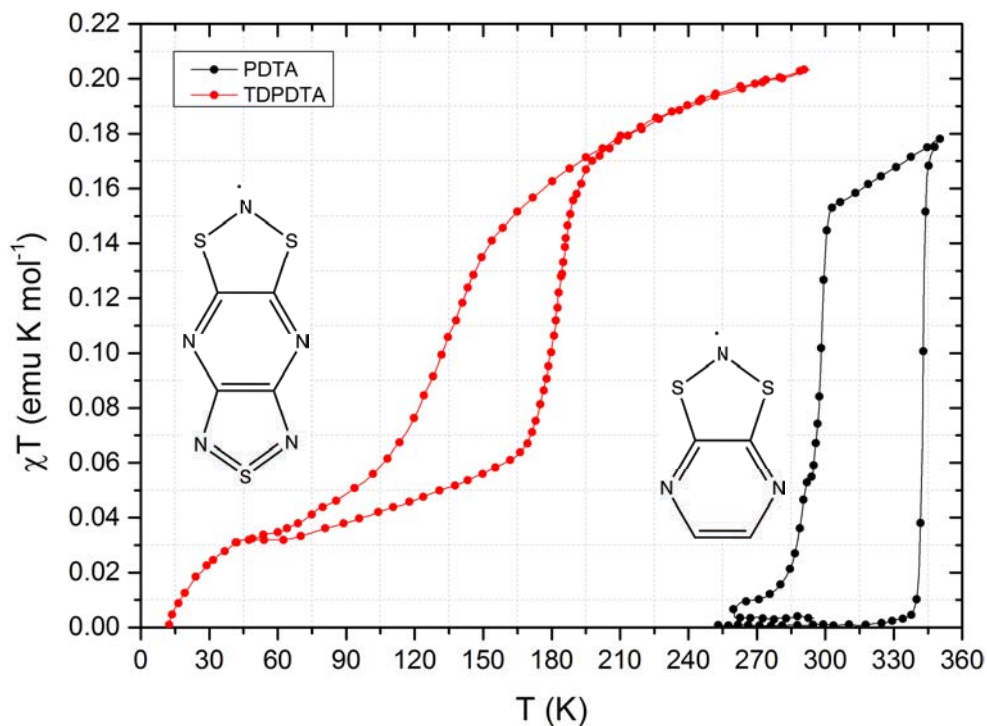


Figure 6.4: Susceptibility curves of PDTA (black) and TDPDTA (red), put in comparison.

6.3 Structural Models

The interpretation and study of material properties follows the proper selection of representative structural models. These have to comprise the correct arrangement of the molecular units in space, but also, throughout the proper approximations, the correct set of forces acting on the system. In this case, because we are dealing with organic molecules, we have to account for the proper long-bond interactions through the Grimme dispersions[31, 32] functions.

Structurally, both in the case of PDTA and TDPDTA polymorphs, LT and HT respectively, we made use of supercells composed of eight molecular columns, each of which formed by a stack of four molecules, as reported in Figures 6.5 and 6.6. In Figure 6.5 the geometry of the molecular columns for the LT-PDTA phase (Figure 6.5a,b) and for the HT-PDTA (Figure 6.5c,d) are displayed. The LT structure features

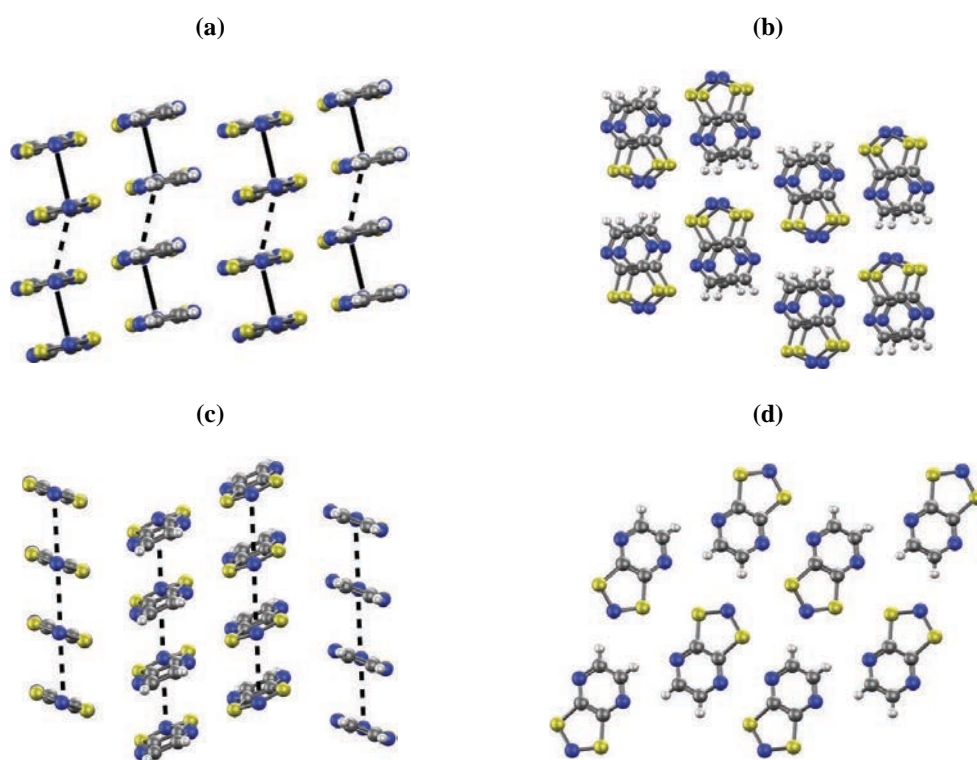


Figure 6.5: Side-view and top-view of the PDTA supercells for the a)-b) LT and c)-d) HT polymorphs.

the aforementioned alternated arrangement between dimerized configurations with shifted ones, while the HT polymorph presents the classical uniform trend, characteristic of the HT DTA-based phases (see Figure 6.5c,d). It can be noticed that in the LT case, the structure presents a lateral displacement, which in turn coincides with the shifted configuration, highlighted by the dashed line (see Figure 6.5a,b). Figure 6.6, instead, summarizes the structural characteristics of the supercells employed in the study of the LT-TDPDTA (Figure 6.6a,b) and HT (Figure 6.6c,d), respectively. Note that, in this case, the general disposition and orientation of the molecules and columns is the same in both the polymorphic phases. The LT structure, in particular, features a peculiar arrangement along the stacking direction of the columns which places itself between a dimerized configuration and a uniform distribution, the last one well caught by the HT phase instead. Note also that the displacement that appears in the LT phase occurs along the longitudinal axis of the molecule, differently

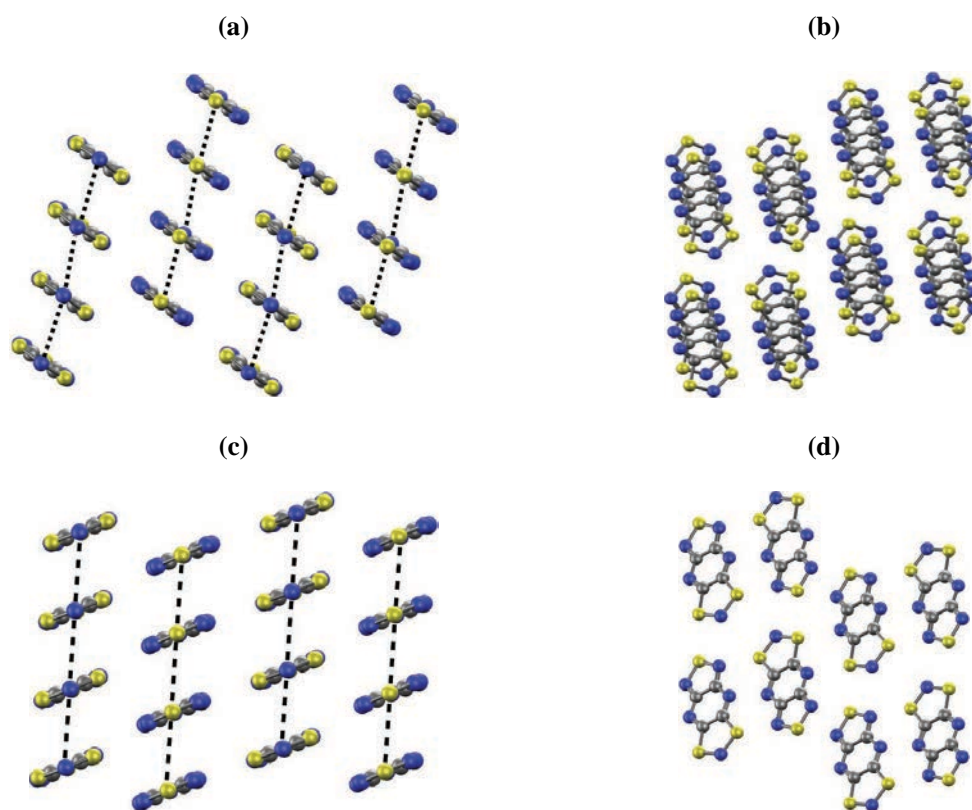


Figure 6.6: Side-view and top-view of the TDPDTA supercells for the a)-b) LT and c)-d) HT polymorphs. The distances within the columns in the LT phase (a) present a different dashed line with respect to the HT phase. This is done with the purpose to highlight the intermediate nature of the structure, which is found to lay in between a dimerized (LT) and a regular structure (HT).

from the LT-PDPA case (see Figure 6.5a,b). These systems are the background on top of which we built the research here presented. Because of the lack of experimental data from the original papers[13–15] describing the resolved structures of PDPA and TDPDTA, in order to explore how the thermal motion affects the behavior of each compound at different temperatures, we obtained several intermediate structures by interpolating the X-ray cell parameters of the HT phases with respect to the cell parameters of the same cells optimized by means of the variable-cell (VC) algorithm at 0 K, as reported in the scheme of Figure 6.7a,b.

Our attention is focused on the HT polymorphs, being the one presenting both structural and magnetic flexibility with respect to the LT phases. The corresponding intermediate structures are first geometrically optimized, keeping frozen the interpolated cell parameters, and allowing for the molecules, from the respective HT models (Figures 6.5c,d and 6.6c,d), to “adapt” to the new cell. Once the geometry optimizations of the intermediate HT structures are completed, then the resulting systems are employed in the AIMD simulation.

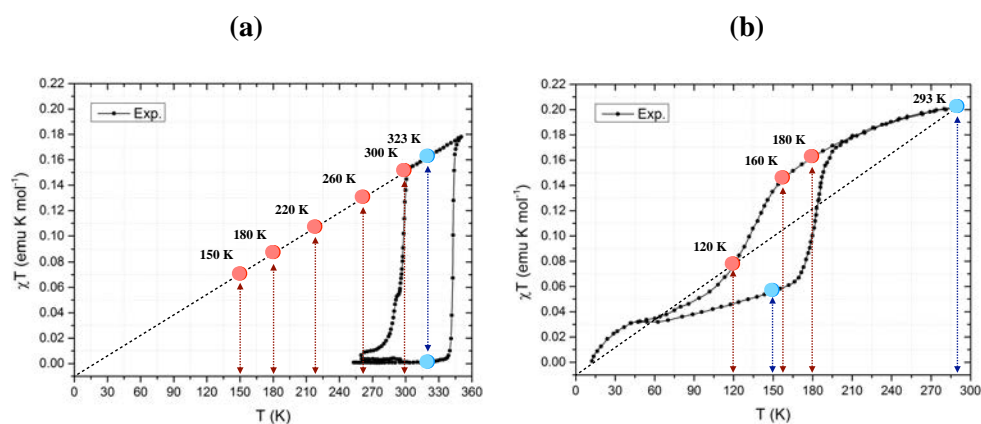


Figure 6.7: Schemes showing the corresponding (a) PDTA and (b) TDPDTA structures obtained at different temperature by means of a linear interpolation of the experimental HT polymorphs cell parameters with the ones obtained by VC optimization with the ones obtained by VC optimization at 0 K. In (a) the experimental LT and HT structures have been resolved at the same temperature (blue dot at 323 K) while in (b) the LT phase has been resolved at 150 K and the HT one at 293 K (see the respective blue dots position). The red rectangles, both in (a) and (b), display the structures obtained by interpolations.

Each AIMD simulation employed in this study consists of two steps, namely the i) equilibration and the ii) production run. The equilibration is essential to adapt the system coming from the geometry optimization to the fictitious thermal bath. In all cases reported here, the systems are equilibrated for *ca.* 3 ps. Once completed, it follows the production run. The goal of step ii) is to collect statistically relevant samples of the structures at a specific temperature. Each production run is carried out for 10 ps. By means of the AIMD technique, the HT-PDTA polymorph is investigated at 150, 180, 200, 220, 260, 300 and 323 K (X-ray resolved), respectively, while the LT-PDTA phase is studied at 323 K (see Figure 6.7a). In the case of HT-TDPDTA instead, the structures at 160, 180 and 293 K (X-ray resolved) are studied, and at

150K in the case of the LT polymorph (see Figure 6.7b).

6.4 Computational Information

The optimization of the supercells described above is performed by means of the CP2K[33] code at DFT level, using the PBE functional[34] within the spin unrestricted formalism. Norm-conserving Goedecker-Teter-Hutter[35–37] pseudopotentials are used for all atomic species in combination with the Gaussian TZV2P basis set[38] and a Γ -point sampling of the Brillouin zone. A 600 Ry cutoff is used for truncating the plane waves expansion. The Grimme’s D3 dispersion potential[32] is added to the Kohn-Sham DFT energy in order to account for the van der Waals interactions between molecules. The same setting applies also in the case of the AIMD simulations, within the canonical ensemble (NVT). The Canonical Sampling through Velocity Rescaling (CSVR) stochastic thermostat is employed[39]. A timestep of 1fs was used.

The calculations of the energy profiles are performed by means of the NEB algorithm (version 6.2), part of the Quantum Espresso suite[40] (version 5.4.0) at DFT level. The ultrasoft pseudopotentials at PBE[34] level with kinetic energy cutoff at 35 Ry and Γ -point sampling of the Brillouin zone are used to describe the atomic species, within the spin unrestricted formalism. The Grimme’s D2[31] dispersion functions are also used for taking into account the van der Waals interactions between molecules. The calculation of the NEB energy profile for the PDTA system counts 12 intermediate images, 14 in the case of TDPDTA.

The PES scans are computed at the same level of theory like the NEB, employing ultrasoft pseudopotentials at PBE[34] level with kinetic energy cutoff of 70 Ry for truncating the plane waves expansion, adding the Grimme’s D2[31] dispersion corrections and Γ -point sampling of the Brillouin zone, within the spin unrestricted formalism.

Finally, the single point NEVPT2[41–43] calculations (see Figure 6.20a,b), are performed by means of the Orca[44] code (version 4.0.1.2), using an active space of 10 π -electrons and 10 π -orbitals for the PDTA case, with the Karlsruhe basis set def2-TZVP[45–48] from Ahlrichs and co-workers. In the case of the TDPDTA instead, an active space of 14 π -electrons and 14 π -orbitals was employed, with the same basis set. The configurations investigated at NEVPT2 level are the one sampled from the PES scans for the PDTA and TDPDTA systems, firstly evaluated at DFT level.

6.5 Results

6.5.1 Optimum Configuration of HT-PDTA and HT-TDPDTA Polymorphs

The results for the optimized HT polymorphs of the PDTA and TDPDTA systems are here presented and discussed. The variable-cell optimized structures, in both cases, are hereafter referred as HT-0. Whereas, the optimized geometry of a single column, extracted from the HT-0 structures, respectively, are denoted as HT-0-ISO. The VC and geometry optimizations are performed within the periodic boundary conditions (PBC) framework.

First, the HT-PDTA structure, resolved experimentally at 323 K (see Figure 6.8a), is displayed. The molecular disposition of the π -slipped dimers follows a uniform trend. The interplanar distance (d_{IP}) between two neighboring molecules is 3.42 Å (highlighted by the red double-head-dashed arrows), while the N*-N* distance is 3.72 Å (highlighted by black dashed bars). The lateral slippage (d_{SL}) between first-neighbors is equal to 1.34 Å (highlighted by violet bars). The variable-cell optimization of the structure at 0 K, see Figure 6.8b, converges towards a dimerized structure. Note that an alteration between π - π eclipsed and π -shifted dimers appears, resembling the LT-X-ray structure (see Figure 6.5a). Like in the case of HT-TTTA-0[23], the HT-0 structure from PDTA preserves the general column orientation, whereas in the LT phase a herringbone geometry is found. This indicates that the HT-0 structure obtained from the optimizing process is most likely a metastable configuration, laying in between the two X-ray resolved polymorphs, and not yet experimentally detected. The monoclinic space group from the X-ray configuration is also kept in the HT-0 structure. The cohesive energies per molecule are $-23.3 \text{ kcal mol}^{-1}$ and $-24.1 \text{ kcal mol}^{-1}$ in the HT-0 and LT-0 systems, respectively.

Note the slight distortion appearing in the HT-0 column as reported in Figure 6.8b. The d_{IP} distance between the dimerized molecules is 3.13 Å, while the shifted central one is 3.45 Å. If the column HT-0 (Figure 6.8b), extracted from the VC-optimized supercell, is further geometrically optimized, the distortions found in Figure 8b disappear, confirming the non-negligible effect that the surrounding columns have (see Figure 6.8c). The conformations resulting both in the HT-0 and HT-0-ISO models are in agreement with the molecular disposition depicted by the LT conformation.

In the HT-TDPDTA (X-ray) structure, resolved at 293 K, molecules pile up in a uniform arrangement. The interplanar distance (d_{IP}) is equal to 3.35 Å (highlighted by

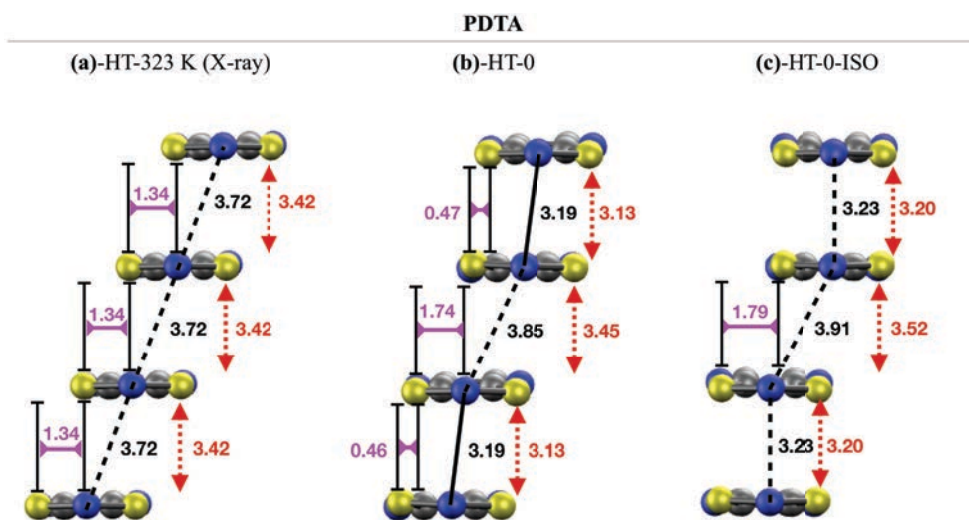


Figure 6.8: Sampled columns from the HT-PDPA (323 K) as resolved by (a) X-ray, (b) VC optimized at 0 K and (c) the VC optimized column geometrically optimized.

the red double-head-dashed arrows), while the d_{SL} slippage is equal to 1.60 Å (highlighted by violet bars). In this case, the presence of the longitudinal displacement (d_{LG}), as already introduced above, has to be considered. The d_{LG} parameter is equal to 2.42 Å (see orange-bars on the lateral view of Figure 6.9a). Finally, the N*-N* distance is 4.45 Å (highlighted by black dashed bars). By means of the VC-optimization procedure, the structure as reported in Figure 6.9b is obtained. The resulting structure at 0K is very close to the experimentally resolved one at 293 K. Note a tiny compression of the geometrical parameters, d_{IP} , d_{SL} , d_{LG} and N*-N*. Nevertheless, the structure is practically frozen (see Figure 6.9b). The cohesive energies per molecule are $-28.7 \text{ kcal mol}^{-1}$ and $-29.4 \text{ kcal mol}^{-1}$ in the HT-0 and LT-0 systems, respectively.

This is the very first indication that something is preventing the molecules to dimerize, like in the PDPA case (see Figure 6.8b,c). The space group of the system is also preserved, suggesting for the possibility that the HT-TDPDPA phase, as resolved by X-ray, is not any longer a metastable configuration like in the other cases[23, 25], resulting from a fast inter-conversion between two degenerate states belonging to a minimum of the PES, but, somewhat, it belongs to a minimum of the PES. If this mechanism is confirmed, it might be one possible way to overcome the dimerization process that, usually, is seen as an irreversible degrading mechanism appearing in organic molecular magnets.

The final analysis of the VC-optimized HT-TDPDTA configuration is pursued by geometrically optimizing, like in the PDTA case (see Figure 6.8c), the column extracted from the HT-0 supercell (see Figure 6.9b), to obtain the HT-0-ISO configuration (see Figure 6.9c). Removing the effect of the surrounding columns allows for a certain degree of relaxation of the atomic positions. In fact, it can be noticed that, while the d_{IP} variable is practically the same like in the X-ray configuration, the d_{SL} parameter, in general terms, increases ($d_{IP}^{X\text{-ray}} = 1.60 \text{ \AA} \rightarrow d_{IP}^{HT\text{-}0\text{-}ISO} = 1.72 \text{ \AA}$), while, on the contrary, the longitudinal slippage d_{LG} shrinks. This modest re-arrangement is simply induced by the absence of the steric effect from the other columns. What is significant, again, is the stability displayed by the system, also in this case. The molecular alignment, as well as the geometrical parameters investigated, confirms the tendency of the system to preserve the spatial configuration that is not subjected to any change.

TDPDTA

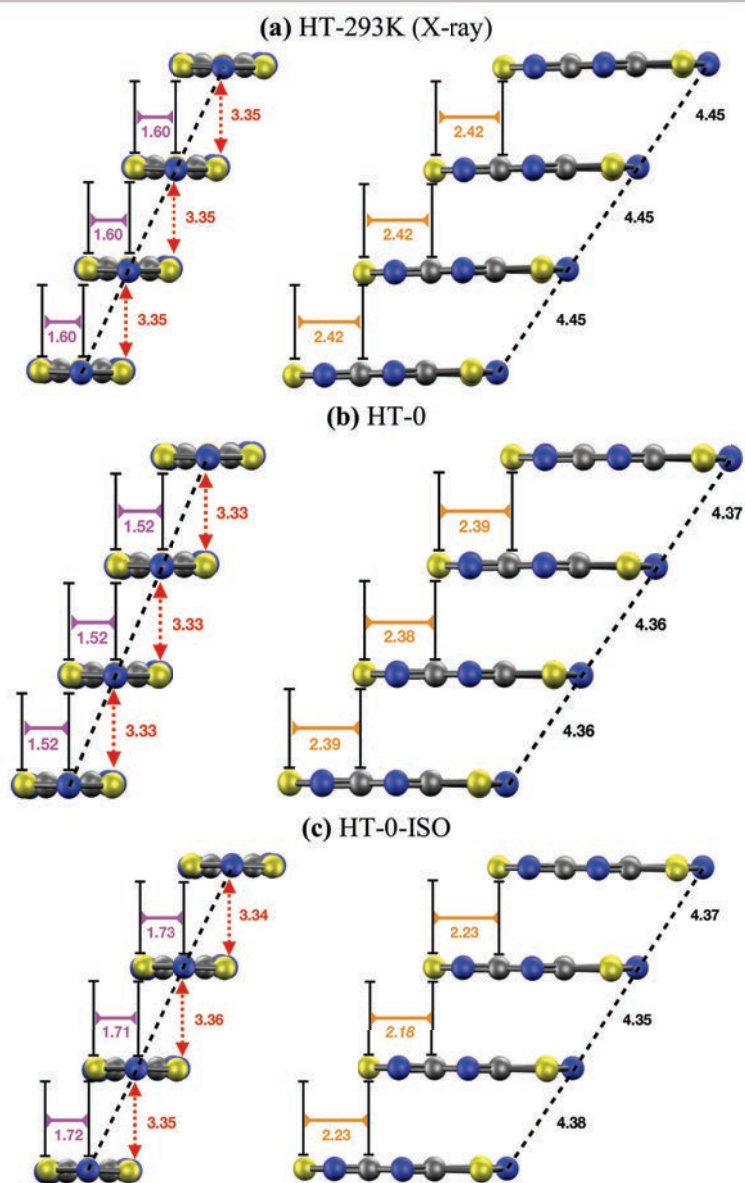


Figure 6.9: Sampled columns from the HT-TDPDTA (293 K) as resolved by (a) X-ray, (b) VC optimized at 0 K and (c) the VC optimized column geometrically optimized

6.6 Dynamics of the HT Polymorphs at Room Temperature

In the next section, the results from the AIMD simulations are reported, comparing the HT-TDPDTA (293 K) and HT-PDTA (300 K) cases, respectively, to better understand the stability of the regular arrangement of the π -stacks detected in the HT-TDPDTA phase. First, the monitoring of the N*-N* distances for a set of three dimers contained in a representative column of the two materials is shown and commented, also describing the average structures of the systems obtained from the respective trajectories. Next, by comparing the experimentally detected thermal ellipsoids with respect to the computed ones from the HT trajectories, in both cases, both the models and the theoretical approach employed are validated. The discussion is then complemented by the computation of the N*-N* distances distribution analysis, a valid tool to detect the presence of the PED mechanism[23]. The PED mechanism is then re-interpreted by taking advantage of the NEB algorithm, which allows to guess an optimal energy path connecting, in the PDTA case, the two structural minima and to estimate the energy barrier separating them. We conclude the discussion of our results by presenting a series of PES scans, developed to define the role of the three geometrical displacements introduced above, d_{IP} , d_{SL} and d_{LG} respectively.

6.6.1 Average Structures Configuration

The dynamical analysis of the HT-PDTA (300 K) and HT-TDPDTA (293 K) starts by analyzing how the trajectories of the selected systems evolve under the same conditions. In this case, this is done by monitoring the N*-N* distances between dimers (see Figure 6.10b,c). Both in the LT-PDTA and LT-TDPDTA cases, the respective trajectories behave as expected, preserving the π -dimers. This is indeed a clear indication of the fact that the LT structures both are to a minimum of their respective PESs. The situation evolves in a more interesting way by focusing on the HT phases, instead, as reported in the Figure 6.10a,c.

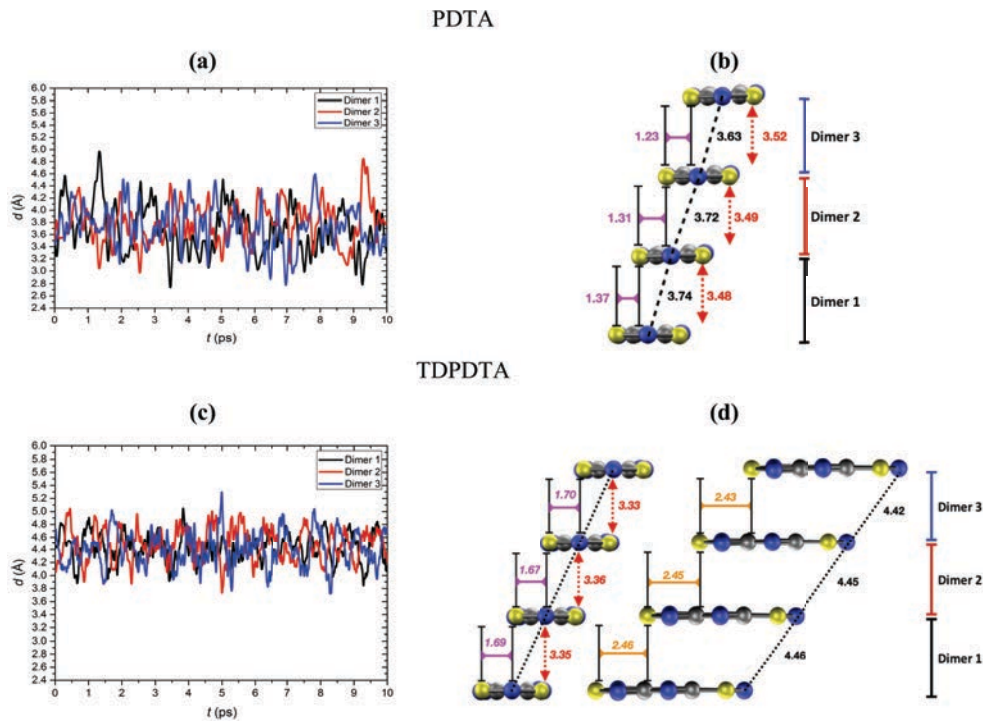


Figure 6.10: Trajectories for (a) PDTA and (b) TDPDTA, and their average structure.

First of all, one column from the supercell used in the simulation is selected. Then, by means of a visualization software like, in this case, VMD[49], the N^*-N^* distances between the dimers selected are tracked, to depict their evolution in time along with the trajectory (see Figure 6.10a,c respectively). The direct analysis of these profiles can give a glimpse of the general response of the system to temperature.

The HT-PDTA (300 K) material displays a trajectory evolution as expected by a system featuring the PED mechanism[23]. In fact, the distinctive periodic switching of the distances of the upper and lower dimers in the column (highlighted in black and blue colors, respectively in Figure 6.10b), with respect to the middle one (red bar), is recognized. The average distances associated to the geometrical variables are also reported. In particular, the N^*-N^* distance is *ca.* 3.70 Å (black dashed line), the d_{IP} *ca.* 3.50 Å (red dashed double-head arrows) and finally d_{SL} is *ca.* 1.30 Å (violet bar). The average distances are very close to the experimentally resolved ones (see Figure 6.8a), corroborating what already has been reported in the case

of TTTA[16–24, 27] and 4-NCBDTA[25]; thus the HT-PDTA (300 K) structure is the result of the continuum fast interchange between the two LT degenerate states $(-A \cdots A-A \cdots A-)_n$ and $(\cdots A-A \cdots A-A \cdots)_n$. At higher temperatures, only the exchange rate between the degenerate configurations increases. An additional amount of energy will inevitably induce the decomposition of the crystal, and, in turn, the loss of its physical-chemical properties.

The HT-TDPDTA (293 K) system, see Figure 6.10c,d, displays a similar trajectory to the HT-PDTA (300 K) one, but at a closer look, the N^*-N^* oscillations present smaller amplitudes compared to the PDTA case. It looks like an exchange is still occurring, but this time there is no swap between the distances associated with dimer 1 and dimer 2. The system does not undergo any dimerization process, maintaining in average, instead, the interplanar distance d_{IP} , as reported in Figure 6.10d. Like in the previous case, the average supercell was computed by averaging the whole set of structures sampled along with trajectory in the production run. The match of the average structure with the experimentally resolved one is good, but this was somehow expected on view of the VC-optimization results aforementioned.

Of course, the semi-quantitative analysis reported until now of the AIMD systems is not sufficient on its own to confirm the absence of the PED mechanism in the TDPDTA material, as well as to confirm the presence of a new stabilization mechanism operating. To this purpose, in the next section, the thermal ellipsoids from the experimental characterization and computed from the AIMD trajectories are compared, being a more sensitive and reliable tool for assuring the presence of the PED process[23] as well as the quality of the *in silico* experiments.

6.6.2 Thermal Ellipsoids

To prove that our analysis is properly catching the correct picture of the systems under investigation, the experimental and computed thermal ellipsoids are compared. The computation of the ellipsoids from the trajectories of the two systems are performed by evaluating the Anisotropic Displacement Parameters (ADPs)[50]. For sake of comparison, the ADP values have been computed also for the LT-PDPA and LT-TDPDPA structure (see Figure 6.11a,c and Figure 6.12a,c for the PDPA and TDPDPA cases, respectively).

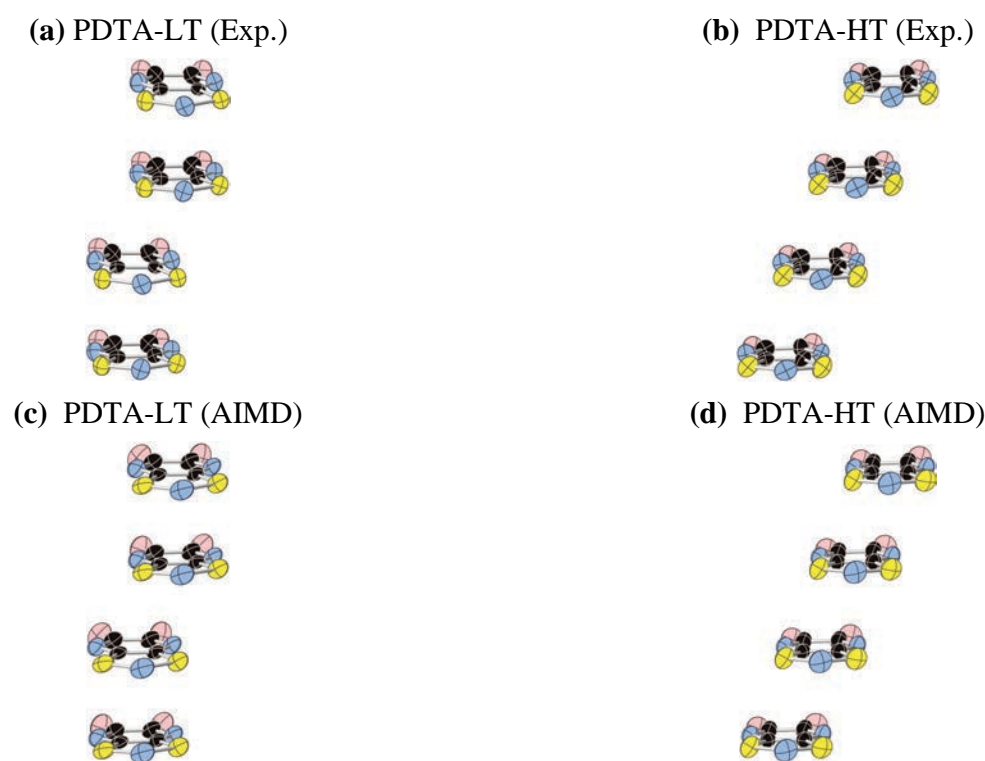


Figure 6.11: Experimental thermal ellipsoids, (a) and (b) for the LT-PDPA and HT-PDPA, respectively. In (c) and (d) instead the thermal ellipsoids computed from the AIMD trajectories, for the LT and HT phases, respectively.

The pictorial representation of the thermal ellipsoids derived from the AIMD simulations, both in the LT-PDPA and -HT configurations, are in very good agreement with respect to the experimental counterpart.

More specifically, by looking at the experimental and computed corresponding B_{150} parameters for the DTA-rings for both the systems, as reported in Table 6.1, it can be seen that the respective values are of the same order of magnitude. A systematic tiny overestimation tendency is found in the case of the LT^{AIMD} values. This might be a side effect of the time sampling of the structures in the trajectory file. Yet, the good representation is not undermined by it.

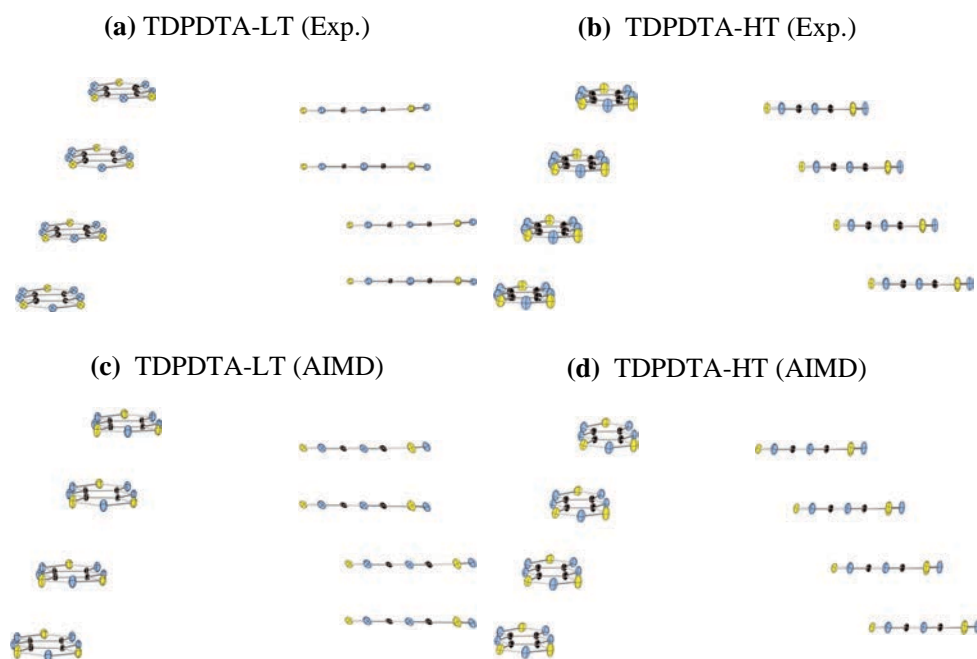
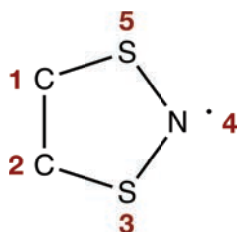


Figure 6.12: Experimental thermal ellipsoids, (a) and (b) for the LT-TDPDTA and HT, respectively. In (c) and (d) instead the thermal ellipsoids computed from the AIMD trajectories, for the LT and HT phases, respectively.

The TDPDTA thermal ellipsoids confirm our assumption that the system is particularly stable, also in the case of the HT phase (see Figure 6.12c,d). Looking at the values reported in Table 6.1, the computed ones match with the experimentally resolved values. The amplitudes of the thermal ellipsoids, as reported in the corresponding images, both in the experimental and computational cases, are indeed portraying a stable system presenting a feeble thermal motion. Also in this case a tiny discrepancy between experimental and computed values, for the HT phase, is found. The computed values are in fact smaller than the experimental ones, but again, they properly catch the dynamics of the system. Comparing the HT-PDTA

Table 6.1: Experimental and computed ADPs parameters for DTA rings of the HT-TTTA(298 K), LT-PDPA(150 K)/HT(300 K) and LT-TDPDPA(150 K)/HT(293 K) systems, respectively. Notice that the anisotropic U_{ij} parameters are reported referring to the stacking direction of the different system. In the case of TTTA and PDPA the column stacking is along y , *i.e.* U_{22} , while in the case of TDPDPA is along x , *i.e.* U_{11} . *Reference[23].

		1-C		2-C		3-S		4-N		5-S	
TTTA*	HT	U_{22}	B_{ISO}	U_{22}	B_{ISO}	U_{22}	B_{ISO}	U_{22}	B_{ISO}	U_{22}	B_{ISO}
		0.03	2.31	0.04	2.37	0.06	3.25	0.06	3.32	0.06	3.08
PDPA	LT ^{EXP.}	U_{22}	B_{ISO}	U_{22}	B_{ISO}	U_{22}	B_{ISO}	U_{22}	B_{ISO}	U_{22}	B_{ISO}
	LT ^{AIMD}	0.03	2.50	0.03	2.65	0.05	3.61	0.05	3.68	0.04	3.25
	HT ^{EXP.}	0.03	2.69	0.04	3.04	0.05	4.13	0.06	4.41	0.05	3.67
	HT ^{AIMD}	0.04	2.83	0.04	3.16	0.06	4.49	0.06	4.42	0.05	4.14
TDPDPA	LT ^{EXP.}	U_{11}	B_{ISO}	U_{11}	B_{ISO}	U_{11}	B_{ISO}	U_{11}	B_{ISO}	U_{11}	B_{ISO}
	LT ^{AIMD}	0.01	0.91	0.01	0.81	0.01	1.14	0.02	1.19	0.01	1.07
	HT ^{EXP.}	0.01	0.85	0.01	0.85	0.02	1.30	0.02	1.33	0.02	1.30
	HT ^{AIMD}	0.02	1.86	0.02	1.80	0.03	2.31	0.03	2.14	0.03	2.21
		0.02	1.21	0.02	1.21	0.02	1.67	0.02	1.66	0.02	1.66



and HT-TDPDPA values with respect to the HT-TTTA system in Table 6.1, it can be noticed that the DTA-ring of the PDPA system is the one presenting greater B_{ISO} values, hence displaying larger oscillations due to thermal motion with respect to TTTA and TDPDPA. The values reported refer to the anisotropic parameter U_{ij} along the stacking direction. In the case of TTTA and PDPA this is along the y axis, thus U_{22} , whereas in the case of TDPDPA it is along the x axis, hence U_{11} . The analysis of the thermal ellipsoids shows clearly the direct effect of the presence/absence of the

PED mechanism (see Figure 6.11b,d). The amplitude of the thermal ellipsoids is significantly increased when the PED process is active, like in the case of TTTA and PDTA, in line with the large oscillations associated to the N*-N* distances (see Figure 6.10a). Its absence, instead, produces considerably smaller oscillations, again matching the N*-N* distances profile reported in Figure 6.10b.

The set of data reported in Table 6.1, as well as the graphical visualization of the thermal ellipsoids associated with the structures investigated, demonstrate the high quality of the calculations performed with the intent to describe the molecular magnet systems. This is, in fact, an important achievement, that allows to safely interpret the results of our dynamical simulations.

6.6.3 Distances Distribution Analysis

The histogram representation of the N*-N* distances, performed along with the increasing of the temperature, as reported in Figure 6.13 for PDTA and in Figure 6.14 for TDPDTA, provides some additional information to the analysis of the thermal ellipsoids. Within the sampled column selected for the analysis, the three stacking dimers are identified, from bottom to top, as Dimer 1 (black), 2 (red) and 3 (blue) (see the legend in Figures 6.13 and 6.14). The monoclinic PDTA system at 150 K displays a bimodal character distribution of the N*-N* distances. In particular, the black and blue bars coinciding with the top and bottom dimers are located around the same maximum peak at *ca.* 3.4 Å, whereas the intermediate dimer (in red), finds its maximum around *ca.* 3.9 Å. In fact, only one of the two possible molecular distributions, thus $(-A \cdots A-A \cdots A)_n$ or $(\cdots A-A \cdots A-A \cdots)_n$, is caught, being the PED frozen.

The emerging of the bimodal distribution for the phase at 150 K, and its subsequent disappearance as temperature increases (see Figure 6.13b-e), exposes the change in the dynamics governing the crystal. The variation of the temperature to higher values is already displayed by the histogram reported for the PDTA system at 180 K, where the two distance probabilities begin to blend to form a unimodal distribution. This feature becomes more and more important as the temperature increases, as reported in Figures 6.13c,d. At 300 K the bimodal character reported for the structure at 150 K is no longer observed, now replaced by a unimodal distribution of the distances. The process portrayed is, actually, the activation of the PED mechanism. This is an important clue that, at this temperature, not only the structure presents a uniform trend propagation, but also it is the most probable[23], like also in the case for the TTTA material. The similarities between TTTA and PDTA, as extensively

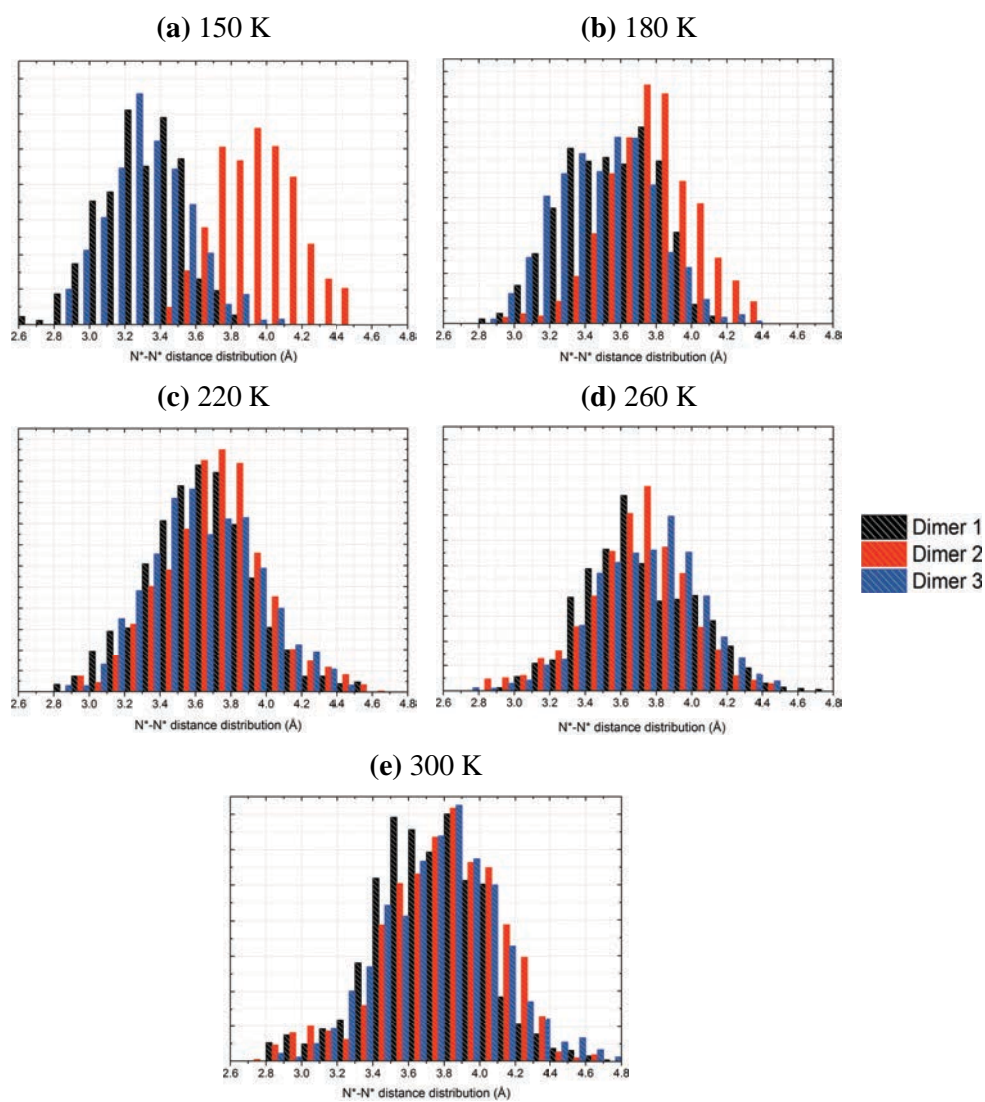


Figure 6.13: Distance distribution analysis of the HT-PDTA at (a) 150, (b) 180, (c) 220, (d) 260 and (e) 300 K, respectively.

reported and discussed, are the proof of concept that the same thermodynamical mechanism is also governing the stabilization in the HT-PDTA (300 K) phase. As a consequence, while the LT-PDTA polymorph belongs to a minimum of the PES, the HT phase, as shown by the transition from a bimodal to unimodal character with

the increasing of the temperature, belongs to a transition point. Thus, the stabilization featured by the HT-PDTA polymorph is a consequence of the fact that, like in TTTA, it is a minimum of the Free Energy Surface (FES)[23]. By applying the same analytical procedure to TDPDTA, see Figure 6.14a-c, a unimodal Gaussian distribution is found for the N*-N* distances, in all the three cases. The range of distances spanned by the N*-N* oscillations is much narrower compared to the one spanned by the PDTA system. These data are in agreement with the experimental thermal ellipsoids analysis, reported in Figure 6.12, proving that TDPDTA preserves its stability along with the scaling of the temperature.

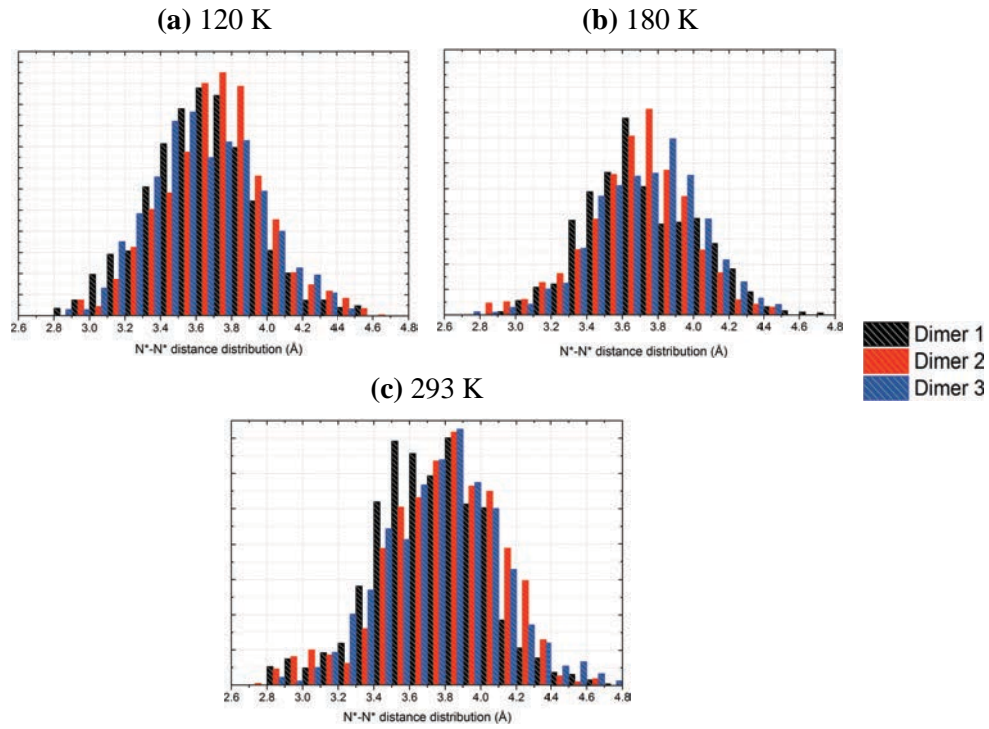


Figure 6.14: Distance distribution analysis of TDPDTA at 120, 160, 180 and 293 K, respectively

In conclusion, based on the collected data, the TDPDTA material is, for the moment, the only spin Peierls DTA-based material known not subjected to the Pair Exchange Dynamics mechanism. This is even more intriguing because it means that the spin transition, which is actually proved to occur as reported by the experimental susceptibility curve (see Figure 6.4), is actually generated by another kind of process.

Extra *in silico* experiments are performed and reported in the next sections to properly draw a conclusion on this peculiar system. The NEB algorithm is, afterwards, used with a three-fold purpose, thus i) to provide an estimate of the energy barrier, associated to the full activation of the PED process, separating the two degenerate minima in the PDTA, ii) to study the direct effect that the increase of the d_{IP} value has on the barrier, and finally iii) to estimate the energy barrier connecting the LT-TDPDTA column with a HT-TDPDTA one.

6.6.4 The Pair-Exchange Dynamic Mechanism *via* Nudged Elastic Band Algorithm

The PED mechanism found in the PDTA compound is further explored with the help of the NEB[40] computational technique within the periodic framework, by employing an isolated column model representative of the two degenerate LT-PDTA states (see Figure 6.15). Provided the two configurations, namely the $(-A \cdots A-A \cdots A-)_n$ and $(\cdots A-A \cdots A-A \cdots)_n$ molecular arrangements, fully optimized at the same level of theory as described above, the NEB algorithm provides a linear interpolation between them. The generated intermediate structures provide a reasonable guess for the energy barrier associated with the PED. In particular, the effect of the thermal expansion in the crystal is explored, by increasing the d_{IP} variable, starting from the HT-0 optimized configurations (see black-dotted line in Figure 6.15). The three d_{IP} values employed are in line with the values obtained upon optimization and from the X-ray structures.

The energy barrier associated with the intermediate uniform stack molecular arrangement, thus the HT polymorph, is *ca.* $5.4 \text{ kcal mol}^{-1}$ higher in energy with respect to the dimerized configurations. By expanding the d_{IP} variable from 3.42 \AA to 3.47 \AA (black-dotted line to blue-dotted line in Figure 6.15), therefore mimicking the thermal expansion effect, the energy barrier separating the two degenerate minima decreases to *ca.* $2.9 \text{ kcal mol}^{-1}$. This is also in line with the Probability Distribution Functions (PDF), reported by Vela and co-workers in the case of the prototype TTTA system, where the increase of the temperature induces an increase of the interplanar distances and, conversely, a decreases of the energy barrier in the double-well model[23].

The regular structure of the HT-TDPDTA polymorph, as already assessed previously, does not belong to a saddle point of the PES. As a consequence, the double-well model applied in the case of the PDTA compound is not appropriate for de-

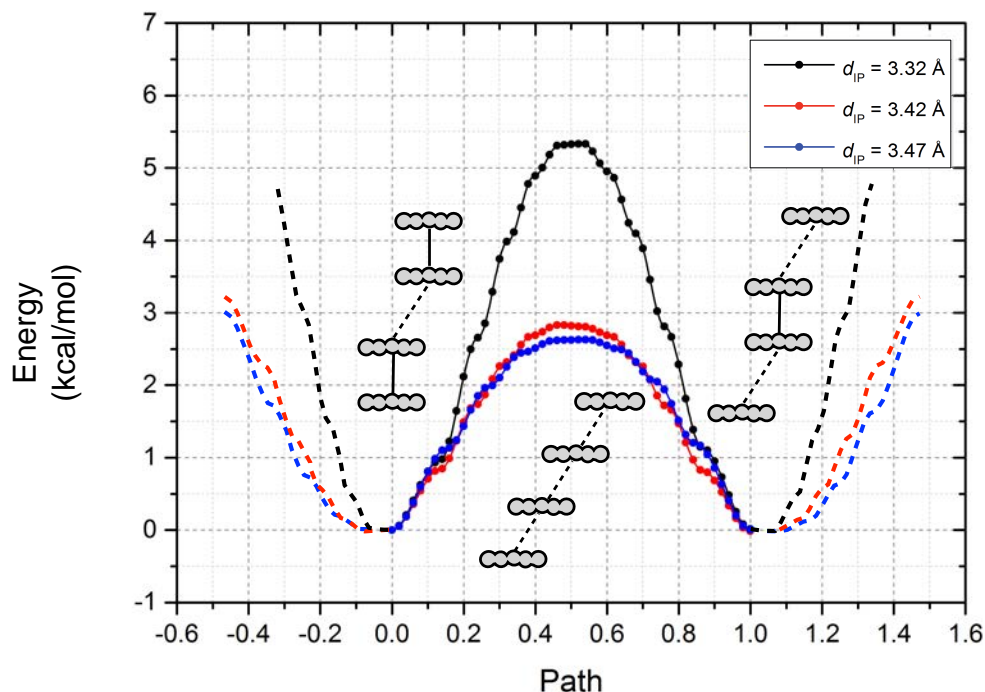


Figure 6.15: NEB profiles of the dimerized and regular structures of the PDTA. In particular, the effect of increasing the interplanar distance d_{IP} is investigated, from the $d_{IP} = 3.32 \text{ \AA}$, moving to $d_{IP} = 3.42 \text{ \AA}$ and $d_{IP} = 3.47 \text{ \AA}$. Note how, as the d_{IP} value increases, consequently the energy barrier associated with the intermediate structure decreases. The energy barrier separating the experimental structures is *ca.* $5.4 \text{ kcal mol}^{-1}$.

describing the three-member ring system. Yet, the NEB algorithm can be exploited to guess, in qualitative terms, the energy barrier connecting the two polymorphic phases of the TDPDTA material. The models employed in this analysis are also single columns, representative of the LT and HT molecular arrangements, respectively. The corresponding NEB profile, connecting the two isolated column arrangements of TDPDTA, is reported in Figure 6.16. Notice that the regular structure is less stable with respect to the dimerized one. The energy barrier separating the two configurations is *ca.* $7.5 \text{ kcal mol}^{-1}$.

These conclusions open a brand-new window in the DTA-based materials characterization panorama. TDPDTA, for the moment, is the only known material to display

bistability associated to two stable coexisting phases with two different magnetic responses and not featuring the PED mechanism. It is also the only DTA-based system to show a longitudinal slippage (d_{LG}) between neighboring molecular units. It can thus be concluded that the d_{LG} parameter is, *a priori*, responsible for the stabilization process undergone by TDPDTA. This might be a promising way to control and exploit the DTA-based materials.

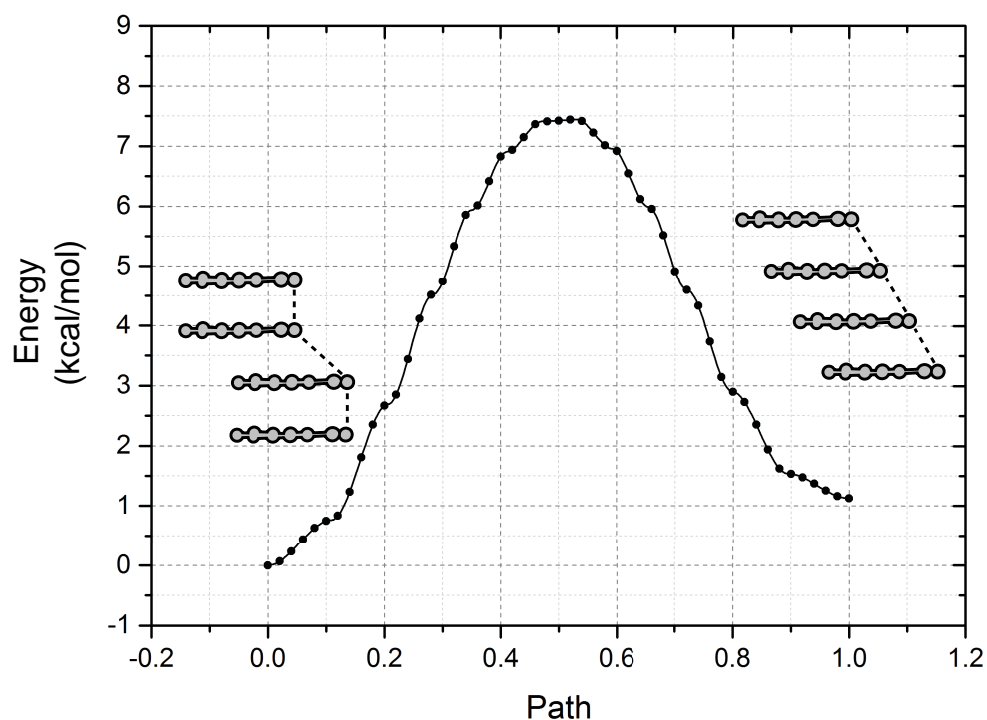


Figure 6.16: NEB of the TDPDTA system between a LT dimerize configuration (point = 0.0) and a HT regular one (point = 1.0).

6.6.5 Maps Scans: Evidence of the Role of the Longitudinal Slip-page

To corroborate the key role played by the longitudinal displacement (d_{LG}) in the stabilization mechanism acting on the regular TDPDTA system, a set of PES scans, based on dimer models within the periodic framework, are employed and thus presented in this section. The main goal is to assess how the energy landscape is influenced by the combination of the d_{SL} and d_{LG} parameters, at fixed d_{IP} values. In the case of the TDPDTA material, three d_{IP} values are used, at 3.1, 3.2 and 3.3 Å (from HT-0), respectively, to also explore the effect of the change of the interplanar distance between monomers, whereas in the case of the PDTA material, for sake of comparison, the d_{IP} is considered at 3.2 Å (from HT-0).

The d_{SL} and d_{LG} parameters are varied, starting from the π -eclipsed configuration, in the ranges from 0 to 4.4 Å and 0 to 7 Å, respectively, with a step of 0.2 Å. Each PES scan comprises an overall set of 770 structure dimers. The single point energy calculations are carried out in the periodic framework by means of the Quantum Espresso suite (see Computational Information section) at PBE-D2 level. Clearly, these are simple models not accounting for the effects of the neighboring columns. Nevertheless, the predictive power is still significant. The PES of the TDPDTA ($d_{IP} = 3.3$ Å), reported in Figure 6.17, displays the effect that the longitudinal displacement conveys. By exploring the d_{LG} variable, a second minimum, which coincides with the regular molecular disposition of the HT phase, hereafter labelled as C, appears, other than the global minimum A, this coinciding with the *quasi*-dimerized configuration (LT phase). The energy barrier separating points C and B computed by evaluating the minimum energy path connecting points A, B and C in the PES, as reported in Figure 6.20a, is *ca.* 1.4 kcal mol⁻¹. This energy barrier, valid for a set of dimer models, was validated by means of the NEVPT2 method (see Figure 6.20a). In fact, by comprising the effect of the surrounding columns, the energy barrier would possibly increase. This was already assessed by the NEB calculation (see Figure 6.16), for one TDPDTA column, within the same theoretical framework.

The decrease of the interplanar distance, d_{IP} , between monomers has no consequences for the formation of the second minimum (point C) in the PES, as reported in Figure 6.18a,b, for the $d_{IP} = 3.2$ Å and $d_{IP} = 3.1$ Å, respectively. The only tangible effect is to decrease the energy separation between the two minima, A and C.

By accounting for the same geometrical variables, namely the d_{SL} and d_{LG} , also in the PDTA case, then a second minimum appears in this case too (see Figure 6.19).

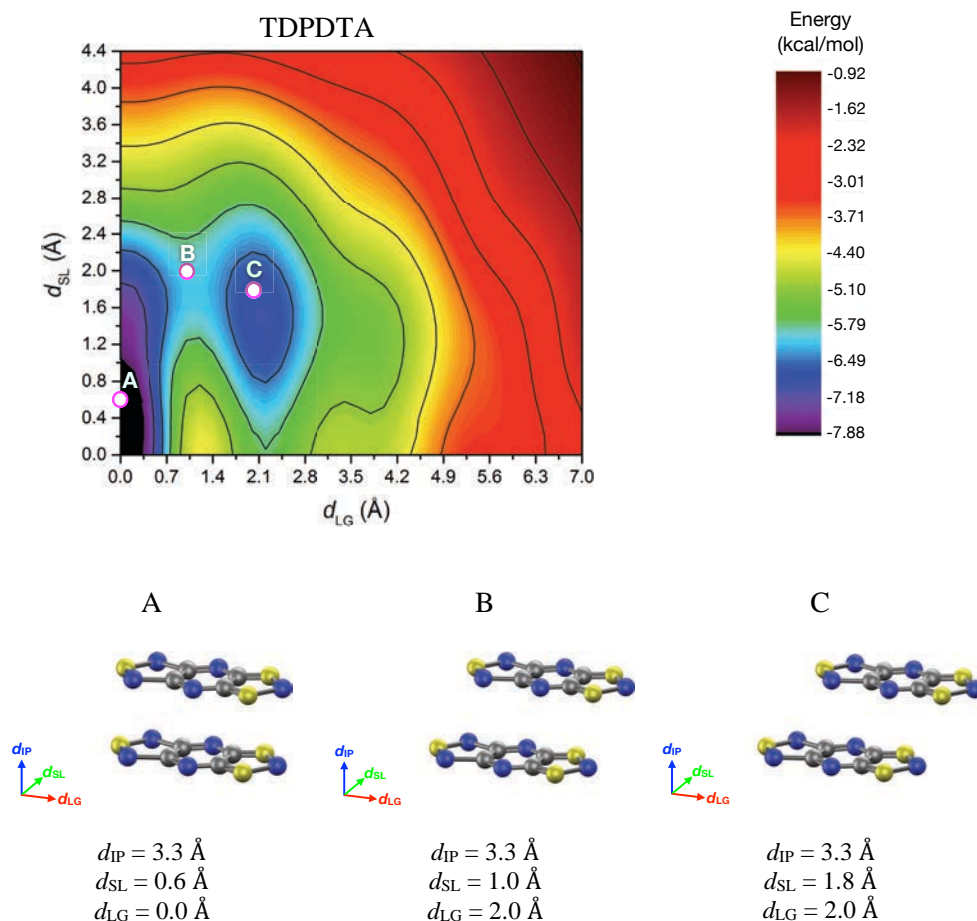


Figure 6.17: The scan map of the TDPDTA system. Note the presence of two minima in the PES, “connected” by the A, B and C points. The configurations for the points A, B and C are also reported with the respective parameters.

The minimum path connecting points A, B and C was explored both at PBE-D2 level and, for validation purposes, at NEVPT2 level as well, as reported in Figure 6.20b. The energy difference separating the dimer models in point B and C, respectively, is $< 1 \text{ kcal mol}^{-1}$. The reason why this second minimum is not observed experimentally is that, laying higher in energy, it would require higher temperatures to be populated.

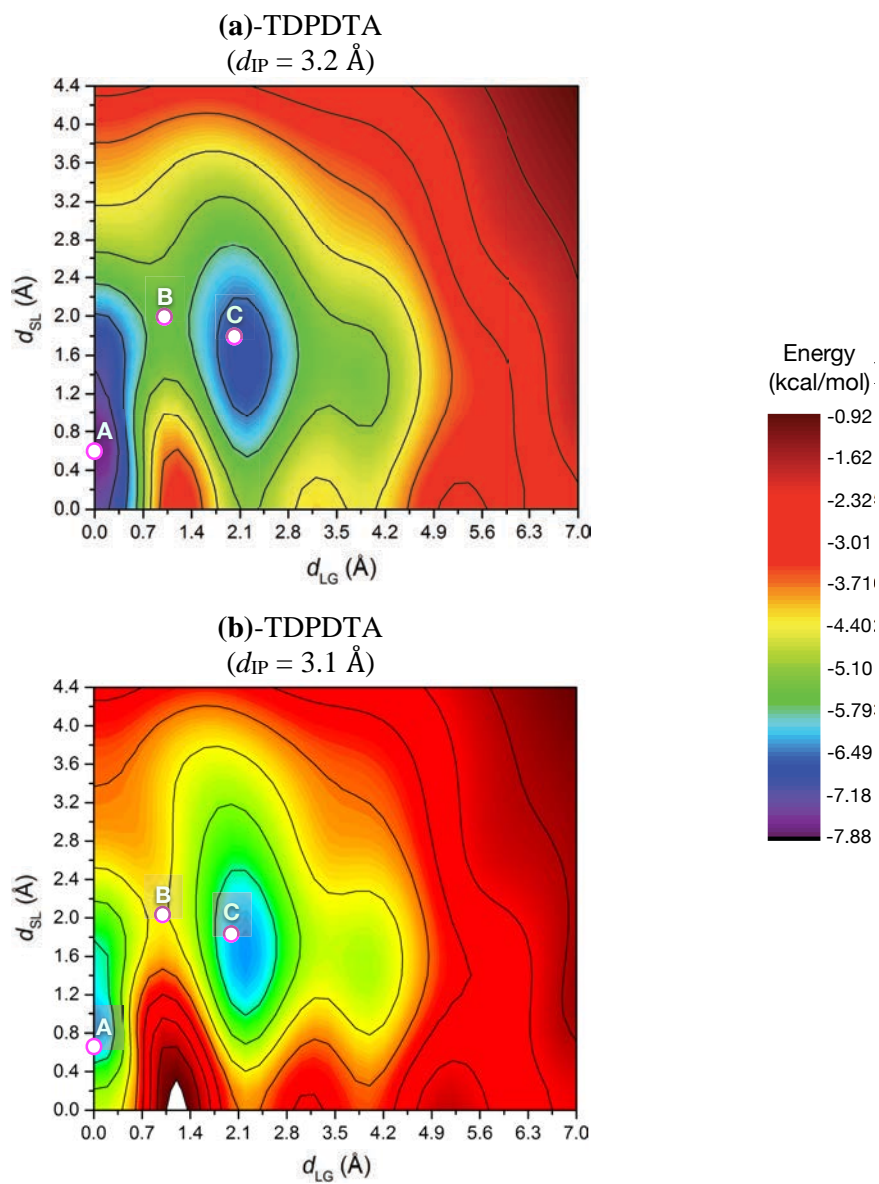


Figure 6.18: The scan map of the TDPDTA system, computed by decreasing the d_{IP} variables to 3.2 \AA and 3.1 \AA , respectively.

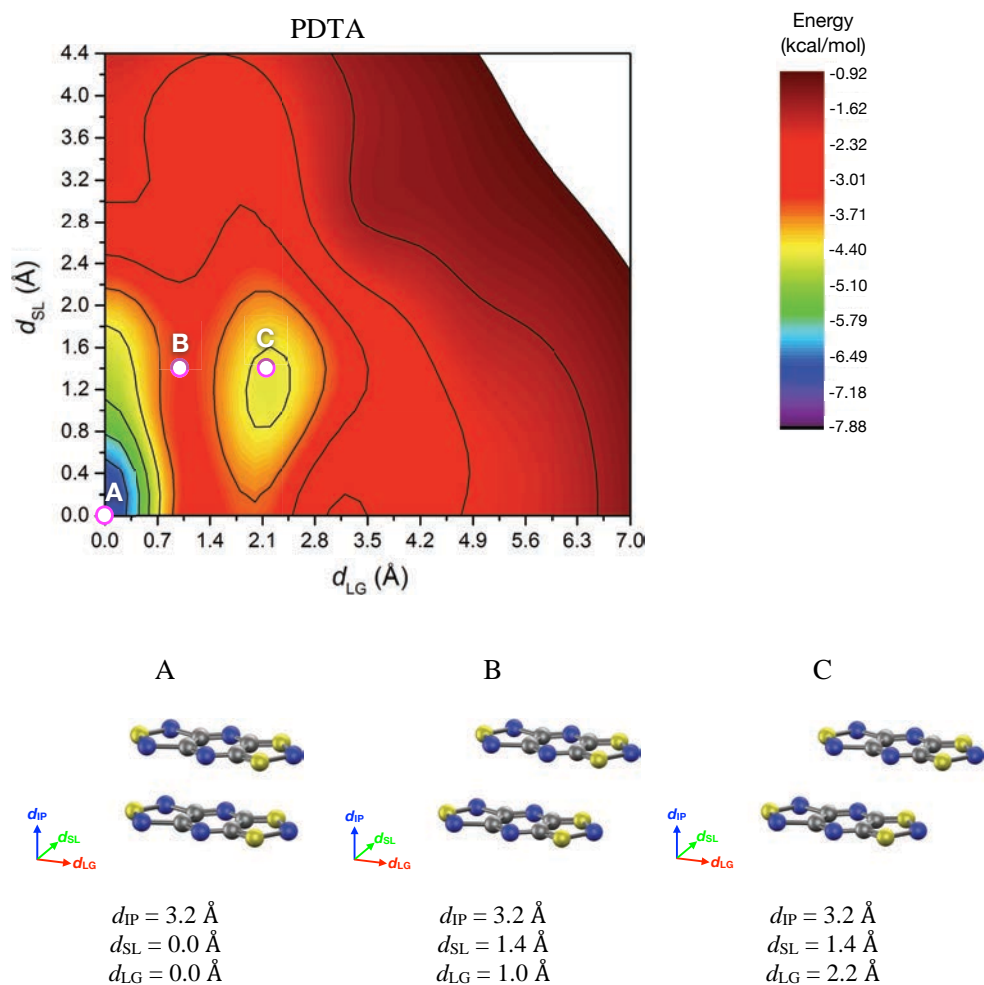


Figure 6.19: The scan map of the PDTA system. Note the presence of two minima in the PES, “connected” by the A, B and C points. The configurations for the points A, B and C are also reported, with the respective parameters.

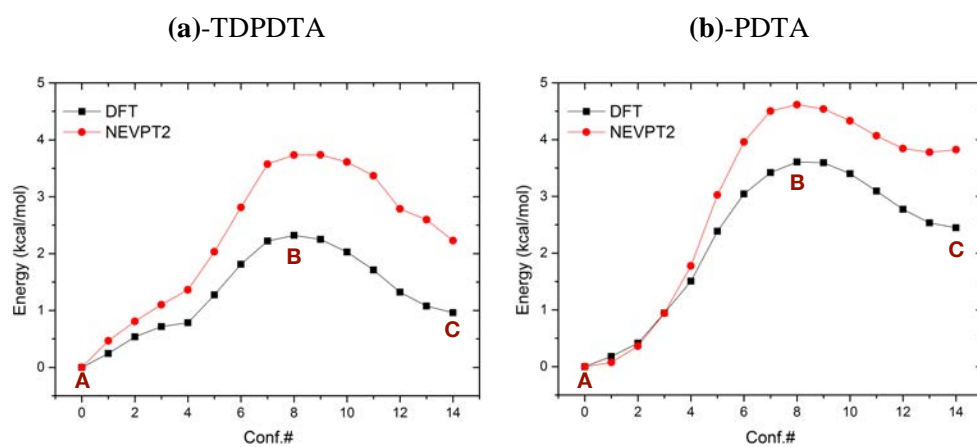


Figure 6.20: The minimum energy profiles path connecting point A, B and C have been investigated both *via* DFT and NEVPT2 methods, in order to estimate the energy barrier separating the two minima. The energy difference between point B (saddle point) and C (second minimum) are of *ca.* $1.4 \text{ kcal mol}^{-1}$ in the case of (a)TDPDTA system, and *ca.* 1 kcal mol^{-1} for the (b)PDTA material.

6.7 Conclusions

The study of the DTA-based materials presenting bistability is currently a hot topic in the material science framework. The implications of the possible uses of these molecular magnetic materials are wide and do not limit themselves to a mere chemical curiosity. The potential to apply these systems in new and strategic fields like the quantum computing or, more in general, the data storage, is prompting an extensive and exhaustive research, with the ultimate goal to have the full control over their properties. So far, a huge achievement was gained by discovering the PED[23] mechanism, a stochastic process responsible for the phase transition and, in turn, the existence of HT polymorphic structures of TTTA, PDTA and 4-NCBDTA. In the case of the PDTA system, it was possible to confirm the presence of the PED mechanism, operating in the same manner as in the prototype TTTA system. In this case, the increasing of the temperature induces the system to consequently increase the rate of exchange between molecular distances. The lateral slippage is found to be the main responsible for the PED activation, as observed by in the AIMD analysis (see Figure 6.10a) and by means of the NEB technique, inducing the LT-PDTA system to lose the π -eclipsed and π -shifted characteristic molecular disposition, favoring the a uniform trend (see also the histogram distances distribution analysis, Figures 6.13 a-e). This process was believed to be ubiquitous among the whole HT phases of the spin Peierls DTA-based family. By means of an extensive and exhaustive investigation over the dynamical properties of both PDTA and TDPDTA compounds, it was possible to uncover, for the first time, a new stabilization process to which last material undergoes.

Depending on which mechanism has to be employed while designing new DTA-based systems, two different parameters have to be account. Specifically, if the compound is required to display the PED process, then the energy barrier separating the two degenerate states configurations needs to be known. Whereas, if the new DTA-based compound has to feature the new stabilization mechanism, then the energy separating the two minima has to be account properly.

In conclusion, the nature of the DTA-based compounds still comprises new and *never-seen-before* processes which may have an important technological impact in the future. The experience gained by analyzing the prototype TTTA material, applied to a very similar scenario, in this case the PDTA, and as a comparative tool to the TDPDTA, gave us the chance to describe for the first time the stabilization process featured by TDPDTA. Moreover, it was possible, by screening in details the AIMD simulation trajectories as well as complementing their study by means of

post processing data, like *e.g.* the thermal ellipsoids, to confirm our discovery and to provide a simple but valid way to predict the chemistry of the DTA-based materials (PES scans). The researcher can now have the possibility to explore and to engineer new DTA-based systems, expanding the spectrum of materials which might feature the PED process or the new spin transition mechanism employing the longitudinal displacement (d_{LG}) of the radicals.

Bibliography

- [1] A. J. Banister, *Nature Physical Science* **1972**, 237, 92.
- [2] R. C. Haddon, *Nature* **1975**, 256, 394.
- [3] R. T. Oakley, *Prog. Inorg. Chem* **1988**, 36, 30.
- [4] R. T. Oakley, *Canadian journal of chemistry* **1993**, 71, 1775–1784.
- [5] A. W. Cordes, R. C. Haddon, R. T. Oakley, *Advanced Materials* **1994**, 6, 798–802.
- [6] J. M. Rawson, F. Palacio in *π -Electron Magnetism*, Springer, **2001**, pp. 93–128.
- [7] S. J. Blundell, F. L. Pratt, *Journal of Physics: Condensed Matter* **2004**, 16, R771.
- [8] T. Chivers, *A guide to chalcogen-nitrogen chemistry*, World Scientific, **2005**.
- [9] J. M. Rawson, A. Alberola, A. Whalley, *Journal of Materials Chemistry* **2006**, 16, 2560–2575.
- [10] I. Ratera, J. Veciana, *Chemical Society Reviews* **2012**, 41, 303–349.
- [11] H. Matsui, M. Yamane, T. Tonami, M. Nakano, M. de Wergifosse, T. Seidler, B. Champagne, *The Journal of Physical Chemistry C* **2018**, 122, 6779–6785.
- [12] D. Marx, J. Hutter, *Ab initio molecular dynamics: basic theory and advanced methods*, Cambridge University Press, **2009**.
- [13] J. L. Brusso, O. P. Clements, R. C. Haddon, M. E. Itkis, A. A. Leitch, R. T. Oakley, R. W. Reed, J. F. Richardson, *Journal of the American Chemical Society* **2004**, 126, 8256–8265.
- [14] J. L. Brusso, O. P. Clements, R. C. Haddon, M. E. Itkis, A. A. Leitch, R. T. Oakley, R. W. Reed, J. F. Richardson, *Journal of the American Chemical Society* **2004**, 126, 14692–14693.
- [15] T. M. Barclay, A. W. Cordes, N. A. George, R. C. Haddon, M. E. Itkis, M. S. Mashuta, R. T. Oakley, G. W. Patenaude, R. W. Reed, J. F. Richardson, H. Zhang, *Journal of the American Chemical Society* **1998**, 120, 352–360.

- [16] G. Wolmershäuser, R. Johann, *Angewandte Chemie International Edition in English* **1989**, *28*, 920–921.
- [17] W. Fujita, K. Awaga, *Science* **1999**, *286*, 261–262.
- [18] G. D. McManus, J. M. Rawson, N. Feeder, J. van Duijn, E. J. McInnes, J. J. Novoa, R. Burriel, F. Palacio, P. Oliete, *Journal of Materials Chemistry* **2001**, *11*, 1992–2003.
- [19] H. Matsuzaki, W. Fujita, K. Awaga, H. Okamoto, *Physical review letters* **2003**, *91*, 017403.
- [20] J. M. Rawson, A. Alberola, A. Whalley, *Journal of Materials Chemistry* **2006**, *16*, 2560–2575.
- [21] D. Bates, C. M. Robertson, A. A. Leitch, P. A. Dube, R. T. Oakley, *Journal of the American Chemical Society* **2018**, *140*, 3846–3849.
- [22] C. S. Clarke, J. Jornet-Somoza, F. Mota, J. J. Novoa, M. Deumal, *Journal of the American Chemical Society* **2010**, *132*, 17817–17830.
- [23] S. Vela, F. Mota, M. Deumal, R. Suizu, Y. Shuku, A. Mizuno, K. Awaga, M. Shiga, J. J. Novoa, J. Ribas-Arino, *Nature communications* **2014**, *5*, 4411.
- [24] S. Vela, M. Deumal, M. Shiga, J. J. Novoa, J. Ribas-Arino, *Chemical science* **2015**, *6*, 2371–2381.
- [25] S. Vela, M. B. Reardon, C. E. Jakobsche, M. M. Turnbull, J. Ribas-Arino, J. J. Novoa, *Chemistry – A European Journal*, *23*, 3479–3489.
- [26] M. Deumal, M. J. Bearpark, J. J. Novoa, M. A. Robb, *The Journal of Physical Chemistry A* **2002**, *106*, 1299–1315.
- [27] T. Francese, J. Ribas-Arino, J. J. Novoa, R. W. Havenith, R. Broer, C. de Graaf, M. Deumal, *Physical Chemistry Chemical Physics* **2018**, *20*, 20406–20416.
- [28] K. E. Preuss, *Polyhedron* **2014**, *79*, 1–15.
- [29] Z.-h. Cui, H. Lischka, H. Z. Beneru, M. Kertesz, *Journal of the American Chemical Society* **2014**, *136*, 12958–12965.
- [30] N. Hoshino, F. Iijima, G. N. Newton, N. Yoshida, T. Shiga, H. Nojiri, A. Nakao, R. Kumai, Y. Murakami, H. Oshio, *Nature Chemistry* **2012**, *4*, 921 EP -.
- [31] S. Grimme, *Journal of Computational Chemistry*, *27*, 1787–1799.
- [32] S. Grimme, J. Antony, S. Ehrlich, H. Krieg, *The Journal of Chemical Physics* **2010**, *132*, 154104.
- [33] J. Hutter, M. Iannuzzi, F. Schiffmann, J. VandeVondele, *Wiley Interdisciplinary Reviews: Computational Molecular Science* **2014**, *4*, 15–25.

- [34] J. P. Perdew, K. Burke, M. Ernzerhof, *Phys. Rev. Lett.* **1996**, *77*, 3865–3868.
- [35] S. Goedecker, M. Teter, J. Hutter, *Phys. Rev. B* **1996**, *54*, 1703–1710.
- [36] C. Hartwigsen, S. Goedecker, J. Hutter, *Phys. Rev. B* **1998**, *58*, 3641–3662.
- [37] M. Krack, *Theoretical Chemistry Accounts* **2005**, *114*, 145–152.
- [38] J. VandeVondele, J. Hutter, *The Journal of Chemical Physics* **2007**, *127*, 114105.
- [39] G. Bussi, D. Donadio, M. Parrinello, *The Journal of Chemical Physics* **2007**, *126*, 014101.
- [40] P. Giannozzi, S. Baroni, N. Bonini, M. Calandra, R. Car, C. Cavazzoni, D. Ceresoli, G. L. Chiarotti, M. Cococcioni, I. Dabo, A. D. Corso, S. de Gironcoli, S. Fabris, G. Fratesi, R. Gebauer, U. Gerstmann, C. Gougoussis, A. Kokalj, M. Lazzeri, L. Martin-Samos, N. Marzari, F. Mauri, R. Mazzarello, S. Paolini, A. Pasquarello, L. Paulatto, C. Sbraccia, S. Scandolo, G. Sclauzero, A. P. Seitsonen, A. Smogunov, P. Umari, R. M. Wentzcovitch, *Journal of Physics: Condensed Matter* **2009**, *21*, 395502.
- [41] C. Angeli, R. Cimiraglia, S. Evangelisti, T. Leininger, J.-P. Malrieu, *The Journal of Chemical Physics* **2001**, *114*, 10252–10264.
- [42] C. Angeli, R. Cimiraglia, J.-P. Malrieu, *Chemical Physics Letters* **2001**, *350*, 297–305.
- [43] C. Angeli, R. Cimiraglia, J.-P. Malrieu, *The Journal of Chemical Physics* **2002**, *117*, 9138–9153.
- [44] F. Neese, *Wiley Interdisciplinary Reviews: Computational Molecular Science*, *2*, 73–78.
- [45] A. Schäfer, H. Horn, R. Ahlrichs, *The Journal of Chemical Physics* **1992**, *97*, 2571–2577.
- [46] A. Schäfer, C. Huber, R. Ahlrichs, *The Journal of Chemical Physics* **1994**, *100*, 5829–5835.
- [47] F. Weigend, R. Ahlrichs, *Phys. Chem. Chem. Phys.* **2005**, *7*, 3297–3305.
- [48] F. Weigend, *Phys. Chem. Chem. Phys.* **2006**, *8*, 1057–1065.
- [49] W. Humphrey, A. Dalke, K. Schulten, *Journal of Molecular Graphics* **1996**, *14*, 33–38.
- [50] K. N. Trueblood, H.-B. Bürgi, H. Burzlaff, J. D. Dunitz, C. M. Gramaccioli, H. H. Schulz, U. Shmueli, S. C. Abrahams, *Acta Crystallographica Section A*, *52*, 770–781.

Chapter 7

Outlook and Future Challenges

The aim of this theoretical and computational work herein presented is to characterize and study the physical-chemical properties of two dithiazolyl-based molecular magnetic systems, namely PDTA[1, 2] and TDPDTA[3], with the intent to rationalize the displayed bistable character and the correlated dynamical process. The work is carried out by also accounting, for sake of comparison, the prototype TTTA material. Some interesting aspects based on the presented research may prompt further the exploration in the field, as well as the design of new DTA-based materials with selected properties. Some of these possible routes are indicated here.

The study of the key forces acting within the two experimentally resolved polymorphs of the TTTA[4–12] prototype system, as reported in Chapter 4, can be further extended to the dynamical case. The use of the Energy Decomposition Analysis[13, 14] (EDA) technique gave the chance to understand which, among the different energy contributions, is the most relevant in the two polymorphs. In particular, the π - π interactions and the four- and six-centers S··N bridges contacts between π -stacks are found to be the energy contributions governing the crystal packing. The interplay between these main factors, without omitting the non-negligible influence of the other minor inter-stack interactions (see Chapter 4), is at the origin of the process that drives the spin and structural transition between the two phases (LT→HT). Thus, it may be interesting for future research, to assess, by monitoring the dynamical evolution in time of the systems, how the aforementioned energy contributions change, specifically outlining the one responsible for the “*jump*” between the LT and HT phases. This would convey to the experimentalist an extremely useful parameter to tune when engineering DTA-based materials. Moreover, hypothetically, by controlling the energetic terms that favor one polymorph of the other, it might be possible to control the same LT→HT transition. In the spectrum of possibilities in

which this phenomenon would find practical application, the most relevant would be in the data processing/storage, where the LT/HT phases alternation, coupled with their respective magnetic responses, might be exploited as 0 and 1 signal, thus avoiding loss of information. There are still open issues regarding the stability[4–9] of the DTA-based systems, that depends upon the environmental conditions. Nevertheless, the DTA-based material displays promising features that require further investigation.

Additional analyses from the static perspective have been performed in Chapter 5[15] of this work. Both the LT and HT polymorphs of the PDTA and TDPDTA materials were analyzed in detail, and compared to the reference TTTA and 4-NCBDTA systems. In particular, the last one does not show bistability, but only spin transition (see Chapter 3). The magnetic investigation performed by accounting for the J_{AB} values, computed from the Heisenberg Hamiltonian for a couple of spin centers A and B, and the subsequent computed susceptibility curves, highlighted a mismatch between experimental and theoretical curves in the HT-PDTA, HT-TDPDTA and LT-TDPDTA. While in the HT cases the origin of the mismatch is known and ascribed to the neglect of thermal fluctuations in the static study of the magnetic interactions, in the LT-TDPDTA case it was not clear. The subsequent employment of magneto-structural correlation maps, that helped us to outline the key role played by the geometrical arrangement based on the lateral slippage (d_{SL}) and interplanar distance (d_{IP}) between monomers to favor or not ferromagnetic (FM) interactions, facilitated the identification of the longitudinal slippage (d_{LG}) as additional variable to account when dealing with the characterization of the TDPDTA material. Particular interesting is the fact that, the use of two-cluster models is sufficient to depict in qualitative terms the best geometrical arrangements which can favor the presence of FM dispositions. Moreover, the energy required to reach a FM configuration can also be inferred by the corresponding map, suggesting for the actual possibility to have a valid tool to design *in silico* the material with desired properties and later on, in the laboratory, to synthesize it, minimizing the trials and waste disposal, which is a major cost affecting many laboratories. The construction of these maps, whose trends have been validated also at Difference Dedicated Configuration Interaction (DDCI) level (see Appendix A.4), might straightforwardly be implemented in an automatic deep-learning, or similar algorithm, for data prediction, screening huge sets of DTA-based materials for a fast and effective material design.

The fact that we discovered a new process to trigger spin transition might help to define not only a way to design new materials, but also to have a certain range of control over their properties, ultimately required for practical application.

Summarizing, to employ the Pair-Exchange Dynamics (PED)[12] mechanism in a newly designed material, two degenerate states should be present, separated by an energy barrier. The interconversion between the two degenerate configurations should be temperature dependent, ultimately providing a stable average structure that, in turn, belongs to the corresponding minimum of the free energy surface. On the other hand, if in the engineering process of a DTA-based material the new spin transition process is targeted, in order for it to feature a stable HT phase, than the energy separation between the two minima, coinciding with the dimerized (LT) and regular (HT) structures, needs to be properly taken into consideration.

Extra contributions to the characterization of the PDTA and TDPDTA materials, and DTA-based materials in general, might be the investigation of their properties from a spectroscopic point of view. This approach might help to outline if a specific fingerprint of the two dynamical processes is present and reflected in their corresponding power spectrum, as a function of the temperature. This would eventually help to design new photo-switchable[16, 17] DTA-based molecular magnets, which, in turn, would meet a potential widespread use for technological purposes.

The work herein reported and discussed is a new starting point for further prompting the study and investigation of the DTA-based materials, but also of other organic molecular-based materials. The improved and refined definition of the key geometrical descriptors, thus d_{IP} , d_{SL} and the d_{LG} parameters, as well as the setting of computational tools to be employed in the validation/study of the mechanisms characterizing the DTA-based compounds, can now play a strategic role in the future development of the field.

Bibliography

- [1] J. L. Brusso, O. P. Clements, R. C. Haddon, M. E. Itkis, A. A. Leitch, R. T. Oakley, R. W. Reed, J. F. Richardson, *Journal of the American Chemical Society* **2004**, *126*, 8256–8265.
- [2] J. L. Brusso, O. P. Clements, R. C. Haddon, M. E. Itkis, A. A. Leitch, R. T. Oakley, R. W. Reed, J. F. Richardson, *Journal of the American Chemical Society* **2004**, *126*, 14692–14693.
- [3] T. Barclay, A. Cordes, N. George, R. Haddon, M. Itkis, M. Mashuta, R. Oakley, G. Patenaude, R. Reed, J. Richardson, et al., *Journal of the American Chemical Society* **1998**, *120*, 352–360.
- [4] G. Wolmershäuser, R. Johann, *Angewandte Chemie International Edition in English* **1989**, *28*, 920–921.
- [5] W. Fujita, K. Awaga, *Science* **1999**, *286*, 261–262.
- [6] G. D. McManus, J. M. Rawson, N. Feeder, J. van Duijn, E. J. McInnes, J. J. Novoa, R. Burriel, F. Palacio, P. Oliete, *Journal of Materials Chemistry* **2001**, *11*, 1992–2003.
- [7] H. Matsuzaki, W. Fujita, K. Awaga, H. Okamoto, *Physical review letters* **2003**, *91*, 017403.
- [8] J. M. Rawson, A. Alberola, A. Whalley, *Journal of Materials Chemistry* **2006**, *16*, 2560–2575.
- [9] D. Bates, C. M. Robertson, A. A. Leitch, P. A. Dube, R. T. Oakley, *Journal of the American Chemical Society* **2018**, *140*, 3846–3849.
- [10] C. S. Clarke, J. Jornet-Somoza, F. Mota, J. J. Novoa, M. Deumal, *Journal of the American Chemical Society* **2010**, *132*, 17817–17830.
- [11] S. Vela, F. Mota, M. Deumal, R. Suizu, Y. Shuku, A. Mizuno, K. Awaga, M. Shiga, J. J. Novoa, J. Ribas-Arino, *Nature communications* **2014**, *5*, 4411.
- [12] S. Vela, M. Deumal, M. Shiga, J. J. Novoa, J. Ribas-Arino, *Chemical science* **2015**, *6*, 2371–2381.

- [13] K. Kitaura, K. Morokuma, *International Journal of Quantum Chemistry* **1976**, *10*, 325–340.
- [14] P. Su, H. Li, *The Journal of chemical physics* **2009**, *131*, 014102.
- [15] T. Francese, J. Ribas-Arino, J. J. Novoa, R. W. Havenith, R. Broer, C. de Graaf, M. Deumal, *Physical Chemistry Chemical Physics* **2018**, *20*, 20406–20416.
- [16] H. Phan, K. Lekin, S. M. Winter, R. T. Oakley, M. Shatruk, *Journal of the American Chemical Society* **2013**, *135*, 15674–15677.
- [17] H. Matsuzaki, W. Fujita, K. Awaga, H. Okamoto, *Physical review letters* **2003**, *91*, 017403.

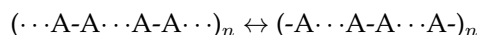
Chapter 8

Summary

8.1 Introduction of the Research Project

In recent years we have witnessed a growing interest in the research of molecular materials that can be switched between two different states through the application of an external stimulus (*e.g.* heat, light) because these materials have a great potential for application in sensors, displays and in information technology[1, 2]. The interest in switchable materials is even greater when the corresponding phase transition between the two different states occurs with a hysteresis loop, thereby giving rise to a bistable material[3], *i.e.* a material that exists in two interchangeable phases under identical conditions (see Fig. 8.1). In the past few years, several computational studies have been conducted, aimed at achieving a detailed understanding of the structural and physical properties of switchable materials in order to facilitate the rational design of new functional materials.

Planar dithiazolyl (DTA)-based[4] radicals have furnished many examples of organic spin-transition materials, some of them occurring with hysteresis and some others without. These materials present low-temperature diamagnetic and high-temperature weak paramagnetic structures, characterized by dimerized $(\cdots A-A \cdots A-A \cdots)_n$ and regular $(\cdots A \cdots A \cdots A \cdots A \cdots)_n$ π -stacks of radicals, respectively. In two recent studies[5, 6], it was demonstrated that the regular π -stacks are not potential energy minima but average structures arising from a dynamic inter-conversion between two degenerate dimerized configurations (see Fig. 8.2):



As a result of the dynamical inter-conversion between degenerate stacks, each DTA radical continually exchanges (in the picosecond timescale) the adjacent neighbor

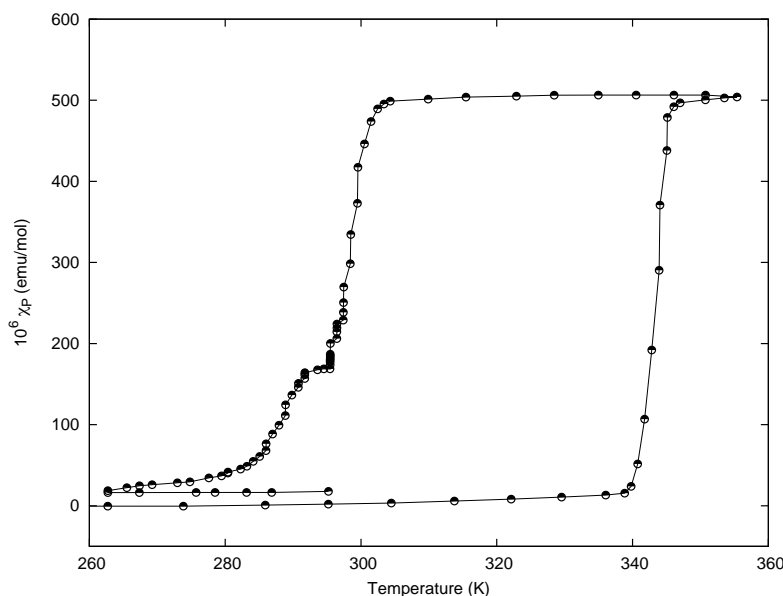


Figure 8.1: Magnetic susceptibility curve of the 1,3,5-trithia-2,4,6-triazapentalenyl (TTTA) material. The TTTA material is the prototype bistable DTA-based material, comprising two stable phases within the same range of temperature (300 K-340 K).

(upper or lower) with which it forms a dimer. This particular dynamic is called Pair-Exchange Dynamics (PED)[5]. The *in silico* experiments have shown that the PED within each stack occurs independently of the PED of neighboring stacks. As a result of the PED, the regular structure $(\cdots A \cdots A \cdots A \cdots A \cdots)_n$ becomes the average configuration and is thus the one observed by X-ray crystallography. In other words, although the regular stacking motif is not a minimum on the potential energy surface (PES) of the system, it is a minimum in the free energy surface (FES) above a given temperature (see red profile in Figure 8.3). Upon cooling, the PED gradually slows down and it ultimately freezes below a given temperature, thereby giving rise to an intra-stack dimerization process (see blue profile in Figure 8.3). The activation/deactivation of the PED upon heating/cooling gives rise to a second-order (or order-disorder) phase transition that is responsible for a change in the dominant magnetic interactions of the system[6]. This suggests that the promotion of a $(\cdots A-A \cdots A-A \cdots)_n \leftrightarrow (-A \cdots A-A \cdots A)_n$ dynamics can be a general mechanism for triggering spin transitions in DTA-based materials. It should also be mentioned that the simulations have demonstrated that the large-amplitude thermal fluctuations accompanying PED play a prime role in defining the magnetic properties of DTA-

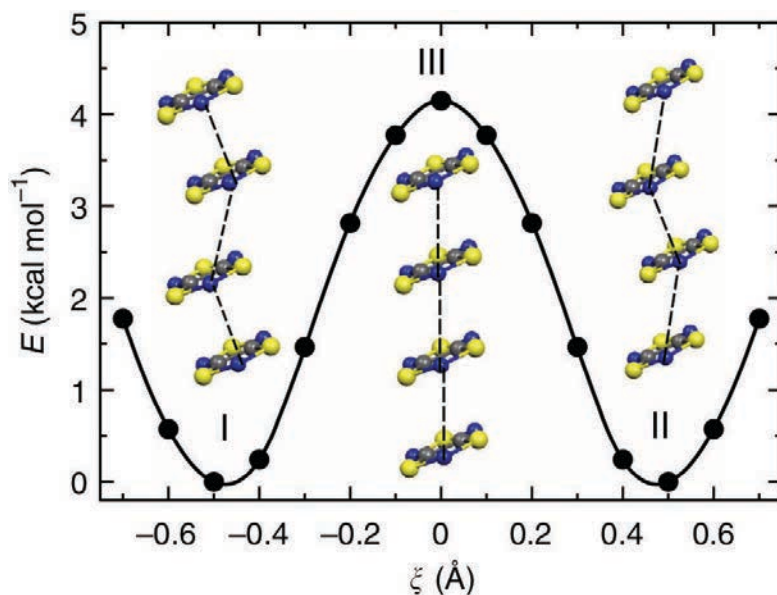


Figure 8.2: Potential energy profile[5] of one column of dithiazolyl radicals with respect to an intra-stack dimerization process.

based crystals[7].



Figure 8.3: Double-Well Model showing the temperature dependence of the free energy profile (blue = low temperature, red = high temperature) associated to one column comprising four TTTA molecules with respect to an intrastack dimerization process.

8.2 Project Goals and Motivations

The PED mechanism is believed to be a common feature among the DTA-based compounds and, as a consequence, to operate in the same way in all the cases, despite the fact that the system shows a hysteretic or non-hysteretic behavior associated to a *first-order*[8] or *second-order*[9] phase transition (like reported in the cases of 1,3,5-trithia-2,4,6-triazapentalenyl (TTTA)[7] and 4-cyanobenzo-1,3,2-dithiazolyl (4-NCBDTA)[9], respectively) (see Fig. 8.4a,d). The project is aimed at studying and testing the validity of the proposed PED mechanism that, ultimately, would explain the presence of bistability in DTA-based crystals. The systems considered are 1,3,2-pyrazinodithiazol-2-yl (PDTA) and 1,2,5-thiadiazole[3,4-b]-pyrazine (TD-PDTA), both bistable, presenting a susceptibility curve with a marked hysteretic behavior (see Fig. 8.4b,c). In particular, the PDTA susceptibility curve encompasses room temperature, defining it as one of the best candidates for potential practical applications. A complete understanding of the mechanism of bistability is only possible if one can describe its origins in terms of energetics (thermodynamic and kinetic) and its effects on the crystal geometry. Molecular crystals can be considered as prototypical cases of supramolecular entities, where the intermolecular bonds play a key role in the structural motif of the system, especially in the LT→HT phase transition. Following this line of thought, the most relevant changes in the inter-molecular bonds relate to the formation of π -dimers or radicals in the LT phase. Therefore, we need more extensive research to determine the driving forces behind the formation and dissociation of π -dimers in DTA-based materials.

The goals of this project are:

- Study the magnetic topology of the PDTA and TDPDTA materials and rationalization of the different magnetic properties of their polymorphs;
- Investigate how the structural changes induced by temperature affect the properties of the low temperature (LT) and high temperature (HT) polymorphs of these two materials;
- Explore the Potential Energy Surface (PES) of PDTA and TDPDTA, trying 1) to locate possible ferromagnetic configurations and 2) to decipher common trends between the materials;
- Study the forming and breaking process of the bonding between molecules and/or molecular columns induced by temperature and their corresponding magnetic topology.

In order to achieve these goals, many different computational models and techniques have been used, as it will be explained in the next section. These allowed

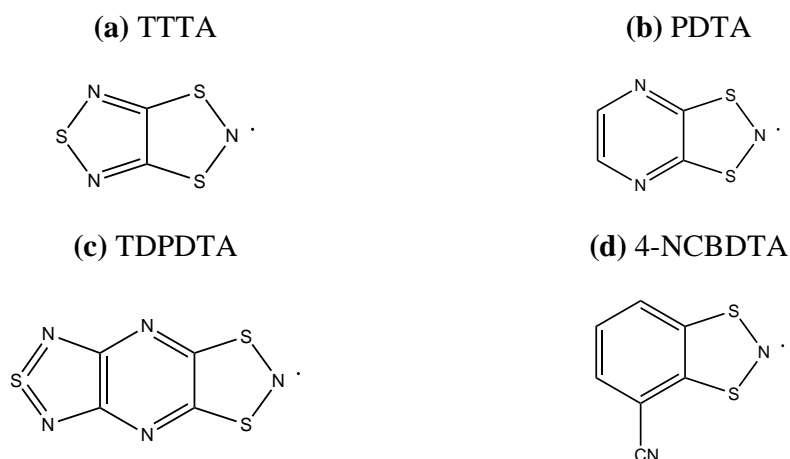


Figure 8.4: Schematic representation of the (a) TTTA, (b) PDTA, (c) TDPDTA and (d) 4-NCBDTA compounds, respectively.

us to extract many different properties and to compare them in such a way that a detailed profile for each material investigated could be drafted.

8.3 The PDTA and TDPDTA systems

The 1,3,2-pyrazinodithiazol-2-yl (PDTA)[10] material is a bistable system characterized by a susceptibility curve with a wide hysteretic loop which encompasses room temperature. The bistability ranges from $T_C^\uparrow = 297$ K to $T_C^\downarrow = 343$ K. The LT phase is diamagnetic (space group $P1$) while the HT phase is weakly paramagnetic (crystal habit $C2/c$). The LT polymorph presents an even alternation of π -dimers and π -shifted dimers, respectively. The HT phase, instead, presents a uniform propagation of the columns along the stacking direction. Each molecule displays the same distance with respect to its nearest neighbors. The HT structure disposition presents a characteristic herringbone arrangement (see Fig. 8.5).

The 1,2,5-thiadiazole[3,4-b]-pyrazine (TDPDTA)[11] system is a bistable system, with a hysteretic susceptibility curve, whose phase transition appears to occur at lower temperature compared to the PDTA case ($T_C^\uparrow = 200$ K and $T_C^\downarrow = 50$ K). The LT and HT phases are both triclinic (crystal habit $P1$). Nevertheless, the structural disposition of the two phases appears to be different in the two cases. In particular, the LT system displays a pseudo-dimerized arrangement, resembling the LT-PDTA. But in this particular case, an even alternation of *quasi*- π -dimerized dimers with *quasi*- π -shifted

dimers is found, each dimer of which is longitudinally translated with respect to the previous one. Conversely, the HT phase of TDPDTA displays a uniform trend like the one found in all the other HT phases (see Fig. 8.5).

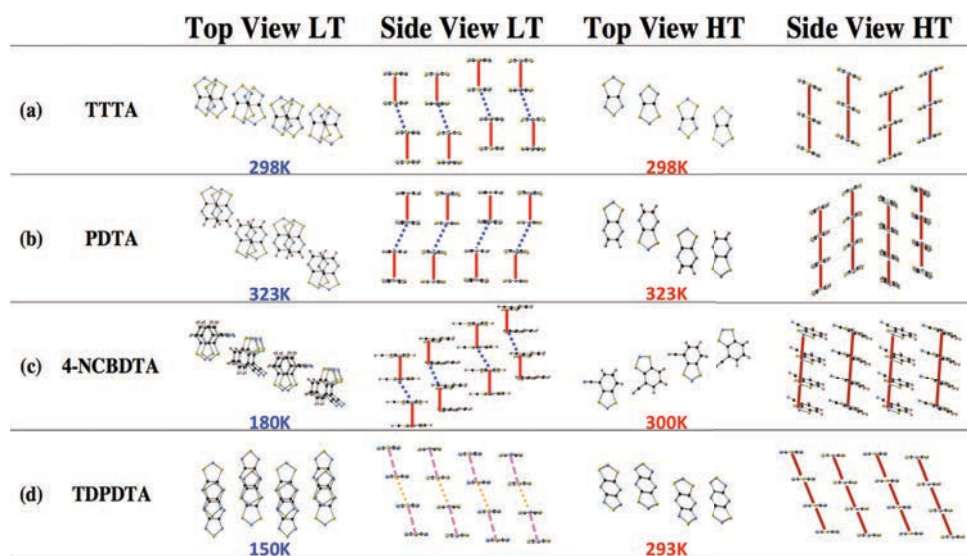


Figure 8.5: Schematic representation of the crystal packing for the (a) TTTA, (b) PDTA, (c) 4-NCBDTA and (d) TDPDTA. For each system, the LT and HT polymorphs are reported, both with a top and side view perspectives. The LT phases, except for the TDPDTA one, present the same trend, where eclipsed π -dimers are alternated to π -shifted ones. The TDPDTA instead shows a similar disposition with respect to the other LT phases, but the pairs are longitudinally displaced. In the case of the HT polymorphs, all the systems present the same uniform stack propagation pattern.

For sake of comparison, in our research of the magneto-structural properties of the compounds mentioned above, we included also the prototype bistable TTTA materials and the spin-switchable 4-NCBDTA (see Fig. 8.5). These two compounds have been analyzed in detail in previous works[7, 9], both from the magnetic point of view, with a static analysis, and from a dynamical viewpoint, accounting for the influence of temperature in an increasing range of values. The TTTA material presents a wide hysteretic susceptibility[12] curve which, as in the case of the PDTA, encompasses room temperature. The LT phase is triclinic ($P1$), presenting an alternation between π -dimers with π -shifted dimers. The magnetic interaction found in the dimerized pairs is extremely antiferromagnetic (AFM), leading to a magnetically

silent system, as experimentally found. On the other hand, the monoclinic ($P2_1/c$) HT phase presents a uniform stack disposition, showing weaker AFM coupling, confirming the weak paramagnetic nature experimentally detected. The general description from the static analysis is also confirmed by the dynamical analysis where the influence of thermal fluctuations is considered. The 4-NCBDTA instead shows a non-hysteretic behavior. Both the LT and HT phases present the same crystalline $P2_1/c$ space group. The LT phase displays the usual alternation between π -dimers with π -shifted dimers, whereas the HT phase is characterized by the uniform stacking arrangement typical of the HT-DTA-based polymorphs. The dominant magnetic coupling in both polymorphs is found along the stacking direction of the molecular columns. Also in the case of the 4-NCBDTA the PED operates, triggered by a rise in temperature. In a recent publication, it was demonstrated that for a system, the presence of hysteresis is not correlated to the presence of the PED[9].

8.4 Computational Tools

The nature of the properties of interest prompted the use of different computational techniques and methods, at different levels of accuracy. In this context, our goal is not to obtain absolute values for the computed quantities, but trends, in order to show patterns between the different structures investigated and, eventually, deviations, highlighting new interesting properties.

8.4.1 Static Analysis

First-Principles Bottom-Up Methodology

In order to study, from a static perspective, the distribution of the magnetic interactions within the selected crystals, we made use of the First-Principles Bottom-Up[13, 14] (FPBU) methodology. First, all the possible magnetically relevant dimers in the crystals were selected from the crystal as resolved experimentally (usually by X-ray powder diffraction). The maximum distance to consider, when selecting the pairs of dimers, is 10 Å[15]. From the general Heisenberg Hamiltonian ($\hat{H} = -2J_{AB}\hat{S}_A \cdot \hat{S}_B$) defined for a A-B pair of $S=1/2$ radicals, we could extract the magnetic J_{AB} couplings, defined as $J_{AB} = E^{BS} - E^T$, where E^{BS} and E^T are the energies of the broken symmetry (BS) and triplet (T) solutions, respectively. These energies have been computed at the DFT/UB3LYP[cit5b, 16] level using the Gaussian09[17] package. The standard 6-31+G(d) basis set[18, 19] was used in all the energy calculations. Once the whole set of J_{AB} values for all possible dimers had been computed, one can define the magnetic topology for the LT and HT of PDTA and TDPDTA systems in terms of

the non-negligible J_{AB} magnetic values. This 3D magnetic skeleton allows to highlight the propagation pattern followed by the most important magnetic interactions within the crystalline structure. At this point, the most representative minimal magnetic models (MMM) can be selected and extracted from the periodic 3D magnetic topology. The finite models, once expanded along x , y and z , should be able to reproduce the 3D periodic magnetic topology. Finally, based on the chosen MMM, one constructs the matrix representation that contains all the J_{AB} values and distances necessary to parametrize the Heisenberg Hamiltonian, whose energy eigenvalues and corresponding spin quantum numbers, computed from its diagonalization, are later on inserted into the statistical mechanic formula used to compute the magnetic susceptibility curve.

Energy Decomposition Analysis

The study of the origin of the difference between the polymorphic phases of the TTTA material, LT and HT respectively, is performed by employing the Energy Decomposition Analysis[20, 21] methodology. By evaluating the single energetic contributions within the TTTA dimers, thus electrostatic, exchange, repulsion, polarization and dispersion components, it is possible to outline which one is mainly contributing to the stabilization process in the polymorphs.

Nudged Elastic Band Calculations

It is not clear yet how the phase transition operates in DTA-based compounds. In order to identify possible variables involved in it, we employed the Nudged Elastic Band[22] (NEB) methodology, as implemented in the Quantum Espresso[23] code. The profiles have been computed at the DFT/PBE[cit21a, cit21b]+D2[24] level, using a kinetic energy cutoff of 70 Ry for the ultra-soft[25] pseudopotentials. In practical terms, once the *reactant* (A) and *product* (B) of the system investigated and at equilibrium, are available, the NEB algorithm allows to perform a linear interpolation between A and B. This creates a series of intermediate *images* that, step by step, should reproduce the displacement occurring within the structure. Once the structure profile is created, then the algorithm applies a series of fictitious springs, in order to mimic an elastic band, preserving the distance between images. The minimal energy path (MEP) is found once the springs between the images are optimized, minimizing the forces acting on each single configuration. The energy profile obtained by means of the NEB algorithm can be used to study the activation energy of the process, likewise the energy barrier separating the two degenerate, dimerized states involved in a PED event (see Fig. 8.2).

Magneto-Structural Correlation Maps

The rationalization process employed to describe the systems takes also advantage from the computed magneto-structural correlation maps, an extremely useful tool used to highlight those structural ferromagnetic (FM) dispositions that might help experimentalists to engineer the material for practical purposes. To achieve it, we employed some dimer models, based on the molecular systems considered, in which we modified the inter-planar distances (d_{IP}) and slippages (d_{SL}) between monomers (see Fig. 8.6). In this way, it was possible to span an extended area comprising >3000 different configurations. For each configuration, the respective magnetic J_{AB} coupling value was computed, leading to antiferromagnetic coupling (AFM) if $J_{AB} < 0$ and ferromagnetic coupling (FM) if $J_{AB} > 0$.

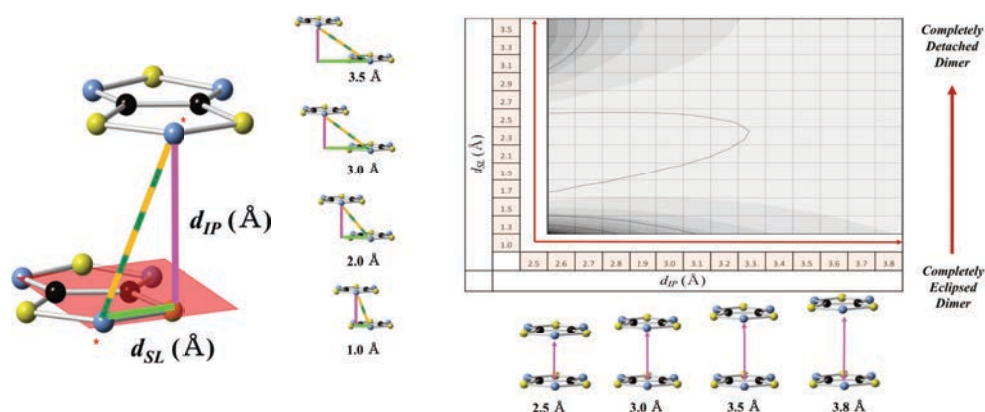


Figure 8.6: Model employed to compute the magneto-structural correlation maps. We modified the inter-planar distance and the slippage, as reported in the scheme on the right-hand side. In this way, it was possible to explore a wide area of molecular configurations.

Variable-Cell and Geometry Optimizations

The computational models used in the study of the dynamical properties of PDTA and TDPDA are based on supercells, representative of the respective crystalline structures as experimentally resolved by X-ray powder diffraction. From the corresponding structural files (.cif), found in the Cambridge Crystallographic Database (CCDC[26]), the unit cells have been expanded along the a , b and c axes in order to have in each supercell 32 molecules. In particular, the unit cells of LT-PDTA,

HT-PDPA and LT-TDPDPA are subjected to a $2 \times 2 \times 2$ expansion, whereas the HT-TDPDPA undergoes a $4 \times 2 \times 2$ expansion. The thermal expansion of the crystals, when the temperature increases, is extremely important when analyzing the organic DTA-based radical systems. To account properly for its role and its correlation with the structure evolution due to phase transition, we made use of intermediate structures whose cell parameters were derived by interpolation between the experimental HT phase and its Variable-Cell (VC) optimized form at 0 K (see Fig. 8.7).

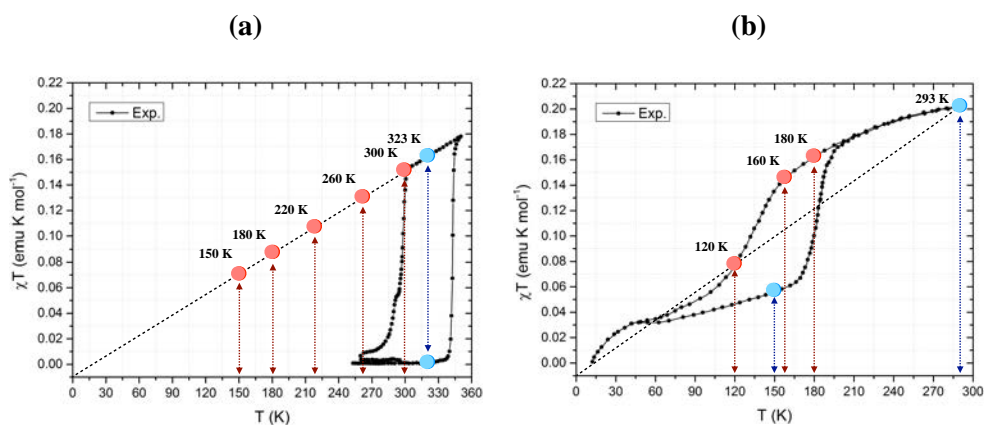


Figure 8.7: The different crystalline cells obtained by means of the linear interpolation between the experimentally resolved HT cells of both (a) PDPA and (b) TDPDPA with respect to their VC optimized structures. In particular, in the case of the system (a), five different crystal cells have been derived and subsequently used to obtain their AIMD trajectories at fixed temperature. In the case of system (b), three structures have been derived and analyzed in the same manner.

Once the cell parameters are defined, the 32 molecules are adapted to the new crystalline cell by means of a geometry optimization. The VC and geometry optimizations were performed using the program CP2K[27], with the PBE exchange-correlation functional within the spin unrestricted formalism. Norm-conserving Goedecker-Teter-Hutter pseudopotentials were used for all atomic species[28–30] in combination with the Gaussian TZV2P basis set[31], and a Γ -point sampling of the Brillouin zone. Grimme’s D3[32] dispersion corrections were also included when optimizing the structures.

8.5 Dynamical Analysis

8.5.1 Ab Initio Molecular Dynamics

The study of how temperature affects the organic crystal investigated in this project is extremely important, because it can help elucidating the mechanisms affecting the phase transition, which, in turn, has a direct impact on the magnetic response of the materials. To this purpose, we employed a precise and accurate method: Ab Initio Molecular Dynamics (AIMD). In particular, we made use of the Born-Oppenheimer MD (BO-MD), which includes the quantum mechanical electronic effects in the calculation of forces and energies, in the NVT ensemble. Each structure was first equilibrated for three picoseconds, followed by the production run of ca. ten picoseconds.

8.6 Results

8.6.1 Static Analysis

The study of the systems from a static perspective is of fundamental importance, because it allows to depict a profile for the materials in terms of energetic and magnetic interactions and how they influence the crystal that, later on, are essential when including the influence of temperature.

Given that the other DTA-based compounds feature common geometrical motifs like the TTTA system, both for the LT and HT phases, the results obtained by analyzing the TTTA throughout the EDA methodology can be extended to the others. The stabilization processes of the two TTTA polymorphs are found in the strong π - π intermolecular interactions along with the π -stacks and in the six- and four-centered N \cdots S bridges, respectively, between the intercolumn interactions. The strong binding generated by the π -stacks in the LT polymorph, in particular, mainly originates by the polarization and dispersion energy components. Whereas, the destabilization of the LT phase is mainly played by the S \cdots S lateral contacts, which are found to be weaker compared to the ones found in the HT phase. Thus, the chemistry between π - π intermolecular interactions with respect to the S \cdots S lateral contacts, without forgetting also the non-negligible effect of the other interactions found within the crystal, marks the difference in energy between the two polymorphic phases.

The detailed study of the TTTA is then followed by the characterization of the PDTA and TDPDTA systems. To this intent, first the FPBU methodology is employed. Two crucial descriptors of the systems investigated were clearly established: 1) the order

of magnitude of the magnetic interactions and 2) their preferential propagation direction. It has been found that, in the case of the PDTA, the strongest magnetic coupling appears in the LT phase, between the dimerized pairs, and it is equal to $J_{AB} = -1657 \text{ cm}^{-1}$. This strong AFM coupling propagates along the stacking direction of the molecular columns. In the HT phase instead, the largest AFM coupling is found to be $J_{AB} = -111 \text{ cm}^{-1}$, also propagating along the stacking direction. This important difference of an order of magnitude between the two polymorphs is reflected in the derived magnetic susceptibility curves that are found to be in agreement with the experimental interpretation, which identifies the LT polymorphs as diamagnetic and the HT one as weakly paramagnetic. Similar to the PDTA case, the TDPDTA system presents a strong AFM coupling in the LT phase, $J_{AB} = -781 \text{ cm}^{-1}$, and a weak AFM coupling in the HT phase, $J_{AB} = -69 \text{ cm}^{-1}$. These results are in line, a priori, with what has already been found in the case of the prototype TTTA material, except for their magnitude. We predict a magnetically silent LT phase, but this is in disagreement with the experimental curve (see Fig. 8.8a) due to limited model employed in the derivation of the respective susceptibility curve, while in the case of PDTA, experimental and theoretical data coincide (see Fig. 8.8b). On the contrary, the HT phases of both the systems investigated display a gap between the computed susceptibility curves and the experimental ones. This is most likely due to the neglect of the influence of thermal fluctuations, as found in the case of the TTTA[33] material.

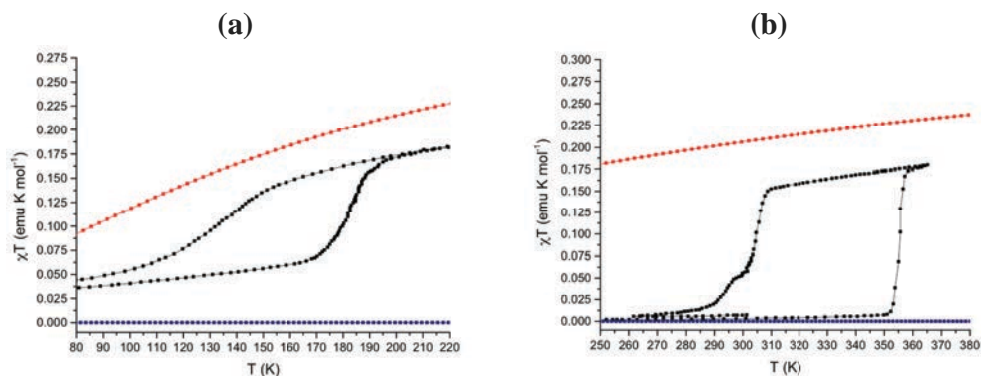


Figure 8.8: The best results from the theoretical predictions of the susceptibility curves for the LT and HT polymorphs of (a) TDPDTA and (b) PDTA, respectively. In particular, the models employed in the derivation of the red and blue curves are 1D models, which account for the strongest coupling within the crystal structure.

Secondly, we evaluated the nature of the magnetic interactions considering the four

compounds described above. The aim of this static analysis was to establish which geometrical disposition of the pairs of dimers tends to favor the presence of ferromagnetic ordering. To this intent, we employed the magneto-structural correlation maps, see Figure 8.9. The limits for the inter-planar distance (d_{IP}) and slippage (d_{SL}) are based on the minimum and maximum distance experimentally detected. In particular, the inter-planar distance range is $2.5 \text{ \AA} < d_{IP} < 3.8 \text{ \AA}$ and the slippage range is $1.0 \text{ \AA} < d_{SL} < 3.5 \text{ \AA}$. Each map is based on the analysis of > 3000 dimers configurations, for each of which we computed the J_{AB} values. For the TTTA, PDTA and 4-NCBDTA a FM area exists, while in the case of TDPDTA, all configurations are AFM (see Fig. 8.9). The calculation of the maps has been complemented with the analysis of the energetics involved in the formation of the FM regions. It turned out that the FM area of PDTA presents a prohibitive energetic cost, which, ultimately, will end up with the decomposition of the crystals. Different are the cases of TTTA and 4-NCBDTA, where a small portion of the FM region is found to be energetically accessible with negative ΔE^{AB} , where ΔE^{AB} is the energy of formation of the dimer composed of monomer A and B ($-0.1 \text{ kcal/mol} < \Delta E^{AB} < -8 \text{ kcal/mol}$). Inside these small FM accessible regions, we tested the predicted FM trend, employing the high level DDCI-3[34] method, in order to compute the magnetic coupling values of four sampled structures, and to compare the resulting values against DFT data. The DDCI-3 results confirm the DFT trend, at least in the sign (FM *vs.* AFM), but not in the predicted values, that are found to differ by one order of magnitude[35]. Nevertheless, this analysis proved that DFT is able to catch correctly the nature of the magnetic interactions. Supplementary analysis based on Kahn's qualitative model, proved that the FM couplings are favored when the Orbital Overlap (OO) (see Fig. 8.10) of the SOMOs of the neighboring molecules is negligible. On the contrary, as put in evidenced by the analysis of the TDPDTA trend, the AFM coupling is favored by the OO.

Finally, a series of *in silico* experiments was carried out in order to establish what is the amount of electronic contribution compared to the structural one in determining the J_{AB} values. To do so, we employed the HT dimers as experimentally resolved and we:

1. compared the J_{AB} values from the models closest to the experimental ones, taken from the respective magneto-structural correlation maps[35];
2. selected the TTTA-HT dimer as a reference, subsequently changing the substituent attached to its DTA ring with the substituents relative to the other DTA-based compounds, while keeping the experimental distance between the DTA rings[35] frozen;
3. selected the four TTTA dimers, from the TTTA magneto-structural correlation

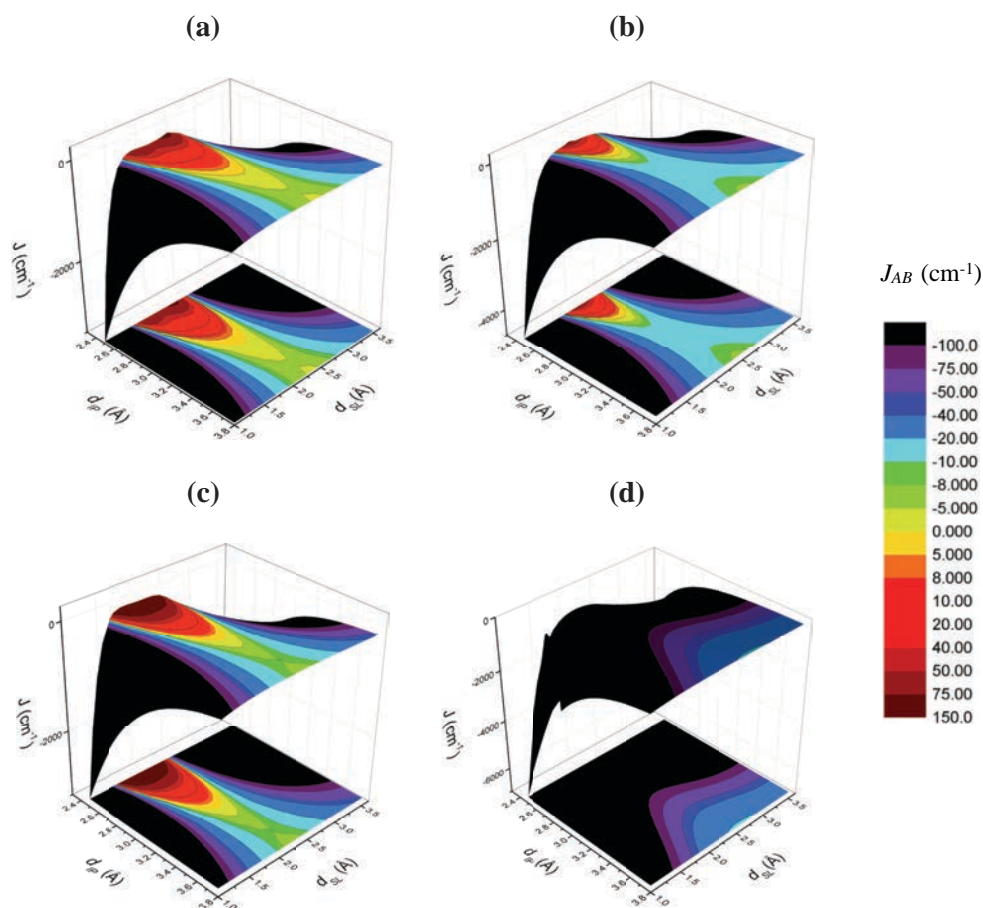


Figure 8.9: Magneto-structural correlation maps of (a) TTTA, (b) PDTA, (c) 4-NCBDA and (d) TDPDTA.

map, which mostly resemble the HT phase compounds dimers, respectively, in terms of geometrical arrangement[35].

In the case of point 1), it was found that the models employed in generating the maps reproduce well the experimental systems, and the corresponding computed J_{AB} values, although a certain error is present, due to the neglect of the inner degrees of freedom. In point 2) we proved that the influence of the nature of the substituent is irrelevant in the derivation of the magnetic properties of the compounds. More specifically, the substituents have only an influence on the crystal packing of the materials, that, in turn, influences the magnetic interaction among DTA rings. Fi-

nally, in the case of point 3), it was shown that the simple correct disposition of the TTTA compound can clearly catch the nature and magnitude of the magnetic interactions of the other three materials, definitively pointing out, like in case of 2), that the substituents do not affect directly the magnetic coupling, but the disposition of the crystal does.

These important conclusions, achieved by complementing different techniques and methods, prove the complex nature of the systems investigated. The chance to have FM coupling is only possible under particular conditions, and not all the systems can get access to them energetically. Finally, the electronic contribution in these materials is found to be independent of the nature of the substituents attached to the DTA rings. On the other hand, the kind of substituent significantly influences the crystal packing of the molecular systems, and thus indirectly affects the magnetic interactions. So, it seems clear that it is not possible to entirely decouple the two contributions entirely, since one is affected by the other and vice versa[35].

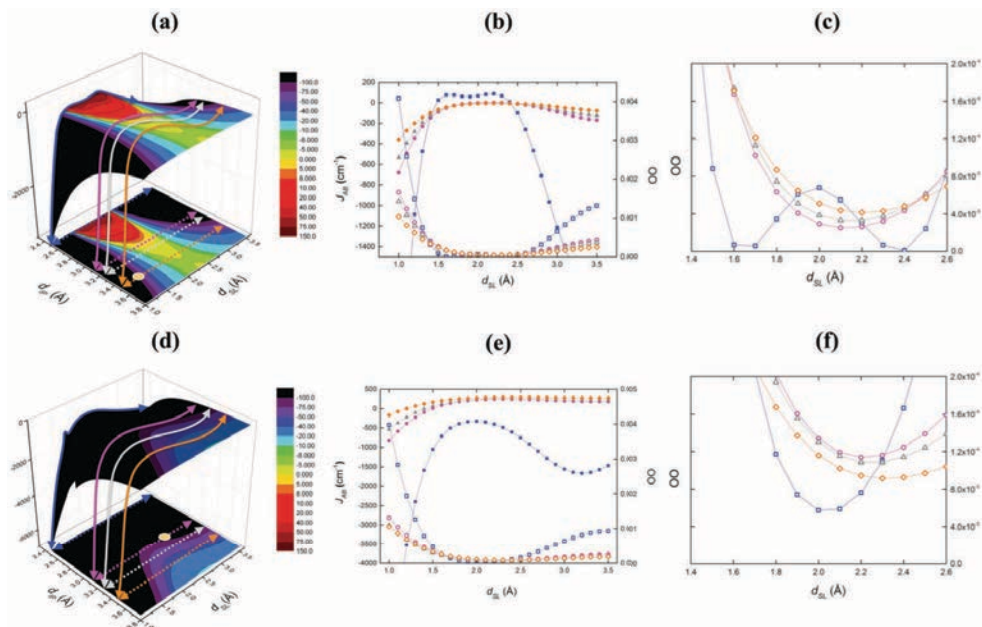


Figure 8.10: Orbital overlap (OO) analysis graphs for TTTA (a-c) and TDPDTA (d-f). (a) Fixed d_{IP} values sampled at 2.5, 3.1, 3.22 and 3.5 Å in order to analyze the most FM region (blue line), the FM boundary ($J_{AB} = 0 \text{ cm}^{-1}$, purple line), the moderate AFM region (gray line), and the region where the experimentally resolved TTTA dimer should be located (orange line and the corresponding orange dot in the projected map). (d) Same regions are analyzed for TDPDTA for comparison reasons. Note that the TDPDTA experimental geometry lies in the FM boundary (purple line). (b and e) Effective orbital analysis compared to the J_{AB} values for the four slices in (a and d). The empty symbols refer to the orbital overlap OO data, while the full symbols refer to J_{AB} data. (c and f) Zoom of the region with the smallest orbital overlap OO, ranging from 1.4 Å and 2.6 Å.

8.7 Dynamical Analysis

The dynamical analyses of the AIMD trajectories were carried out to evaluate some variables and parameters which, based on the previous experiences, turn out to be powerful descriptors for the material characterization (*e.g.* d_{IP} , d_{SL} , etc). In particular, we:

- studied the activation/deactivation of the PED mechanism, extracting one col-

umn from the supercells, selecting the distance between the nitrogen atoms formally hosting the unpaired electrons, and monitoring how the distances change along the ten picoseconds trajectory (see Figure 8.11a,c). Although simple, this first analysis is extremely useful because it allows to discriminate if the distances are preserved, as commonly found in the LT-DTA phases, or they mix, hence suggesting a possible PED mechanism operating (see Figure 8.11a);

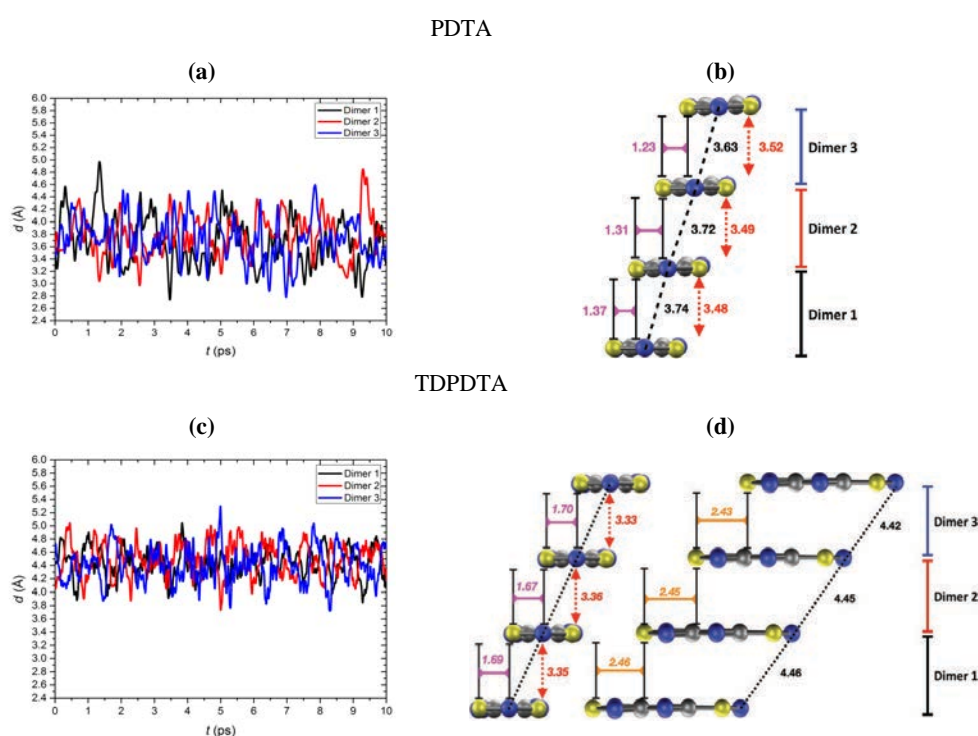


Figure 8.11: Analysis of the trajectories of the dimers from the selected column for (a) PDTA (300 K) and (b) TDPDTA (293 K), and the corresponding distances computed from the respective average structures, in (c) and (d) respectively.

- computed the averaged structure from the HT polymorph trajectory of PDTA (see Figure 8.11b,d). It was found that, like in the TTTA case, the HT phases of PDTA is an averaged system, as a result of an extremely fast interconversion between two degenerate states, *i.e.* $(\cdots A-A \cdots A-A \cdots)_n \leftrightarrow (-A \cdots A-A \cdots A)_n$;
- computed the thermal ellipsoids, to highlight the averaged position of each

atomic species and compare it directly with the X-ray powder diffraction data. It has been proven that, while in the PDTA case (see Figure 8.12) the thermal ellipsoids describe an important influence of temperature on the system, in the case of TDPDTA these oscillations are very small (see Figure 8.13).

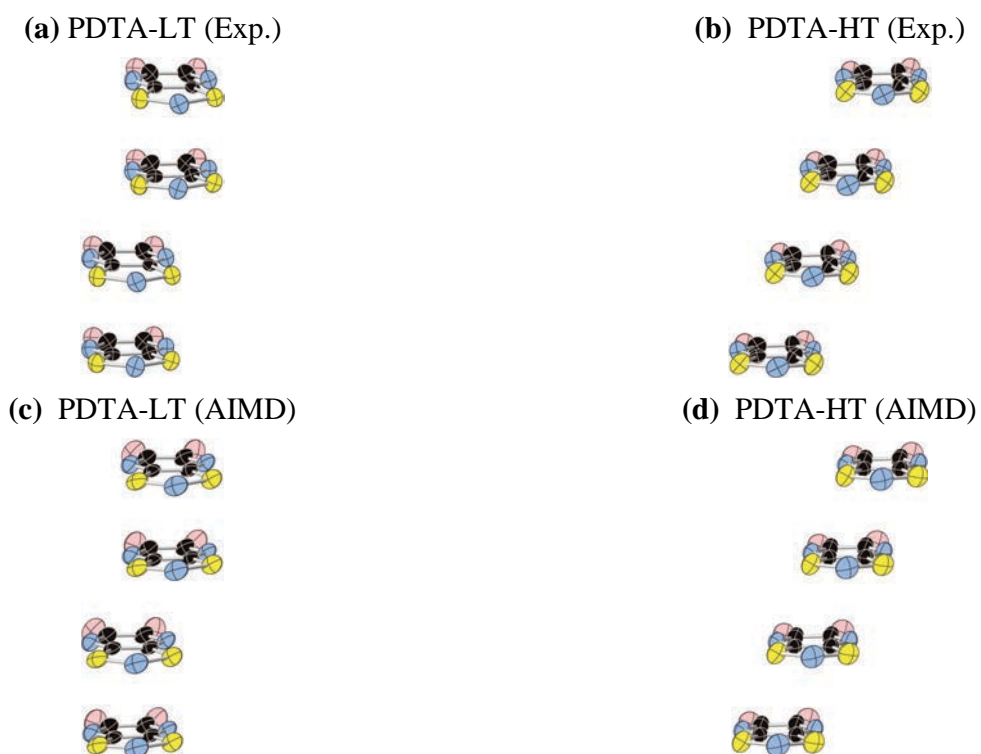


Figure 8.12: Experimental (a) LT and (b) HT and computed (c) LT and (d) HT thermal ellipsoids of the PDTA material.

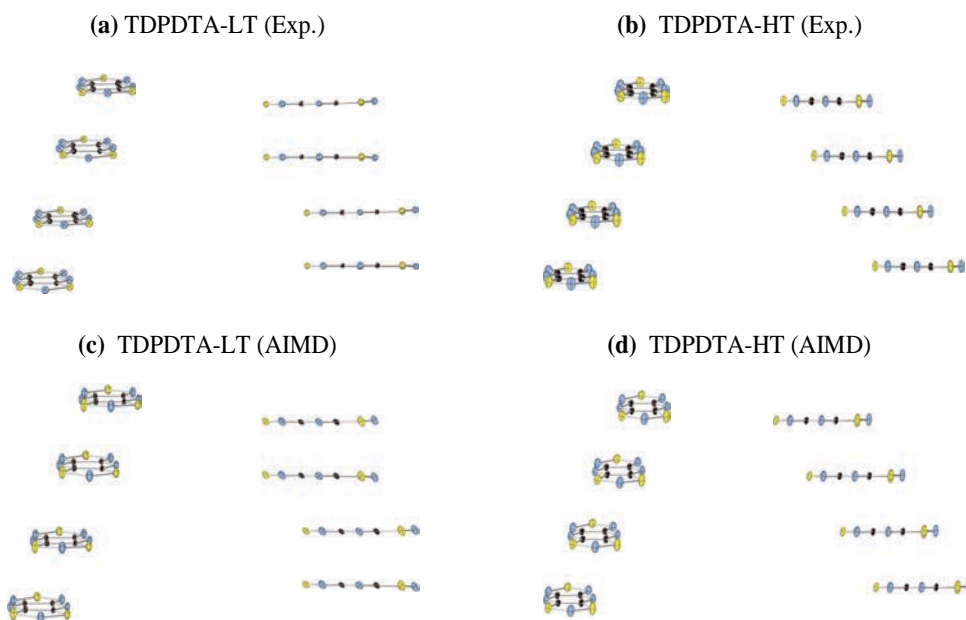


Figure 8.13: Experimental (a) LT and (b) HT and computed (c) LT and (d) HT thermal ellipsoids of the TDPDTA material.

- computed the N*-N* distances distribution analysis (see Figure 8.15 and ??) for the whole set of AIMD trajectories, both for HT-PDTA and HT-TDPDTA (herein only the two temperatures, the lower and higher respectively, are shown). These data provides additional information to the thermal ellipsoids analysis computed for each structure at different temperatures, exposing the change in the dynamics governing the crystal associated with temperature. The HT-PDTA system at 150 K displays a bimodal distribution of the distances that, once the temperature increases, converges to a unimodal one, describing the activation of the PED mechanism.

Conversely, in the case of the HT-TDPDTA system, both at 150 K and 293 K, a unimodal distribution of the N*-N* distances is found. These data confirms the thermal ellipsoids analysis reported, where a very small amplitude of the ellipsoids is found both experimentally and theoretically, suggesting that this system is not subjected to the PED process like PDTA.

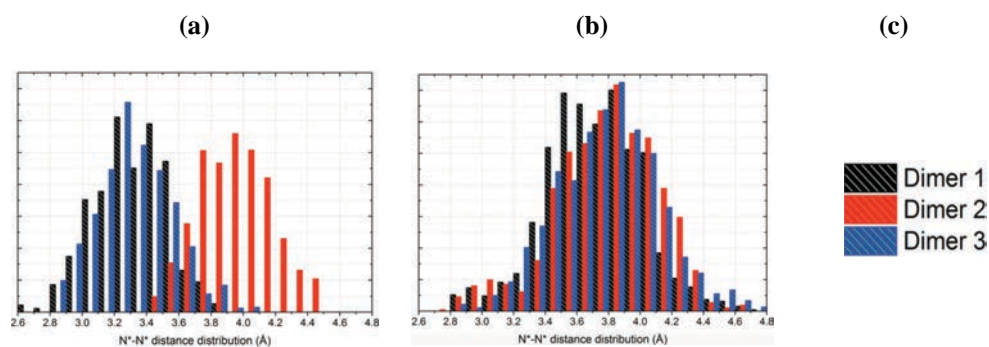


Figure 8.14: Distance distribution analysis of the HT-PDPTA at (a) 150 K and (b) 300 K, respectively. In (c) the color legend of the three dimers analysis from one extracted column for the respective AIMD trajectories.

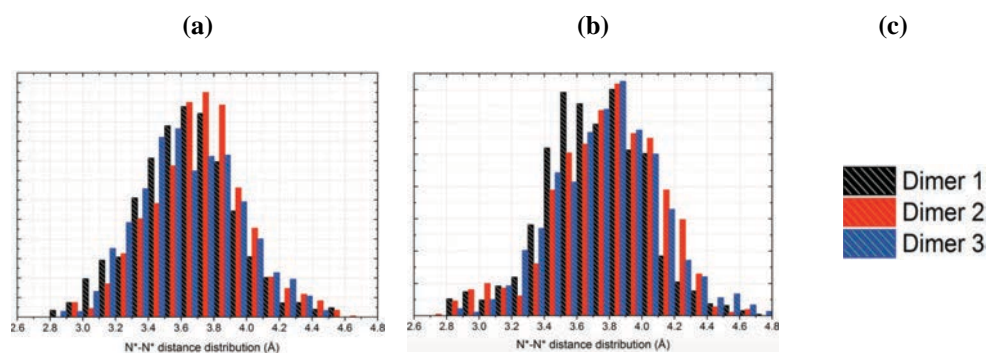


Figure 8.15: Distance distribution analysis of the HT-TDPDPTA at (a) 150 K and (b) 293 K, respectively. In (c) the color legend of the three dimers analysis from one extracted column for the respective AIMD trajectories.

These extended and detailed investigations point out, for the first time, the presence of a new stabilization mechanism operating in the HT temperature phase of the TDPDPTA material, that is found to be a minimum energy structure.

To assess the origin of the new mechanism, the key role played by the concomitant presence of three geometrical variables, thus d_{IP} , d_{SL} and d_{LG} , is explored both in the PDTA and TDPDTA cases, by employing a set of potential energy surfaces scans (see Figures 8.16 and 8.17). In particular, the d_{SL} and d_{LG} parameters span a set of predefined values, at fixed d_{IP} ranges (the interplanar distance is found to have the same behavior in the whole set of DTA-based materials).

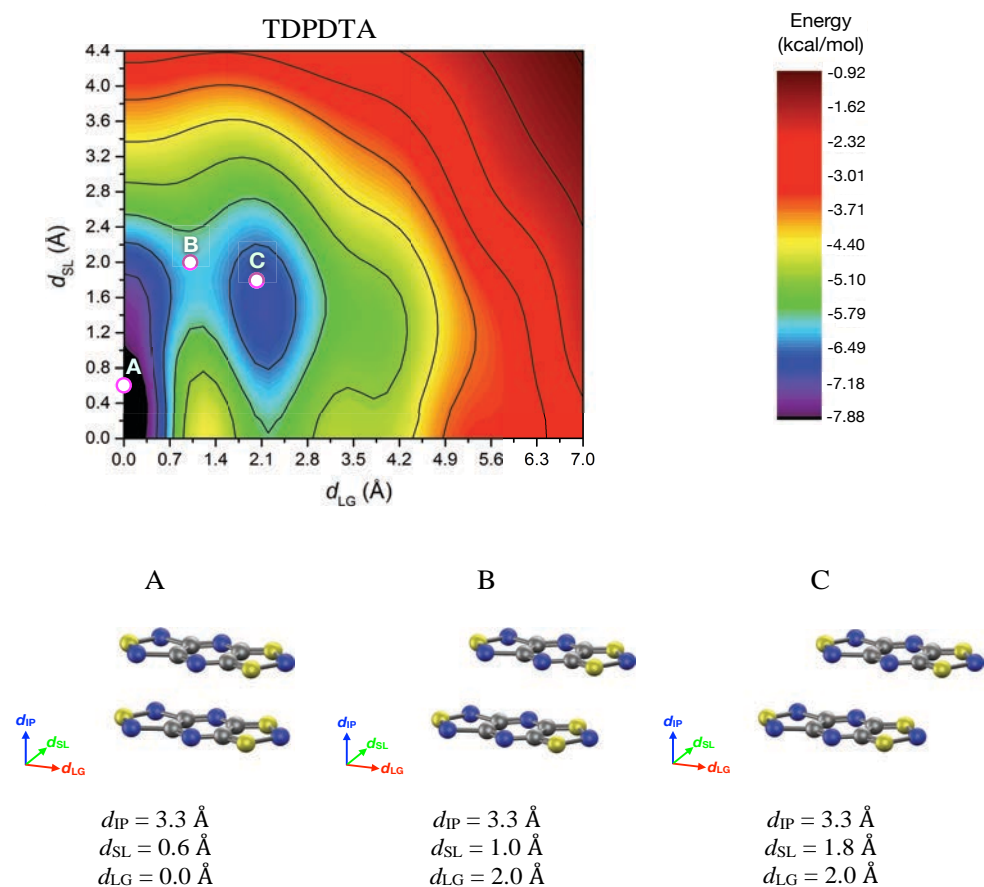


Figure 8.16: The scan map of the TDPDTA system. Note the presence of two minima in the PES, ideally connected by points A (= first minimum), B (= saddle point) and C (= second minimum).

In particular, by exploring the d_{LG} variable, a second minimum in the PES scans appears, in both cases. Yet, the chemistry of the two systems, in these points, is rather different.

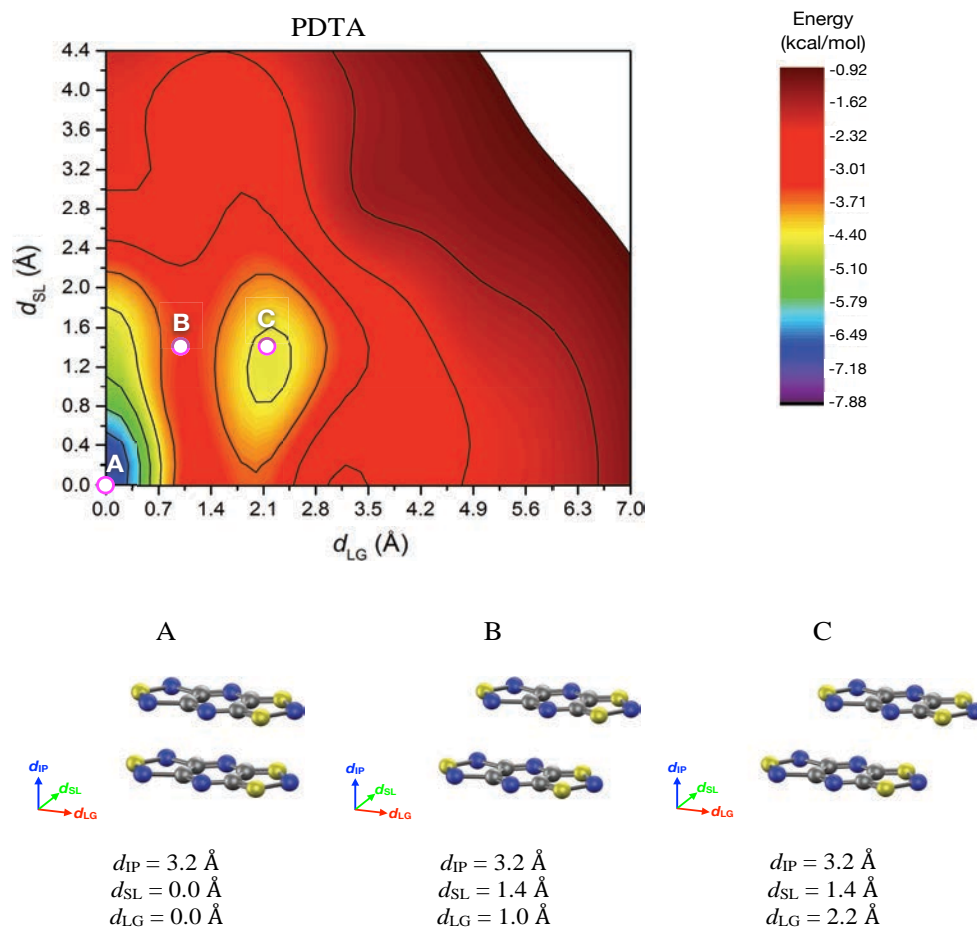


Figure 8.17: The scan map of the PDTA system. Note the presence of two minima in the PES, ideally connected by points A (= first minimum), B (= saddle point) and C (= second minimum)..

In fact, in the PDTA case it lies quite high in energy, as displayed by the minimum energy profile reported in Figure 6.20b of Chapter 6. The saddle point is found at *ca.* 3.5 kcal/mol with respect to the π -eclipsed configuration (where point A coincides with the dimer disposition found in the PDTA-LT phase), whereas the C point, corresponding to the second minimum is at *ca.* 2.5 kcal/mol with respect to A. This suggests that the system requires higher temperatures to populate point C. On the

contrary, in the TDPDTA case the energy barrier, coinciding with point B as found in Figure 6.20a of Chapter 6, is at *ca.* 2.3 kcal/mol with respect to point A (where point A coincides with the dimer disposition found in the TDPDTA-LT phase). But, differently from the previous case, the second minimum found in C (where point C coincides with the dimer disposition found in the TDPDTA-HT phase) lies quite close in energy to A ($\Delta AC \approx 1$ kcal/mol), differently from the PDTA case. The models employed in these scans are dimers. So, the picture outlined lacks of the information of the effect from the surrounding columns. Nevertheless, these models are able to catch the proper chemistry of the systems, in a simple and interpretative way. The new mechanism of spin transition is well described by these models as well as the corresponding energetics involved.

8.8 Discussion and Conclusions

In this work, we characterized and studied the properties associated to DTA-based bistable organic molecular magnetic systems, namely PDTA and TDPDTA, respectively. In both cases, the low and high temperature phases have been considered, in order to highlight the common and different physical-chemical properties, both from a structural perspective and also in terms of magnetic and thermodynamic properties. The high temperature phases are found to present a uniform stack propagation of the monomers in the columns, whereas the low temperature present, in the case of PDTA, π -dimers alternated to π -shifted dimers, and for TDPDTA, the same similar distribution but combined with a longitudinal slippage which induces a crystalline distortion. The study of these materials was divided into *static* and *dynamic* investigations, allowing for a systematic and step-by-step investigation, uncovering new and unexpected properties. In particular:

- We explored the origin of the different stability of the two TTTA polymorphs, LT and HT, highlighting the primary role played by the π - π intermolecular interactions as well as the S \cdots S/N bridges, in driving the crystal packing of the DTA-based molecular magnets;
- We studied the magnetic interactions of the PDTA and TDPDTA, both in the LT and HT phases, and defined how they propagate within the crystalline structures. Afterwards, these results have been used to compute the magnetic susceptibility curves for the LT and HT polymorphs, respectively, exploring several computational models, ranging from 0D to 3D systems. It was found, in both the systems, that for computational purposes, the best representative models for the LT and HT phases are the 1D models, where the spin centers align along the stacking direction of the molecular columns. This is due to the fact that the J_{AB} values are found to be much stronger along this direction than in the others. The data obtained for the compounds compare well with the experimental evidences of a diamagnetic LT phase, in both cases, and weakly paramagnetic in the HT ones. On the other hand, a deviation, in terms of magnitude of the magnetic couplings, is found for the respective phases of TDPDTA. These differences prompted the investigation of what might be the reason for its peculiar behavior;
- The study of the magnetic properties of the PDTA and the TDPDTA materials was complemented with a series of *in silico* experiments aimed at 1) predicting possible interesting FM molecular arrangements and 2) to benchmark, making use of a high level theoretical approach, our discoveries. Point 1) has been achieved by generating a series of magneto-structural correlation maps,

which, accounting for the simultaneous variation of two geometrical parameters (d_{IP} and d_{SL}) and the evaluation of the J_{AB} magnetic coupling for each dimer in the map, allowed to discover the presence of favorable and interesting FM regions. Nevertheless, the TDPDTA compound does not show any suitable FM area, again deviating from the other compounds behavior. The presence of the FM areas found in TTTA, PDTA and 4-NCBDTA have been tested in terms of energy cost to reach them. Only a small portion of the FM region is accessible, and only in the case of TTTA. In this tiny region, we benchmarked the DFT results for the J_{AB} values against DDCI-3. It was found that the signs of the couplings are in agreement, while the associated values of the couplings differ substantially. Nevertheless, these remarkable results prove the qualitative predictive capabilities of DFT and that, being aware of its limits, we can rely on it;

- Based on the previous results, we could plan a series of AIMD calculations aimed at studying the structural response of the PDTA and TDPDTA systems at different temperatures. How the systems respond to temperature and, indirectly, how the magnetic interactions are affected, is of primary importance when projecting the use of these materials for practical purposes. The additional investigation performed by computing the thermal ellipsoids of the two HT phases of PDTA and TDPDTA, as well as the performing the N*-N* distances analysis, proved the presence of new type of stabilization mechanism that is found to operate in the HT phase of the TDPDTA. By exploring the related PES scans and the key role of the d_{IP} , d_{SL} and d_{LG} geometrical variables, it was possible to assess their role in originating the new mechanism as well as the energetic involved in the process. The material undergoing to this *magnetic phase* transition mechanism can be exploited for building up a new generation of data storage devices, for instance.

The nature of the substituents is one of the keys to look at, in order to drive the synthesis of these new materials. In fact, it actually happens that the second stabilization mechanism is only found in the TDPDTA material, whereas the PED is featured by a wider spectrum of DTA-based compounds. Nevertheless, this should encourage researchers to pursue the synthesis and study materials that might present this new process. In fact, it is probable that other similar processes might be found to directly or indirectly affect the phase or spin transition, which have not yet been discovered.

Bibliography

- [1] M. A. Halcrow, *Spin-crossover materials: properties and applications*, John Wiley & Sons, **2013**.
- [2] O. Sato, *Nature chemistry* **2016**, *8*, 644.
- [3] O. Kahn, *Chemistry in Britain* **1999**, *35*, 24–27.
- [4] J. M. Rawson, A. Alberola, A. Whalley, *Journal of Materials Chemistry* **2006**, *16*, 2560–2575.
- [5] S. Vela, F. Mota, M. Deumal, R. Suizu, Y. Shuku, A. Mizuno, K. Awaga, M. Shiga, J. J. Novoa, J. Ribas-Arino, *Nature communications* **2014**, *5*, 4411.
- [6] S. Vela, M. B. Reardon, C. E. Jakobsche, M. M. Turnbull, J. Ribas-Arino, J. J. Novoa, *Chemistry—A European Journal* **2017**, *23*, 3479–3489.
- [7] S. Vela, M. Deumal, M. Shiga, J. J. Novoa, J. Ribas-Arino, *Chemical science* **2015**, *6*, 2371–2381.
- [8] M. Fujita, K. Yamada, H. Hiraka, P. Gehring, S. Lee, S. Wakimoto, G. Shirane, *Physical Review B* **2002**, *65*, 064505.
- [9] S. Vela, M. B. Reardon, C. E. Jakobsche, M. M. Turnbull, J. Ribas-Arino, J. J. Novoa, *Chemistry—A European Journal* **2017**, *23*, 3479–3489.
- [10] J. L. Brusso, O. P. Clements, R. C. Haddon, M. E. Itkis, A. A. Leitch, R. T. Oakley, R. W. Reed, J. F. Richardson, *Journal of the American Chemical Society* **2004**, *126*, 8256–8265.
- [11] T. Barclay, A. Cordes, N. George, R. Haddon, M. Itkis, M. Mashuta, R. Oakley, G. Patenaude, R. Reed, J. Richardson, et al., *Journal of the American Chemical Society* **1998**, *120*, 352–360.
- [12] C. S. Clarke, J. Jornet-Somoza, F. Mota, J. J. Novoa, M. Deumal, *Journal of the American Chemical Society* **2010**, *132*, 17817–17830.
- [13] M. Deumal, M. J. Bearpark, J. J. Novoa, M. A. Robb, *The Journal of Physical Chemistry A* **2002**, *106*, 1299–1315.

- [14] C. De Graaf, R. Broer, *Magnetic interactions in molecules and solids*, Springer, **2016**.
- [15] C. Herring, G. Rado, H. Suhl, *Magnetism edited by GT Rado und H. Suhl (Academic Press New York)* **1965**, *2*, 1–181.
- [16] A. D. Becke, *Physical review A* **1988**, *38*, 3098.
- [17] M. Frisch, G. Trucks, H. Schlegel, G. Scuseria, M. Robb, J. Cheeseman, G. Scalmani, V. Barone, B. Mennucci, G. Petersson, et al., *Gaussian Inc. Wallingford CT* **2009**.
- [18] P. C. Hariharan, J. A. Pople, *Theoretica chimica acta* **1973**, *28*, 213–222.
- [19] W. J. Pietro, M. M. Francl, W. J. Hehre, D. J. DeFrees, J. A. Pople, J. S. Binkley, *Journal of the American Chemical Society* **1982**, *104*, 5039–5048.
- [20] K. Kitaura, K. Morokuma, *International Journal of Quantum Chemistry* **1976**, *10*, 325–340.
- [21] P. Su, H. Li, *The Journal of chemical physics* **2009**, *131*, 014102.
- [22] H. Jónsson, G. Mills, K. W. Jacobsen in *Classical and quantum dynamics in condensed phase simulations*, World Scientific, **1998**, pp. 385–404.
- [23] P. Giannozzi, *J. Phys.: Condens. Matter* **2017**, *29*, 465901.
- [24] S. Grimme, *Journal of Computational Chemistry* **2006**, *27*, 1787–1799.
- [25] K. F. Garrity, *Computational Materials Science* **2014**, *81*, 446–452.
- [26] The Cambridge Crystallographic Data Centre (CCDC), <https://www.ccdc.cam.ac.uk/structures/>?
- [27] J. Hutter, M. Iannuzzi, F. Schiffmann, J. VandeVondele, *Wiley Interdisciplinary Reviews: Computational Molecular Science* **2014**, *4*, 15–25.
- [28] S. Goedecker, M. Teter, J. Hutter, *Phys. Rev. B* **1996**, *54*, 1703–1710.
- [29] C. Hartwigsen, S. Goedecker, J. Hutter, *Phys. Rev. B* **1998**, *58*, 3641–3662.
- [30] M. Krack, *Theoretical Chemistry Accounts* **2005**, *114*, 145.
- [31] J. VandeVondele, J. Hutter, *The Journal of Chemical Physics* **2007**, *127*, 114105.
- [32] S. Grimme, J. Antony, S. Ehrlich, H. Krieg, *The Journal of Chemical Physics* **2010**, *132*, 154104.
- [33] S. Vela, M. Deumal, M. Shiga, J. J. Novoa, J. Ribas-Arino, *Chem. Sci.* **2015**, *6*, 2371–2381.
- [34] J. P. Malrieu, R. Caballol, C. J. Calzado, C. de Graaf, N. Guihéry, *Chemical Reviews* **2014**, *114*, 429–492.

- [35] T. Francese, J. Ribas-Arino, J. J. Novoa, R. W. Havenith, R. Broer, C. de Graaf, M. Deumal, *Phys. Chem. Chem. Phys.* **2018**, *20*, 20406–20416.

Appendices

Appendix A

Supplementary Information of Chapter 5

A.1 Spin Density of TTTA, PDTA, 4-NCBDTA and TDPDTA

The spin density is mainly localised in the dithiazolyl (DTA) ring that is formally hosting the unpaired electron (see Figure A1.1). It has been calculated at UB3LYP/6-31+G(d) level. Note that in the case of TDPDTA, the degree of delocalisation of the spin density on the fused rings to the DTA-moiety is larger than in the other three compounds. We will show that this delocalisation can be related to the peculiar behavior that this compound reflects in its crystal packing and magnetic properties, as reported in the analysis presented in the Results and Discussion Section of main text.

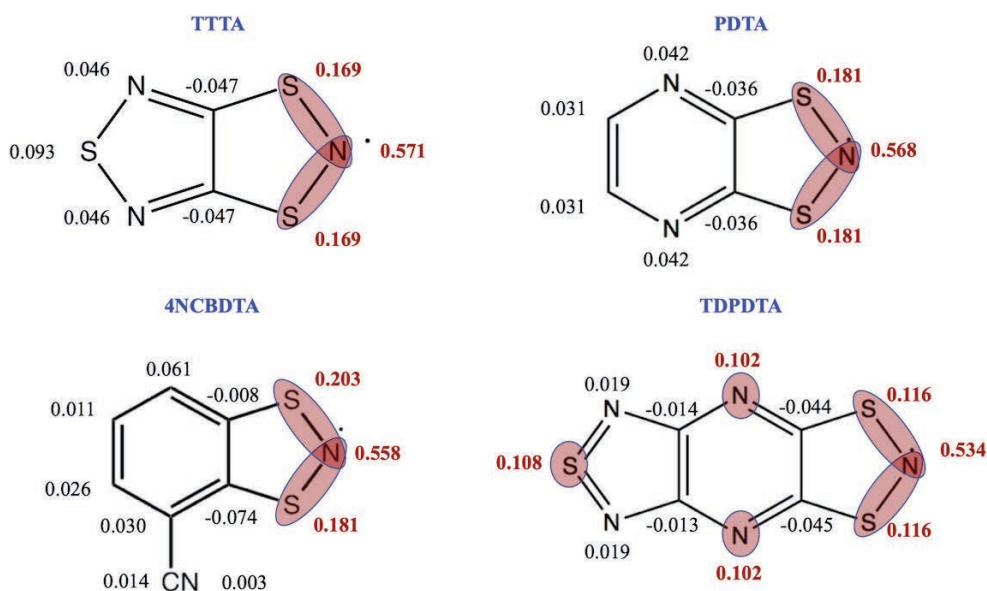
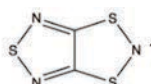
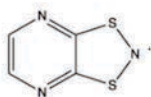


Figure A1.1: Spin Distribution of TTTA, PDTA, 4-NCBDTA and TDPDTA. The spin density is computed at DFT/UB3LYP level with 6-31+G(d) basis set using Gaussian09 package.

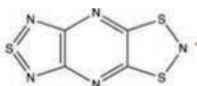
A.2 Atomic coordinates of LT and HT magnetically dominant pairs of radicals for TTTA, PDTA, TDPDTA, and 4-NCBDTA.



TTTA (LT)				TTTA (HT)			
S	7.017869	3.528611	2.391652	C	-5.404471	3.289059	27.295334
S	6.860811	0.922766	5.877941	C	-5.404471	7.000060	27.295334
S	6.283892	3.661160	5.589922	C	-4.215476	2.779168	27.910383
S	2.864724	1.439537	5.066989	C	-4.215476	6.490168	27.910383
S	3.650688	1.282305	1.653478	N	-6.409525	3.476836	28.124630
N	4.940720	0.299579	1.959795	N	-6.409525	7.187836	28.124630
C	5.658859	2.500437	2.070545	N	-3.667667	3.044876	25.428326
N	7.405249	2.485445	5.873195	N	-3.667667	6.755876	25.428326
C	5.190507	1.246917	5.542320	S	-2.901669	2.530902	26.809999
N	4.151770	0.453770	5.383418	S	-2.901669	6.241902	26.809999
N	4.395377	2.742960	1.781632	S	-5.239064	3.539181	25.587189
C	5.967436	1.101723	2.175104	S	-5.239064	7.250181	25.587189
N	3.626287	2.895732	5.138529	N	-4.331583	2.579887	29.208981
C	4.893901	2.643292	5.398551	N	-4.331583	6.290887	29.208981
N	8.142387	2.351230	2.686206	S	-5.864902	3.030031	29.612698
S	7.622173	0.787062	2.602696	S	-5.864902	6.741031	29.612698



PDTA (LT)				PDTA (HT)			
S	11.420697	3.386343	5.954659	S	13.641384	0.505276	19.956530
S	12.086512	3.019699	8.648816	S	13.641384	4.223276	19.956530
N	11.608969	6.097880	6.269624	S	11.330449	1.492777	18.741070
N	11.704055	2.329956	7.200106	S	11.330449	5.210777	18.741070
N	12.281935	5.717186	9.005960	N	12.479155	0.768139	22.394579
C	11.691873	4.886400	6.815408	N	12.479155	4.486138	22.394579
C	12.033943	4.701696	8.162380	N	12.865252	0.937308	18.557928
C	12.152071	6.920034	8.447459	N	12.865252	4.655308	18.557928
H	12.284244	7.667953	8.984765	N	10.158782	1.818846	21.164713
C	11.834007	7.122205	7.121682	N	10.158782	5.536846	21.164713
H	11.773183	7.993818	6.802690	C	12.377047	0.906077	21.084503
S	8.203823	3.411146	6.668417	C	12.377047	4.624077	21.084503
S	8.824556	3.017956	9.373914	C	11.216861	1.426968	20.469570
N	8.856610	5.707689	9.794433	C	11.216861	5.144969	20.469570
N	8.246903	6.116859	7.050677	C	10.277138	1.670497	22.482214
C	8.675016	4.699078	8.936016	C	10.277138	5.388497	22.482214
C	8.380676	4.903523	7.571026	H	9.570744	1.941911	23.024366
C	8.440322	7.112913	7.905915	H	9.570744	5.659911	23.024366
H	8.376490	7.983756	7.586923	C	11.392958	1.134734	23.080811
C	8.733759	6.926567	9.255008	C	11.392958	4.852734	23.080811
H	8.847609	7.673074	9.797611	H	11.393660	1.023565	24.003210
N	8.516750	2.355026	7.902736	H	11.393660	4.741565	24.003210

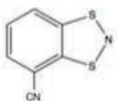


TDPDTA (LT)

S	5.440273	2.844307	1.777912
S	4.493224	3.695218	4.232299
S	7.014531	8.888763	1.868495
N	6.354748	5.307971	1.175639
N	5.341591	6.205177	3.764935
N	4.719520	2.471524	3.194461
N	7.093616	7.548491	0.955929
N	6.228106	8.319828	3.150133
C	5.731672	4.545158	2.046768
C	6.488840	6.582737	1.622767
C	5.980711	7.045249	2.909224
C	5.214939	4.970018	3.345752
S	2.151970	4.001494	1.361621
N	3.134270	6.460264	0.824874
N	3.900130	8.687148	0.612874
C	2.790346	8.128676	2.552678
C	3.289093	7.717694	1.279711
C	2.482656	5.680455	1.673840
N	1.356586	3.627508	2.739623
N	2.135635	7.324135	3.435370
N	3.026743	9.446116	2.810933
C	2.007699	6.089762	2.970896
S	1.244345	4.813554	3.842026
S	3.822868	10.014162	1.534112

TDPDTA (HT)

S	4.191966	13.421474	1.587884
S	8.637566	13.421474	1.587884
S	5.157586	12.222906	3.890637
S	1.288139	7.895475	1.605201
S	5.733740	7.895475	1.605201
N	2.655645	11.282433	1.022916
N	7.101244	11.282433	1.022916
N	3.723209	9.995331	3.422793
N	8.168810	9.995331	3.422793
N	5.144155	13.532299	2.910877
N	1.391520	9.287677	0.775250
N	5.837120	9.287677	0.775250
N	2.331975	8.177945	2.806514
N	6.777575	8.177945	2.806514
C	3.537994	11.840479	1.832710
C	7.983594	11.840479	1.832710
C	2.284055	10.042721	1.422224
C	6.729655	10.042721	1.422224
C	2.817256	9.401522	2.604112
C	7.262856	9.401522	2.604112
C	4.057328	11.208543	3.027608
C	8.502928	11.208543	3.027608
N	9.589755	13.532299	2.910877
S	9.603187	12.222906	3.890637



4-NCBDTA (LT)

S	1.118100	1.868779	6.428535
S	0.407686	1.070790	3.867140
N	0.770323	0.616836	5.411868
N	1.922761	5.329255	7.922333
C	0.985822	3.188674	5.298812
C	0.613933	2.801671	4.008739
C	0.440654	3.734704	2.992912
H	0.197270	3.458905	2.117006
C	0.630364	5.072871	3.283948
H	0.509699	5.718685	2.596936
C	0.992128	5.492136	4.551633
H	1.111683	6.416747	4.733531
C	1.179935	4.551394	5.564383
C	1.587664	4.988647	6.878521
S	4.975579	2.107463	6.834866
S	4.350674	1.082924	4.339653
N	4.697307	0.762872	5.911947
N	5.492218	5.639742	8.095835
C	4.693814	3.330142	5.624828
C	4.352426	2.828365	4.364139
C	4.090179	3.673034	3.289545
H	3.857384	3.317580	2.440224
C	4.176156	5.039181	3.481237
H	3.994744	5.625896	2.755046
C	4.522564	5.570222	4.718139
H	4.583861	6.510964	4.831476
C	4.780760	4.722269	5.788536
C	5.160791	5.252739	7.074410

4-NCBDTA (HT)

S	2.331424	6.021108	4.075249
S	3.057357	5.153251	6.616846
N	2.700199	6.441206	5.610444
N	0.118001	1.691282	8.015320
C	2.488163	4.289837	4.188551
C	2.864778	3.868450	5.463206
C	3.055355	2.491058	5.701591
C	2.823176	1.602418	4.659711
H	3.015437	0.845641	4.879866
C	2.459700	2.048172	3.406090
H	2.296612	1.433290	2.706362
C	2.291051	3.385431	3.163499
H	1.966441	3.683555	2.355797
C	-0.213923	2.035272	6.994474
C	3.451177	2.035272	6.994474
C	-0.609745	2.491058	5.701591
N	3.783102	1.691282	8.015320
C	-0.841924	1.602418	4.659711
C	-0.800322	3.868450	5.463206
H	-0.649663	0.845641	4.879866
C	-1.205400	2.048172	3.406090
C	-1.176938	4.289837	4.188551
S	-0.607743	5.153251	6.616846
H	-1.368488	1.433290	2.706362
C	-1.374049	3.385431	3.163499
S	-1.333676	6.021108	4.075249
N	-0.964901	6.441206	5.610444
H	-1.698659	3.683555	2.355797

A.3 Selection of magnetic model of PDTA and TDPDTA.

The calculation of the magnetic susceptibility χ curves, both for the LT/HT phases of PDTA and TDPDTA, follows the selection process accurately described by Clarke et al¹. Here, we report the corresponding curves of $\chi T(T)$ for the best models for PDTA and TDPDTA compounds.

Based upon the value of the calculated J_{AB} magnetic couplings, we investigated several arrangements of the spin-carrying radicals, *i.e.* 1D, 2D and 3D magnetic models have been explored. This study has been performed both for the LT and HT phases of the PDTA and TDPDTA. The magnetic models selected propagate along a, b and c axes, and reproduce the magnetic topology of the crystal accordingly.

1D magnetic models consist of n radicals magnetically connected along the DTA π -stacking direction, *i.e.* chains of n spins containing radicals ($n = 4, 8, 12$ or 16). 2D magnetic models contain a given m number of 1D chains that are connected by J_{AB} magnetic couplings. Finally, 3D magnetic models involve J_{AB} magnetic interactions along all three crystallographic axes.

Here we report the magnetic susceptibility calculated using some examples of 1D, 2D and 3D magnetic models (see Figure A3.1, A3.2 and A3.3). Note that in the schematic representation of the magnetic models each radical has been replaced by a point-spin-center.

The $\chi T(T)$ data computed using all magnetic models for LT-PDTA and LT-TDPDTA converge to the same calculated χT data irrespective of the dimensionality (1D, 2D or 3D) because the antiferromagnetic J_{AB} π -stack coupling is orders of magnitude larger than any other J_{AB} interaction between pairs of radicals within the crystal (see Figures A3.1, A3.2 and A3.3). Specifically, the exceedingly large AFM J_{AB} interaction (LT-PDTA -1656.8 cm^{-1} ; LT-TDPDTA -781.3 cm^{-1}) along the DTA π -stacking direction of the crystal results in the crystal being magnetically silent.

¹ C.S. Clarke, J. Jornet-Somoza, F. Mota, J.J. Novoa, M. Deumal, J. Am. Chem. Soc. 2010, 132, 17817-17830

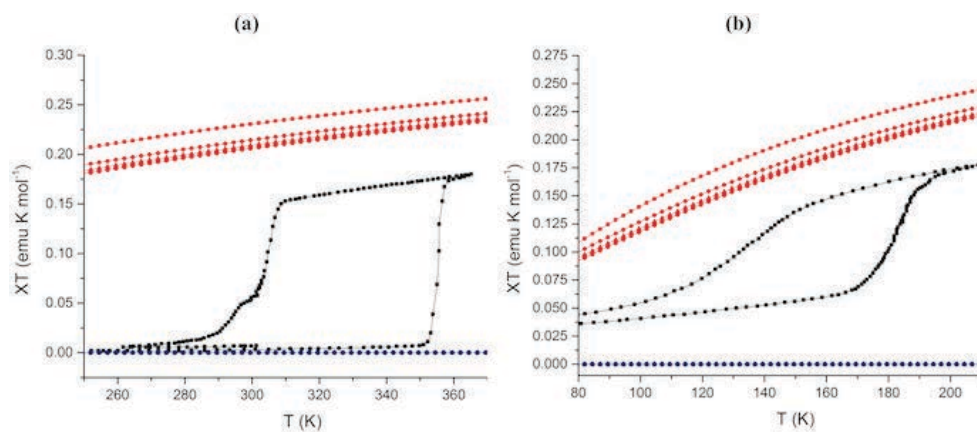
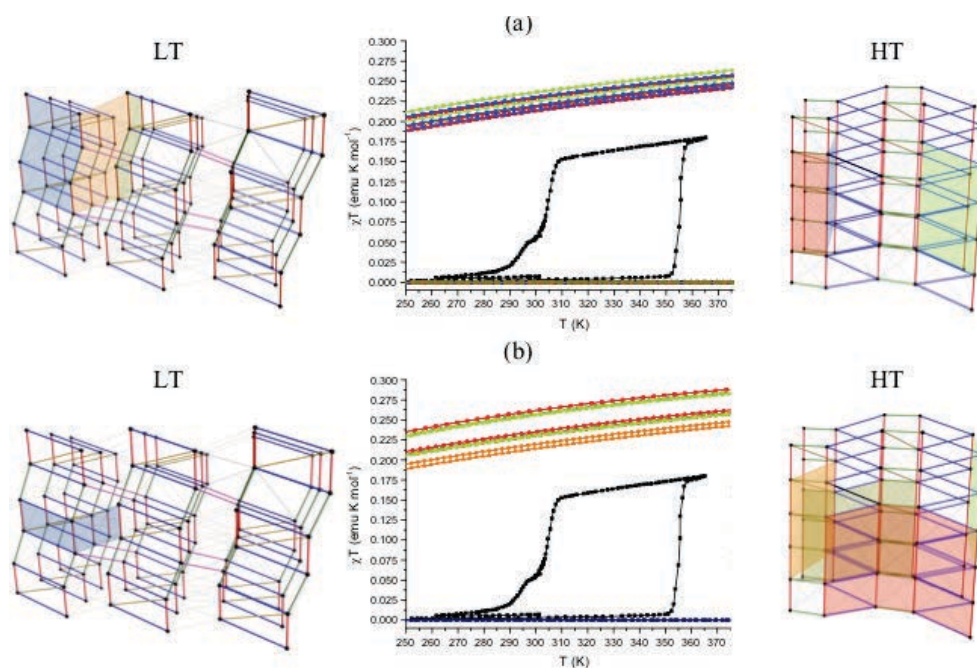


Figure A3.1: Comparison between experimental $\chi T(T)$ data in black and calculated LT and HT $\chi T(T)$ data in blue and red, respectively, using 1D magnetic models made of chains of n spin-containing DTA-radicals ($n = 4$ (■), 8 (●), 12 (▲) or 16 (◆) for (a) PDTA and (b) TDPDTA).



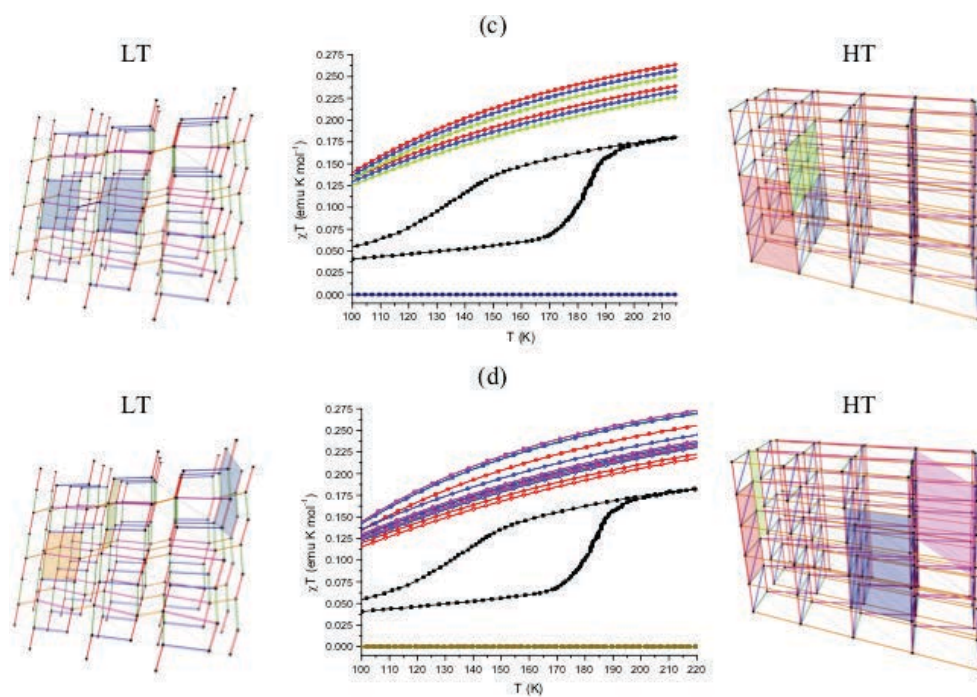


Figure A3.2: Comparison between experimental $\chi T(T)$ data in black and calculated LT and HT $\chi T(T)$ data for (a,b) PDTA and (c,d) TDPDTA, using 2D magnetic models as schematically represented at right and left. Note that the color code is in agreement with the color sketching the magnetic model. Note also that as the chain length increases with DTA-radicals the symbol changes from (■) to (●) and finally (▲).

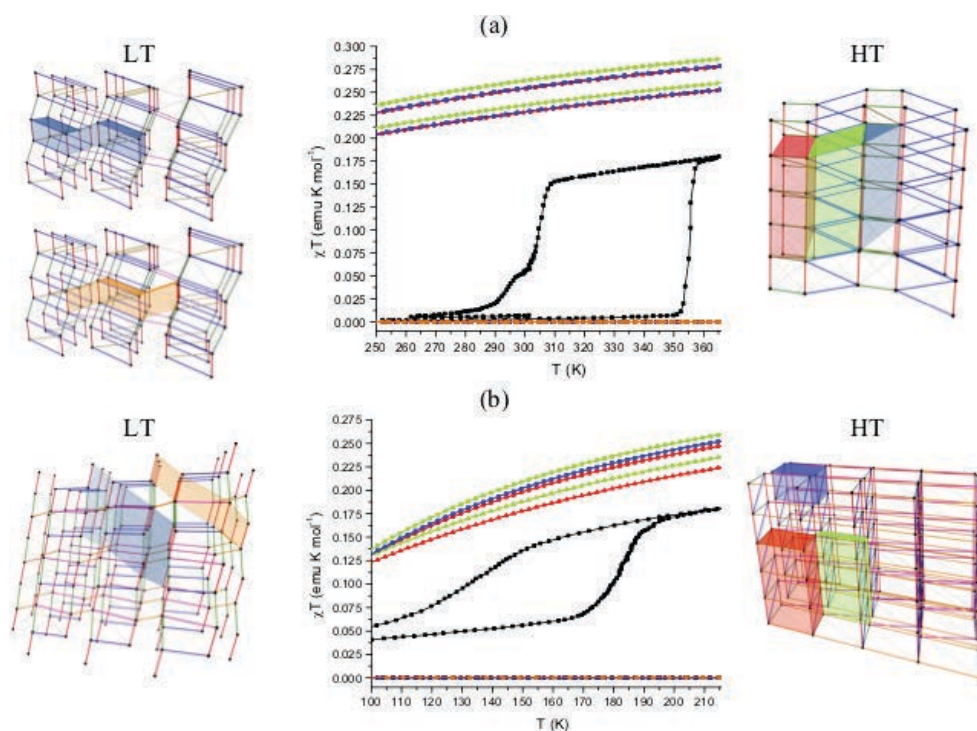


Figure A3.3: Comparison between experimental $\chi T(T)$ data in black and calculated LT and HT $\chi T(T)$ data for (a) PDTA and (b) TDPDTA, using 3D magnetic models as schematically represented at right and left. Note that the color code is in agreement with the color sketching the magnetic model. Note also that as the chain length increases with DTA-radicals the symbol changes from (■) to (●) and finally (▲).

In general, for both HT-PDTA and HT-TDPDTA, increasing the magnetic model size implies an improvement of the model performance to reproduce the experimental data. Figures A3.1-A3.3 show that, for a number of models the best convergence is always achieved using the largest magnetic model. For instance, for 1D magnetic models, in both HT cases, the calculated $\chi T(T)$ data converge to the experimental data as n enlarges (see Figure A3.1).

As for 2D and 3D magnetic models, it is possible to see that the calculated $\chi T(T)$ data for HT-PDTA not only converges as the model increases (see Figures A3.2a-b and A3.3a) but also overlap with the $\chi T(T)$ data obtained using the 1D model with chain-length alike ($J_{\pi\text{-stack}} = -110.5 \text{ cm}^{-1}$ and $J_{\text{inter-}\pi\text{-stack}} \leq |10.1| \text{ cm}^{-1}$) (see Figure A3.4a for 3D and 1D overlap). Therefore, for simulation purposes a 1D magnetic

model is adequate for HT-PDPA. On the contrary, for HT-TDPDPA, comparison between $\chi T(T)$ data calculated using 2D and 3D models against 1D with chain-length alike shows that increasing the dimensionality matters in this case (see Figure A3.4b for 3D and 1D overlap). This is due to the fact that J_{AB} π -stack (-69.1 cm^{-1}) and inter- π -stack ($\leq |-23.8| \text{ cm}^{-1}$) couplings have more similar magnitude than for HT-PDPA.

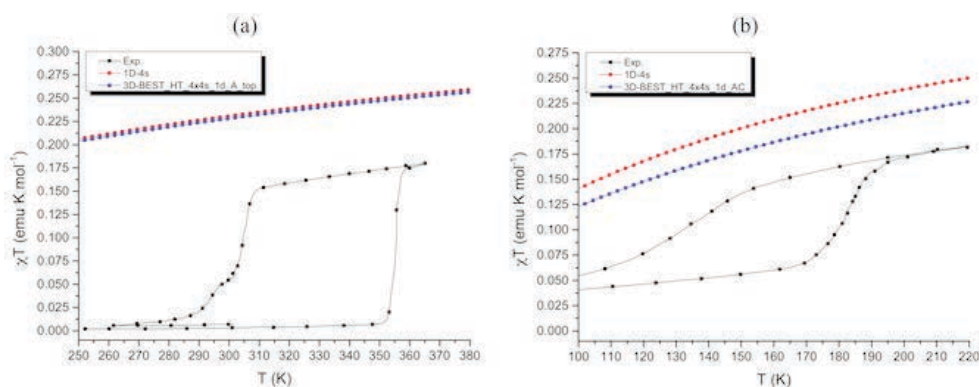


Figure A3.4: Overlap of $\chi T(T)$ data obtained using 3D (blue) and 1D (red) magnetic models with chain-length alike for (a) HT-PDPA and (b) HT-TDPDPA. Experimental $\chi T(T)$ data in black is also shown.

Furthermore, it can also be clearly observed that, although calculated and experimental $\chi T(T)$ values show the correct trend, neither LT-TDPDPA nor HT-TDPDPA $\chi T(T)$ data show numerical agreement with the experimental curve (see Figures A3.1b, A3.2c-d, and A3.3b). In first approximation, we believe that this is related to the presence of thermal fluctuations that affect the magnetic response of both phases. Further investigation will be carried out in the future. Nevertheless, the improvement is to some extent small enough to enable us to simulate $\chi T(T)$ using 1D magnetic models.

To sum up, simulated $\chi T(T)$ data using simple 1D models shows good agreement with experiment for both PDPA and TDPDPA. Therefore, analyses of the 3D magnetic topology of PDPA and TDPDPA crystals enable us to conclude that 1D magnetic models are adequate for simulation of magnetic properties.

A.4 Benchmarking the J_{AB} magnetic coupling interactions computed at DFT/UB3LYP level with Difference Dedicated Configuration Interaction (DDCI-3) method.

The objective of the benchmarking process described here is to corroborate the sign and value predicted by DFT/UB3LYP² using the standard 6-31+G(d)³ basis set for J_{AB} interactions. We will thus evaluate four FM TTTA dimers from the corresponding magneto-structural correlation map (see A-D models in Figure A3.1) at Difference Dedicated Configuration Interaction⁴ (DDCI-3) level. Moreover, the HT-TTTA experimental dimer is also evaluated and compared to the corresponding DFT results.

First of all, the single TTTA monomer is analysed within the Hückel⁵ theory framework, using the HuLiS⁶ program. All possible π -orbital combinations are identified in a simplistic way, as reported in Figure A4.2.

According to the Hückel model for TTTA, we have eight π -orbitals, which are occupied by eleven π -electrons. The singly occupied molecular orbital (SOMO) hosts the unpaired electron mainly on the nitrogen of the DTA-ring (Figure A4.2f). This is in qualitative agreement with a ROHF calculation with minimal STO-3G⁷ basis set. Subsequently, the ROHF/STO-3G wave functions were taken as initial guess orbitals for a CASSCF(11,8)/STO-3G calculation. This calculation was done in order to generate a good initial set of orbitals, and to directly select the π -orbitals to include in the active space for subsequent CASSCF calculations with the larger def2-TZVP⁸

² (a) A.D. Becke, Phys. Rev. A 1988, 38, 3098; (b) C. Lee, W. Yang, R.G. Parr, Phys. Rev. B 1988, 37, 785.

³ (a) P.C. Hariharan, J.A. Pople, Theor. Chim. Acta. 1973, 28, 213; (b) M.M. Francl, W.J. Pietro, W.J. Hehre, J.S. Binkley, M.S. Gordon, D.J. DeFrees, J.A. Pople, J. Chem. Phys. 1982, 77, 3654.

⁴ (a) J. Miralles, J. P. Daudey, R. Caballol, Chem. Phys. Lett. 1992, 198, 555; (b) J. Miralles, O. Castell, R. Caballol, J.-P. Malrieu, Chem. Phys. 1993, 172, 33.

⁵ E. Hückel, Zeitschrift für Physik 1931, 70, 204; *ibid* 1931, 72, 310; *ibid* 1932, 76, 628; *ibid* 1933, 83, 632.

⁶ Y. Carissan, et al. HuLiS Code: Lewis embedded in Hückel Theory, <http://www.hulis.free.fr>; Y. Carissan, D. Hagebaum-Reignier, N. Goudard, S. Humbel, J. Phys. Chem. A. 2008, 112, 13256-13262.

⁷ (a) W.J. Henre, R.F. Steward, J.A. Pople, J. Chem. Phys., 1969, 51, 2657-64; (b) J.B. Collins, P.v.R. Schleyer, J.S. Binkley, J. A. Pople, J. Chem. Phys., 1976, 64, 5142-51.

⁸ (a) F. Weigend, R. Ahlrichs, Phys. Chem. Chem. Phys., 2005, 7, 3297-305; (b) F. Weigend, Phys. Chem. Chem. Phys., 2006, 8, 1057-65.

basis set. These calculations were performed with the Orca⁹ code, version 4.0.0.2.

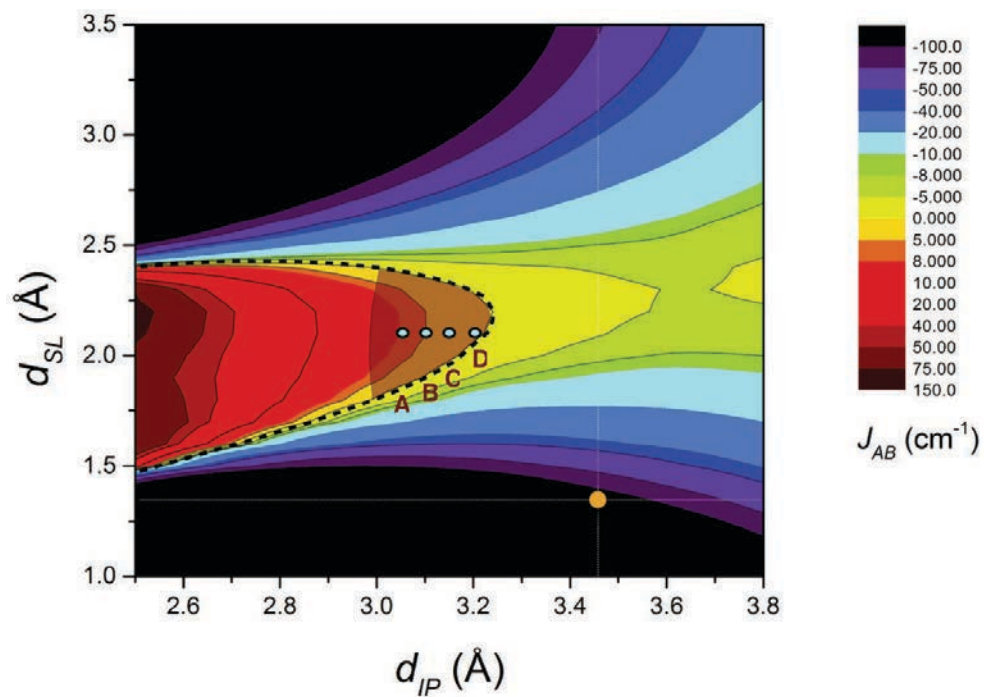


Figure A4.1: Magneto-structural correlation map showing the four TTTA models, referred to as A, B, C and D, extracted from the FM area. The orange dot represents the position of the HT-TTTA experimental dimer as a function of d_{IP} and d_{SL} .

⁹ F. Neese, "The ORCA program system". Wiley Interdisciplinary Rev: Computational Molecular Science. 2012, 2, 73-78.

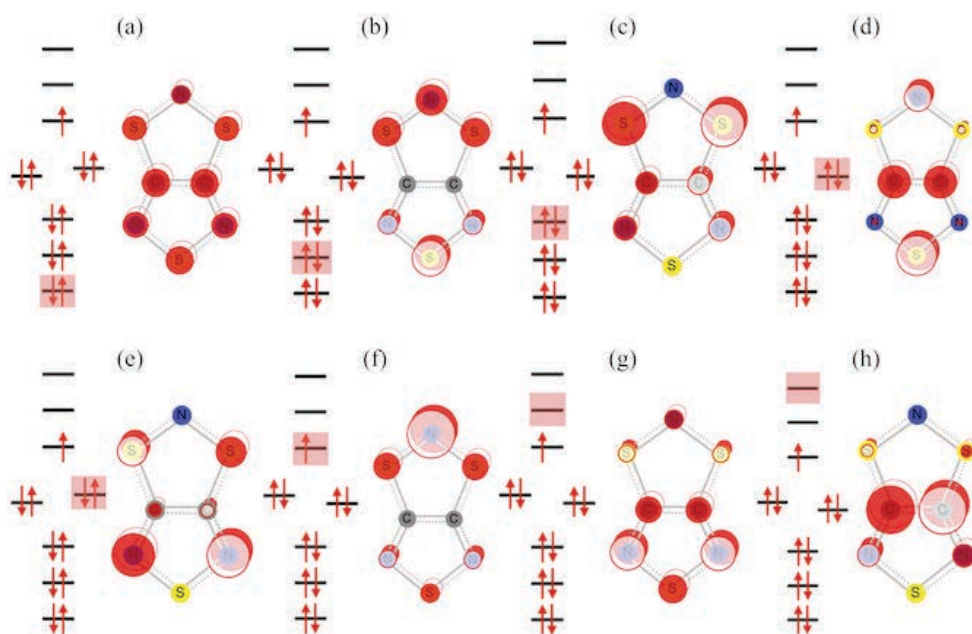


Figure A4.2: Hückel model of the TTTA prototype compound, which highlights the relevant π -orbitals and corresponding energy levels (a)-(h). The SOMO representation is orbital (f).

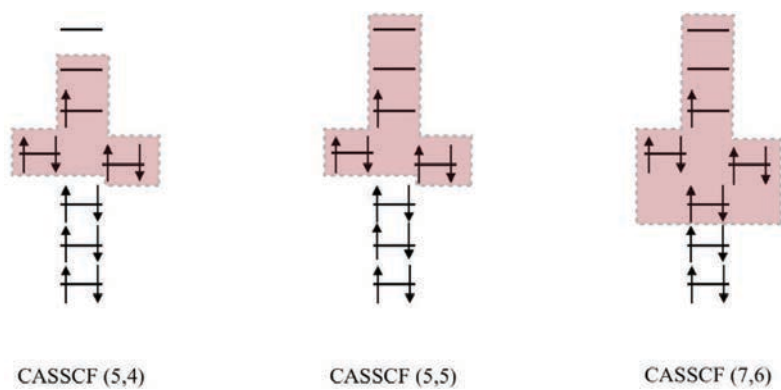
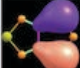
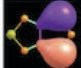
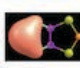

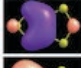
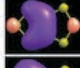
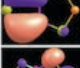
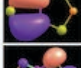
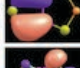

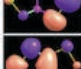
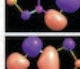
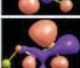




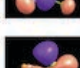



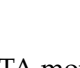

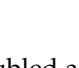


Figure A4.3: Different active spaces used for the TTTA monomer in the CASSCF(n, m) calculations, where n stands for number of electrons and m for number of orbitals.

We evaluated three possible active spaces: CASSCF(5,4), CASSCF(5,5) and CASSCF(7,6) (Figure A4.3).

A comparison between total energies, occupation number and orbital character for the three active spaces is reported in Table A4.1. Whereas the addition of a formally unoccupied orbital to the complete active space CAS leads to significant energy lowering and important changes in the natural occupation numbers, including an extra doubly occupied orbital does not affect the multiconfigurational wave function. Hence, the CASSCF (5,5) appears to be the most appropriate active space to take as reference.

Table A4.1: Three Complete Active Spaces (CAS) are evaluated for the TTTA monomer, namely, (a) CASSCF (5,4), (b) CASSCF(5,5) and (c) CASSCF(7,6). In each corresponding block, the total energy (E_T), the occupancy (Occ.) and the orbitals included in the respective active spaces (highlighted in yellow) are reported. Notice that only π -orbitals are used.

(a)				(b)				(c)			
CASSCF (5,4)				CASSCF (5,5)				CASSCF (7,6)			
E_T (E _h)				E_T (E _h)				E_T (E _h)			
-1431.7218				-1431.7535				-1431.7569			
	Occ.	Orb.			Occ.	Orb.			Occ.	Orb.	
HOMO-3	2	π		HOMO-3	2	π		HOMO-3	1.99	π	
HOMO-2	1.98	π		HOMO-2	1.94	π		HOMO-2	1.94	π	
HOMO-1	1.94	π		HOMO-1	1.90	π		HOMO-1	1.90	π	
SOMO	1	π		SOMO	1	π		SOMO	1	π	
LUMO	0.07	π		LUMO	0.11	π		LUMO	0.11	π	
LUMO+1	0	σ		LUMO+1	0.06	π		LUMO+1	0.06	π	
LUMO+2	0	σ		LUMO+2	0	σ		LUMO+2	0	σ	

Moving from the TTTA monomer to the TTTA dimer, the CAS space is doubled accordingly, preserving the orbital set as found in the TTTA monomer. CASSCF(10,10)

calculations are thus the new starting point to perform DDCI-3 higher level wave function calculations. In particular, our analysis was extended to four dimers from the TTTA ferromagnetic FM area and the experimental dimer configuration taken from the high temperature crystal structure (see Figure A4.1). Here we highlight the general idea behind DDCI-3¹⁰.

Using the CASSCF wave function as reference, DDCI generates eight different types of excited Slater determinants. As illustrated in Figure A4.4, these determinants can be classified according to the number of holes and electrons in the occupied and virtual orbitals, respectively. The DDCI-3 variant considers all determinants except those with 2 holes and 2 particles (*2h-2p*). Although this class is the most numerous and contributes typically more than 90% to the total correlation energy, its contribution to the vertical energy difference between electronic states is negligible and can be left out when aiming at magnetic coupling parameters.

Using the CASSCF(10,10) wave functions as reference would lead to an unmanageably large CI wave function. Moreover, it has been shown that accurate DDCI estimates can be obtained with a reference that includes just the minimal active space¹¹. Therefore, we reduce the active space to two orbitals and two electrons, and express the Slater determinants with the molecular orbitals optimized in the CASSCF(10,10) calculation.

¹⁰ (a) P. de Loth, P. Cassoux, J.-P. Daudey, J.-P. Malrieu, J. Am. Chem. Soc. 1981, 103, 4007. (b) J.-P. Malrieu, J. Chem. Phys. 1967, 47, 4555. (c) J.-P. Malrieu, P. Claverie, S. Diner, Theor. Chim. Acta 1968, 8, 404

¹¹ (a) E. Bordas, R. Caballol, C. de Graaf, J.P. Malrieu, Chem. Phys., 2005, 309, 259-269. (b) J.P. Malrieu, R. Caballol, C.J. Calzado, C. de Graaf, N. Guihery, Chem. Rev., 2013, 114, 429-492.

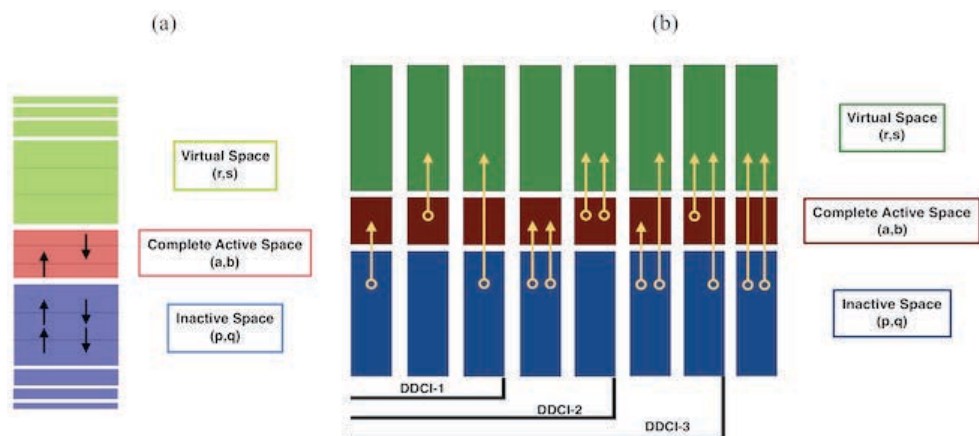


Figure A4.4: Schematic representation of (a) the MO set partition and (b) DDCI-1, DDCI-2 and DDCI-3 configurations.

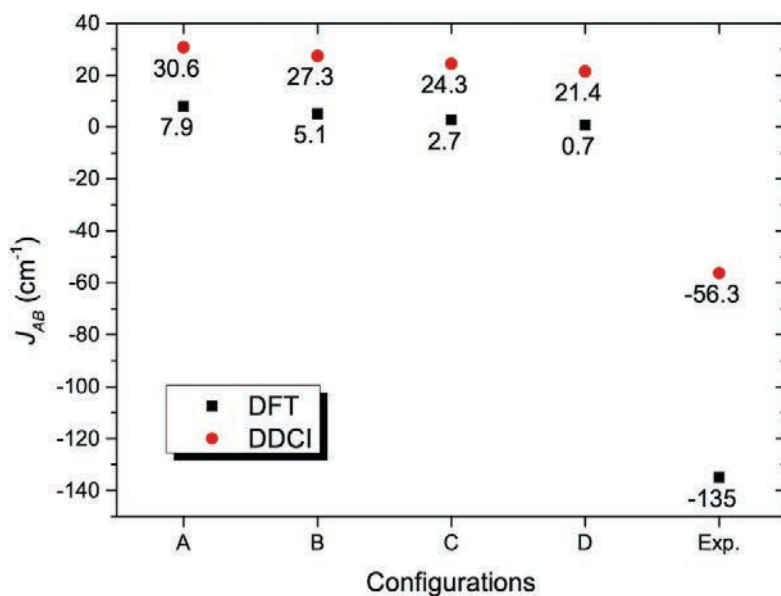


Figure A4.5: Comparison between J_{AB} magnetic coupling calculated at DFT and DDCI level for four TTTA models sampled from the FM area of the magneto-structural correlation map (A-D) and for the HT-TTTA experimental dimer.

Table A4.2: Value of J_{AB} interactions for A, B, C and D models and HT-TTTA experimental dimer at DFT and DDCI-3 levels. Note that J_{AB} at DDCI(2,2) level is defined as $J_{AB} = \Delta E/2$, where $\Delta E = E_S^{\text{DDCI}(2,2)} - E_T^{\text{DDCI}(2,2)}$. All DFT calculations are performed with Gaussian09¹² at UB3LYP/6-31+G(d) level. ^aThis value has been reported in literature¹³.

	J_{AB}/cm^{-1}				Exp. Dimer
	Model A	Model B	Model C	Model D	
DFT	7.9	5.1	2.7	-0.7	-135.0 ^a
DDCI(2,2)	30.6	27.3	24.3	21.4	-56.3

The calculations were performed in two steps:

1. State-average CASSCF(10,10) for the singlet and triplet states starting from the same set of orbitals (state-average), using def2-TZVP as basis set;
2. DDCI calculation using the previously generated CASSCF(10,10) orbitals, without further orbital optimization, including all single and double vertical excitations (the reference wave function was the CASCI(2,2) wave function).

In Table A4.2 and Figure A4.5, the results for each model at DDCI-3 level are reported, and compared with the DFT counterpart. It can be clearly seen that the FM trend in J_{AB} predicted at DFT level, is well reproduced at DDCI-3 high level theoretical wave function method. Therefore, our calculations have corroborated that the sign and value predicted by DFT/UB3LYP using the standard 6-31+G(d) basis set for J_{AB} interactions can be qualitatively trusted.

A.5 TDPDTA shifted configurations.

To stress the complex behaviour of the TDPDTA compound, an extra analysis has been performed showing that, in this specific case, not only the variables referring to the interplanar distance d_{IP} and lateral slippage d_{SL} have to be taken into account, but also the longitudinal translation d_{LG} between monomers has to be considered.

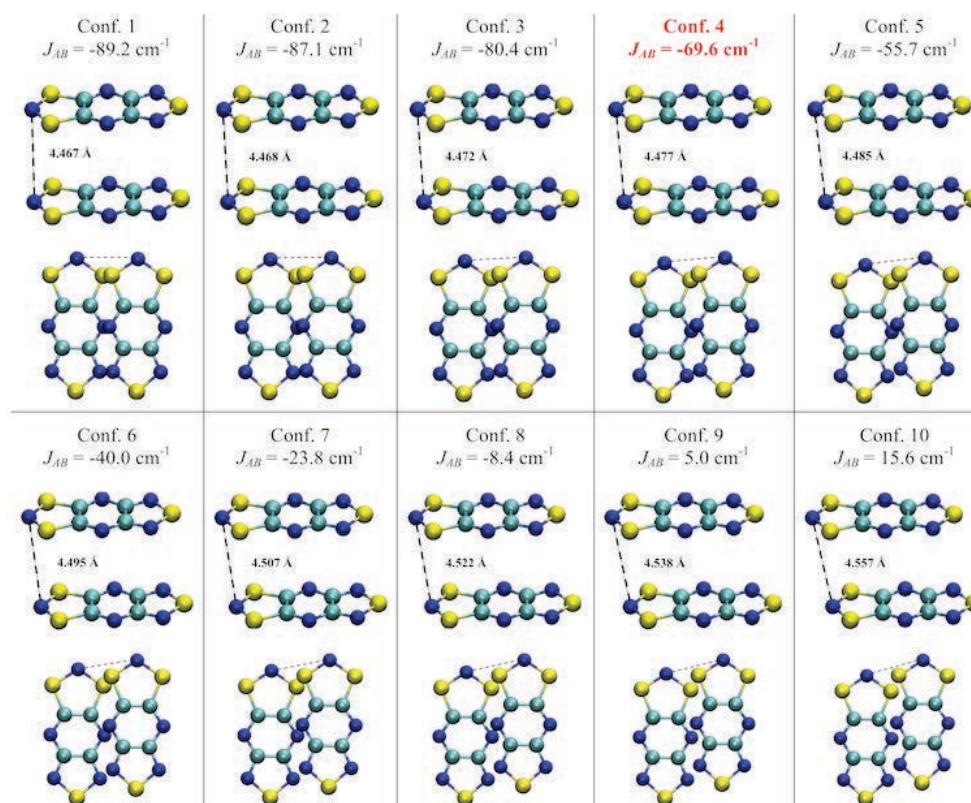


Figure A5.1: TDPDTA configurations considered to explore the effect of the longitudinal translation d_{LG} . The longitudinal shift applied to Conf. #1 is a continuous d_{LG} increase of 0.1 Å . The distance $N^* \cdots N^*$ and corresponding J_{AB} value are reported on top of each dimer. Note that both geometry and J_{AB} value of Conf. #4 (in red, $d_{LG} = 0.3 \text{ Å}$) are in agreement with the experimentally characterised dimer and corresponding calculated J_{AB} data. Top: side view; Bottom: top view of configurations.

The starting point of the extra-analysis here reported is extracted from the TDPDTA magneto-structural correlation map. Let us remind that this correlation map

Table A5.1: Parameters for the experimentally resolved structure and Configuration #4 (see Figure A5.1). Differences (in absolute value) between experimental and configuration #4 data are reported

	d_{IP}	d_{SL}	N*-N*	J_{AB}
	\AA	\AA	\AA	cm^{-1}
Experimental	3.31	2.97	4.45	-69.1
Configuration #4	3.28	3.05	4.48	-69.6
Δ Exp.-Conf. #4	0.03	0.08	0.03	0.72

gives information about the magnetic J_{AB} coupling interaction as a function of two variables, namely, d_{IP} and d_{SL} . Within this geometrical framework, we chose the TDPDTA configuration closer to the experimental one as initial geometry (Configuration 1 with $d_{LG} = 0$ in Figure A5.1). Configuration 1 was then evaluated under longitudinal translation between monomers. It thus follows that a displacement $d_{LG} = 0.1 \text{ \AA}$ was applied to this model, moving one monomer with respect to the other (see Figure A5.1 for d_{LG} configurations ranging from 0 (Conf. 1) to 1 \AA (Conf. 10)).

The configuration that better matches the experimentally resolved one in terms of magnetic coupling is configuration number 4 (see Figure A5.1 and Table A5.1). The geometrical parameters are slightly different with respect to the experimental structure, but still of the same order of magnitude. The ultimate goal of this analysis has been thus achieved since we have provided evidence of the complexity undergone by TDPDTA in terms of structural arrangement. Further analysis will be reported in the future.

A.6 Interaction Energy Maps of TTTA, PDTA, 4-NCBDTA, and TDPDTA.

The interaction energy maps (IEMs) give the possibility to assess which is the energetic cost needed to reach the FM region highlighted in pale yellow in the middle of Figures A6.1a (TTTA) and A6.1c (4-NCBDTA). These two regions range from 0 kcal mol⁻¹ to -6 kcal mol⁻¹, namely an interval of stability in which the FM dimers can form. On the other hand, in the case of PDTA, it can be seen that the FM area (as predicted from the corresponding magneto-structural correlation map) only encompasses regions where the binding energy is highly positive. Hence, in turn, every possible FM dimer is definitively prevented.

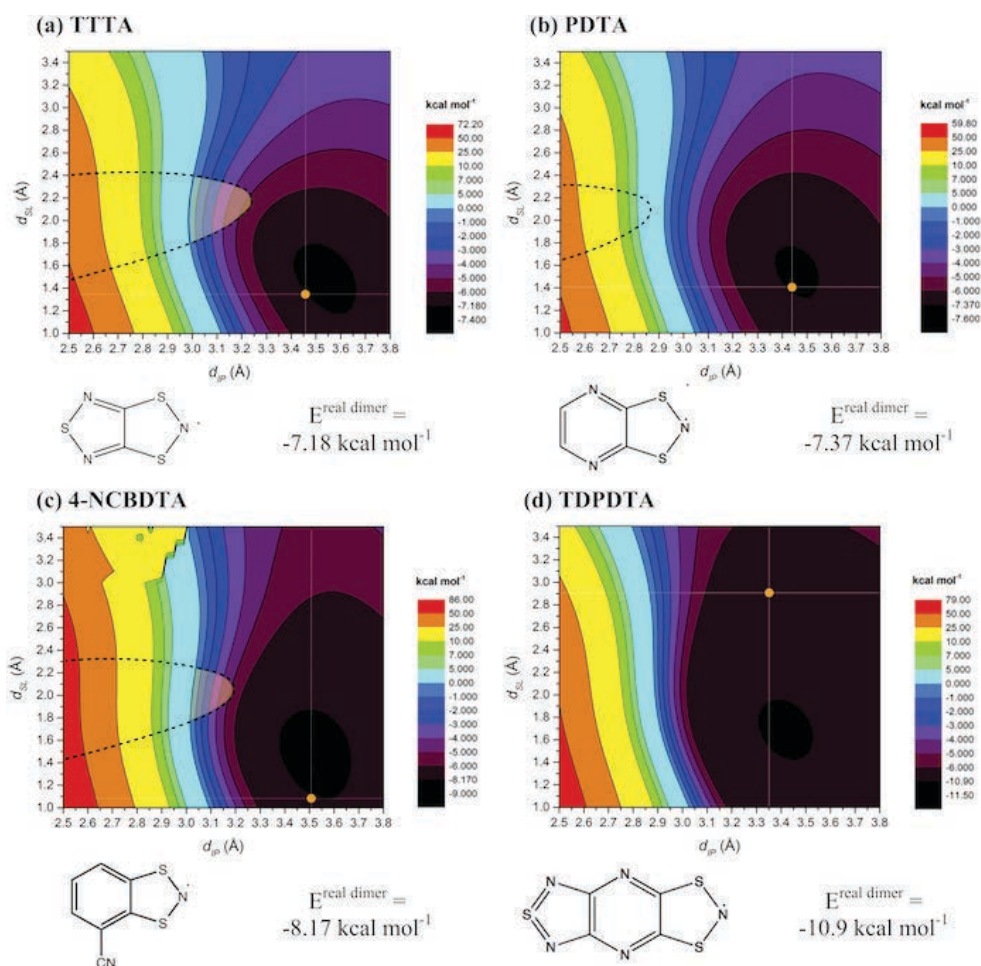


Figure A6.1: Interaction Energy Maps (IEMs) of (a) TTTA, (b) PDTA, (c) 4-NCBDTA and (d) TDPDTA. The IEMs are computed at DFT/UB3LYP level using 6-31+G(d) basis set by means of Gaussian09 package.

On top of the interaction energy maps IEMs, the evaluation of the Binding Energy (BE) for the TTTA periodic structure has been performed in order to assess if dimers, with small d_{IP} values, were (i) meaningful or not, and (ii) how good the gas models used in the IEM maps performed compared to periodic structure calculations. To check it, the unit cell was doubled along the b -axis, in agreement with the propagation direction of the molecular columns in the real crystal. Then, the cor-

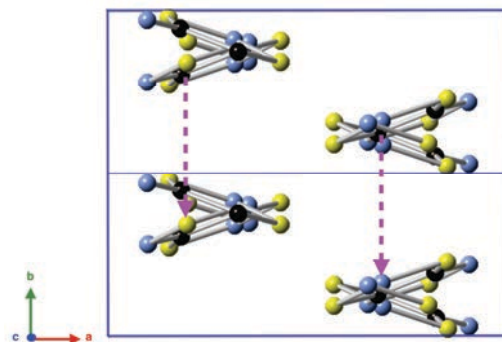


Figure A6.2: TTTA double unit cell. The purple arrows show the direction to which the compression has been performed, *i.e.* along the *b*-axis.

Table A6.1: Binding energy (in kcal mol⁻¹) per unit cell and per molecule as a function of the compression of the *b*-axis using 0.05 Å as step size.

	Compression	Binding Energy	Binding Energy
	along <i>b</i> -axis		per Molecule
	Å	kcal mol ⁻¹	kcal mol ⁻¹
Experimental Unit Cell	0	-132.1	-16.5
A	-0.05	-130.6	-16.3
B	-0.10	-128.2	-16.0
C	-0.15	-122.9	-15.4

responding total energy was computed by means of the Quantum Espresso¹⁴ code, with the D3 semi-empirical dispersion functions¹⁵, with kinetic energy cutoff of 30 Ry and ultrasoft pseudopotentials¹⁶, at PBE¹⁷ level. To obtain BE, the total energy of an isolated TTTA molecule was computed, using exactly the same setting as described above ($E_{\text{T}}^{\text{sm}} = -143.619928$ Ry). This value was used to compute all set of BEs reported in Table A6.1. After checking the BE for the real double unit cell (see Figure A6.2), the upper layer of molecules was compressed by 0.05, 0.10 and 0.15 Å. For each new cell, the total energy was computed and the corresponding BE derived (see Table A6.1). In all three A, B and C models, the BE turns out to be negative.

¹⁴ (a) P. Giannozzi, et al. J. Phys.: Condens. Matter, 2009, 21, 395502 <http://dx.doi.org/10.1088/0953-8984/21/39/395502>; (b) P. Giannozzi, et al. J. Phys.: Condens. Matter, 2017, 29, 465901.

¹⁵ S. Grimme, J. Antony, S. Ehrlich, H. Krieg, J. Chem. Phys, 2010, 132, 154104.

¹⁶ K.F. Garrity, J.W. Bennett, K.M. Rabe, D. Vanderbilt, Comp. Mat. Science, 2014, 81, 446-452.

¹⁷ J.P. Perdew, K. Burke, M. Ernzerhof, Phys. Rev. Lett., 1996, 77, 3865.

This, along with the previous results from the IEM maps, confirms that the models chosen, albeit ideal, are representative for the real systems investigated.

Acknowledgments

My experience as a PhD student could not have been the same without the people I met along my journey. These acknowledgments are only indicative of how thankful I am to everyone, and cannot represent completely my admiration and respect.

First of all, I would like to acknowledge my two thesis supervisors, Professor Ria Broer and Professor Juan Novoa. They gave me the chance to join the Theoretical Chemistry and Computational Modelling PhD program, both supporting and believing in me. This was extremely important not being very familiar with the Theoretical Chemistry world. Nevertheless, they both were able to transfer to me their passion and love for this subject. I will keep their example wherever I go.

Then, I would like to say THANK YOU to Professor Jordi Ribas and Professor Mercè Deumal, who co-tutored me since the very beginning and with whom I planned the research line and tasks to accomplish. In particular, I would like to thank Professor Jordi Ribas once more, who took to heart my work, supporting and helping me to achieve a scientific maturity that is now my duty to enhance even more. I want to thank Dr. Remco W. A. Havenith, that during the Groningen period has greatly helped me to learn new computational methods, expanding once more my background and raising my scientific curiosity.

I want to acknowledge Professor Shirin Faraji, for her precious help and very useful suggestions and support, but also Dr. Sergi Vela, for his help, suggestions and discussions! Of course, I want to thank also Dr. Gerrit-Jan Linker, for the nice and interesting debates on science!

I want to thank the "Barcelona" family, in particular my office mates, Cristina, Raul, Julia, Andi, Toni, Isaac, Maria but also Stefan, Francesc, Francis, and all the people I met. It was a great time and I am in love with the city.

I want to thanks the "Groningen" family, all the people who made the last year a great period, in particular Luis, Selim, Riccardo, Kathir, Maria, Meilani, Goran,

Kiana, Wouter, Siva, Isaac, Francesca, Enrico, Vito and Jordi. I would like to remember my friend Michele. I want to acknowledge all the PhD students from the ITN program with whom I shared many travels, schools and conferences, Neus, Maximilian, Maria, Meilani, Carles, Stefano, Francesco, Martina, Giovanna, Dmytro, Andi, Ewa, Gabriele and Jelle.

To the guys in Venice (“I fioy”) for always being welcoming. In particular Eleonora, *ti xe forte 'more!*

The possibility to join such a beautiful PhD program, that gave me incredible chances to meet marvelous people and to gain experience as a scientist and human being around the world could not have been possible without the support and help of great people and professors, Stefano Fabris, Matteo Farnesi Camellone, Patrizia Canton and Andrea Pietropolli Charmet. In particular I want to acknowledge Patrizia, for addressing me towards the right project at the proper time, and Patrizia and Stefano (once more!) for believing and supporting me to achieve this important step in my career.

The encouragement and support is essential when facing such ambitious program, especially when it brings you far away from your Family. This is why I want to say THANK YOU to my family, Alessandra, Stefano and Ludovico for the huge, enormous support they gave me when I was feeling down or upset, and encouraging me to always look at life in a positive way. I want to thank Genny for being part of our family. I want to say THANK YOU to my soulmate and love Alessandra. Distance becomes irrelevant when your partner shares your dreams! Thanks for everything! Finally, I want to saying thanks to all the people that (probably!) I forgot to mention, but that contributed to make this PhD a marvelous experience.

Tommaso Francese

Venice
Barcelona
Groningen